University of Kerbala
College of Science
Department of Chemistry

Functionalization of New Porphyrin Derivatives for Some Applications

A Dissertation

Submitted to the Council of the College of Science/ University of Kerbala in a Partial Fulfillment of the Requirements for the Degree of Doctor of Philosophy of Science / Chemistry

By

Mohammed Thamer Jaafar

B.Sc. Chemistry (2007) / Al Mustansiriyah University
M.Sc. Chemistry (2013) / Cairo University

Supervised by

Prof. Dr. Luma Majeed Ahmed   **Prof. Dr. Rahman Tama Haiwal**

2023 AD   **1445 AH**

بِسْمِ اللَّهِ الرَّحْمَٰنِ الرَّحِيمِ

اللَّهُ نُورُ السَّمَاوَاتِ وَالْأَرْضِ ۚ مَثَلُ نُورِهِ كَمِشْكَاةٍ فِيهَا مِصْبَاحٌ ۖ الْمِصْبَاحُ فِي زُجَاجَةٍ ۖ الزُّجَاجَةُ كَأَنَّهَا كَوْكَبٌ دُرِّيٌّ يُوقَدُ مِن شَجَرَةٍ مُّبَارَكَةٍ زَيْتُونَةٍ لَّا شَرْقِيَّةٍ وَلَا غَرْبِيَّةٍ يَكَادُ زَيْتُهَا يُضِيءُ وَلَوْ لَمْ تَمْسَسْهُ نَارٌ ۚ نُّورٌ عَلَىٰ نُورٍ ۗ يَهْدِي اللَّهُ لِنُورِهِ مَن يَشَاءُ ۚ وَيَضْرِبُ اللَّهُ الْأَمْثَالَ لِلنَّاسِ ۗ وَاللَّهُ بِكُلِّ شَيْءٍ عَلِيمٌ ٣٥

صدق الله العلي العظيم

سورة النور
الآية (35)

Dedication

To my father for support, assistance, and kindness, all thanks and appreciation to you.

To mother soul (may God have mercy on them)

To my beloved wife and my sons for your support, all thanks to yours

To whom I greatly appreciate and respect, Prof. Dr. Luma M. Ahmed

Mohammed thamer

Acknowledgments

Praise be to **Allah**, Lord of the worlds, and may Allah's blessings be upon **Mohammad** and his pure family, and praise be to Allah for his countless blessings and gifts.

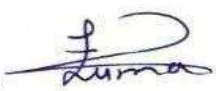I would like to extend my sincere thanks, gratitude, and appreciation to:

My supervisors are ***Prof. Dr. Luma Majeed Ahmed*** *and* **Prof. Dr. Rahman Tama Haiwal** for her continuous support, invaluable suggestions, and great contributions since the inception of this work.
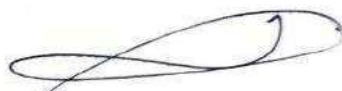
I also thank all the faculty members of the Chemistry Department of the College of Science at the University of Karbala for their valuable support for the work.

Finally, I thank my **father**, my **wife,** and my **sons**, who was the main supporter in completing my scientific career, as well as everyone who supported me even with a word.

Supervisor Certification

We certify that this thesis **" Functionalization of New Porphyrin Derivatives for Some Applications"** is conducted under our supervision at the department of chemistry, College of science, University of Kerbala, as a partial fulfillment of the requirements for the degree of philosophy in chemistry.

Signature:

Name: **Dr. Luma M. Ahmed**

Title: Professor

Date: / / 2023

Signature:

Name: **Dr. Rahman Tama Haiwal**

Title: Professor

Date: / / 2023

Report of the Head of Chemistry Department

According to the recommendation presented by the Chairman of the Postgraduate Studies Committee, I forward this thesis for discussion.

Signature:
Head of Chemistry Department: Prof. Dr. Luma Majeed Ahmed
Address: University of Kerbala / College of Science
Date: /   / 2023

Examination Committee Certification

We, the examining committee, certify that we have read this thesis "**Functionalization of New Porphyrin Derivatives for Some Applications**" and examined the student (**Mohammed Thamer Jaafar**) in its contents and that in our opinion, it is adequate as a thesis for the degree of philosophy of science in chemistry.

(Chairman)
Signature:
Name: Dr. Hamida Idan Salman
Title: Professor
Address: University of Kerbala / College of Education for pure Science
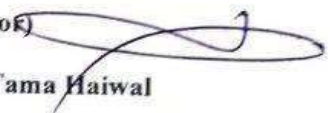Date: 7 / 12 2023

(Member)
Signature:
Name: Dr. Zeid Hassan Abood
Title: Professor
Address: University of Kerbala / College of Science
Date: /   / 2023

(Member)
Signature:
Name: Dr. Mohanad Mousa Kareem
Title: Professor
Address: University of Babylon / College of Science
Date: /   / 2023

(Member)
Signature:
Name: Dr. Haitham Dalol Alshebly
Title: Professor
Address: University of Kerbala / college of Science
Date: / / 2023

(Member)
Signature:
Name: Dr. Ahmed Hadi abid AlAmeer
Title: Assistant Professor
Address: University of Kerbala / College of Science
Date: /   / 2023

(Member & Supervisor)
Signature:
Name: Dr. Luma Majeed Ahmed
Title: Professor
Address: University of Kerbala / College of Science
Date: / / 2023

(Member & Supervisor)
Signature:
Name: Dr. Rahman Tama Haiwal
Title: Professor
Address: University of Kerbala / College of Science
Date: / / 2023

Approved by the council of the College of Science in its session No. in   /   / 2023
Signature: Hassan.J. Jawad
Name: Dr. Hassan Jameel Jawad Al-fatlawy
Title: Professor
Address: University of Kerbala - Dean of College of Science
Date: / 11 2023

Abstract

This work investigates series of new heterocyclic derivatives that synthesized from several porphyrin derivatives (4,4',4'',4'''-(porphyrin-5,10,15,20-tetrayl) tetra benzoic acid) compound (3), (4-(10,15,20-tris(3-hydroxyphenyl) porphyrin-5-yl) benzoic acid) compound (8), and (4,4'-(10,20-bis(3-hydroxyphenyl) porphyrin-5,15-diyl) di benzoic acid) compound (12) obtained. These compounds were obtained by reacting Pyrrole with 4-formyl benzoic acid and 3-hydroxy benzaldehyde at different molar ratios. Subsequently, porphyrin derivative-component amides 5a-f and 6a-f were produced by reacting compound (3) with different amine derivatives at different molar ratio via a one-pot, Porphyrin derivative-component amides 9a-d and 11a-e were produced by reacting compound (8) with different amine derivatives different molar ratio via a one-pot. Porphyrin derivative-component amides 13a-f were produced by reacting compound (12) with different amine derivatives at a 1:2 molar ratio via a one-pot.

The graphene quantum dots (GQD) were synthesised from starch as a precursor that has been performed in a single pot using a hydrothermal process. The TiO$_2$/GQD nano-composite was prepared using an in-depth ultrasonic technique to use as an anode in a solar cell. The analysis demonstrated that GQD is nanomaterial with mean crystal size and average particle size equal to 9.25 nm and 11.05 nm, and increase after its composite to 34.39 nm and 79.47 nm respectively.

The synthesis of cadmium ferrite semiconductors (CdFe$_2$O$_4$) from ferric nitrate (Fe(NO$_3$)$_3$.9H$_2$O) with cadmium chloride (CdCl$_2$.2H$_2$O) was performed via a precipitation process in the presence of positive surfactant (CTAB). The TiO$_2$/CdFe$_2$O$_4$ nano-composite was prepared using an in-depth ultrasonic

technique to use as an anode in a solar cell. XRD data observed the mean crystal size of $CdFe_2O_4$ increases after being its composite from 21.07 nm to 36.96 nm.

In this work, TiO_2 with dyes 3 and 8 as anodes was used to analyze dye-sensitive solar cells (DSSCs). In terms of Photoelectric Conversion Efficiency (PEC%) with TiO_2, dye 8 performed better than dye 3 and showed the potential for improved solar cell performance. Additionally, DSSCs utilizing a $TiO_2/CdFe_2O_4$ composite anode explained greater PCE% values than those using a TiO_2/GQD anode.

The activity of synthesized materials was investigated as a corrosion inhibitor using carbon steel (CS) as a model for corroded materials. The obtained results showed that the synthesized porphyrins derivatives were effective corrosion inhibitors to 0.1 M hydrochloric acid solution for CS. In the case of the derivative (5c), a maximum inhibition efficiency (IE%) was recorded and it was around 74%.

Table of Contents

List of abbreviations and Symbols

Abbreviation and Symbols	The Meaning
AcOH	Acetic acid
Bg	Band gap
C	Concentration
CB	Conduction band
CE	Conversion efficiency
^{13}C-NMR	Carbon Nuclear Magnetic Resonance
CTAB	Cetyltrimethylammonium bromide
d	Doublet
D*	Photoexcited dye
DDQ	2,3-dichloro-5,6-dicyanoquinon
DFT	Density functional theory
DMSO	Dimethyl sulfoxide
DMSO-d_6	Deuterated Dimethyl Sulphoxide
DSSCs	Dye-sensitized solar cells
Ecorr	Corrosion potential
EDX	Energy dispersive X-rays
E_f	Fermi Level
E_g	Energy gap
ESI-MS	Electrospray Mass Spectrometry
Et_3N	Triethylamine
EtOAc	Ethyl acetate
EtOH	Ethanol
eV	Electron Volt
FE-SEM	Field Emission Scanning Electron Microscopy
FF	Fill factor
FTIR	Fourier Transform Infrared Spectrophotometry
FTO	Fluorine-doped tin oxide
FWHM	Full width half –maximum
^{1}HNMR	Proton Nuclear Magnetic Resonance Spectroscopy
HOMO	Highest Occupied Molecular Orbital
I_{corr}	Corrosion current density
IE	Inhibitory efficiency
I_{max}	Maximum current
I_o	Total incident irradiance
I_{sc}	short circuit current
ITO	Indium tin oxide
J	Coupling constant
J_{max}	Maximum power point current
J_{sc}	Short circuit current
L	Crystallite Size
LUMO	Lowest Occupied Molecular Orbital
M	Multiplet
m.p.	Melting points
m/z	Mass/charge
M^+	Molecular ion
R_f	Retention factor

Rp	polarization resistance
r.t	Room Temperature
S	Singlet
T	Temperature
TLC	Thin Layer Chromatography
US	Ultrasound
UV-Vis	Ultraviolet light in the range from 315 to 830 nm
VB	Valance Band
V_{max}	Maximum voltage
V_{oc}	open circuit voltage
XRD	X-Ray diffraction
δ	chemical shift in NMR
η	Efficiency
λ	Wavelength
μ_{eff}	Magnetic Moment
βa	Anodic Tafel
βc	Cathodic Tafel

CHAPTER ONE

Introduction

1.1 General Introduction

Porphyrins and their derivatives, which include chlorine, bacterio-, and iso bacterio-chlorins…etc. Figure (1-1), are without a doubt the most researched members of the family of tetrapyrrolic macrocycles[1].
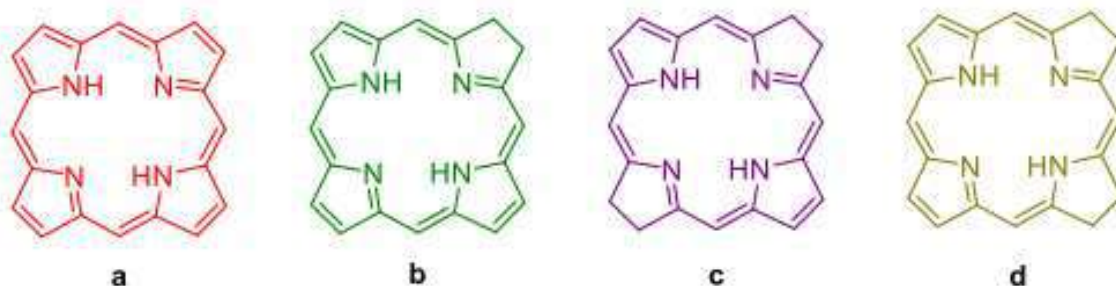
Figure 1-1: Structures of (a) Porphyrin,(b) Chlorin,(c) Bacteriochlorin, and (d) Isobacteriochlorin[2].

These pigments, which can be found in both animals and plants, are essential for a wide variety of biological processes, such as the transport of oxygen in animals, which is made possible by heme [3] and hematoporphyrin [4] Figure (1-2), photosynthesis, which is made possible by chlorophylls, and the brain and nervous system, which are made possible by vitamin B12 or cobalamin [5] as pictured in Figure (1-3). These compounds belong to a family of photosensitive molecules that are of interest because of the specific optical features they possess.

Heme b   Hematoporphyrin
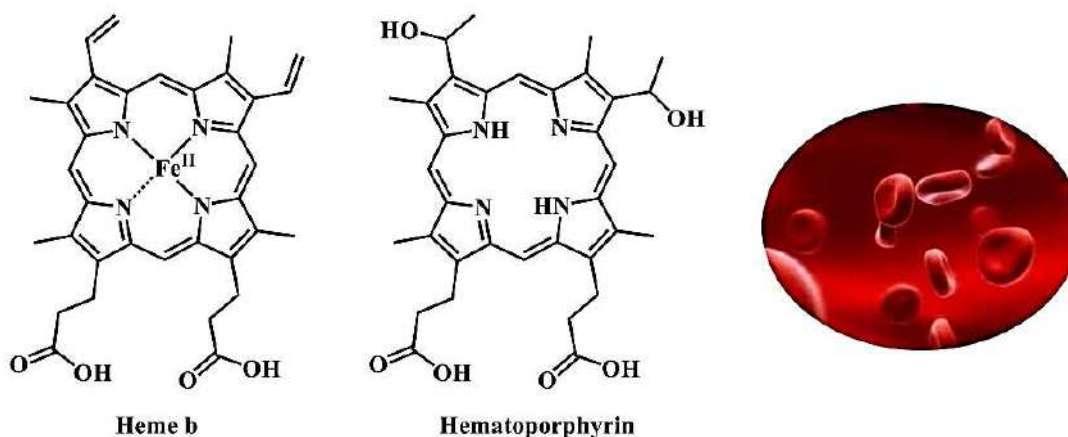
Figure 1-2: Heme b and hematoporphyrin are two examples of porphyrins that may be found in nature[4].
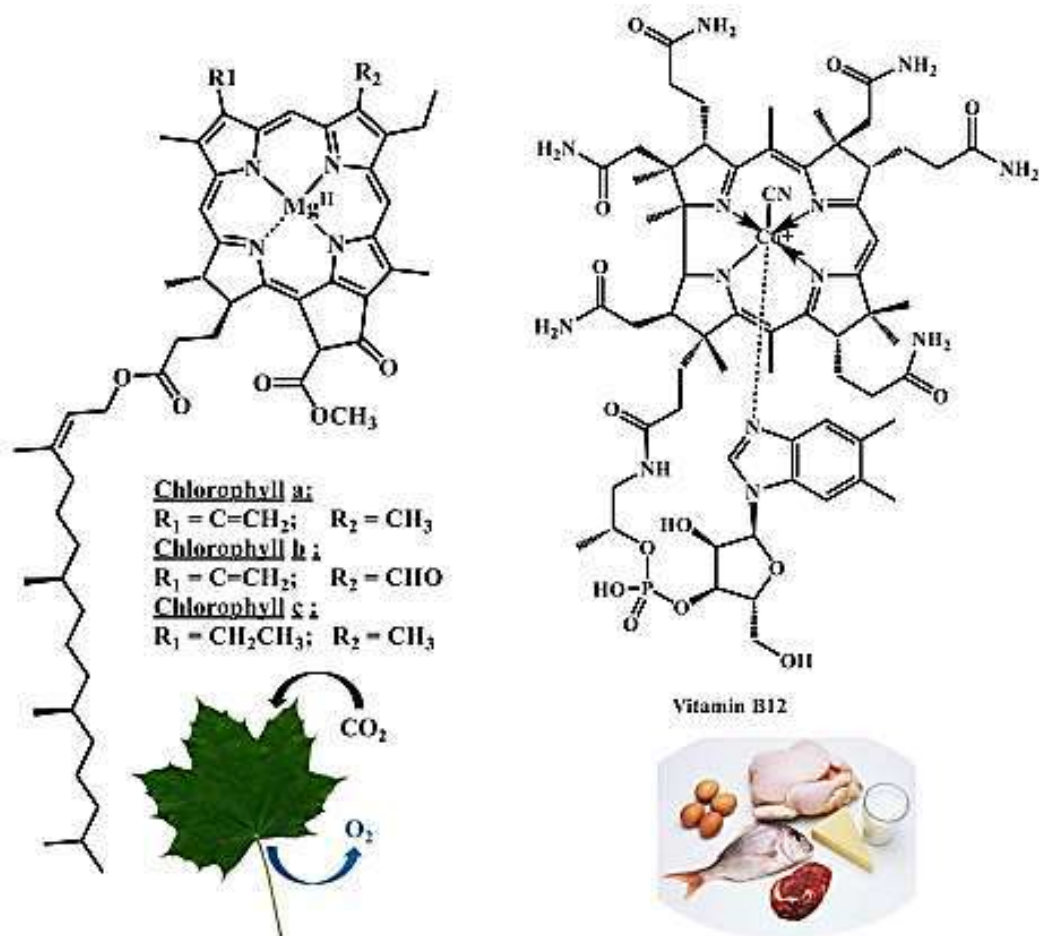
Figure 1-3: Chlorophyll and vitamin B12 are two examples of porphyrins that may be found in nature[5].

The origin of the term "porphyrin" may be traced back to ancient Greece, and the name itself indicates the unique quality of the substance. The word "porphyria" which refers to the dark purple or violet of several of these compounds, derives from the Greek word "Porphyra" or its Latin equivalent, porphurá. The term "pigments of life" was given to porphyrins because of their brilliant color as well as their important biological role in the natural world [6]. Since J. L. W. Thudichun 1867 first isolated porphyrin from blood, particularly hematoporphyrin (which was first dubbed creatine[7, 8].This one-of-a-kind tetra pyrrolmacrocycle and its derivatives have garnered a lot of attention in the scientific world.

These compounds are extremely simple to chemically modify, particularly in the meso- and omega positions, to either boost their water solubility or generate

new features specifically suited for certain applications [9-11]. Without wishing to be complete, some examples that may be given include photosynthesis imitation, optoelectronics, and medicinal applications [12, 13] or the process of catalysis [14]. In addition, historically speaking, since the significant discovery of an isomeric porphyrin called porphycene by E. Vogel [15] which has revolutionized porphyrinoid chemistry, a wide range of porphyrins and their derivatives have been available to researchers. Calixpyrroles, contracted porphyrinoids, extended porphyrinoids, heteroatom-exchanged porphyrinoids, and inverted porphyrinoids are some further instances that may be cited[16-18]. The formation of highly conjugated derivatives was achieved by the elongation of the -system by using fused polycyclic aromatic rings on the periphery of the macrocyclic core [19]. In the same manner Figure (1-4), a novel family of completely synthesized tetrapyrrolic macrocycles known as phthalocyanines [20] and its derivatives have evolved in recent years (e.g., sub-phthalocyanines), Phthalocyanines were discovered by accident in 1907 when researchers were investigating the characteristics of 1,2-cyanobenzamide; the discovery was announced for the first time the same year[21]. Later, in the year 1927, Swiss researchers were attempting to produce phtalonitriles when they accidentally made copper phthalocyanines along with other chemicals [22]. In today's world, modern chemistry provides a whole toolbox full of new synthetic protocols, which enable the more efficient preparation of novel porphyrinoids with newly discovered properties to be researched.
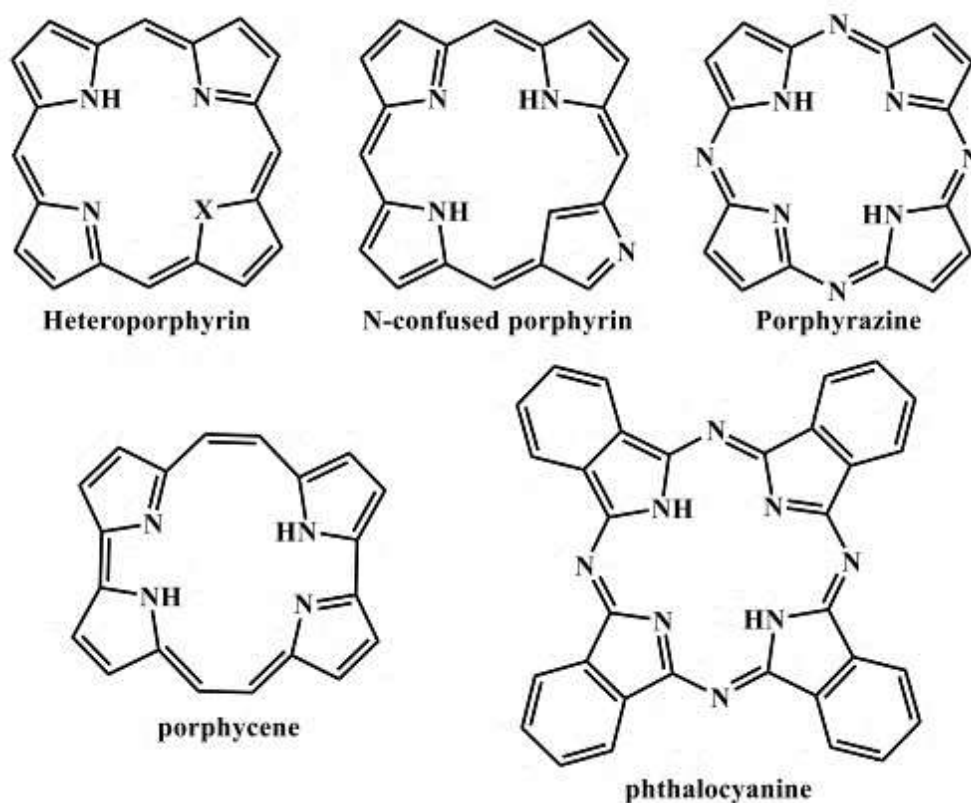
Figure 1-4: Porphyrinoids and their derivatives' structures[19].

1-2 Structure

Derivatives of porphyrin, also known as porphyrins Figure (1-5). This substance is made up of four pyrrole rings that are connected using methine bridges (=CH-) at the carbons of each ring. As a consequence, two pyrrole units (-NH) and two pyrrole nine units (=N) are produced. W. Küster was the first person to propose the structure of the cyclic tetrapyrrole in 1912 [23], and later research demonstrated that the trans-NH-tautomer was the most stable form of the compound. Porphyrins all have the same fundamental structure, but different substituents can be attached to either the carbons (positions 2, 3, 7, 8, 12, 13, 17, and 18) of the pyrrole core (also called pyrrolic) or the meso carbons (positions 5, 10, 15, and 20)[1, 24].

The two nitrogen atoms located in the center can donate protons, which results in the formation of a diction [25]. On the other hand, the two NH groups can donate a proton, which results in the formation of a dianion.

Also, [26] the synthesis of this dianion is likely to result in the metalation of porphyrins when numerous different metals are present. The complexes that are obtained as a result are referred to as "metalloporphyrin" as opposed to "free base" in the absence of metalation, as shown in Figure (1-6). They can exhibit a wide range of different geometries depending on the type of metallic ion that is present [27].

1*H*-pyrrole
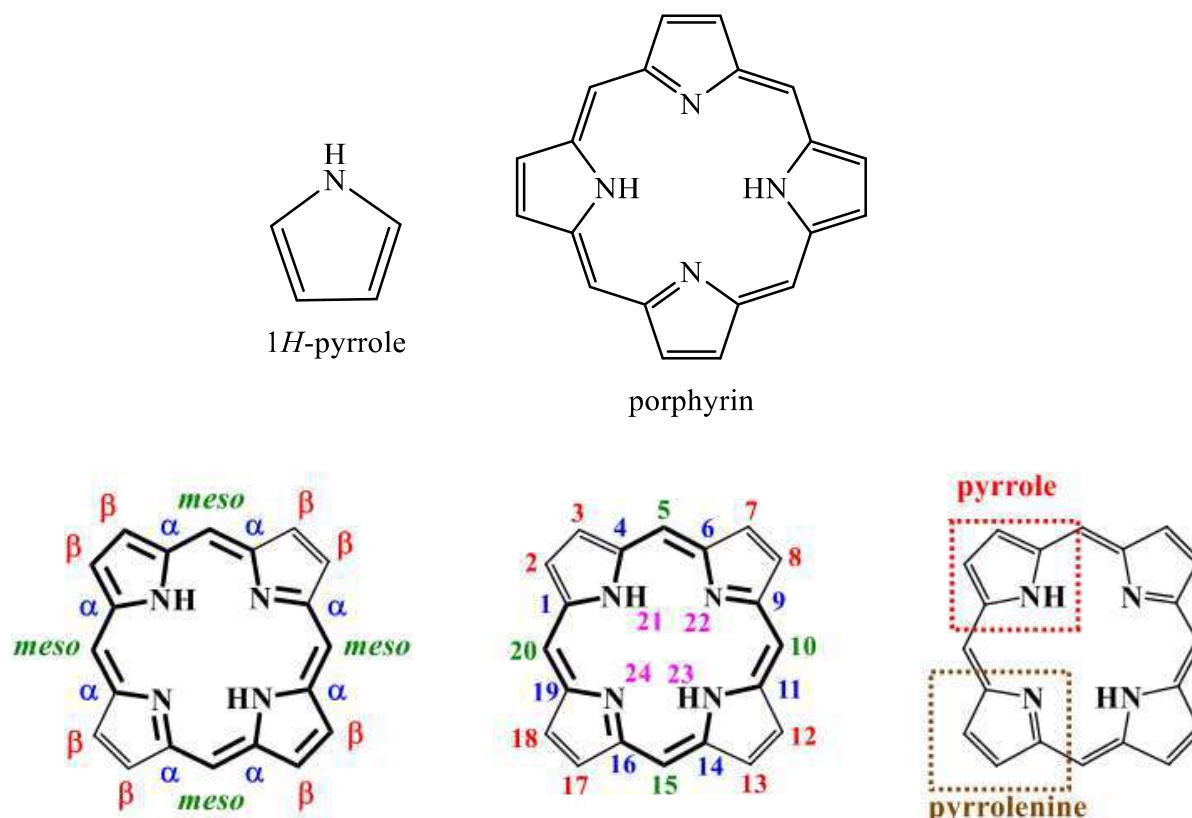
porphyrin

Figure 1-5: The IUPAC has numbered and named the porphyrin locations using the porphyrin core.

free base
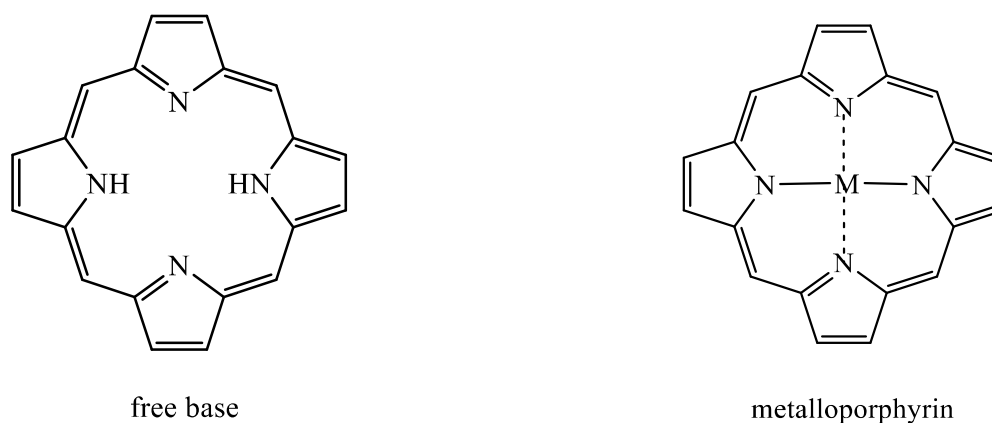
metalloporphyrin

Figure 1-6: General structure of the free base and metalloporphyrin

It is generally agreed upon that the aromaticity of porphyrin is one of a kind and that it originates from the diatopic ring that is spread everywhere over the macrocycle. The system is made up of 22 electrons, of which 18 are engaged in the aromaticity of the porphyrin macrocycle and hence adhere to the Hückel criteria. However, due to their similarity to annulene [28, 29], they are sometimes described as multiple bridged aromatic diaza18 annulene systems in the scientific literature [30].

Chlorophyll is the most prominent example of chlorine, also known as 2,3-dihydroporphyrin. Chlorins are mostly organic molecules. Their structure is comparable to that of porphyrins, except for the reduction of a double bond that is located on the periphery Figure (1-1). Therefore, their system consists of just 20 electrons, but even so, 18 of those electrons are engaged in the aromaticity of the macrocycle. In the year 1932, Van Niel identified a second group of porphyrin derivatives called bacteriochlorins. These compounds fall within the bacteriochlorins category [31]. The most well-known photosynthetic pigments are called bacteriochlorophylls, and they are found in phototropic bacteria (such as Chloracidobacterium thermophilus[32], purple bacteria, and green sulfur bacteria, among others). These compounds feature two reduced double bonds, which may be on two nearby pyrrolic patterns (isobacteriochlorins) or in opposite positions (bacteriochlorins) Figure (1-1). The aromaticity of the macrocycle requires the participation of all 18 electrons that make up the system. Phthalocyanines, which have only been discovered in tiny amounts in nature, might be thought of as synthetic porphyrin derivatives, such as tetra benzo [5,10,15,20]-tetraazaporphyrin, as shown in Scheme (1-1). They are aromatic macrocycles with a planar structure and contain 18 electrons, which classifies them as porphyrins. Tetraazaisoindole macrocycle is the name given to its structural arrangement, which consists of four groups of isoindoles connected in positions one through three by nitrogen bridges Figure (1-6). As

porphyrins, they are chemically and thermally stable, and they can integrate a variety of different metallic ions into their core[33].
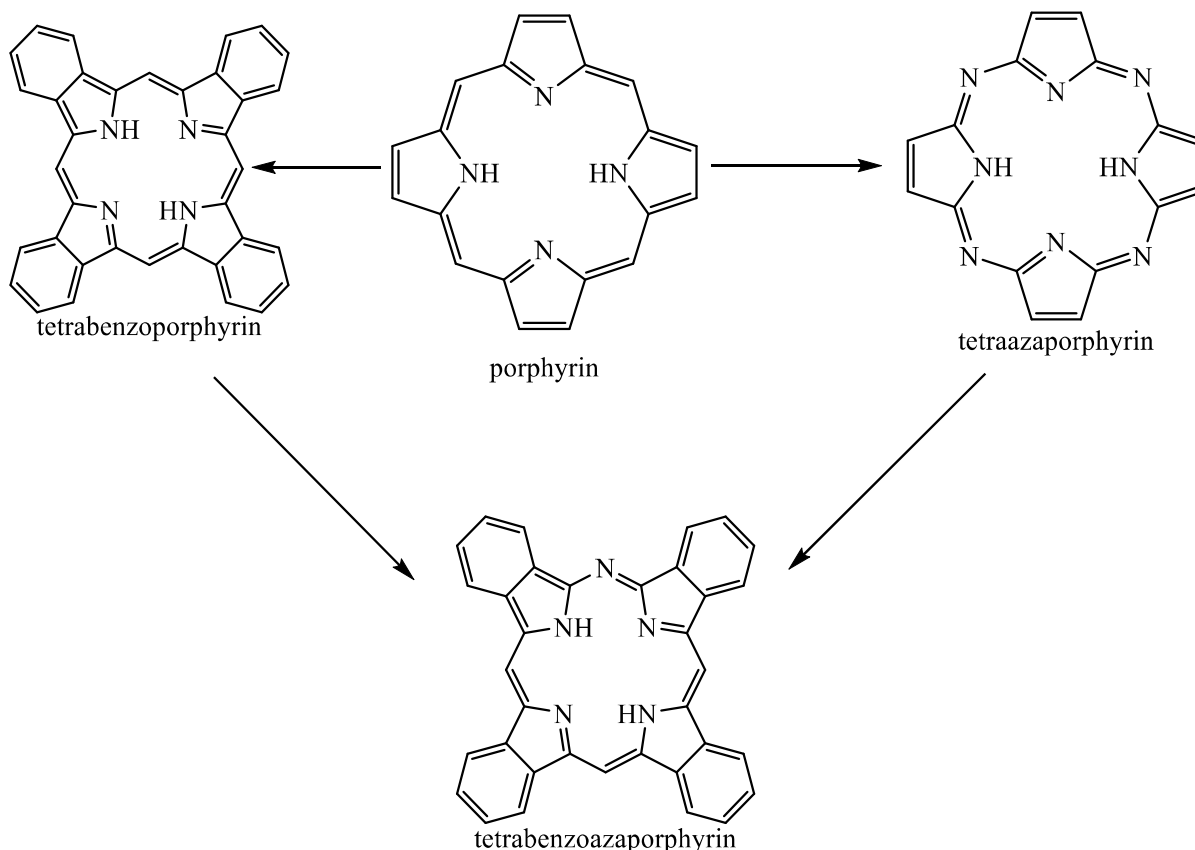
Scheme 1-1: Structural relationships between porphyrins and phthalocyanines.

1.3 Synthesis pathways

There are just too many potential synthetic routes for producing tetrapyrrolic macrocycles for this article to discuss them all in depth. This section will focus on the major routes that may be followed to generate porphyrin.

1.3.1 Symmetrically substituted porphyrins (tetra-substituted porphyrins)

The type porphyrins are common because of how easy they are to prepare. They also provide room for potential future chemical alterations. Condensation of pyrrole in the presence of the required aldehyde often occurs in one step or two step one flask reactions throughout the synthesis process that is demonstrated in Scheme (1-2) [34, 35].
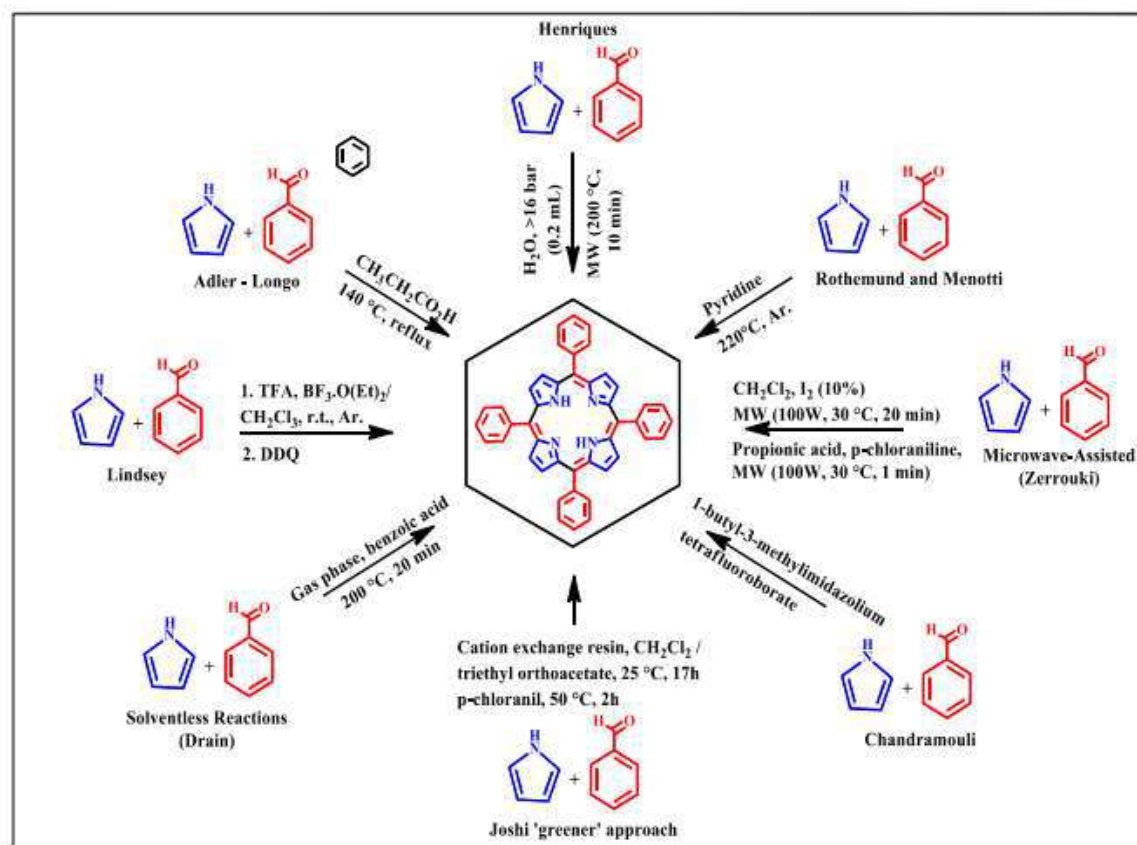
Scheme 1-2: The tetraphenyl porphyrin's general synthesis processes, along with the requirements that must be met; r.t. stands for room temperature, MW for microwave, Ar for argon, TFA for trifluoracetic acid, and DDQ for 2,3-dichloro-5,6-dicyanobenzoquinone[36].

1.3.2 Pathway condensation between pyrrole and aldehyde

A. Rothemund synthesis

In 1935, Rothemund [37] documented the first synthesis of porphyrins in sealed tubes using condensation between pyrrole and aldehydes. This condensation took place between pyrrole and aldehydes. In 1939, he succeeded in obtaining numerous meso-tetrakis porphyrins, one of which was meso-tetraphenyl porphyrin (TPP), which was likewise contained in tubes and heated at 142-150 degrees Celsius for 24 hours. In the latter part of 1941, he was succeeded, especially in the creation of TPP in sealed tubes by heating them at 220 degrees Celsius for 48 hours [38]. Only the aldehydes that could withstand heat the best were able to create meso-tetryl porphyrins under the challenging circumstances of the experiment, although the yields were only between 5 and

10%. Chlorins that were produced during the synthesis were converted into porphyrin by utilizing DDQ (2,3-dichloro-5,6-dicyanoquinone) as an oxidant. The reduction ranged from 10 to 20% is explained in Scheme (1-3).
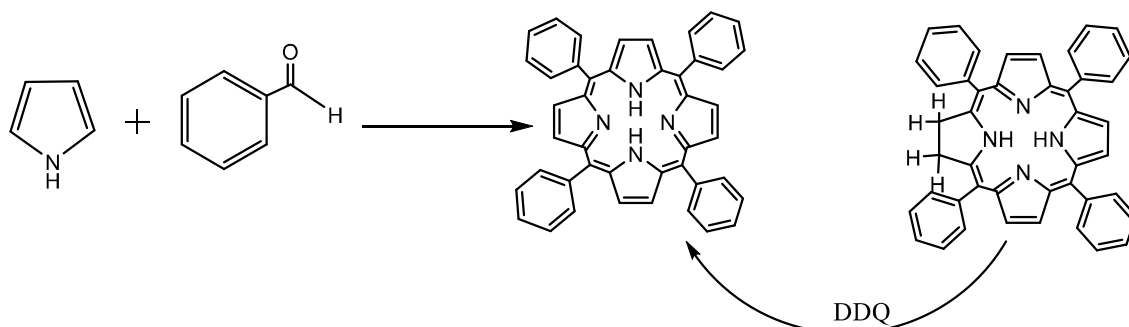
Scheme 1-3: Example of *tetra*-phenyl porphyrin synthesis performed according to Rothemund.

B. Adler-Longo synthesis

Adler and Longo [39] successfully synthesized TPP in 1964 by bubbling air through a combination of pyrrole and benzaldehydes that was refluxed in acetic acid for thirty minutes. This was done in order to oxidize any porphyrinogen intermediates that were produced throughout the process. Then, in 1967[40], they established a relationship among acidity, temperature, solvent, and amounts of introduced reactants on the one hand, and the condensation yield of pyrrole and benzaldehyde on the other. Their approach was perfected by refluxing an equal-molar combination of the two reactants in propionic acid for thirty minutes while aerating the environment. Under these circumstances, TPP may be made with a yield of 20% by first washing it with methanol and then washing it with hot water, as obtained in Equation (1-1). Despite this, there were still two major caveats to consider about this synthesis. The use of aldehydes that are air-sensitive is prohibited, and there is also a worry about purification. Even while TPP crystallizes in propionic acid after being cooled to ambient temperature, this behavior is not shared by all porphyrins. In addition, it is often impossible to reproduce the results.
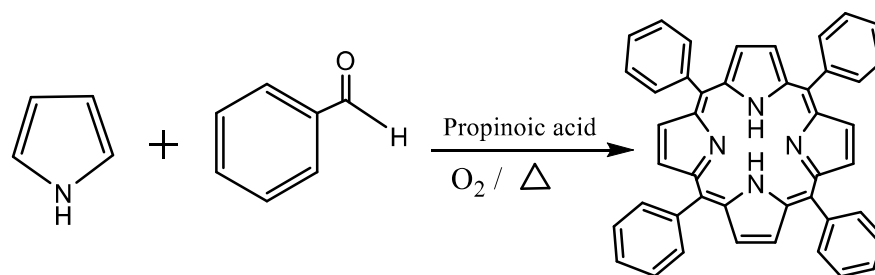
Equation 1-1: TPP synthesis according to optimized Adler and Longo's method.

C. Little's Synthesis

This technique, which was developed in 1975 [41] and is also known as the "mixed aldehydes method," is based on Adler and Longo's approach. It is necessary to reflux pyrrole together with two separate aldehydes in propionic acid for thirty minutes to create non-symmetric *meso*-aryl porphyrins Equation (1-4).
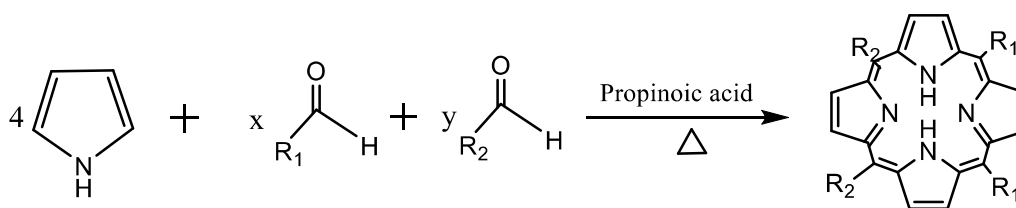
Equation 1-2: Porphyrins synthesis according to Little's method.

This method generates a diverse selection of porphyrins, but there is no way to regulate the substituent reactivity that occurs during the reaction itself. As a result, the reaction produces a mixture of six distinct compounds: the two parent porphyrins (A_4 and B_4), as well as the four hybrid porphyrins (A_3B, A_2B_2 cis and A_2B_2 trans, and AB_3), as occurred in Scheme (1-4).
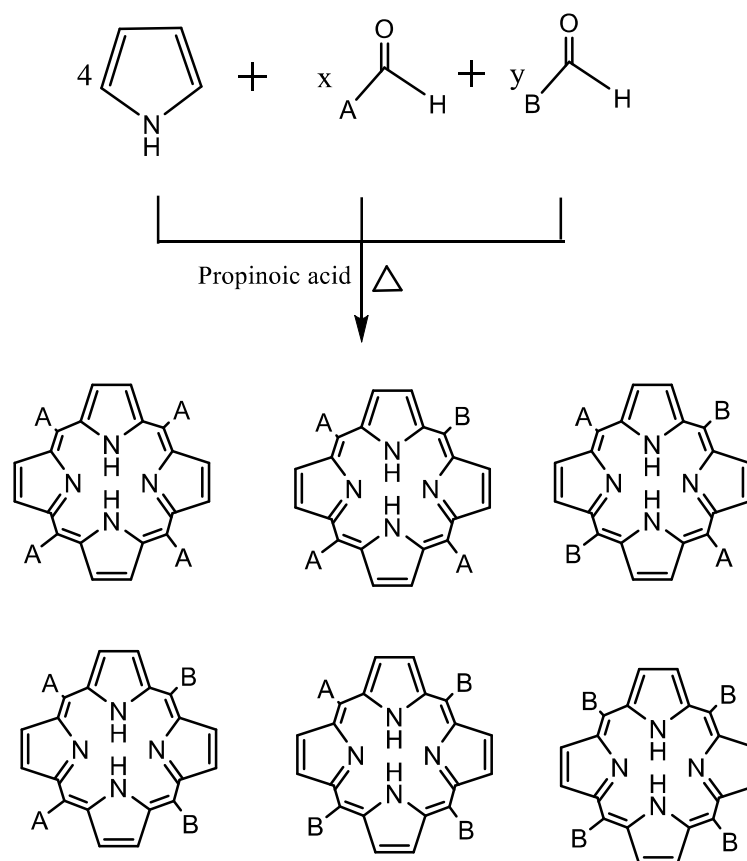
Scheme 1-4: Porphyrins synthesized by using two aldehydes via Little's method.

One may adjust the amount of aldehyde equivalents in order to prefer one chemical over another. For instance, an increased concentration of A_3B-porphyrin may be achieved in the combination by using a ratio of the A and Bn aldehydes that is more than 1:1. When using a 3:1 ratio, the relative concentration of A_3B-porphyrin is 42.2% as opposed to 25% when using a 1:1 ratio;[42] this indicates that for an overall yield of porphyrins that is equal to 40%, the A_3Bporphyrin is generated in a yield that is equal to 16% [43, 44].

D. Lindsey synthesis

A novel method for the synthesis of symmetric porphyrins was suggested by Lindsey in 1987 [45]. It was based on the research conducted by Rothemund, Adler, and Longo, as explained in Scheme (1-5).
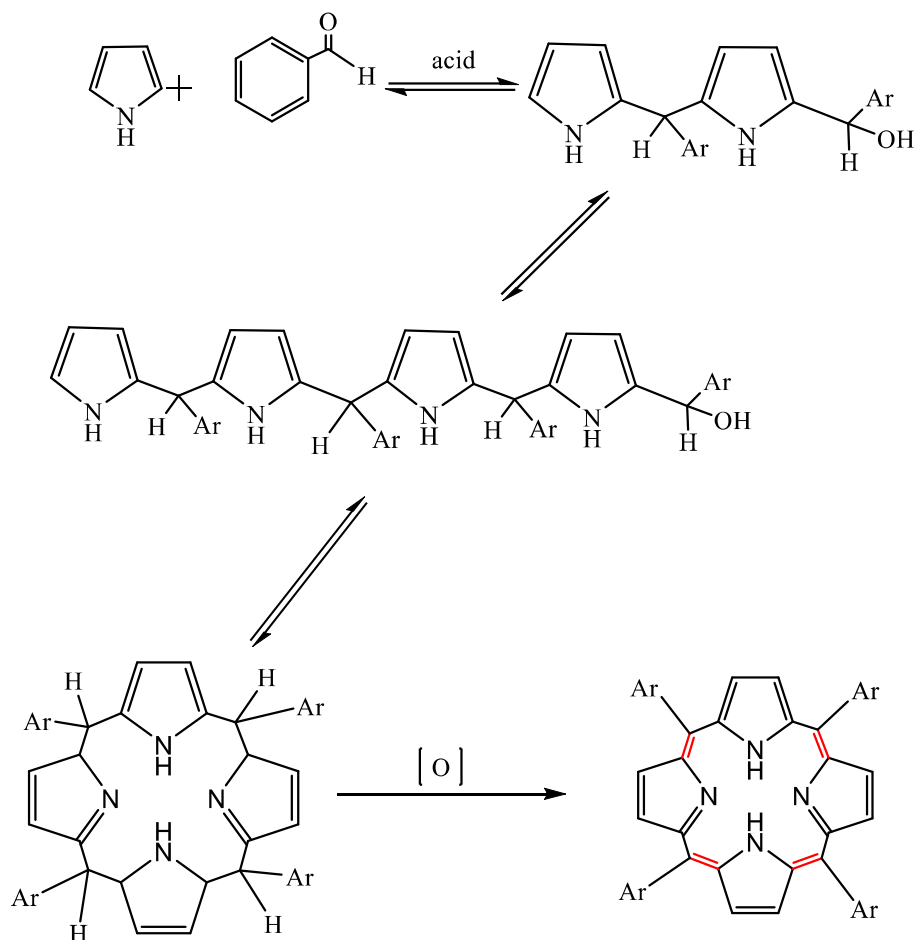
Scheme 1-5: Lindsey's method mechanism.

This process results in the manufacture of meso-tetrakis porphyrins with excellent yields (for example, TPP with a yield of 35-55%), and it does so under moderate temperatures, which makes it possible to deal with thermally sensitive aldehydes and eliminates the need for purification challenges. In this procedure, a Lewis acid (such as BF_3 or BCl_3) was utilized under catalytic quantities in anhydrous circumstances (dichloromethane and TEOA (triethyl orthoacetate) as water scavengers), and a nitrogen gas environment was present during the whole process. Under these experimental circumstances, it is possible to get porphyrinogen as the thermodynamically stable product. Porphyrinogen is finally oxidized into porphyrins with the addition of DDQ or p-chloranil Scheme (1-5). Using this method, one may get the highest possible yields even for very dilute solutions (C less than 10^{-2} M). However, it is even

plausible that Lindsey's approach may be used to synthesis asymmetric porphyrins[42, 46]. Nevertheless, in every instance, many unwanted side reactions, such as pyrrole polymerization, an uncontrolled combination of aldehyde and pyrrole patterns. The formation of non-cyclized chains can interfere with the experiments. These reactions both lengthen the purification process and make it more difficult.

E. Microwave activations

Since the beginning of the 21st century, researchers have been looking into the use of microwave irradiations in the synthesis of porphyrin because of the significant benefits they offer. These benefits include reduction in the amount of time needed for the reaction as well as the number of solvents required, high selectivity, an absence of chlorin contamination, and a relevant alternative to propionic acid[47]. When discussing symmetric porphyrins, it is important to bring up the research conducted by Nascimento and colleagues, who at first used a home microwave oven [48] and then a laboratory microwave reactor. Using combination of aldehyde and pyrrole in propionic acid and nitrobenzene, which was activated for five minutes, it was possible to get certain meso-tetra-aryl porphyrins with a yield of up to twenty percent (for TPP). They have also demonstrated an interest in heterogeneous oxidation with manganese dioxide [49]under microwave conditions for the synthesis of meso-tetraarylporphyrin, which makes the purification process easier and is more cost-effective than the quinones that are typically used (as p or o-chloranil) Scheme (1-6).
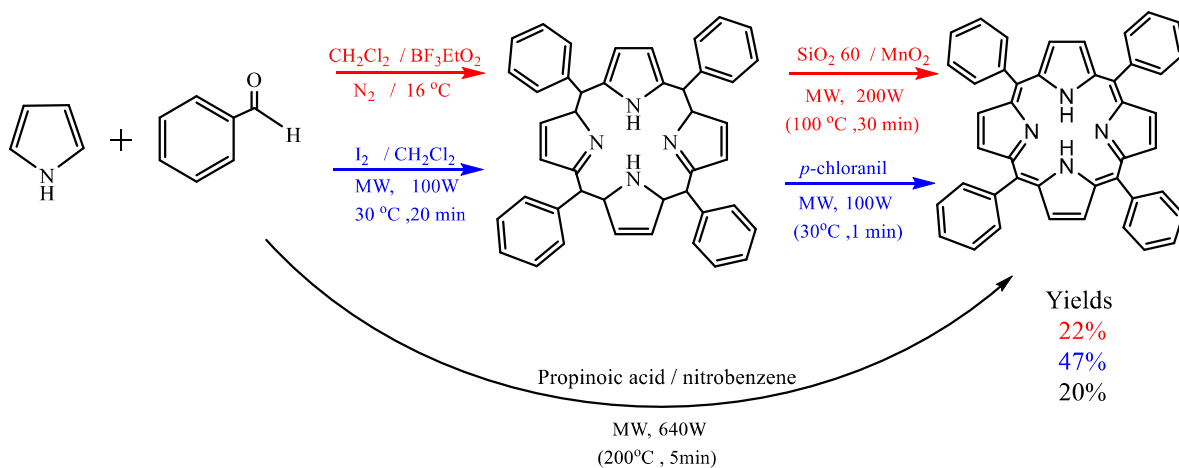
Scheme 1-6: Microwave porphyrin synthesis, when Nascimento's works gives green and black products, and Zerrouki's results give blue products.

Zerrouki and colleagues have devised a novel strategy that utilizes diiodine as the catalyst. In this procedure, the synthesis of porphyrinogens occurs first, followed by the oxidation of those molecules using chloral (Scheme 1-6). When compared to more traditional methods, the most significant benefits come from the simplified execution of the technique and the enhanced outputs it produces [50, 51].

In addition, Lindsey developed a synthetic route derived from pyrrole-carbinols[46]. It involves subjecting one pyrrole unit to the action of acyl chloride in order to produce ketopyrrole, which is subsequently reduced to produce pyrrole-carbinol. This compound undergoes a reaction when exposed to acidic and oxygenated conditions, which results in the formation of the corresponding meso-porphyrin Scheme (1-7). By way of illustration, TPP was successfully extracted from propionic acid at a yield of 41% using this method.
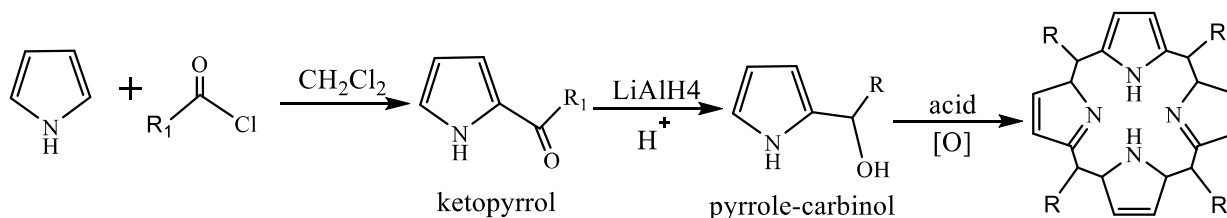
Scheme 1-7: Porphyrin synthesis via pyrrole-carbinol

F. Active charcoal

An alternative method, which was developed in our laboratory by Vignaud *et al.*, was created in order to avoid the use of catalysts and solvents that are hazardous to the environment. Through the use of active charcoal that has been pretreated with nitric acid and acts as an acid promoter, this method makes it possible to obtain meso-tetra aryl porphyrins without the need for any solvents in the process[52]. It was possible to obtain relatively high yields of symmetric meso-porphyrins by using tetra-tolyl or tetra-anisyl porphyrins. The yields were 40% and 33%, respectively.
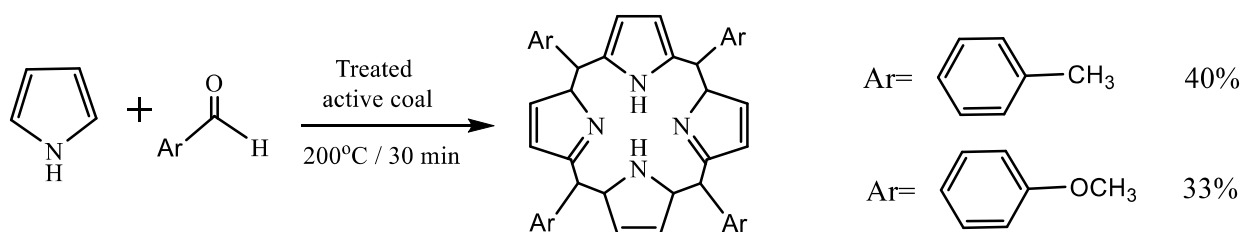
Scheme 1-8: Synthesis catalyzed by active charcoal.

1.4 Electronic absorption properties of porphyrins

The delocalized aromatic property of porphyrins, which derives from extensive conjugation Figure (1-7), provides for one of the most prominent characteristics of these chromophores, which is their bright color. This characteristic is one of the reasons why porphyrins are found in chromophores.
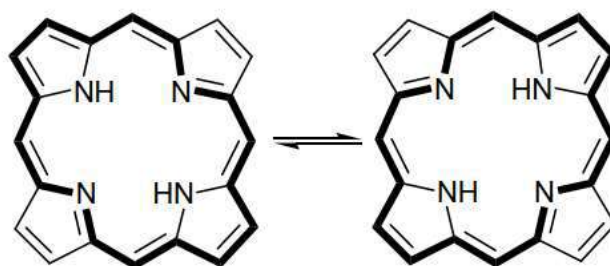
Figure 1-7: Delocalized 18 π-electron conjugation pathway and tautomerism of porphyrins.

The vivid color of porphyrins is a result of their strongly conjugated electron systems, which exhibit distinctive UV-Visible absorption spectra

characteristics in the ultraviolet and visible ranges. The absorption bands, known as Q-bands (weak) and Soret band (intense), are depicted in Figure (1-8) [53]. Gouterman's four-orbital model has been widely used to interpret the spectra of porphyrins, which proposes that the unique absorption bands are caused by transitions from the two highest occupied molecular orbitals (HOMOs) - a_{1u} and a_{2u} - to the two lowest unoccupied molecular orbitals (LUMOs) - a set of e_g. .These transitions,[54] in combination with further orbital mixing and splitting of the two energy states, lead to Soret (B) bands with higher intensity, originating from high-energy states, and Q-bands with weaker oscillation strength from lower energy levels.
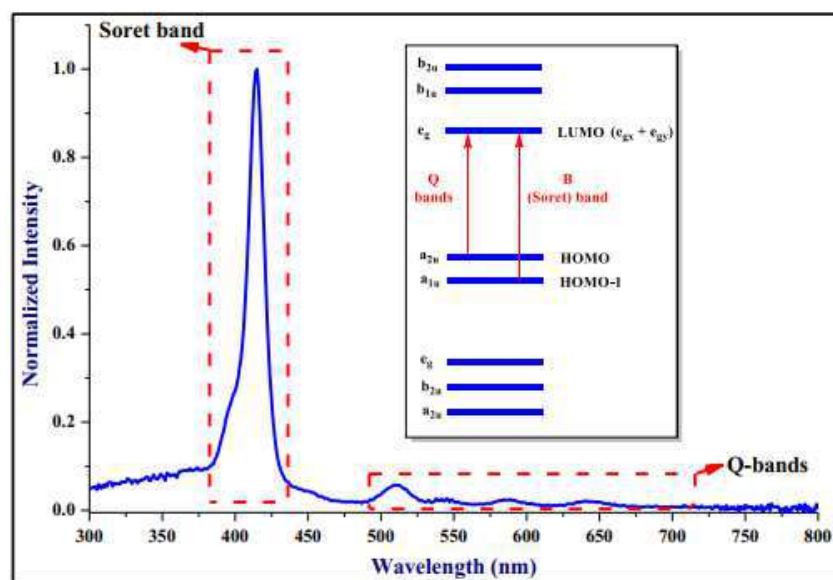
Figure 1-8: Spectra of a free-base 5,10,15,20-tetra(4-pyridyl) porphyrin's UV-visible absorption. Incorporate; Gouterman's four orbital HOMOs and LUMOs electronic transitions illustrative of the origin of the Soret (B) band and Q-band in a porphyrin molecule[54].

The N-H protons breaking the symmetry result in the presence of four Q-bands for a free base Figure (1-8), while only two bands are visible for metal porphyrins. Depending on the porphyrin and meso substituents, the Soret band varies between 380 and 500 nm, and the Q-bands between 500 and 750 nm. [55, 56]

1.5 Photophysical and photochemical parameters of porphyrins

A particular molecule's characteristics as it changes energy levels in response to photoexcitation are known as photophysical parameters. The porphyrins' fluorescence quantum yields (φF) and lifetimes (τF), as well as singlet oxygen quantum yields ($\phi\Delta$), were investigated. When exposed to the light of the right wavelength, a porphyrin molecule may be photoexcited to the singlet excited state ($S_o \rightarrow *S_1...*S_n$ Figure) (1-9), where many conflicting processes occur after the molecule has relaxed[57-59]. The porphyrin substituents (meso and beta), the kind of central metal, photo-induced electron transfer (PET), the type of solvent, and temperature may all have a significant influence on all of these factors[60, 61].
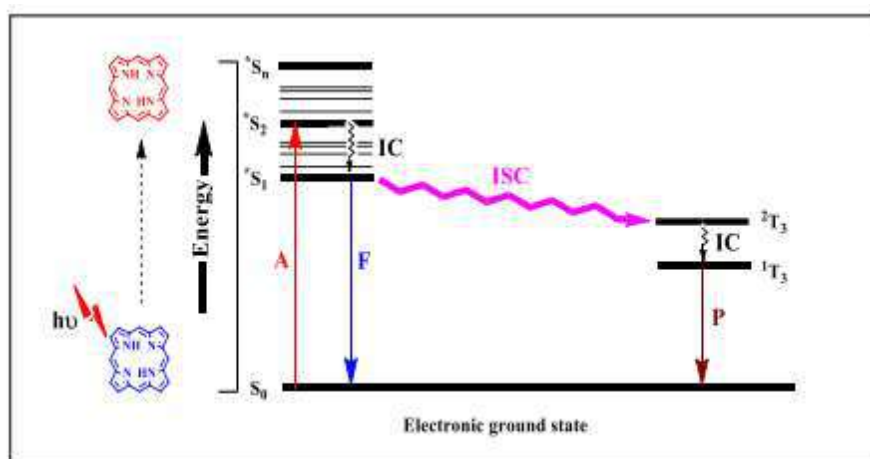
Figure 1-9: A simplified Jablonski diagram for further illustration of the photophysical processes of porphyrins: A = photon absorption; F = fluorescence; IC = internal conversion; ISC = intersystem crossing; P = phosphorescence; S_0 = Ground state; $*S1$ = First singlet excited state; $*S_1$ = Second singlet excited state; $*S_n$ = n singlet excited state; $^1T_3$ = First triplet excited state, $^2T_3$ = Second triplet excited state[57].

1.6 General Nanotechnology

Nanotechnology refers to the field of studying and manipulating matter at dimensions ranging from 1 to 100 nanometers, where unique phenomenon allows for novel applications [62]. This interdisciplinary field encompasses various disciplines such as chemistry, physics, magnetism, electrochemistry, energy, and material science, among others, making it an incredibly intriguing area of

research. Over the past few decades, much of the research in nanotechnology has been focused on designing and developing nanomaterials, given their distinct physical, chemical, electrical, and magnetic properties [63]. Examples of nanomaterials include nanotubes, quantum dots, nanowires, nano colloids, nanoparticles, and nanofilms. In contrast, bulk materials consist of particles larger than 100 nm in diameter in all directions and do not exhibit size-sensitive physical properties. It is noteworthy that the radius of a DNA double helix is approximately 1 nm, whereas human hair has a thickness of 60,000 nm Figure (1-10)[64].
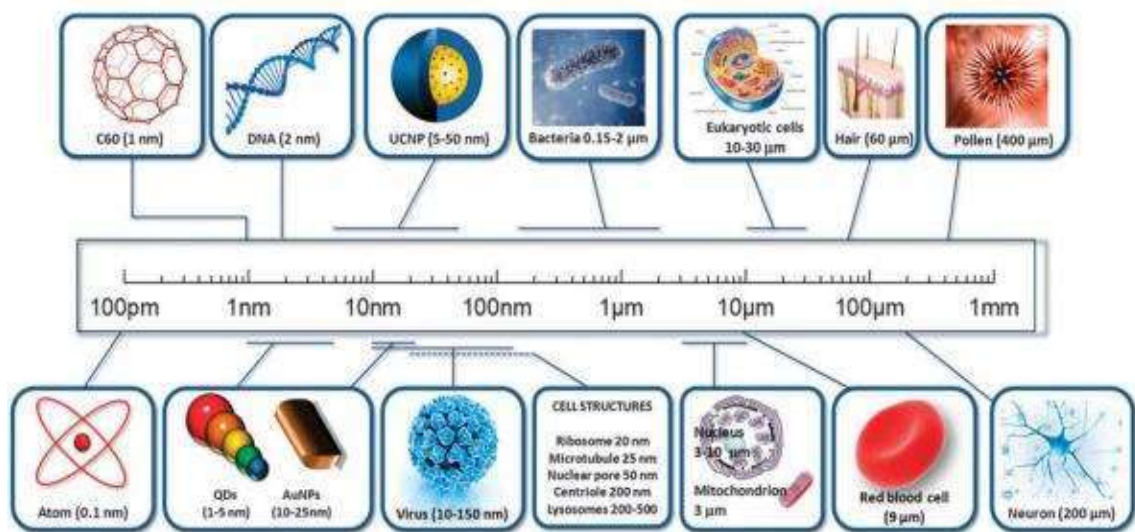
Figure (1-10): Compared the sizes of bulk materials with sizes of nanomaterials. reproduced from source with permission [64].

Nanotechnology and nanoscience are two distinct but interconnected fields. Nanotechnology refers to the ability to observe, measure, manipulate, assemble, control, and build matter at the nanoscale level. On the other hand, nanoscience is an interdisciplinary field that combines physics, materials science, and biology to explore the manipulation of materials at atomic and molecular dimensions.

While several papers discuss the foundations of nanoscience and nanotechnology, few provide a chronological overview of their development from inception to the present day. Understanding the evolution of these fields requires a review of key events[65], as depicted in Figure (1-11).
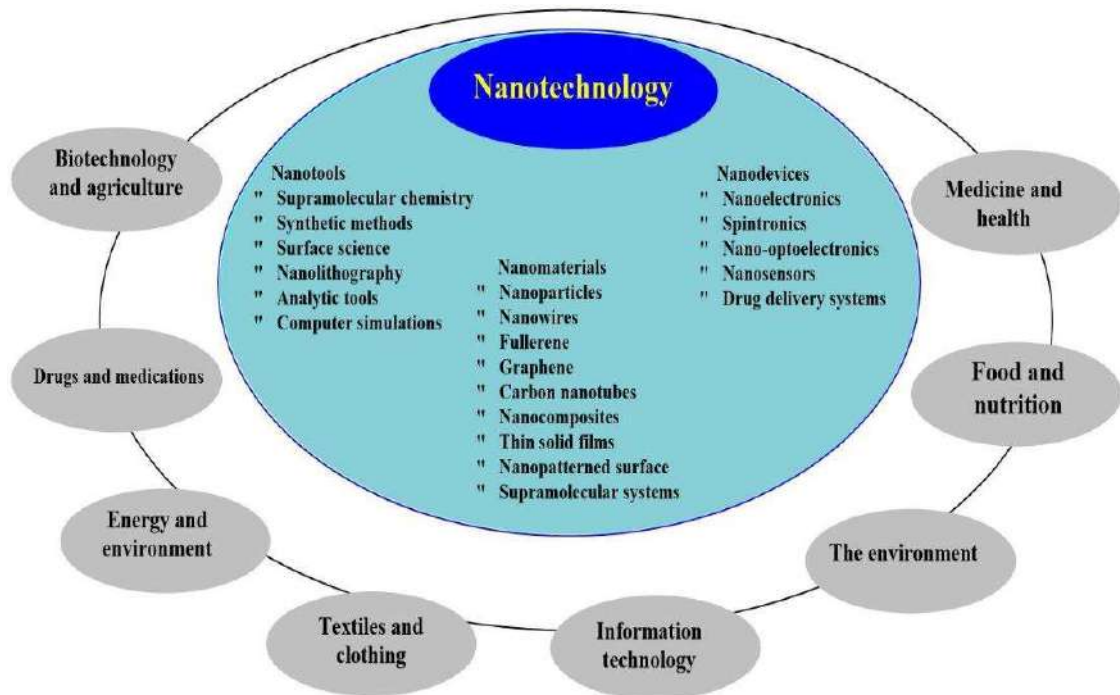
Figure (1-11): Diagram showing nanotechnology and its nanotools, nanomaterials, nanodevices, and applications[65].

1.7 Classification of nanomaterials

Nanomaterials can be classified based on various criteria, including their size, shape, state, and chemical composition, as mentioned in reference[66]. Among these criteria, size is often used to categorize nanomaterials, as depicted in Figure (1-12) [67]. Specifically, nanomaterials are defined as materials that have at least one dimension between 1 and 100 nanometers.
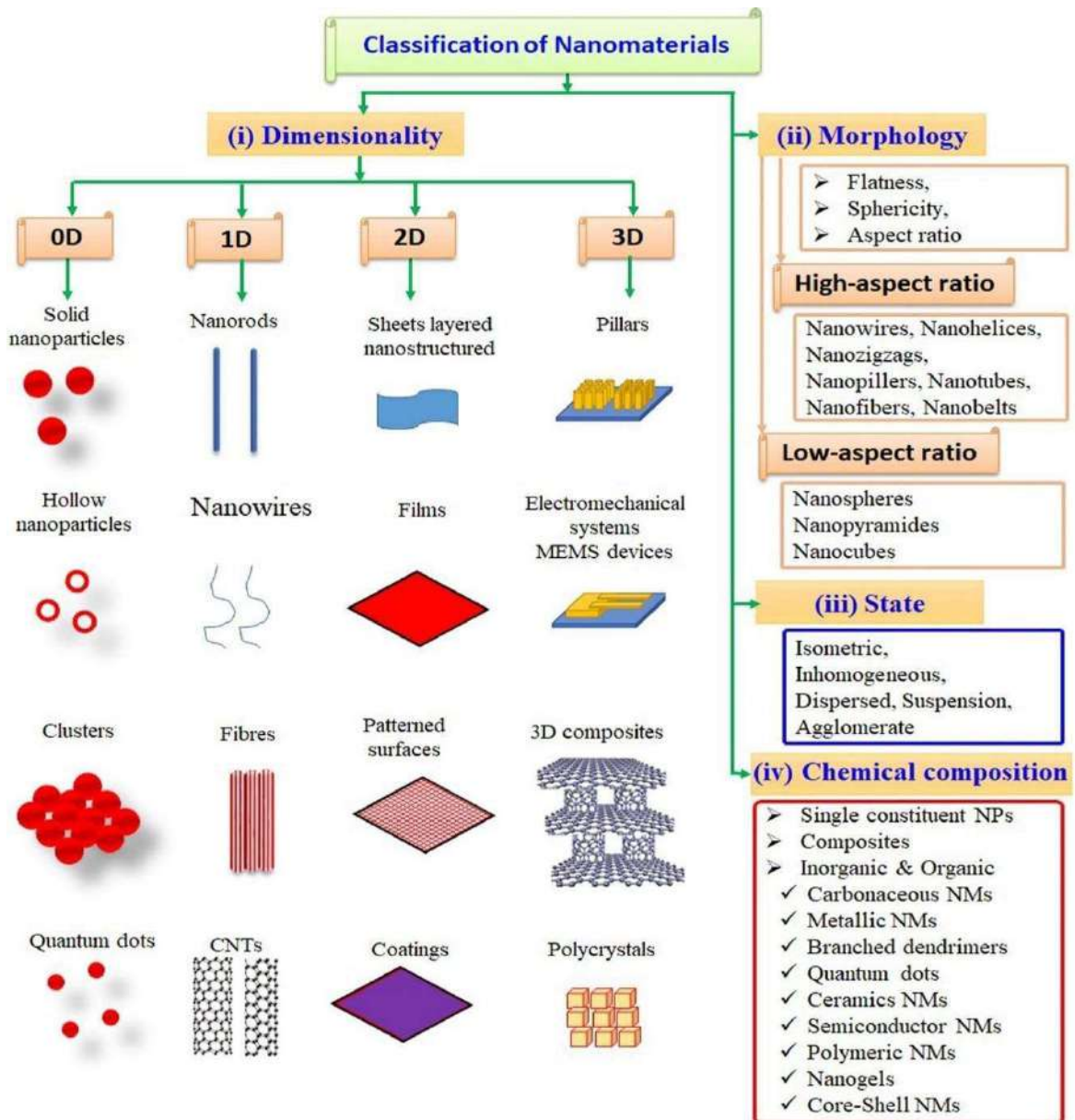
Figure (1-12): The classification of nanomaterials based on many parameters [67].

1.8 Graphene Quantum Dots

The exceptional electronic, surface chemistry, and tunable fluorescence properties of graphene quantum dots (GQDs), which are made of a special zero-dimensional (0D) nanometer-sized graphene particle and benefit from the edge-shape effect and quantum confinement effect, have drawn attention[68, 69]. It is well known that GQDs contain a graphene structure within the dots, but they also have several distinctive properties that are similar to graphene, including a high specific surface area (about 2630 m^2/g), excellent electrical

conductivity (about 1738 siemens/m), strong mechanical strength (about 1100 GPa), and distinctive thermal conductivity (about 5000 W/m/K) [70-72]. Due to its zero-band gap, graphene film is notable for lacking optical emission, which restricts its use [73]. Due to their single or few layers of sp^2 hybridized carbon atoms arranged in a honeycomb lattice, non-zero band gap, and nanometer-sized particles, GQDs exhibit distinctive properties such as size-dependent quantum dot properties, tunable fluorescence in the visible spectral range [74], and biocompatibility because of its low in vivo toxicity. It has several potential uses in photovoltaics, light-emitting diodes, sensors [75], and biosensing and bioimaging [76]. Additionally, as was mentioned, the majority of applications have emphasized the optical characteristics of GQDs. Through surface modifications and various synthesis circumstances, GQDs are anticipated to exhibit adjustable photoluminescence (PL) colors as the band gap changes. Thus, development of their applications utilizing a variety of methods is the focus of the controlled synthesis of GQDs[77]. There are numerous methods for creating GQDs, which can be broadly divided into top-down and bottom-up approaches. The top-down technique entails severe reaction conditions and chopping down bulk carbonaceous materials (such as graphene sheets, carbon nanotubes, and bulk graphite) into nanometer-sized particles[78]. Because the oxygen-containing functional groups on the surface of graphene are easily converted into nanometer-sized, single-layered GQD particles[79], graphene oxide is another strong contender. The top-down technique, however, has drawbacks since it requires many steps and post-treatment with surface passivating chemicals [80], and it often prevents exact product morphology and size distribution. As it uses building blocks from atom or molecule precursors and uniformly regulates the size, which is directly related to the band gap of quantum dots, the bottom-up approach is suitable for controlling the size of GQDs[81]. There are reports on the bottom-up synthesis of GQDs, including pyrolysis, carbonization, hydrothermal, exfoliation, self-

assembly of molecules, microwave-assisted reduction, electrochemical, and exfoliation processes. Among these, carbonization offers clear benefits in modifying the chemical makeup and physical characteristics of GQDs [82]. In essence, carbonization is a process that uses pyrolysis distillation to change organic precursors into carbon.

Figure 1-13: Green synthesis of GQDs and their recent applications in electrochemical sensors. [83, 84].

1.9 Spinel semiconductor

Spinel is a mixed oxide known for its exceptional chemical and thermal stability, with a chemical formula of AB_2O_4. Its applications in catalysis are numerous, owing to the presence of cations with varying charges that promote internal redox reactions and facilitate reduction-reoxidation cycles. The spinel structure consists of cations dispersed between oxygen anions arranged in a nearly

cubic close-packed structure. Out of the 32 oxygen anions present in a spinel cell, only a small fraction of interstices is filled by cations, namely eight tetrahedral interstices (A sites) and sixteen octahedral interstices (B sites). The cations occupy the interstices in rows of octahedra connected by tetrahedra, with the majority of spinels adopting an ideal stoichiometric spinel structure with an average cation charge of 2.33[85]. Spinels are classified into two types: common (normal) spinel, represented by the formula $[A_{Td}^{2+}]$ $[B_{Oh}^{3+}]_2$ $[O^{2-}]_4$, with A^{2+} cations occupying tetrahedral sites (Td) and B^{3+} cations in octahedral sites (OH), such as Mn_3O_4, $ZnFe_2O_4$, and $FeCr_2O_4$. In contrast, inverse spinel structure is obtained when half of the observed B^{3+} cations are replaced with A^{2+} cations, with the general formula represented as $[B_{Td}^{3+}]$ $[A_{Oh}^{2+}B_{OH}^{3+}]$ $[O^{2-}]$. Examples of inverse spinel include Fe_3O_4, $CoFe_2O_4$, and $NiFe_2O_4$ [86].

1.10 Spinals CdFe$_2$O$_4$ Semiconductor

Recently, cadmium ferrite ($CdFe_2O_4$) has gained interest lately due to its many uses in several sectors,[87, 88]. Bulk cadmium ferrite has been labeled as antiferromagnets and is thought to represent a typical spinel structure with cadmium ions filling the tetrahedral positions[89]. Cadmium-substituted ferrites exhibit n-type semiconductor behavior, and the see beck coefficient steadily lowers as the cadmium level increases [90]. In a face-centered-cubic tight packing of oxide ions, Cd^{2+} and Fe^{3+} ions are present at the tetrahedral sites (A sites) and the octahedral sites (B sites), respectively. The B sites' Fe^{3+} ions organize into a pyrochlore lattice. Therefore, when the vertices of a 3D network of corner-sharing tetrahedra, such as the pyrochlore lattice, are filled by spins with anti-ferromagnetic interaction among closest neighbors, severe magnetic frustration based on geometry is seen. A vast family of oxides with extraordinary magnetic characteristics is known as ferrites. The ferrites have been identified by their very nonconductive grain borders that divide their highly conductive grains. The electrical characteristics are specially regulated by the grain boundaries. When compared to soft magnetic alloys, the high

electrical resistance of ferrites was significantly used in numerous magnetic devices. Spinel ferrites are becoming more and more important in the metallurgical industry and other high-temperature industries due to their advantageous features, such as strong thermodynamic stability, high electrical conductivity, and high corrosion resistance. Spinel ferrites, garnet ferrites, and hexagonal ferrites are three separate kinds of ferrite materials that may be used for magnetic recording, data storage, and radar absorption materials[91-93]. Spinel ferrites have generated a great deal of technical attention due to their potential use as electrode materials [94], drug-loading materials [95], microwave adsorption [96], and environmental remediation[97]. The most promising among the ferrites, MW absorbing materials have attracted a lot of attention in the last ten years due to their major roles in waste water treatment. Numerous techniques have been used for $CdFe_2O_4$ particle synthesis, but the most recent ones used include the combustion method, ball milling[98], co-precipitation, pulsed laser deposition (PLD), and hydrothermal method [99, 100].

1.11 Composite nanomaterials

Composites are solid materials having many phases, at least one of which is smaller than 100 nm, or structures with nanoscale repetition spacing between phases[101, 102]. In the creation of composite structures, nanometer-scale physical dimensions are often used. Numerous features, including flexural strength, water absorption, optical properties, wear, and gloss retention, may be found in a composite material made of different components[103]. The Box-Behnken design may be used to create more energy- and chemical-efficient chitosan-tripolyphosphate/TiO_2 nanocomposites for reactive orange dye adsorption [104]. The materials' surface area increased from 0.156 m^2/g to 2.75 m^2/g when the components were mixed to create nanocomposites. The adsorption capacity of composite materials may be improved by several

interactions, including electrostatic interactions, n-interactions between lone pairs of electrons delocalized into the -orbital, dipole-dipole hydrogen bonding, and Yoshida H-bonding[105]. Based on their matrix components, nanocomposite materials may be categorized into three classes, much like micro composites[106]: Metal, Polymer, and Ceramic Matrix Nanocomposites (MMNC, PMNC, and CMNC).

Nanocomposite Materials

| Metal Matrix Composite (MMNC) | Polymer Matrix Composite (PMNC) | Ceramic Matrix Composite (CMNC) |
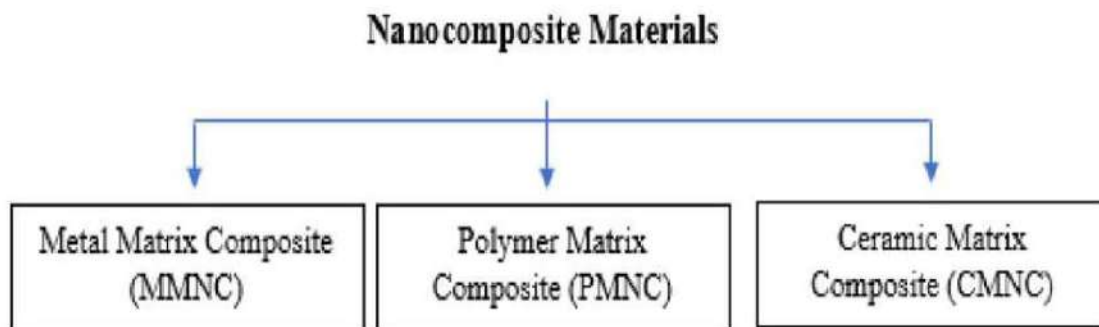
Figure 1-14: Types of nanocomposites according matrix[106].

1.12 Solar Power

One of the biggest and most pressing issues facing the world now is pollution and astonishing energy use. The main issues with these concerns are the influence on human health, the environment, and resource depletion. These factors have contributed to a surge in interest in alternative energy sources around the globe during the last 20 years. One of the most significant scientific and technological problems confronting mankind in the twenty-first century is the provision of clean, sustainable energy. Wind, tidal, thermal, and, most significantly, solar cells are all examples of renewable energy sources. These sources have the capacity to considerably reduce pollution and the climate-related effects that come with it [107]. In most cases, the solar energy that the earth receives in a single hour is more than the total amount of energy that the whole world consumes in a single year [108]. So solar energy alone has the potential to meet the planet's energy demands in the near future. The most widely used kind of solar energy today is solar photovoltaic (PV) technology,

which is powered by light, operates at temperatures close to ambient[109], has no moving parts, and is an unrestricted, cost-free source of energy [110]. A solar cell, usually referred to as a photovoltaic cell, is a kind of electrical appliance that uses the photovoltaic effect to convert light energy directly into electricity[111]. The foundational elements of photovoltaic modules, usually referred to as solar panels, are solar cells. The bulk of the energy used today is generated by fossil fuels, but these fuels also release very harmful and deadly chemicals, including carbon monoxide, into the atmosphere continuously. As a consequence, clean energy that is both ecologically beneficial and doesn't upset the economy is produced using solar cells. Solar cells may be produced to utilize more solar energy. Solar cells convert solar energy into electrical energy, which can then be stored in batteries via charging. A solar cell's ability to function depends on a number of variables, including:[112, 113].

1-Electron-hole pairs are produced by light absorption.

2-Electron and hole separation, charge carrier collection.

The separation of charge carriers of diametrically opposing kinds.

The semiconducting substance from which solar cells are formed bears their name, but only certain types of materials can effectively absorb sunlight. Some of these cells are made to be used in space, while others are made to be used on the surface of the Earth[114].

1.13 Background of solar cells

When French scientist Edmond Becquerel discovered the photovoltaic effect through the electrolytic cell in 1839, the first description of photovoltaic technology was initiated. Adam and Day carried out the first studies on selenium-based solid-state photocells in London in 1876. It took more than 50 years to develop the first solar photocells, which had an efficiency of little more than 1% [115]. Since the 1950s, when the first Si-based p/n junction capable of converting sunlight into electrical energy was developed, solar cells and

photovoltaic (PV) modules have been the focus of considerable study. The first silicon-based photovoltaic device was created in 1954 by Daryl Chapin, Calvin Fuller, and Gerald Pearson of Bell Telephone Laboratories in the United States of America. Initially known as a solar battery, the device is now known as a solar cell [116]. With an initial energy conversion efficiency of 6%, this device used the basic p-n junction ideas established in the early 1950s. However, by 1957 [117] and 1960[118], it had risen to 11% and 14%, respectively. Since 1980. Public utility buildings, solar farms, concentrating solar power systems, street lighting, and floating systems are just a few of the applications that PV has evolved into. Rooftop solar systems have prospered in the home market, whereas other forms of renewable energy have had difficulty finding a market [119].

1.14 How solar cells work

When photons from the sun impact the film surface of solar cells, free electrons obtained by obtaining more energy are transitioned. A solar cell's band structure was examined, and it was found that the binding energy of the film drops, suggesting that the greatest number of electrons are formed when the cell obtains energy from photons and creates free electrons, which recombine to produce some photovoltaic current. The thin film-based approach must thus be employed to boost solar cells' efficiency. It covers a bigger percentage of the solar spectrum by absorbing a lot of light [120].

The stages that make up the solar cell hypothesis are as the following:

1. When photons from the sun hit the solar panel, semiconducting components like silicon and germanium absorb them.

2. Electrons that have left their existing atomic or molecular orbitals and have been stimulated (charged negatively). Once excited, these electrons have two options: they may either release their energy and return to their orbital, or they can move through the cell until they reach an electrode,

when current starts to flow through the material to cancel the potential, capturing the electricity. Electrons are only permitted to flow in one direction due to the unique makeup of solar cells.

3. Solar energy is transformed into usable direct current (DC) power via a solar cell array[121, 122].

The intermediate electrical conductivity between a conductor and an insulator that the semiconductor materials used in solar cells possess distinguishes them from one another[123].

1.15 Various kinds of solar cells

There are many different ways to categorize photovoltaic cells according to their semiconductor materials, morphology, and fabrication technique, all of which are easily analyzed and broken down into three primary groups that are referred to as "generations" [124, 125]. These generations can be studied individually or in comparison with one another. Since Chapin and Fuller [126] established the theory of creating energy from the sun's rays using a photovoltaic method in the 1960s, silicon (Si) solar cell manufacturing technology has been the dominant trend. This technology is also known as "first generation." It is differentiated by the increasing expense of raw materials in the Si solar cell, which is then followed by the "second-generation" technology, which is characterized by a thin layer (thin film), as well as other solar cells constructed of a-Si, CdTe, and CuInSe$_2$, respectively (CIS). This new type of solar cell is known as the "third generation," and one of these types is the Dye-sensitized Solar Cell (DSSC), the operating principle of which is a dye reaction. As technology and solar cell fabrication have advanced, a new type of solar cell has emerged that makes use of abundant natural raw materials, is non-toxic, and is capable of producing high efficiency while being fabricated with a simpler process. This type of solar cell uses abundant natural raw materials, is non-toxic, and is capable of "fourth generation," which is shortened to "fourth generation," while "fourth generation" is the full phrase (4GEN). It combines

the low cost and flexibility of polymer thin films with the stability of novel inorganic nanostructures such as metal nanoparticles and metal oxides or organic-based nanomaterials such as carbon nanotubes, graphene, and their derivatives [127, 128]. In other words, it is a nanomaterial that combines the best of both worlds. In addition, there is a difference of opinion about the fourth generation, with some writers holding the belief that it is distinct from the third generation, while others hold the belief that it is a component of the third generation [127, 129].

1.16 Solar Cell with Dye Sensitization (DSSC)

It is anticipated that this type of solar cell will be able to supply alternative energy concepts at a lower cost of production and with a simpler fabrication technology than its predecessors, which are made from crystalline silicon[124, 127, 128]. This is the manufacturing process for this type of solar cell is expected to be less complicated. This cell has five different layers, which are as the following:

1. A transparent anode made of a glass sheet with one side coated with a transparent conductive oxide layer (also known as TCO glass) (for example, fluorinated tin oxide (FTO) SnO_2: F coated glass).

2. In order to increase electronic conduction, a layer of mesoporous oxide is often formed on the anode. This layer is typically made of titanium dioxide.

3. A monolayer of charge-transfer dye is covalently linked to the surface of the mesoporous oxide layer to increase the amount of light that the material can absorb. In order to facilitate better dye regeneration, an electrolyte has to include.

4. A redox mediator dissolved in an organic solvent.

5. A cathode that is constructed using a crystal that has been treated with a catalyst (often platinum or gold) to make the collection of electrons easier[129].
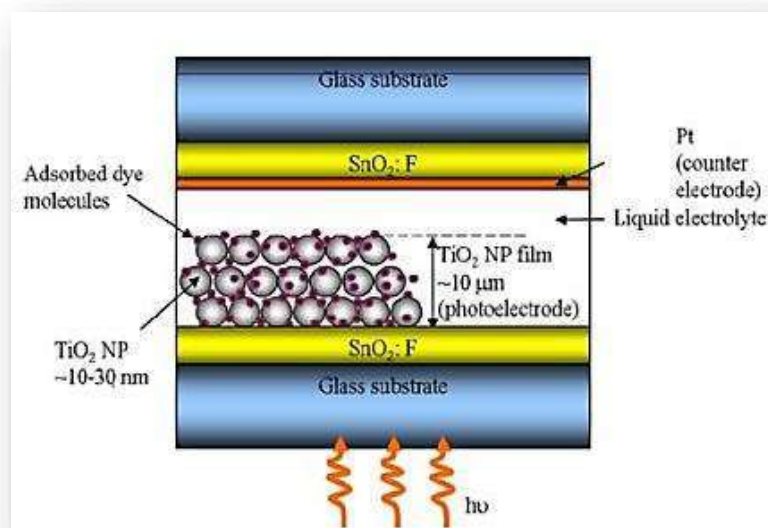
Figure 1-15: The common construction for a DSSC[130].

Due to their strong electronic absorption, effective visible light harvesting with high molar extinction coefficients, tunability, photochemical and electrochemical stability, and sensitizing properties, porphyrins and their derivatives have attracted a lot of attention as sensitizers for applications in DSSCs[131].

Porphyrin dyes need at least one anchoring or bridged-binding group to be utilized as sensitizers in DSSC devices so they can adhere to the TiO_2 surface. Porphyrins, as we have already seen, contain eight and four meso places; this abundance of functional able sites makes porphyrins a flexible molecule for the creation of several colors[132].

1.17 Transparent conducting substrate

Transparent conducting substrates, also known as TCO glass, are often used as substrates for DSSCs since they are readily available, have a cheap cost, and have a high level of optical transparency in the visible and infrared parts of the solar spectrum. Doping ordinary glass with a thin layer of metal oxide results in the production of TCO glass. The most prevalent form consists of electrically conductive TCO coatings that have been doped with fluorine.

Tin oxide-FTO (SnO_2: F, FTO) and indium tin oxide (ITO) are two types of the same material (In_2O_3: Sn, ITO)[133]. In direct-sequence solar cells (DSSCs), fluorine-doped tin oxide (FTO) glass rather than indium tin oxide (ITO) coated glass is employed because the former has higher thermal stability at high temperatures. Typically, the resistance of the conducting film sheet on the TCO substrate is between 10 and 20 Ω per square area[134].

1.18 Nanocrystalline semiconductor film photoelectrode

A photoelectrode, also known as a photoanode, may be generated in a DSSC by depositing a thin layer of sensitized wide-bandgap nanostructured semiconductor (usually composed of TiO_2, ZnO, SnO_2, and Sb_2O_5) onto the TCO substrate. This creates the photoelectrode. The nanostructured semiconductor layer has to have a large surface area (high roughness) in order to achieve high light-harvesting efficiency (LHE)[135, 136]. This will enable a large number of sensitizer molecules to adsorb on the layer. In dye-sensitized solar cells, the anatase form of titanium dioxide is the one that is most often used (DSSC). To get a greater amount of active surface area for light absorption, a layer of semiconductive oxide with a nanocrystalline structure may be used. The amount of monochromatic incoming light that is absorbed is less than 1% if the surface is smooth and coated with a single layer of dye. Titanium dioxide must possess an n-type conductivity if it is to be used in a DSSC[137]. This will allow the material to accept electrons that have been transmitted from the sensitizer. Due to its large energy bandgap and sufficiently low position of the conduction band edge in relation to the redox potential of organic substances in an aqueous solution, this oxide is thought to be the most suitable material for covering the DSSC electrode. This is because of its wide energy bandgap. Because of this, dyes that can absorb light in the visible spectrum may be used. Two of the criteria that need to be selected are the surface development of the layer and the size of the pores that are present in

the layer[138]. This is done to ensure that the promised performance of maximum light absorption is achieved and that the electrolyte can easily fill the pores.

1.19 Redox electrolyte

The electrolyte is considered to be one of the most essential elements of DSSCs [139]. During DSSC operation, the electrolyte is responsible for the inner charge carrier transport between electrodes. Additionally, the electrolyte continuously regenerates the dye and itself. According to reference [140], the electrolyte has a significant impact on the light-to-electric conversion efficiency as well as the long-term stability of the devices. Another definition of an electrolyte is a substance that offers pure ionic conductivity between the positive and negative electrodes of an electrochemical device [141]. This definition of an electrolyte is more common. The long-term functional lifetime stability of DSSCs is significantly impacted by the electrolyte characteristics in a significant way. As a consequence of this, the electrolyte is required to possess the qualities listed in [142].

1. High electrical conductivity and a low viscosity will allow electrons to move more quickly.
2. The nanocrystalline semiconductor and the counter electrode have very good contact with one another at the interface.
3. It must not be the reason why dye is lost from the surface that has been oxidized or that dye is degraded.
4. It cannot take in any light that falls inside the visible spectrum.

There are three different kinds of DSSC electrolytes, and they are solid-state electrolytes, liquid electrolytes, and quasi-solid-state electrolytes [143-145].

Iodide/triiodide ($^-I/I_3^-$) in a solvent is commonly used as an electrolyte in a DSSC [146]. This is due to its excellent solubility, rapid dye regeneration, low absorbance of light in the visible region, suitable redox potential, and very slow

recombination kinetics between injected electrons into the semiconductor and triiodide.

1.20 Counter Electrode

Electrolyte regeneration is accomplished with the help of the counter electrode. The oxidized electrolyte migrates toward the counter electrode, which is located at the location where electrons are obtained from the external circuit. A catalyst is necessary in order to speed up the reduction process, and platinum (Pt) is the catalyst of choice owing to the high exchange current density it has, the excellent catalytic activity it possesses, and its transparency. The technique used to deposit Pt onto the TCO substrate [147] is what determines the level of performance achieved by the CE. Recently, several other carbon materials, including graphite, carbon black, and carbon nanotubes (CNTs), have been investigated as potential low-cost replacements for platinum (Pt) for counter-electrodes in DSSC[148]. These carbon materials include graphite and carbon black. Carbon materials are well recognized for their strong corrosion resistance [149, 150], this is in addition to their abundance in the material world.

1.21 The operational principle of the DSSC

An illustration of how a dye-sensitized solar cell works can be seen in Figure (1-16) and its functionality is broken out in more detail below.
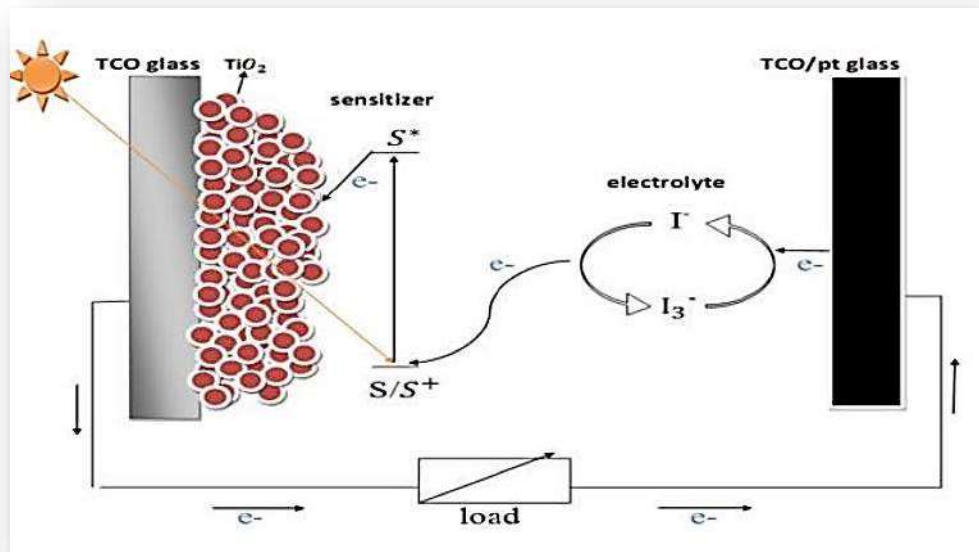
Figure 1-16: A diagram of the DSSC's operational principles[151]

1- When a sensitizer is exposed to light, a photon is absorbed by the substance. The sensitizer is excited to the excited state (S*) as a result of the following equation.

$$S + h\upsilon = S^* \quad \text{----(1-1)}$$

(Light absorption by a dye molecule)

2- The TiO_2 conduction band receives the excited electrons. After being excited, the sensitizer is oxidized to S^+.

$$S^* \longrightarrow S^+ + e^- \quad \text{----(1-2)}$$

$$e^- + TiO_2 \longrightarrow e^-_{cb} (TiO_2) \quad \text{----(1-3)}$$
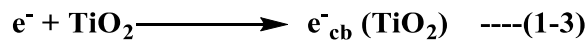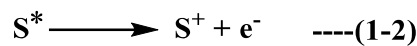
(Charge injection)

3- In the meantime, electrons diffuse through the nano-crystalline TiO_2 layer to the back contact of the conducting substrate and move through the external circuit to the counter electrode.

$$e^- (TiO_2) \longrightarrow e^- (CE) \quad \text{----(1-4)}$$
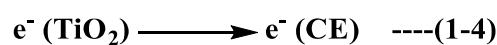
(Charge transportation)

4- Then, via iodide reduction, the electron from the electrolyte returns the sensitizer (S) to its initial state. However, the DSSC's conversion efficiency is lowered by two significant (unwanted) recombination reactions: The oxidized sensitizer or the electrolyte's oxidized redox couple can directly recombine with the excited electron in TiO_2 [152].

$$2S^+ + 3I^- \longrightarrow 2S + I_3^- \qquad ----(1-5)$$

Dye regeneration

$$S^+ + e^- (TiO_2) \longrightarrow S \qquad ----(1-6)$$
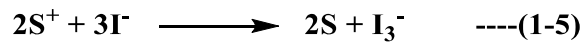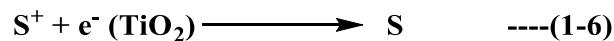
Recombination

5- The counter electrode regenerates the iodide by decreasing the tri-iodide.

$$I_3^- + 2e^- \longrightarrow 3I^- \qquad ----(1-7)$$
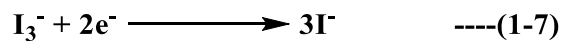
Iodine regeneration

When exposed to light, the sensitizer is photoexcited in a femtosecond, and the process of injecting electrons from the excited state dye (S*) into the TiO_2 conduction band (CB) occurs in a sub-picosecond. On a timeframe of nanoseconds, the redox electrolyte reduces the rate of an oxidized dye. In a matter of microseconds, photoinjected CB electrons recombine with either oxidized dye molecules or the oxidized version of the electrolyte redox couple (I_3^- ions) [153].

Charge recombination is the key unfavorable factor limiting DSSC performance. This occurred when the major recombination channel was thought to be the back-electron transfer at the TiO_2 photoanode-electrolyte interface before reaching the collecting electrode, such as fluorine-doped tin oxide (FTO), decreasing the efficiency of DSSC[154]. The efficiency of the DSSC is expected to be greatly increased by strengthening the conduction paths from the position of the photogenerated carriers to the collecting

electrode[155]. In order to prevent recombination and enhance transport, a number of techniques are employed, including[156]:

(1) The use of a composite semiconductor photoanode with various bandgaps.

(2) The insertion of some doping elements into the TiO_2 photoanode.

(3) The incorporation of charge carriers to guide the photogenerated electron formalized phrasing. The TiO_2 photoanode and CNTs were added to increase the DSSC's efficiency to a limited degree[157].

1.22 Current-Voltage (I-V) Measurements

The current-voltage measurement of a DSSC is the most crucial and popular method for assessing photovoltaic performance. It is done on a Keithley 2400 source meter with simulated sunlight present. Figure (1-17) shows an example of an I-V curves. It is possible to calculate the four parameters (V_{oc}, I_{sc}, FF, and η) using the I-V measurement. The current that passes through a solar cell when the voltage across it is zero is known as the short circuit current (I_{sc}). The maximum voltage produced by a solar cell when the current flowing through it is zero is known as the open circuit voltage (V_{oc})[158]. The solar cell's maximum output is known as the maximum power (P_{max}), and its maximum current and voltage are known as I_{max} and V_{max}, respectively. Metrics are used to evaluate the effectiveness of solar cells including the fill factor (FF) and conversion efficiency (CE)[159]. Calculating the fill factor involves dividing P_{max} by the sum of V_{oc} and I_{sc}. The conversion efficiency is calculated as the ratio of P_{max} to the total of the solar cell's surface area (E) and input light irradiance (E).

$$FF = \frac{VmIm}{V_{oc}\,I_{sc}} \qquad\qquad ----(1-8)$$

$$\%\eta = \frac{V_{oc}\,I_{sc}\quad FF}{Pi_n} \times 100 \qquad\qquad ----(1-9)$$
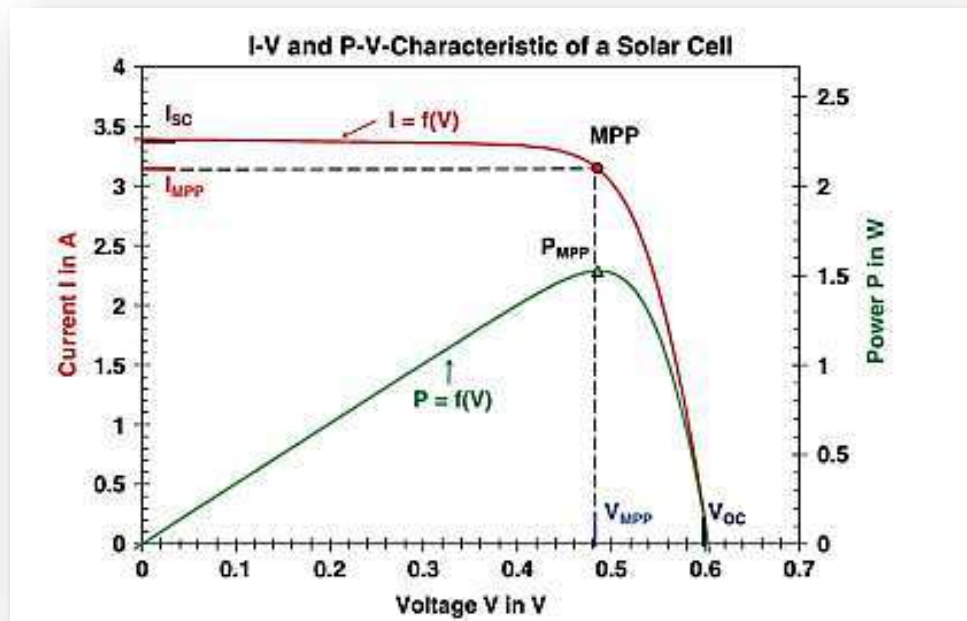
Figure 1-17: Characteristic curves I-V and P-V of a mono-crystalline silicon solar cell with a cell area of 102 cm^2 [160]

1.23 General Corrosion

One form of corrosion happens when metal surfaces are subjected to the same degree and rate of corrosion as the thickness starts to degrade [161]. Due to its predictability at the beginning of an occurrence, such as in the corrosion of iron automobiles and windows under the right conditions like air and water, it is regarded as a non-dangerous species[162]. The metal's surface layer becomes an oxidizing layer, and this kind does not persist deeply. It is made out of a very thin layer that starts with metal binders. Since it can be distinguished from other species by looking at the metal after it has rusted, as is the case with carbon iron rust, it is not regarded as a harmful species [163].

1.24 Type of corrosion
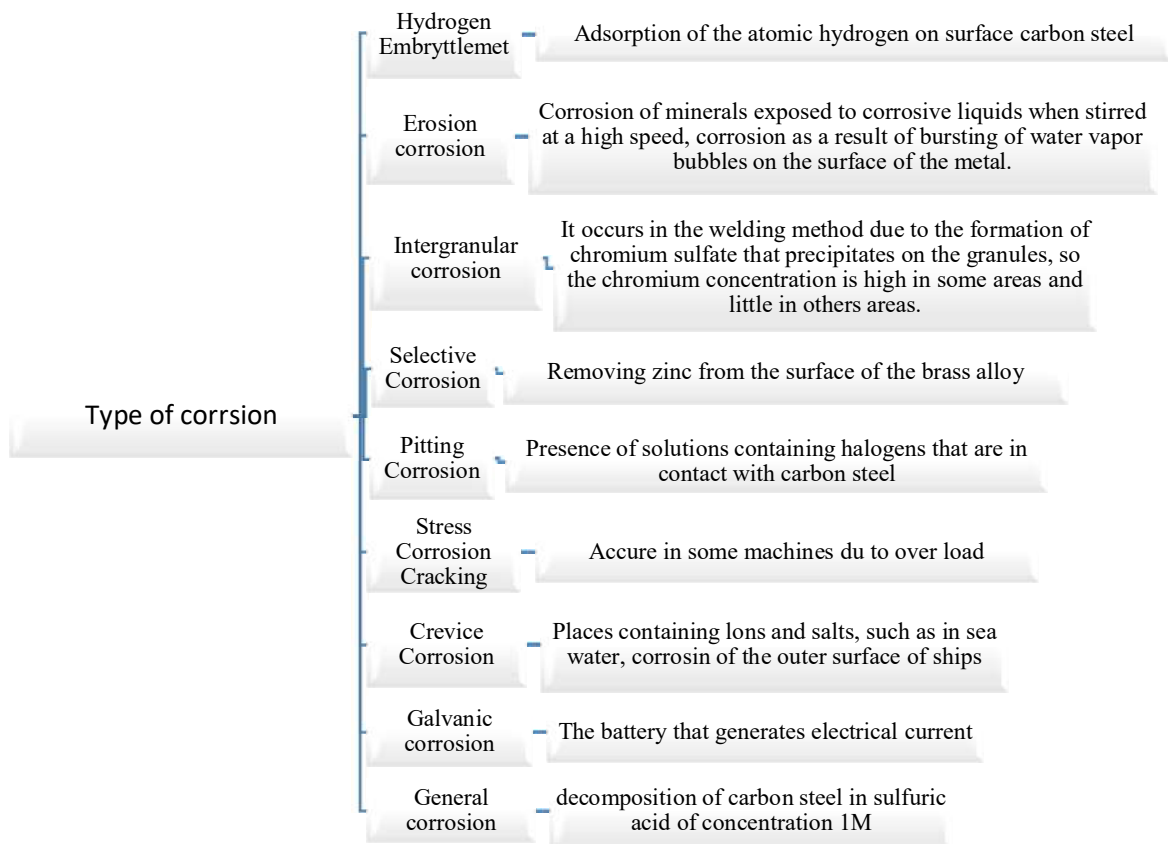
Figure 1-18: Scheme diagram of the type of corrosion and the reason for its occurrence [164].

1.25 Corrosion Inhibitor of Carbon Steel

As a raw material, carbon steel is one of the most significant industrial materials. It is made from an alloy of iron, carbon, and traces of other metals [165, 166]. Since carbon steel has good mechanical, welding, and annealing properties and because it is inexpensive[167]. Additionally, carbon steel has great properties that support its use in a variety of industries, including industry, oil, and gas [166, 168-170]. The carbon steel used for oil exploration in wells will corrode as a result of the harsh effects of the acid solutions, which have been used as a solvent to dissolve the rocks in the oil wells. Acid solutions are used in many industrial fields to clean and descale steel substrates, dissolve rubble, remove mud, and create channels through rocks to access crude oil[171]. The use of (5-28 percent) HCl is thought to be the most common

approach for improving the production of additional oil and gas worldwide [166, 172]. Today, it has become crucial to control corrosion damages using various techniques and methods, such as coating the surfaces or adding materials, such as inorganic or organic compounds, to act as corrosion inhibitors and cathodic protection. This is because corrosion damages have an impact on the main three fields: economy, safety, and conservation [173-176]. However, taking into account the fact that mentioned by using acidic as corrosive solutions for various purposes, the use of the inhibitor is considered one of the most effective methods that have been shown and improve the controlling of the corrosion process because it is readily practicable, effective, and economically [177]. Numerous different inorganic and organic substances have been employed to prevent corrosion in acidic corrosive media for carbon steel [178]. Typically, inhibitors develop a compact protective or passive coating on the metal's surface after adhering to it to slow the rate of corrosion [179]. It has been discovered that organic compounds having N, S, and O heteroatoms, particularly when combined with aromatic or other -electronic systems, have strong anticorrosion potential [180]. The porphyrin molecule has the chemical structure of a possible corrosion inhibitor since it is a Lewis acid with a network of conjugated-electron systems and four nitrogen atoms at its center. It is a tetradentate chelating agent with strong bonding properties and a clear capacity to engage surfaces via a variety of physical and/or chemical processes [181]. The flexible model compounds for metalloenzymes and electron transport in biological systems are metal-porphyrin complexes. As ligands for the spectrophotometric detection of cations, stationary phases in high-pressure liquid chromatography (HPLC), biosensors, catalysis, photovoltaic cells, and membrane components for ion selective electrodes, porphyrins are used in a wide variety of other processes [182-185]. They have also been used as carbon steel corrosion inhibitors in aqueous mineral acids, according to reports [186-188]. Porphyrin molecules may change the electron

distribution of their conjugated aromatic rings to generate ordered molecular layers on electrode surfaces, according to a number of studies on the corrosion prevention abilities of various porphyrin molecules[189, 190]. These molecular layers operate as a barrier to stop electroactive substances from diffusing toward the metal surface. Peripheral functional groups, steric hindrance, and electron density at donor centers are some of the variables that have an impact on the adsorption of porphyrin molecules and their ability to suppress corrosion [191] . However, very few articles have focused on its capacity to guard against iron corrosion up to this point [192, 193].

1.26 The Aim of the Study

This work is aimed, for first time, to investigate the synthesis and applications of new series of porphyrin derivatives in DSSCs and as anti-corrosion by following steps below:

1. Prepare some heterocyclic compounds derivatives such as porphyrin derivatives.

2. Study the characterization of prepared heterocyclic compounds derivatives by FT-IR, m.p, ^{1}H-NMR, ^{13}C-NMR, or Mass analysis and CHNS.

3. Prepare some nanomaterials such as Graphene Quantum Dot (GQD) and metal oxide (Cd Fe$_2$O$_4$) nanomaterial.

4. Prepare of TiO$_2$/GQD, and TiO$_2$/CdFe$_2$O$_4$as composites.

5. Identification of all prepared nanomaterials using FT-IR, XRD, FE-SEM ,EDX, Ramman analysis, and Bandgap.

6. Apply some prepared porphyrin derivatives as a sensitizer for different prepared photocatalysts to manufacture a solar cell.

7. Study the efficiencies for the produced solar cell with semiconductors.

8. Apply some prepared porphyrin derivatives as anti-corrosion.

To the best of our knowledge,

CHAPTER TWO

Experimental

2. Experimental and Methods

2.1. Chemical

Table (2-1), The chemical and materials which are used in this study.

Table (2-1): The chemical and materials

No.	Materials	Company	Purities % or percentage
1.	1-(4-Aminophenyl) Ethan-1-one	Fluka	99.98
2.	2-Amino benzimidazole	Merck, Germany	99.98
3.	2-Amino benzothiazole	Merck, Germany	99.98
4.	3-Hydroxybenzaldehyde	ChemChina, China	98
5.	4,4'-Methylenedianiline	Fluka	99.98
6.	4,4'-Oxydianiline	Merck, Germany	99.98
7.	4,4'-Sulfonyldianiline	Merck, Germany	99.98
8.	4-Aminobenzamide	Fluka	99.98
9.	4-Formylbenzoic acid	ChemChina, China	98
10.	5-Methoxybenzo thiazol-2-amine	Sigma Aldrich	99.98
11.	Acridine-3,6-diamine	Merck, Germany	99.98
12.	Benzidine	Merck, Germany	99.98
13.	$CdCl_2.2H_2O$	Sigma cheml co. USA.	99
14.	Ethanol absolute	Honeywell, Germany	99.99
15.	Ferric nitrate $Fe(NO_3)_3.9H_2O$	Sigma cheml co. USA.	99
16.	HCl	Sigma Aldrich	37 %
17.	*N,N*-dimethylformamide	Thomas beaker, India	99.98
18.	Propanoic acid	BDH, England	99.98
19.	Pyrrole	Alfa aesar, German	99.98
20.	Sulfurous dichloride	Merck, Germany	99
21.	Titanium dioxide (TiO_2)	Riedel-De-Haen AG, Seelze, Hannover,Germany	99.98
22.	Triethylamine	Merck, Germany	98
23.	Triton X -100	Himedia, USA	98

2.2 Instruments

Table (2-2) describes the employed instruments in this study with their companies and places.

Table (2-2): Employed instruments

No.	Instruments	Companies	Location
1.	^{13}C-NMR spectra	JEOL 125 MHz in (DMSO-d_6), Japan	National research center-Giza-Egypt
2.	^{1}HNMR spectra	Varian INOVA 500 MHz	Center Tehran Laboratory College, university of Tehran., Iran
3.	Electrospray Ionization Mass Spectrometry (ESI-MS)	Shimadzu LCMS 2010	Center Tehran Laboratory College, university of Tehran., Iran
4.	FT-IR Spectrometers	Shimadzu,8400S Japan	University of Kerbala, Science College
5.	Melting points	SMP 30 capillary melting point apparatus, UK	University of Kerbala, College of Science
6.	Micro elemental analysis	Euro EA3000 Elemental Analyzes, Italy	Center Tehran Laboratory College, university of Tehran., Iran
7.	Oven	Memmert, Germany.	University of Kerbala, College of Science
8.	Potentiostate	WENKING M Lab Bank Electronik-Intelligent controls GmbH, Germany	Al-Nahrain University, College of Science
9.	Raman spectra	Teksan TakramN1-541	Center Tehran Laboratory College, university of Tehran., Iran
10.	Scanning Electron Microscopy (EDAX)	thermos scientific, Dutch	Alkhora company for general trading -Nano lab
11.	Scanning Electron Microscopy (FE-SEM)	Inspect f 50, Fei, Dutch	Alkhora company for general trading -Nano lab
12.	Scanning Electron Microscopy (SEM) (EDAX)	(kyky EM) 320., USA.	Isfahan University, Iranian Islamic Republic
13.	Ultrasonic bath high-frequency ≥ 100kHz	DAIHAN Scientific, Korea.	University of Kerbala, College of Science
14.	X-Ray Diffraction Spectroscopy	Lab X- XRD 6000, Shimadzu, Japan	The Ministry of Science and Technology

2.3 Preparation Methodology

2.3.1 Preparation of 4,4',4'',4'''-(porphyrin-5,10,15,20-tetrayl) tetra benzoic acid (3).

Pyrrole (1.93 mL, 0.028 mol) was added to a solution of substituted aldehyde (4-formyl benzoic acid) (4.2 g, 0.028 mol) in propionic acid (20 mL), and the reaction mixture was refluxed for one hour in the dark after that. TLC (*n*-hexane: EtOAc, 2: 3) showed that the reactions were completed, to give a green precipitate that was filtered under reduced pressure, washed well with hot distilled water, and recrystallized from ethanol [194].

Figure (2-1): Structures compound **3**
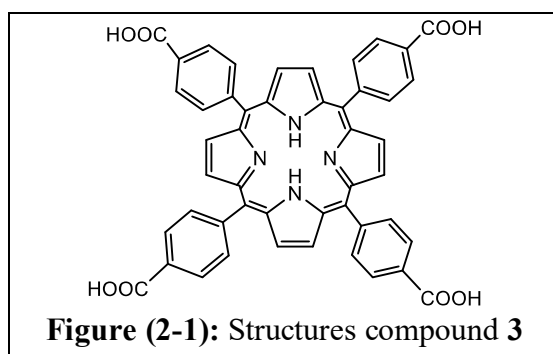
4,4',4'',4'''-(porphyrin-5,10,15,20-tetrayl) tetra benzoic acid (3), as shown in Figure (2-1). Color: dark green powder: Yield 21%, mp > 350°C R_f =0.067 (*n*-hexane: EtOAc,2:3) FT-IR (KBr, Cm^{-1}): 3371(NH), 3600-2400(OH carboxylic acid) ,3043(C-H aromatic), 1674(C=O), 1604(C=N), 1573(C=C). ^{1}H-NMR (500 MHz, DMSO-d$_6$) δH (ppm): 12.91(s,<u>4H</u>, COOH), 8.79(d, J = 7.6 Hz,<u>8H</u> ,Pyrrole), 8.38-7.13(m, 16<u>H</u>, Ar-<u>H</u>), -2.29 (s,2 <u>H</u>, N<u>H</u>), ^{13}C-NMR (125MHz, DMSO-d$_6$) δ C: 122.25,126.64,126.92,129.53,129.55,130.57,130.57,130.61,130.63,138.03,139.17,143.88,147.65,168.14., UV-Vis. Spectrum: (λ_{max}), (419 nm.); ESI-MS(*m/z*) calcd. exact mass (C$_{48}$H$_{30}$N$_4$O$_8$), 790.21; found, 790.20.

2.3.2. General procedure for the Preparation of porphyrin derivatives 5a-f.

(2.9 mL, 0.04 mol) of $SOCl_2$ was added to (7.907 g, 0.01 mol) of 4,4',4'',4'''-(porphyrin-5,10,15,20-tetrayl) tetra benzoic acid (3). The mixture was stirred at 70 rpm for 30 minutes at room temperature, and then DMF (5 mL) was added with continuous stirring at the same temperature for 10 minutes. The final solution was transferred to round bottom flask volume (100 mL), (0.04 mol) of amines (2-aminobenzothiazole, 5-Methoxybenzo Thiazol-2-Amine, Acridine-3,6-diamine, 1-(4-aminophenyl)ethan-1-one, 4-Amino benzamide, 2-aminobenzimidazole) were added to the last solution with reflux for (2-3) hours, and then (11.2 mL, 0.08 mol) of triethyl amine (Et_3N) was added with continuous reflux for one hour. TLC (*n*-hexane: EtOAc, 2:3) showed that the reactions were completed. The black solution was added to the ice crystal, and the black precipitate was filtered and washed with ethanol. Then recrystallized from mixture ethanol and DMF[195].
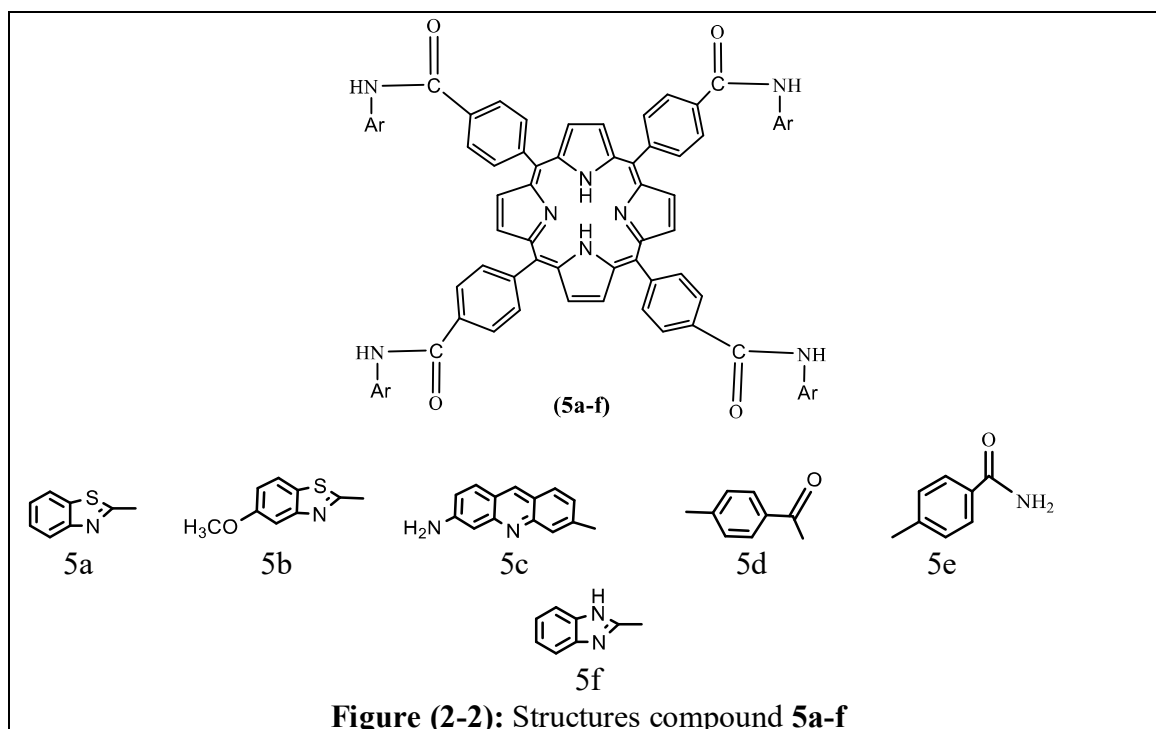
Figure (2-2): Structures compound **5a-f**

4,4',4'',4'''-(Porphyrin-5,10,15,20-tetrayl)tetrakis(*N*-(benzo[d]thiazol-2-yl)benzamide) (5a) as shown in Figure (2-2). Color: Black powder: Yield 80%, mp > 350°C FT-IR (KBr, cm^{-1}): 3425(NH Stretch), 3055(C–H aromatic), 1701(C=O), 1608(C=N),1489(C=C aromatic), 1095(C-S). ^{1}H-NMR (500 MHz, DMSO-d$_6$) δH (ppm): 10.51 (s,4<u>H</u>-CO N<u>H</u>), 8.66-8.11 (m, 8H Pyrrole-<u>H</u>), 8.09-7.16(m, 32H, Ar-<u>H</u>), -2.29 (s,2H, N<u>H</u>$_{int}$)., ^{13}C-NMR (125 MHz, DMSO-d$_6$) δC:120.03,120.93,122.2,123.60,125.64,126.64,129.43,129.52, 129.54,130.61,130.64,130.71,132.15,138.01,138.72,139.35,143.88,147.65, 150.32,156.83, 159.77,166.95., UV-Vis. Spectrum: (λ_{max}), 417nm.; Anal.Calcd for (C$_{76}$H$_{46}$N$_{12}$O$_4$S$_4$): C, 69.18; H, 3.51; N, 12.74; S, 9.72 found C, 68.21; H, 3.32; N, 11.48; S, 9.52 %., ESI-MS(*m/z*) calcd exact mass 1318.26; found, 1318.20.

4,4',4'',4'''-(porphyrin-5,10,15,20-tetrayl)tetrakis(N-(5methoxybenzo[d] thiazol-2-yl) benzamide) (5b) as shown in Figure (2-2). Color: Black powder: Yield 83%, mp > 350°C FT-IR (KBr, cm^{-1}):3441 (NH), 3059 (C–H aromatic), 2924(C–H aliphatic), 1693(C=O), 1612(C=N), 1454(C=C aromatic), 1099(C-S).^{1}H-NMR (500 MHz, DMSO-d$_6$) δH (ppm): 10.46 (s,4<u>H</u>-CON<u>H</u>), 8.41-8.34 (m, 8H, Pyrrole), 8.22-7.30 (m 28H, Ar-<u>H</u>), 3.89 (s,12H, OC<u>H$_3$</u>), -3.00 (s,2H, N<u>H</u>$_{int}$)., ^{13}C-NMR (125 MHz, DMSO-d$_6$) δ C: 60.14,98.39,113.61,115.82, 116.22,122.63,122.82,122.83,126.76,127.09,127.78,129.51,129.53,129.61, 129.62,131.90,137.82,138.04,138.22,139.02,150.74,157.77,159.02,159.17, 161.55,166.50.,Anal. Calcd for (C$_{80}$H$_{54}$N$_{12}$O$_8$S$_4$): C, 66.75; H, 3.78; N, 11.68; S, 8.91 found C, 65.70; H, 3.32; N, 10.50; S, 8.35%.

54,4',4'',4'''-(porphyrin-5,10,15,20-tetrayl)tetrakis(*N*-(6-aminoacridin-3-yl) benzamide) (5c) as shown in Figure (2-2).Color: Black powder: Yield 80%, mp > 350°C FT-IR (KBr, cm^{-1}): 3333 and 3300(NH$_2$), 3201(NH), 3055(C–H aromatic),1693(C=O), 1600(C=N), 1489(C=C aromatic). ^{1}H-NMR (500MHz, DMSO-d$_6$) δH (ppm): 10.47 (s,4<u>H</u>-CON<u>H</u>), 8.41-8.37 (m, 8<u>H,</u> Pyrrole), 8.10-7.19 (m, 44H Ar-<u>H</u>), 6.46(s,8H, N<u>H$_2$</u>), -2.94 (s,2H, N<u>H</u>$_{int}$)., ^{13}C-NMR (125

MHz, DMSO-d_6) δ C:- 98.64,111.89,115.82,116.22,116.47,119.87,121.01, 122.82,12.83,124.64,127.78,129.09,129.51,129.53,129.61,129.62,131.23,133 .48,137.82,138.04,138.22,138.94,139.76,147.24,174.42,150.66,159.00,159.1 4,166.30)., Anal.Calcd for ($C_{100}H_{66}N_{16}O_4$): C, 77.20; H, 4.28; N, 14.41 found C, 76.41; H, 4.05; N, 13.22%., ESI-MS(m/z) calcd exact mass ($C_{100}H_{66}N_{16}O_4$), 1555.55; found, 1555.50.

4,4',4'',4'''-(porphyrin-5,10,15,20-tetrayl)tetrakis(N-(4-acetylphenyl) benzamide) (5d) as shown in Figure (2-2). Color: Black powder: Yield 82%, mp > 350°C FT-IR (KBr, cm^{-1}): 3309(NH), 3059(C–H aromatic),2924(C–H aliphatic),1697(C=O), 1604 (C=N),1485(C=C aromatic).^{1}H-NMR (500MHz, DMSO -d_6) δH (ppm): 9.94 (s,4<u>H</u>-CON<u>H</u>),8.71-8.37 (m, 8H, Pyrrole), 8.13-7.45 (m, 32H Ar-<u>H</u>), 2.68 (s,12H, OC<u>H</u>$_3$), -1.81 (s,2H, N<u>H</u>$_{int}$)., Anal.Calcd for ($C_{80}H_{58}N_8O_8$): C, 76.30; H, 4.64; N, 8.90 found C, 75.68; H, 4.20; N, 7.85 %.

4,4',4'',4'''-(porphyrin-5,10,15,20-tetrayl) tetrakis(N-(4-carbamoyl phenyl) benzamide) (5e) as shown in Figure (2-2). Color: Black powder: Yield 84%, mp > 350°C FT-IR (KBr, cm^{-1}): 3420-3395(NH$_2$), 3290(NH), 3059(C–H aromatic), 1697(C=O), 1600(C=N), 1484(C=C aromatic). ^{1}H-NMR (500MHz, DMSO-d_6) δH (ppm): 9.84 (s,4<u>H</u>-CON<u>H</u>), 8.67-8.64 (m, 8<u>H</u>, Pyrrole), 8.15-7.31 (m, 32H, Ar-<u>H</u>), .693 (s,8H, N<u>H</u>$_2$), - 1.99 (s, 2H, N<u>H</u>)., Anal.Calcd for ($C_{76}H_{54}N_{12}O_8$): C, 72.26; H, 4.31; N, 13.30 found C, 71.80; H, 4.15; N, 12.57 %.

4,4',4'',4'''-(porphyrin-5,10,15,20-tetrayl)tetrakis(N-(1H-benzo[d]imidazol -2-yl) benzamide) (5f) as shown in Figure (2-2). Color: Black powder: Yield 82%, mp > 350°C FT-IR (KBr, cm^{-1}): 3421(NH Stretch), 3036(C–H aromatic), 1705(C=O), 1624(C=N), 1485(C=C aromatic). ^{1}H-NMR (500MHz, DMSO-d_6) δH (ppm): 11.37 (s,4N<u>H</u>), 10.69 (s,4<u>H</u>-CON<u>H</u>), 8.86-8.37 (m,8<u>H</u>, Pyrrole), 8.10-7.12 (m, 32H Ar-<u>H</u>), -2.25 (s,2H, N<u>H</u>), Anal.Calcd for ($C_{76}H_{50}N_{16}O_4$) : C, 72.95; H, 4.03; N, 17.91; found C, 72.60; H, 3.90; N, 17.50 %., ESI-MS (m/z) calcd exact mass 1250.42; found, 1250.38.

2.3.3 General procedure for the Preparation of porphyrin derivatives 6a-f.

(2.17 mL, 0.03 mol) of SOCl$_2$ was added to (7.907 g, 0.01 mmol) of 4,4',4'',4'''-(porphyrin-5,10,15,20-tetrayl)tetrabenzoic acid (3). The mixture was stirred at 70 rpm for 30 minutes at environmental temperature, then DMF (5 mL) was added with continuous stirred for 10 minutes at the same temperature. The final solution was transferred to a round bottom flask volume (100 mL), (0.03 mol) of amines (2-aminobenzothiazole, 5-methoxybenzo thiazol-2-Amine, 1-(4-aminophenyl)ethan-1-one, 2-amino benzimidazole, 4,4'-sulfonyldianiline, benzidine) were added to the last solution with for (2-3) hours, and then (8.3 mL, 0.06 mol) of triethylamine (Et$_3$N) was added with continuous for one hour. TLC (*n*- hexane: EtOAc, 2:3) showed that the reactions were completed. The black solution was added to ice crystal, filtration, and washed with ethanol. Then recrystallized from mixture ethanol and DMF [195].
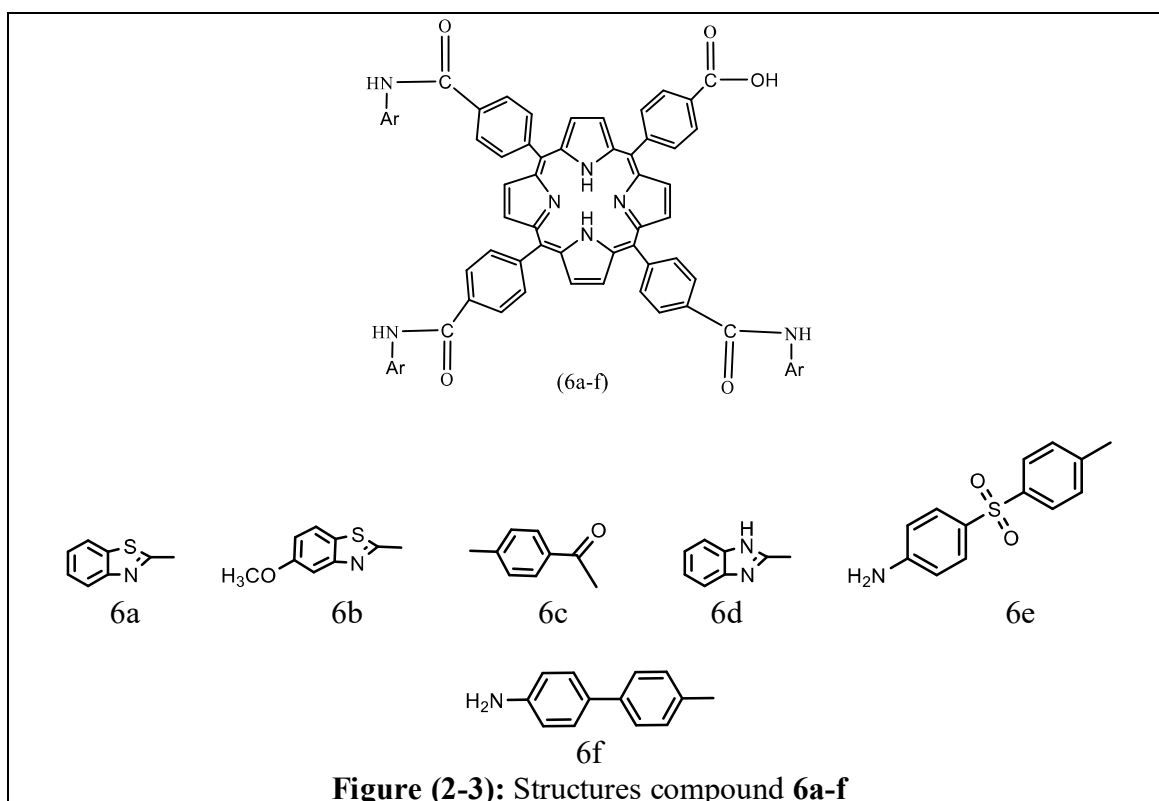
Figure (2-3): Structures compound **6a-f**

4-(10,15,20-tris(4-(benzo[d]thiazol-2-ylcarbamoyl)phenyl)porphyrin-5-yl)benzoic acid (6a) as shown in Figure (2-3). Color: Black powder: Yield 75%, mp > 350°C FT-IR (KBr, cm^{-1}):3421(NH), 3600-2400(OH carboxylic acid), 3031(C–H aromatic), 1701(C=O), 1612(C=N), 1496(C=C aromatic), 1138(C-S). ^{1}H-NMR (500MHz, DMSO-d$_6$) δH (ppm): 12.40 (s, 1<u>H</u>, COO<u>H</u>), 10.59 (s,3<u>H</u>, CON<u>H</u>). 8.47-8.04(m,8<u>H</u> Pyrrole), 7.93-7.16 (m 28H, Ar-<u>H</u>), -0.82 (s,1H, N<u>H</u>$_{int}$), -1.76 (s,1H, N<u>H</u>$_{int}$)., ^{13}C-NMR (125 MHz, DMSO-d$_6$) δC:-94.40,100.01,115.66,123.03,126.94,129.82,130.04,130.43,130.57,138.63,144.17,144.77,147.97,156.63,156.83,162.84,163.35,167.30,168.90.,Anal.Calcd for (C$_{69}$H$_{42}$N$_{10}$O$_5$S$_3$): C, 69.80; H, 3.57; N, 11.80; S, 8.10 found C, 69.55; H, 3.35; N, 11.33; S, 7.83 %., ESI-MS(m/z) calcd exact mass (C$_{69}$H$_{42}$N$_{10}$O$_5$S$_3$), 1186.25; found, 1186.20.

4-(10,15,20-tris(4-((5-methoxybenzo[d]thiazol-2-yl) carbamoyl) phenyl) porphyrin-5-yl) benzoic acid (6b) as shown in Figure (2-3). Color: Black powder: Yield 65%, mp > 350°C FT-IR (KBr, cm^{-1}): 3421(NH), 3600-2400(OH carboxylic acid), 3066(C–H aromatic), 2962(C–H aliphatic), 1701(C=O), 1604(C=N), 1492(C=C aromatic), 1103(C-S). ^{1}H-NMR (500MHz, DMSO-d$_6$) δH (ppm): 12.72 (s, 1<u>H</u>, COO<u>H</u>), 10.68 (s,3<u>H</u>, CON<u>H</u>). 8.40-8.31(m,8H, Pyrrole), 8.05-7.19 (m 25H, Ar-<u>H</u>), 3.65 (s, 9H, OC<u>H</u>$_3$), -0.82 (s,1H, N<u>H</u>$_{int}$), -1.76 (s,1H, N<u>H</u>$_{int}$)., Anal. Calcd for (C$_{72}$H$_{48}$N$_{10}$O$_8$S$_3$): C, 67.70; H, 3.79; N, 10.97; S, 7.53 found C, 67.42; H, 3.20; N, 10.36; S, 7.15 %. ESI-MS(m/z) calcd exact mass (C$_{72}$H$_{48}$N$_{10}$O$_8$S$_3$), 1276.28; found, 1276.21.

4-(10,15,20-tris (4-((4-acetyl phenyl) carbamoyl) phenyl) porphyrin-5-yl) benzoic acid (6c) as shown in Figure (2-3). Color: Black powder: Yield 64%, mp > 350°C FT-IR (KBr, cm^{-1}):3421 (NH), 3600-2400 (OH carboxylic acid) 3066(C–H aromatic), 2931(C–H aliphatic), 1701(C=O), 1612(C=N), 1489 (C=C aromatic). ^{1}H-NMR (500MHz, DMSO-d$_6$) δH (ppm): 12.00 (s, 1<u>H</u>, COO<u>H</u>), 9.63 (s,3<u>H</u>, CON<u>H</u>), 8.86-7.29 (m,36H, Pyrrole and Ar-<u>H</u>),3.06 (s, 9H, C<u>H</u>$_3$), -0.82 (s,1H, N<u>H</u>$_{int}$), -1.76 (s,1H, N<u>H</u>$_{int}$)., Anal. Calcd for

($C_{80}H_{58}N_8O_8$): C, 75.71; H, 4.750; N, 8.58 found C, 75.15; H, 4.20; N, 8.19 %. ESI-MS(*m/z*) calcd exact mass ($C_{72}H_{51}N_7O_8$), 1141.38; found, 1141.32.

4-(10,15,20-tris(4-((1H-benzo[d]imidazol-2-yl) carbamoyl) phenyl) porphyrin-5-yl) benzoic acid (6d) as shown in Figure (2-3). Color: Black powder: Yield 62%, mp > 350°C FT-IR (KBr, cm^{-1}): 3414(NH) 3600-2400(OH carboxylic acid), 3031(C–H aromatic), 1701(C=O), 1612(C=N), 1485(C=C aromatic)., ^{1}H-NMR (500MHz, DMSO-d$_6$) δH (ppm): 12.57 (s, <u>1H</u>, COO<u>H</u>), 11.32 (s, 3H, N<u>H</u>), 10.40 (s,3<u>H</u>, CON<u>H</u>), 8.48-7.27 (m,36<u>H</u>, Pyrrole and Ar-<u>H</u>), -0.82 (s,1H, N<u>H</u>$_{int}$), -1.76 (s,1H, N<u>H</u>$_{int}$)., ^{13}C-NMR (125 MHz, DMSO-d$_6$) δ C:- 64.07,96.48,115.66,123.03,126.94,129.82,130.04,130.43,130.57,138.63 ,144.17,144.77,147.97,156.63,156.83,162.84,163.35,167.30,168.90., Anal. Calcd for ($C_{69}H_{45}N_{13}O_5$): C, 72.94; H, 3.99; N, 16.03 found C, 72.34; H, 3.79; N, 15.85%., ESI-MS(*m/z*) calcd exact mass ($C_{69}H_{45}N_{13}O_5$), 1135.37; found, 1135.31.

4-(10,15,20-tris(4-((4-((4aminophenyl)sulfonyl)phenyl)carbamoyl)phenyl) porphyrin-5-yl)benzoic acid (6e) as shown in Figure (2-3). Color: Black powder: Yield 55%, mp > 350°C FT-IR (KBr, cm^{-1}): 3425 and 3389(NH$_2$), 3600-2400(OH carboxylic acid) 3031(C–H aromatic),1701(C=O), 1616 (C=N), 1489(C=C aromatic). ^{1}H-NMR (500MHz, DMSO-d$_6$) δH (ppm): 12.66 (s, <u>1H</u>, COO<u>H</u>), 9.96 (s,3<u>H</u>, CON<u>H</u>), 8.45-6.54 (m,48H, Pyrrole and Ar-<u>H</u>), 5.41(s, 6H, N<u>H</u>$_2$), -0.82 (s,1H, N<u>H</u>$_{int}$), -1.76 (s,1H, N<u>H</u>$_{int}$)., Anal.Calcd for ($C_{84}H_{60}N_{10}O_{11}S_3$): C, 68.09; H, 4.08; N, 9.45; S, 6.49 found C, 67.75; H, 3.90; N, 8.85; S, 6.18 %., ESI-MS(*m/z*) calcd exact mass ($C_{84}H_{60}N_{10}O_{11}S_3$), 1480.36; found, 1480.29.

4-(10,15,20-tris(4-((4'-amino-[1,1'-biphenyl]-4-yl)carbamoyl)phenyl) porphyrin-5-yl) benzoic acid (6f) as shown in Figure (2-3). Color: Black powder: Yield 60%, mp > 350°C FT-IR (KBr, cm^{-1}): 3406 and 3320(NH$_2$), 3600-2400(OH carboxylic acid) 3020(C–H aromatic), 1701(C=O), 1616(C=N) , 1489(C=C aromatic). ^{1}H-NMR (500MHz, DMSO-d$_6$) δH (ppm): 11.79 (s, <u>1H</u>,

COO$\underline{H}$), 9.89(s,$\underline{3H}$, CON$\underline{H}$), 8.78-6.73 (m,48H, Pyrrole and Ar-$\underline{H}$), 5.31(s, 6H, N$\underline{H_2}$), -0.82 (s,1H, N$\underline{H}_{int}$), -1.76 (s,1H, N$\underline{H}_{int}$)., Anal. Calcd for ($C_{84}H_{60}N_{10}O_5$): C, 78.24; H, 4.69; N, 10.86; found C, 77.94; H, 4.55; N, 10.35%., ESI-MS(m/z) calcd exact mass ($C_{84}H_{60}N_{10}O_5$), 1288.47; found, 1288.40.

2.3.4 Preparation of 4-(10,15,20-tris(3-hydroxyphenyl)porphyrin-5-yl) benzoic acid (8).

Pyrrole (1.93 mL, 0.028 mol) was added to a solution of substituted aldehyde {(4-formyl benzoic acid) (1.05 g ,0.007 mol) and (3-hydroxy benzaldehyde) (2.6 g, 0.021 mol)} in propionic acid (20 mL), and the reaction mixture was refluxed for one hour in the dark after that. TLC (*n*-hexane: EtOAc, 2:3) showed that the reactions were completed, to give latency precipitate that was filtered under reduced pressure, washed well with hot distilled water, and recrystallized from ethanol [196].

Figure (2-4): Structures compound **8**
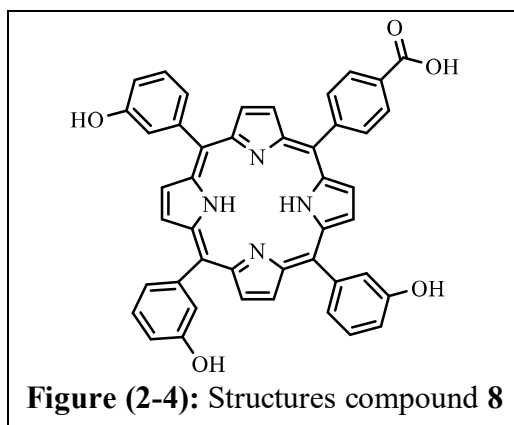
4-(10,15,20-tris(3-hydroxyphenyl)porphyrin-5-yl)benzoic acid (8) as shown in Figure (2-4). Color: green: Yield 25%, mp > 350°C FT-IR (KBr, cm^{-1}): 3309(OH) 3600-2400(OH carboxylic acid), 3009(C–H aromatic), 1708 (C=O), 1585 (C=N), 1485(C=C aromatic). ^{1}H-NMR (500 MHz, DMSO-d$_6$) δH (ppm): 12.49 (s,$\underline{1H}$, COO$\underline{H}$). 8.83-8.41 (m,8H, Pyrrole), 8.11-7.06 (m 16H, Ar-$\underline{H}$), 6.76 (s, 3H, O$\underline{H}$), -1.45 (s,1H, N$\underline{H}_{int}$), -2.64 (s,1H, N$\underline{H}_{int}$)., ^{13}C-NMR (125 MHz, DMSO-d$_6$) δ C: 115.59,120.25,120.28,122.22,122.52,123.76,123.89,

123.99,126.57.126.64,126.99,127.06,128.55,128.94,129.60,129.67,130.56,
130.64,136.36,136.52,139.86,143.44,143.88,146.84,153.68,153.68,156.14,
169.36., ESI-MS(*m/z*) calcd exact mass ($C_{103}H_{67}N_{11}O_8$) 706.22; found, 706.1.

2.3.5 General procedure for synthesis of amides (9a-d) from 4-(10,15,20-tris(3-hydroxyphenyl) porphyrin-5-yl) benzoic acid (8)

(0.72 mL, 0.01 mol) of $SOCl_2$ was added of 4-(10,15,20-tris(3-hydroxyphenyl) porphyrin-5-yl) benzoic acid (8) (7.1 g ,0.01 mol). The mixture was stirred at 70 rpm for 30 minutes at environmental temperature, then DMF (5mL) was added with continuous stirred for 10 minutes at the same temperature. The final solution was transferred to round bottom flask volume (100 mL), (0.01 mol) amines (2-aminobenzothiazole, 2-aminobenzimidazole, 1-(4-aminophenyl)ethan-1-one, 4-aminobenzamide) were added to the last solution with for (2-3) hours, and then (2.79 mL, 0.02 mol) triethylamine (Et_3N) was added with continuous for 1hours. TLC (*n*- hexane: EtOAc, 2:3) showed that the reactions were completed. The black solution was added to ice crystal, filtration, and washed with ethanol. Then recrystallized from mixture ethanol and DMF [195].
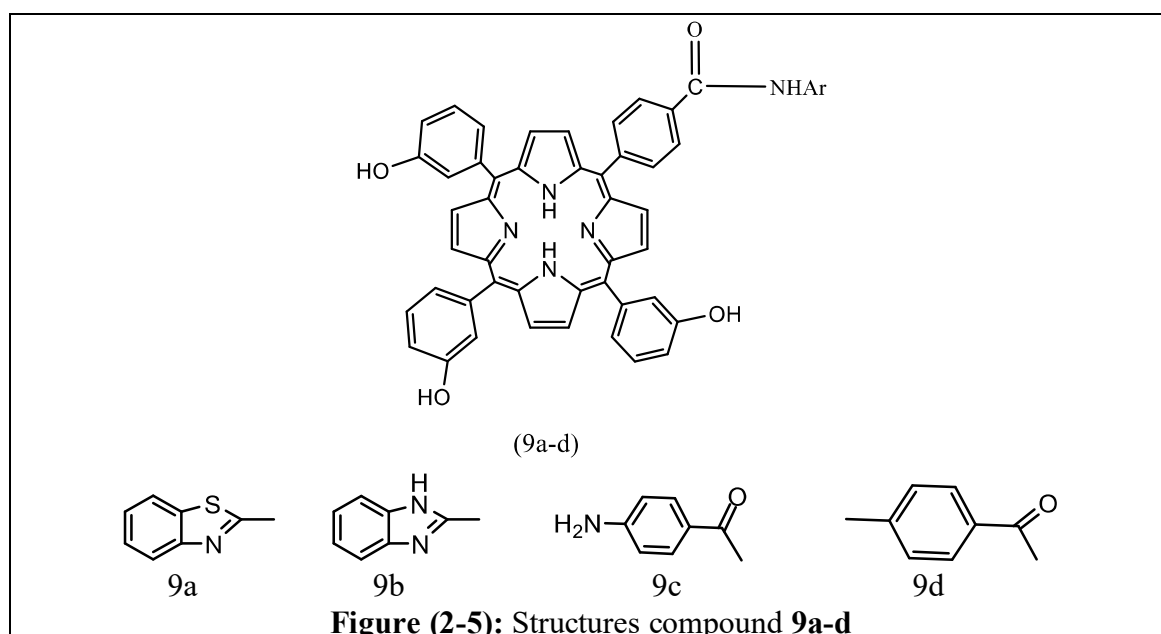

Figure (2-5): Structures compound **9a-d**

N-(benzo[d]thiazol-2-yl)-4-(10,15,20-tris(3-hydroxyphenyl)porphyrin-5-yl) benzamide (9a) as shown in Figure (2-5). Color: Black powder: Yield 65%, mp > 350°C FT–IR (KBr, cm^{-1}): 3421(OH), 3228(NH), 3039(C–H aromatic), 1701(C=O), 1604(C=N), 1446(C=C aromatic), 1099(C-S).^{1}H-NMR (500MHz, DMSO-d$_6$) δH (ppm): 10.80 (s,1$\underline{H}$, CON$\underline{H}$), 8.45-7.06 (m,28H, Pyrrole and Ar-$\underline{H}$), 6.86 (s,3H, O$\underline{H}$), -1.45 (s,1H, N$\underline{H}_{int}$), -2.64 (s,1H, N$\underline{H}_{int}$)., ^{13}C-NMR (125 MHz, DMSO-d$_6$) δ C:- 94.40,100.01,115.66,123.03,126.94,129.82, 130.04,130.43,130.57,138.63,144.17,144.77,147.97,156.63,156.83,162.84, 163.35,167.30,168.90.,ESI-MS(*m/z*) calcd exact mass (C$_{52}$H$_{34}$N$_6$O$_4$S), 838.24; found, 838.20.

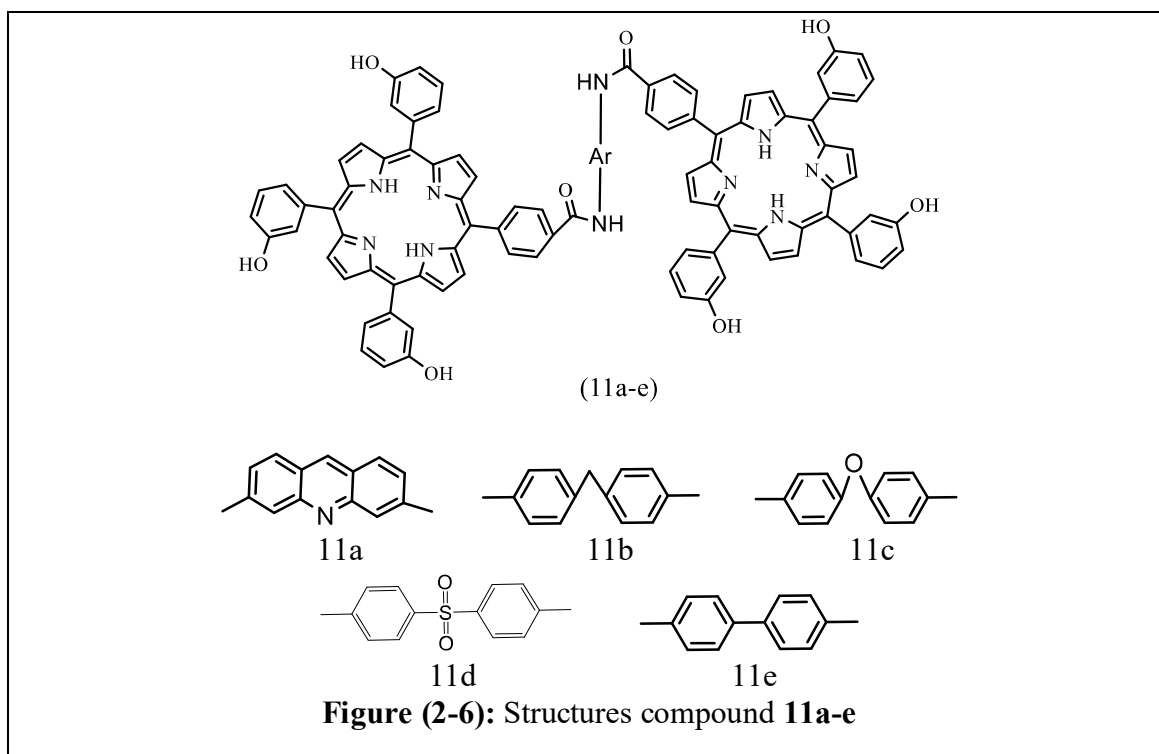*N*-(4-acetylphenyl)-4-(10,15,20-tris(3-hydroxyphenyl)porphyrin-5-yl) benzamide (9b) as shown in Figure (2-5). Color: Black powder: Yield 60%, mp > 350°C FT–IR (KBr, cm^{-1}): 3302(OH), 3112(NH), 3016(C–H aromatic), 2928 (C–H aliphatic), 1697(C=O), 1597(C=N), 1481(C=C aromatic). ^{1}H-NMR (500MHz, DMSO-d$_6$) δH (ppm): 9.26 (s,1$\underline{H}$, CON$\underline{H}$), 8.52-8.36 (m,8H, Pyrrole), 8.14-7.02 (m 20H, Ar-$\underline{H}$), 6.84 (s, 3H, O$\underline{H}$), 3.64 (s,3H, C$\underline{H}_3$), -1.45 (s,1H, N$\underline{H}_{int}$), -2.64 (s,1H, N$\underline{H}_{int}$)., Anal. Calcd for (C$_{53}$H$_{37}$N$_5$O$_5$): C,77.26; H, 4.53; N, 8.50 found C, 76.80; H, 4.32; N, 8.05%.,

N-(4-carbamoyl phenyl)-4-(10,15,20-tris(3-hydroxyphenyl) porphyrin-5-yl) benzamide (9c) as shown in Figure (2-5). Color: Black powder: Yield 63%, mp > 350°C FT-IR (KBr, cm^{-1}): 3535(OH) 3495 and 3120(NH$_2$), , 3047(C–H aromatic), 1697(C=O), 1600(C=N), 1446(C=C aromatic). ^{1}H-NMR (500MHz, DMSO-d$_6$) δH (ppm): 9.28 (s,1$\underline{H}$, CON$\underline{H}$), 8.45-7.05 (m, 28H, Pyrrole and Ar-$\underline{H}$), 6.92(s, 2H, N$\underline{H}_2$), 6.85 (s, 3H, O$\underline{H}$), -1.45 (s,1H, N$\underline{H}_{int}$), -2.64 (s,1H, N$\underline{H}_{int}$)., ^{13}C-NMR (125 MHz, DMSO-d^6) δ C:- 94.40,100.01,115.66,123. 03,126.94, 129.82,130.04,130.43,138.63,144.17,144.77,147.97,156.63,156.83,162.84, 163.35,167.30,168.90., Anal. Calcd for (C$_{52}$H$_{36}$N$_6$ O$_5$): C, 75.72; H, 4.40; N, 10.19 found C, 75.23; H, 4.33; N, 10.05%.,

N-(1H-benzo[d]imidazol-2-yl)-4-(10,15,20-tris(3-hydroxyphenyl) porphyrin-5-yl) benzamide (9d) as shown in Figure (2-5). Color: Black powder: Yield 66%, mp > 350°C FT-IR (KBr, Cm⁻¹): 3410(OH), 3248 (NH), 3066(C–H aromatic), 1697(C=O), 1600(C=N), 1481(C=C aromatic). ¹H-NMR (500 MHz, DMSO-d₆) δH (ppm): 11.37(s, 1H, N<u>H</u>), 10.43 (s,1<u>H</u>, CON<u>H</u>), 8.45-7.06(m,28H, Pyrrole and Ar-<u>H</u>), 6.90(s, 3H, O<u>H</u>), -1.45 (s,1H, N<u>H</u>int), -2.64 (s,1H, N<u>H</u>int)., Anal. Calcd for ($C_{52}H_{35}N_7O_4$): C, 75.99; H, 4.29; N, 11.93 found C, 75.59; H, 4.20; N, 11.54%.,

2.3.6 General procedure for synthesis of amides (11a-e) from 4-(10,15,20-tris(3-hydroxyphenyl) porphyrin-5-yl) benzoic acid (8)

(1.45 mL, 0.02 mol) of $SOCl_2$ was added of 4-(10,15,20-tris(3-hydroxyphenyl) porphyrin-5-yl) benzoic acid (8) (14.2 g, 0.02 mol). The mixture was stirred at 70 rpm for 30 minutes at environmental temperature, then DMF (5 mL) was added with continuous stirred for 10 minutes at the same temperature. The final solution was transferred to a round bottom flask volume (100 mL), (0.01 mol) amines (acridine-3,6-diamine, 4,4'-methylene di aniline, 4,4'-oxydianiline, 4,4'-sulfonyldianiline, benzidine) were added to the last solution with for (2-3) hours, and then (5.58 mL, 0.04 mol) triethylamine (Et₃N) was added with continuous for 1huore. TLC (*n*- hexane: EtOAc, 2:3) showed that the reactions were completed. The black solution was added to ice crystal, filtration, and washed with ethanol. Then, it was recrystallized from mixture ethanol and DMF [195].

Figure (2-6): Structures compound **11a-e**

***N,N′*-(acridine-3,6-diyl)bis(4-(10,15,20-tris(3-hydroxyphenyl)porphyrin-5-yl)benzamide) (11a)** as shown in Figure (2-6). Color: Black powder: Yield 60%, mp > 350°C FT-IR (KBr, cm^{-1}): 3414(OH), 3218(NH), 3097(C–H aromatic), 1651(C=O), 1593(C=N), 1446(C=C aromatic). ^{1}H-NMR (500 MHz, DMSO-d$_6$) δH (ppm): 10.19(s,2$\underline{H}$, CON$\underline{H}$). 8.88-8.27 (m,16H, Pyrrole), 8.14-7.08(m 55H, Ar-$\underline{H}$), 6.81(s,6H, O$\underline{H}$), -1.45 (s,1H, N$\underline{H}_{int}$), -1.65 (s,1H, NH$_{int}$)., ESI-MS(m/z) calcd exact mass (C$_{103}$H$_{67}$N$_{11}$O$_8$) 1586.52; found, 1586.51.

***N,N′*-(methylenebis(4,1-phenylene))bis(4-(10,15,20-tris (3hydroxy phenyl) porphyrin-5-yl)benzamide) (11b)** as shown in Figure (2-6). Color: Black powder: Yield 70%, mp > 350°C FT-IR (KBr, cm^{-1}): 3398(OH), 3112(NH), 3012(C–H aromatic), 2982(C–H aliphatic), 1701(C=O), 1593(C=N), 1469 (C=C aromatic). ^{1}H-NMR (500 MHz, DMSO-d$_6$) δH (ppm): 9.03 (s,2$\underline{H}$, CON$\underline{H}$). 8.65-8.19 (m,16H, Pyrrole), 8.13-7.07 (m 40H, Ar-$\underline{H}$), 6.82 (s, 6H, O$\underline{H}$), 3.75(s,2H, C$\underline{H}_2$), -1.45 (s,2N$\underline{H}_{int}$), -1.50 (s,2N$\underline{H}_{int}$)., ESI-MS (m/z) calcd exact mass (C$_{103}$H$_{70}$N$_{10}$O$_8$), 1575.54; found, 1575.51.

N,N′-(oxybis(4,1-phenylene))bis(4-(10,15,20-tris(3hydroxyphenyl) porphyrin-5-yl)benzamide)(11c)** as shown in Figure (2-6). Color: Black powder: Yield 68%, mp > 350°C FT-IR (KBr, cm^{-1}): 3414(OH), 3214(NH), 3051(C–H aromatic), 1693(C=O), 1581(C=N), 1442(C=C aromatic), 578(C-O)., ^{1}H-NMR (500MHz, DMSO-d$_6$) δH (ppm): 9.90 (s,2H, CONH), 8.88-8.27 (m,16H, Pyrrole), 8.13-7.09(m,40H, Ar-H), 6.61(s,6H, OH), -1.43 (s,2H, NH$_{int}$), -1.61(s,2H, NH$_{int}$)., ESI-MS(*m/z*) calcd exact mass (C$_{102}$H$_{68}$N$_{10}$O$_9$), 1577.52; found, 1577.50.

N,N′-(sulfonylbis(4,1-phenylene))bis(4-(10,15,20-tris(3-hydroxyphenyl) porphyrin-5-yl)benzamide)(11d)** as shown in Figure (2-6). Color: Black powder: Yield 64%, mp > 350°C FT-IR (KBr, cm^{-1}): 3394(NH Stretch), 3214(OH), 3051(C–H aromatic), 1697(C=O), 1597(C=N), 1458(C=C aromatic), 570(C-S)., ^{1}H-NMR (500MHz, DMSO-d$_6$) δH (ppm): 10.06(s,2H, CONH). 8.88-827(m,16H, Pyrrole), 8.13-7.08(m40H, Ar-H), 6.83(s,6H, OH), -1.45 (s,2H, NH$_{int}$), -1.74 (s,2H, NH$_{int}$)., ESI-MS(*m/z*) calcd exact mass (C$_{102}$H$_{68}$N$_{10}$O$_{10}$S), 1625.49; found, 1625.47.

N,N′-([1,1′-biphenyl]-4,4′-dial)bis(4-(10,15,20-tris(3hydroxyphenyl) porphyrin-5-yl)benzamide)(11e)** as shown in Figure (2-6). Color: Black powder: Yield 71%, mp > 350°C FT-IR (KBr, cm^{-1}):3406(OH), 3186(NH), 3051(C–H aromatic), 1697(C=O), 1600(C=N), 1508(C=C aromatic). ^{1}H-NMR (500MHz, DMSO-d$_6$) δH (ppm): 9.61(s,2H, CONH). 8.80-814(m,16H, Pyrrole), 8.06-7.05(m40H, Ar-H), 6.86(s,6H, OH), -1.45(s,2H, NH$_{int}$), -1.74 (s,2H, NH$_{int}$)., ESI-MS(*m/z*) calcd exact mass (C$_{102}$H$_{68}$N$_{10}$O$_8$), 1561.53; found, 1561.51.

2.3.7 Preparation of 4,4′-(10,20-bis(3-hydroxyphenyl)porphyrin-5,15-diyl) dibenzoic acid (12)

Pyrrole (1.93 mL, 0.028 mol) was added to a solution of substituted aldehyde {(4-formyl benzoic acid) (2.18 g, 0.014 mol) and (3-hydroxy benzaldehyde) (1.78 g, 0.014 mol)} in propionic acid (20 mL), and the reaction

mixture was refluxed for one hour in the dark after that. TLC (*n*- hexane: EtOAc, 2:3) showed that the reactions were completed, to give latency precipitate that was filtered under reduced pressure, washed well with hot distilled water, and recrystallized from ethanol [196].

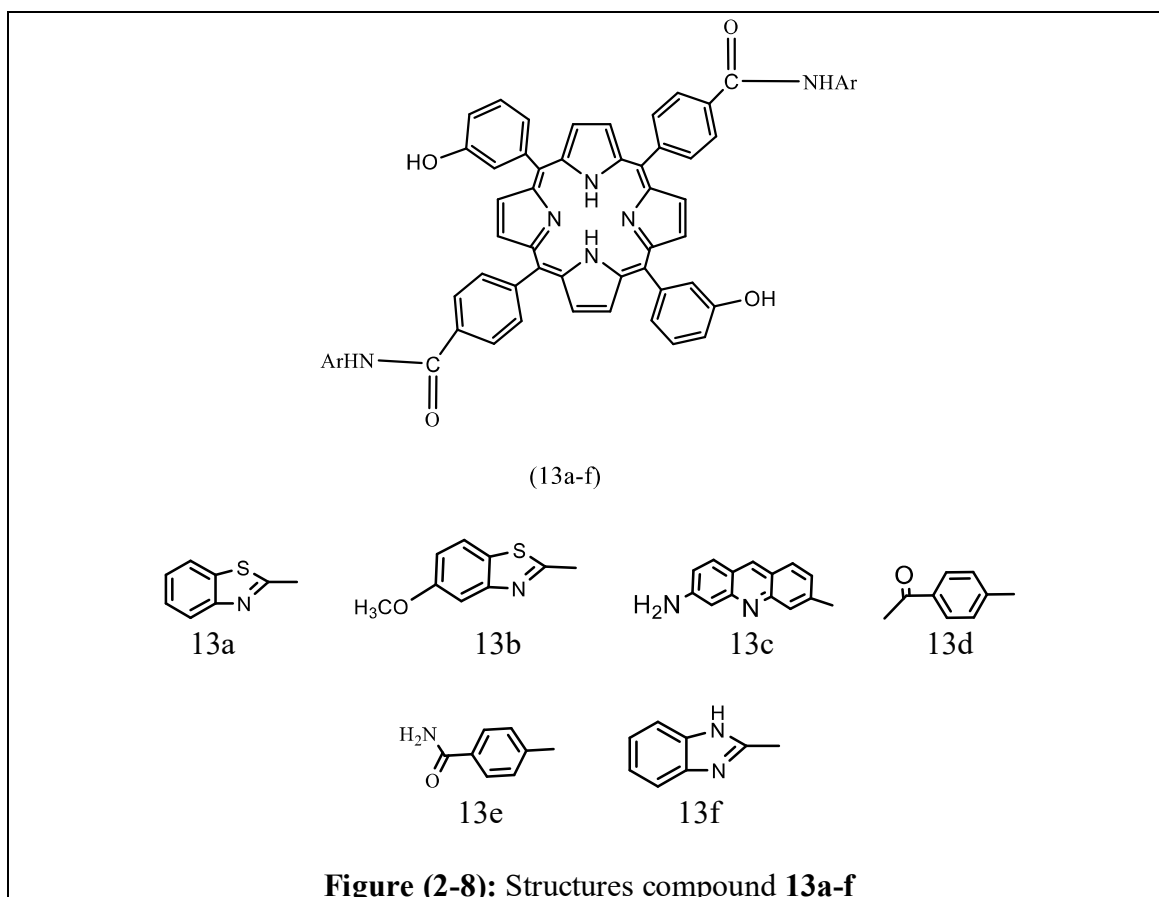**Figure (2-7):** Structures compound **12**
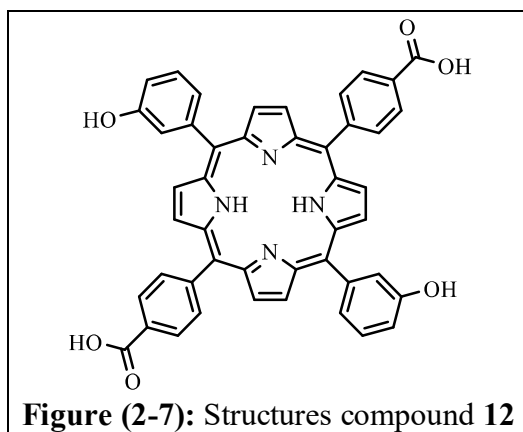
4,4'-(10,20-bis(3-hydroxyphenyl) porphyrin-5,15-diyl) di benzoic acid (12) as shown in Figure (2-7). Color: dark green: Yield 27%, mp > 350°C FT-IR (KBr, cm^{-1}): 3333(OH) 3201-2400(OH carboxylic acid), 3063(C–H aromatic), 1693(C=O), 1604(C=N), 1489(C=C aromatic). ^{1}H-NMR (500 MHz, DMSO-d$_6$) δH (ppm): 12.94(s,2H, COOH), 8.33-8.36(m,8H, Pyrrole), 8.11-7.02 (m16H, Ar-H), 6.80 (s,2H, OH), - 3.01 (s,2H, NH)., ^{13}C-NMR (125 MHz, DMSO-d$_6$) δ C:-115.40,120.22,120.38,122.22,122.24,123.76,123.82,126.57, 126.64,126.84,126.92,128.53,128.55,128.94,129.29,130.57,130.64,136.37,137.01,138.91,143.10,143.88,146.65,146.88,151.84,153.20,153.21,165.14., ESI-MS(*m/z*) calcd exact mass (C$_{76}$H$_{50}$N$_{16}$O$_4$), 734.22; found, 734.20.

2.3.8 General procedure for synthesis of amides (13a-f) from 4,4'-(10,20-bis(3-hydroxyphenyl) porphyrin-5,15-diyl) di benzoic acid (12)

(1.45 mL, 0.02 mol) of SOCl$_2$ was added of 4,4'-(10,20-bis(3-hydroxyphenyl)porphyrin-5,15-diyl) dibenzoic acid (12) (7.41 g, 0.01 mol). The mixture was stirred at 70 rpm for 30 minutes at environmental temperature, then DMF (5 mL) was added with continuous stirred for 10 minutes at the same temperature. The final solution was transferred to round bottom flask volume

(100 mL), (0.02 mol) amines (2-aminobenzothiazole, 5-methoxy benzothiazol-2-Amine, acridine-3,6-diamine, 1-(4-aminophenyl)ethan-1-one, 4-amino benzamide, 2-aminobenzimidazole) were added to the last solution with for (2-3) hours, and then (5.58 mL, 0.04 mol) triethylamine (Et₃N) was added with continuous for 1 hours. TLC (*n*- hexane: EtOAc, 2:3) showed that the reactions were completed. The black solution was added to ice crystal, filtration, and washed with ethanol. Then it was recrystallized from ethanol and DMF[195].

Figure (2-8): Structures compound **13a-f**

4,4'-(10,20-bis(3-hydroxyphenyl) porphyrin-5,15-diyl) bis (*N*-(benzo [*d*]thiazol-2-yl) benzamide) (13a) as shown in Figure (2-8). Color: Black powder: Yield 61%, mp > 350°C FT-IR (KBr, cm⁻¹): 3414(OH), 3190(NH), 3059(C–H aromatic), 1701(C=O), 1608(C=N), 1450 (C=C aromatic), 1087(C-S). ¹H-NMR (500 MHz, DMSO-d₆) δH (ppm): 10.65 (s,2H, CON<u>H</u>), 8.84-8.26 (m,8H, Pyrrole), 8.14-7.01(m,24H, Ar-<u>H</u>), 6.89(s,2H, O<u>H</u>), -1.47(s,2H, N<u>H</u>).,

^{13}C-NMR (125 MHz, DMSO-d$_6$) δ C:- 115.30,120.63,121.69,123.10, 123.81, 124.08,125.77,125.87,127.00,127.23,127.61,130.44,131.43,131.72,132.52,136.71,137.71,137.97,138.34,144.88,145.40,150.04,150.32,155.07,155.90,159.70,160.25,172.63., ESI-MS (*m/z*) calcd exact mass (C$_{60}$H$_{38}$N$_8$O$_4$S$_{2)}$), 998.25; found, 998.22.

4,4'-(10,20-bis(3-hydroxyphenyl)porphyrin-5,15-diyl)bis(*N*-(benzo[d] thiazol-2-yl)benzamide) (13b) as shown in Figure (2-8). Color: Black powder: Yield 63%, mp > 350°C FT-IR (KBr, cm^{-1}): 3406(OH), 3221(NH), 3029(C–H aromatic), 2947(C–H aliphatic), 1701(C=O), 1608(C=N), 1485 (C=C aromatic), 1095(C-S). ^{1}H-NMR (500 MHz, DMSO-d$_6$) δH (ppm): 10.68 (s,2H, CONH), 8.84-8.27(m,8H, Pyrrole), 8.14-7.03(m,22H, Ar-H), 6.80 (s,2H, OH), 3.66 (s,6H, OCH$_3$), -1.47 (s,2H, NH)., ^{13}C-NMR (125 MHz, DMSO-d$_6$) δ C:- 98.43,113.43,115.52,120.16,120.28,122.23,122.25,123.76, 123.88,126.57,126.64,126.84,126.92,128.17,128.94,129.43,129.52,129.54,130.16,130.29,130.68,131.61,132.18,147.80,149.68,154.21,156.82,159.16,170.82., Anal. Calcd for (C$_{62}$H$_{42}$N$_8$O$_6$S$_2$): C, 70.31; H, 4.00; N, 10.58; S, 6.05 found C, 70.15; H, 3.92; N, 10.32; S, 5.80 %.,

4,4'-(10,20-bis(3-hydroxyphenyl)porphyrin-5,15-diyl)bis(*N*-(6-amino-acridin-3-yl)benzamide) (13c) as shown in Figure (2-8). Color: Black powder: Yield 55%, mp > 350°C FT-IR (KBr, cm^{-1}): 3414 and 3322(NH$_2$), 3202(NH), 3055(C–H aromatic), 1701(C=O), 1604(C=N), 1485(C=C aromatic ^{1}H-NMR (500MHz, DMSO-d$_6$) δH (ppm): 10.45(s,2H, CONH), 8.69-8.3 (m,8H, Pyrrole), 8.13-7.05(m30H, Ar-H), 6.81(s,2H, OH), 6.25(s, 4H, NH$_2$), -1.47 (s,2H, NH)., Anal. Calcd for (C$_{72}$H$_{48}$N$_{10}$O$_4$): C, 77.40; H, 4.33; N, 12.54 found C, 77.15; H, 4.13; N, 12.34 %.,

4,4'-(10,20-bis(3-hydroxyphenyl)porphyrin-5,15-diyl)bis(*N*-(4-acetyl phenyl)benzamide) (13d) as shown in Figure (2-8). Color: Black powder: Yield 65%, mp > 350°C FT-IR (KBr, cm^{-1}): 3417(OH), 3217(NH), 3070(C–H aromatic), 2982(C–H aliphatic), 1705(C=O), 1600(C=N), 1446(C=C aromatic

). ^{1}HNMR (500MHz, DMSO-d$_6$) δH (ppm): 9.78 (s,2H, CON$\underline{H}$), 8.71-8.37 (m,8H, Pyrrole), 8.13-7.06(m24H, Ar-$\underline{H}$), 6.82(s,2H, O$\underline{H}$), 2.63 (s,6H, C$\underline{H}_3$), -1.83 (s,2H, N$\underline{H}$)., ESI-MS(m/z) calcd exact mass (C$_{62}$H$_{44}$N$_6$O$_6$), 968.33; found, 968.30.

4,4'-(10,20-bis(3-hydroxyphenyl)porphyrin-5,15-diyl)bis(N-(4-carbamoyl phenyl)benzamide) (13e) as shown in Figure (2-8).Color: Black powder: Yield 60%, mp > 350°C FT-IR (KBr, cm^{-1}): 3414 and 3359(NH$_2$), 3220(NH), 3059(C–H aromatic), 1701(C=O), 1608(C=N), 1450(C=C aromatic).,^{1}HNMR (500 MHz, DMSO-d$_6$) δH (ppm): 9.72(s,2H, CON$\underline{H}$), 8.66-8.25 (m,8H, Pyrrole), 8.11-7.07(m24H, Ar-H), 6.93(s,2H, OH), 6.59(s,4H, N$\underline{H}_2$), -1.66 (s,2H, N$\underline{H}$ pyrrole)., ^{13}C-NMR (125 MHz, DMSO-d$_6$) δ C:- 117.27,119.74, 120.28,122.22,122.25,123.76,126.57,126.64,128.94,129.57,130.64,132.84,135.90,137.76,138.01,138.72,142.50,143.88,147.44,153.88,158.41,170.20., ESI-MS (m/z) calcd exact mass (C$_{60}$H$_{42}$N$_8$O$_6$), 970.32; found, 970.30.

4,4'-(10,20-bis(3-hydroxyphenyl)porphyrin-5,15-diyl)bis(N-(1H-benzo[d] imidazole-2-yl)benzamide) (13f) as shown in Figure (2-8).Color: Black powder: Yield 63%, mp > 350°C FT-IR (KBr, cm^{-1}): 3414(OH), 3214(NH), 3059(C–H aromatic), 1701(C=O), 1608(C=N), 1450(C=C aromatic)., ^{1}H-NMR (500MHz, DMSO-d$_6$): δH (ppm): 11.26 (s,2H, N$\underline{H}$), 10.46 (s,2H, CON$\underline{H}$), 8.83-8.27(m,8H, Pyrrole), 8.14-7.09(m 24H, Ar-H), 6.85(s,2H, OH), -1.66 (s,2H, NH pyrrole). Anal. Calcd for (C$_{60}$H$_{40}$N$_{10}$O$_4$): C, 74.68; H, 4.18; N, 14.51 found C, 74.38; H, 3.71; N, 14.25 %.

2.4 Preparation of Graphene Quantum Dot (GQD)

The starch was used as the green precursor in the quick and simple hydrothermal process that produced the GQDs. The chemical mechanism is explained, that the synthetic process includes both the initial hydrolysis of starch to create glucose units and the subsequent ring-closure condensation of glucose units to make GQDs. Due to the comparatively large levels of the ionic product of H$^+$ and OH$^-$ under hydrothermal conditions, water is first employed

as a hydrolytic medium. The starch will then constantly hydrolyze with water and no chemical agent in the presence of H^+ to produce a variety of components, such as glucose, fructose, maltose, and aldehydes. According to the carbon balances, traces of gaseous products are also created, albeit they are comparatively minor. As the hydrolysis process progresses, the output of glucose rises while that of other carbohydrates drastically declines. As a result, the starch is mostly transformed into glucose, with trace quantities of other carbs remaining. Accordingly, in hydrothermal circumstances, dehydration occurs via interactions between hydrogen atoms of one glucose molecule and the hydroxyl groups of an adjacent glucose molecule as well as from reactions between formyl groups and hydroxyl groups. As a result, carbon atoms engage in covalent interactions with one another to create aromatic rings, the fundamental building block of the graphene structure. In this manner, the ring-closure condensation of glucose molecules results in the formation of GQDs. On the other hand, the carbonization process converts the remaining carbohydrates into carbide precipitates at high temperatures and pressures. Generally, the GQDs solution is produced by filtering the precipitates away [197].

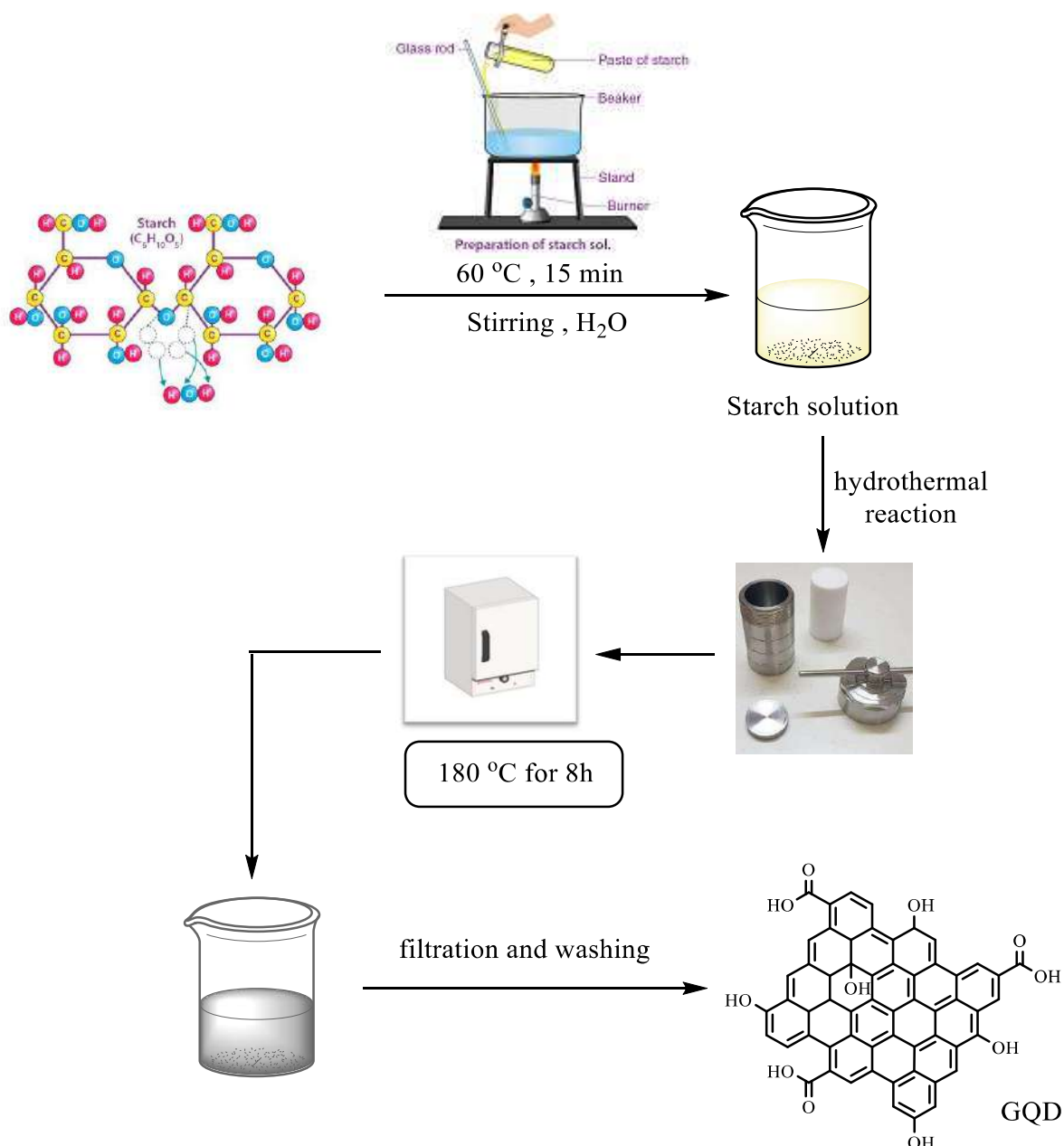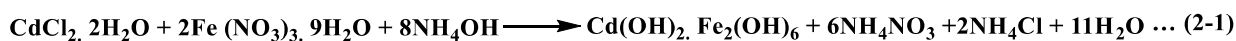All of the steps for the preparation of GQD are shown in Figure (2-9).

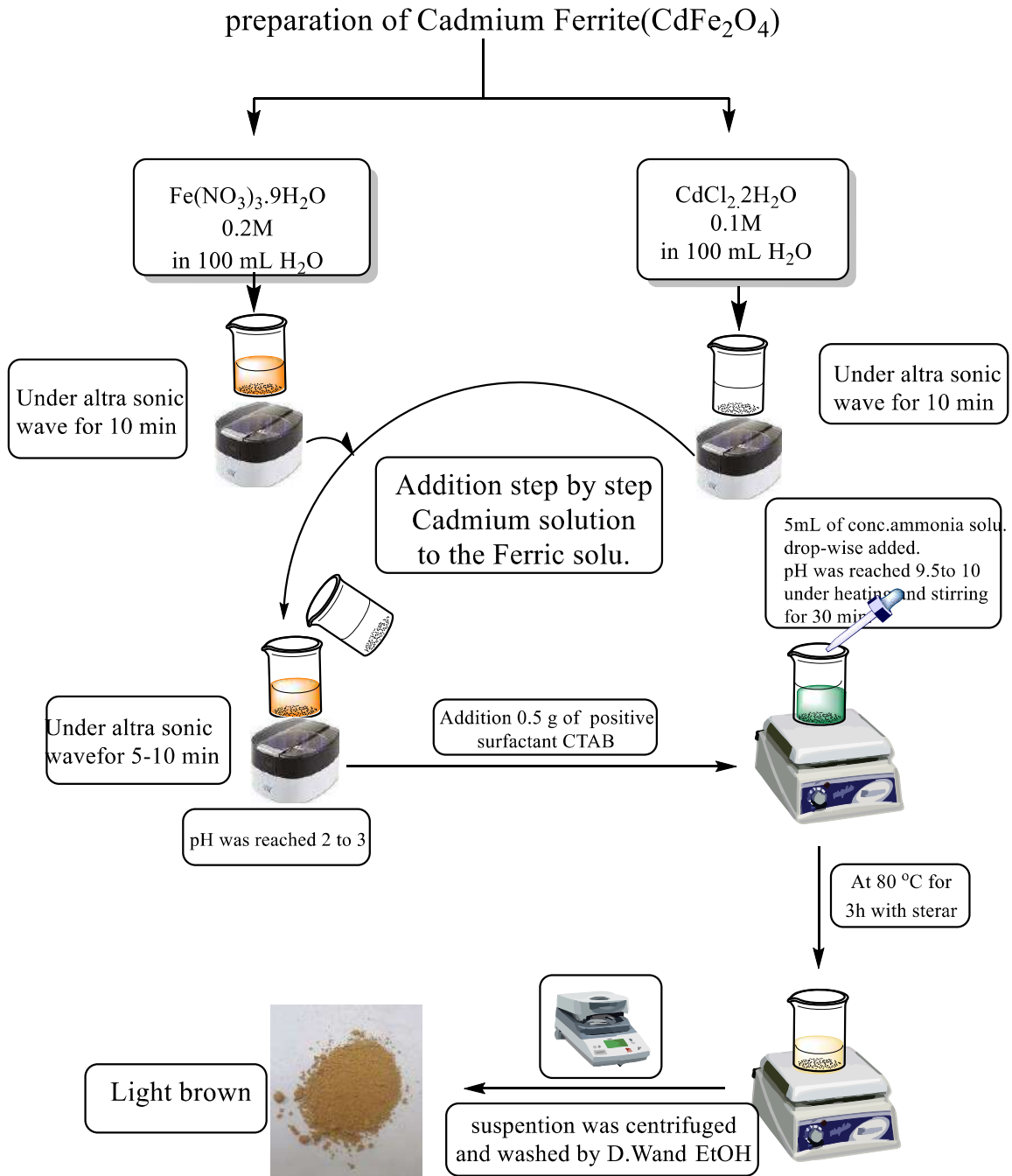**Figure (2-9).** The schematic diagram of the steps of GQD preparation

2.5 Preparation of Cadmium Ferrite Semiconductor

The synthesis of cadmium ferrite semiconductors involves several steps. Firstly, a (0.2 M) solution of ferric nitrate ($Fe(NO_3)_3.9H_2O$) was prepared by dissolving (8.08 g) of this compound in (100 mL) of deionized water (D.W) using ultrasonic waves (46 kHz) for 10 minutes.

Secondly, a (0.1 M) solution of cadmium chloride ($CdCl_2.2H_2O$) was prepared by dissolving (2.193 g) of this compound in (100 mL) of D.W using ultrasonic waves (46 kHz) also for 10 minutes. The cadmium chloride solution was added to the ferric nitrate solution step by step and then mixed using an ultrasonic bath for 5-10 minutes. The final solution was measured their pH; which was equal to 2-3. An exact 0.5 g of the positive surfactant (CTAB) was added as a template and a capping agent. This mixture was continuously stirred using a magnetic stirrer for 10 minutes to reach a pH of 4-5. The concentrated ammonia solution was added drop-wise to the mixed solution until the pH reached a range of 9.5 to 10 altering the solution color to olive green. The last solution was heated and stirred at 80 °C for 3 hours until a light brown precipitate of cadmium ferrite happened. The resulting suspension was centrifuged and washed with deionized water and ethanol. The chemical reaction can happen by the following equations:
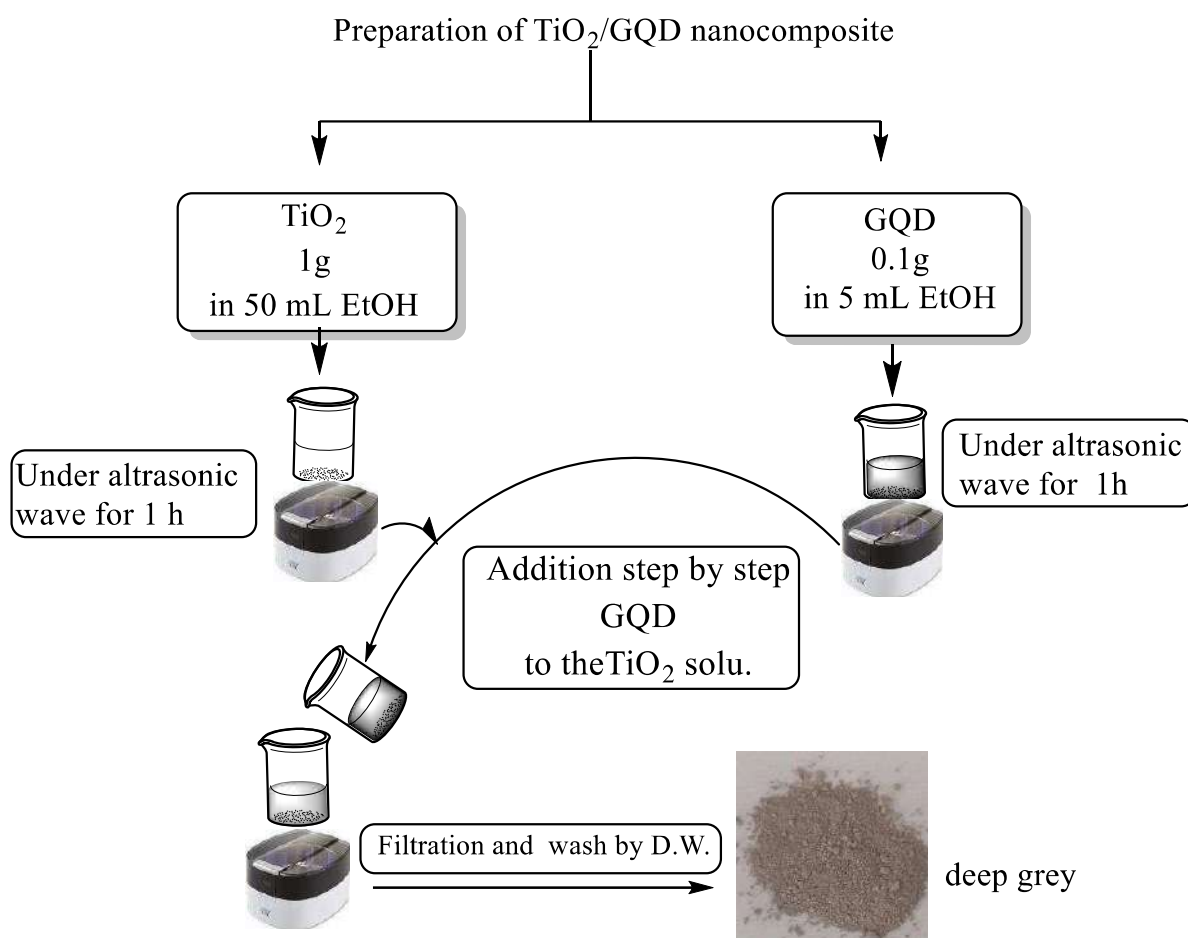
$$CdCl_2.\,2H_2O + 2Fe\,(NO_3)_3.\,9H_2O + 8NH_4OH \longrightarrow Cd(OH)_2.\,Fe_2(OH)_6 + 6NH_4NO_3 + 2NH_4Cl + 11H_2O \cdots (2\text{-}1)$$

$$Cd(OH)_2.\,Fe_2(OH)_6 \longrightarrow CdOFe_2O_3 + 4H_2O \qquad \cdots (2\text{-}2)$$

All of the steps for the preparation of Cadmium Ferrite are shown in Figure (2-10).

preparation of Cadmium Ferrite($CdFe_2O_4$)

$Fe(NO_3)_3.9H_2O$
0.2M
in 100 mL H_2O

$CdCl_2.2H_2O$
0.1M
in 100 mL H_2O

Under altra sonic wave for 10 min

Under altra sonic wave for 10 min

Addition step by step Cadmium solution to the Ferric solu.

5mL of conc.ammonia solu. drop-wise added.
pH was reached 9.5to 10 under heating and stirring for 30 min

Under altra sonic wavefor 5-10 min

Addition 0.5 g of positive surfactant CTAB

pH was reached 2 to 3

At 80 ^{o}C for 3h with sterar

Light brown

suspention was centrifuged and washed by D.Wand EtOH

Figure (2-10): The schematic diagram of the steps of Cadmium Ferrite nanoparticle preparation

2.6 Preparation of TiO₂/GQD nanocomposite

The GQD was modified by TiO_2 using an indirect ultrasonic method. 1 g of TiO_2 was dispersive in 50 mL of ethanol in a beaker, using an ultrasonic for 1h. In other bakers, 0.1g from the GQD was dispersive in the 5 mL of ethanol using an ultrasonic bath also for 1h. The GQDs and TiO_2 nanoparticles were linked together as nano-composites depending on the ultrasonic energy that enhanced their interaction and bonding.

Preparation of TiO_2/GQD nanocomposite

TiO_2 1g in 50 mL EtOH	GQD 0.1g in 5 mL EtOH

Under altrasonic wave for 1 h

Under altrasonic wave for 1h

Addition step by step GQD to theTiO₂ solu.

Filtration and wash by D.W.

deep grey

Figure (2-11): The schematic diagram of the steps of preparation of TiO₂/GQD nanocomposite

2.7 Preparation of TiO₂/CdFe₂O₄ nanocomposite

The $CdFe_2O_4$ nanoparticle was modified by TiO_2 using an indirect ultrasonic method. 1 g of TiO_2 was dispersive in 50 mL of ethanol in a beaker, using an ultrasonic for 1h. In another beaker, 0.1g from the $CdFe_2O_4$ was dispersive in the 5 mL of ethanol using an ultrasonic bath also for 1h. The

$CdFe_2O_4$ and TiO_2 nanoparticles were linked together as nano-composites depending on the ultrasonic energy that enhanced their interaction and bonding.

Preparation of $TiO_2/CdFe_2O_4$ nanocomposite

TiO$_2$
1g
in 50 mL EtOH

CdFe$_2$O$_4$
0.1g
in 5 mL EtOH

Under altrasonic wave for 1h

Under altrasonic wave for 1h

Addition step by step
GQD
to theTiO$_2$ solu.

Filtration and wash by D.W.

light-yellow
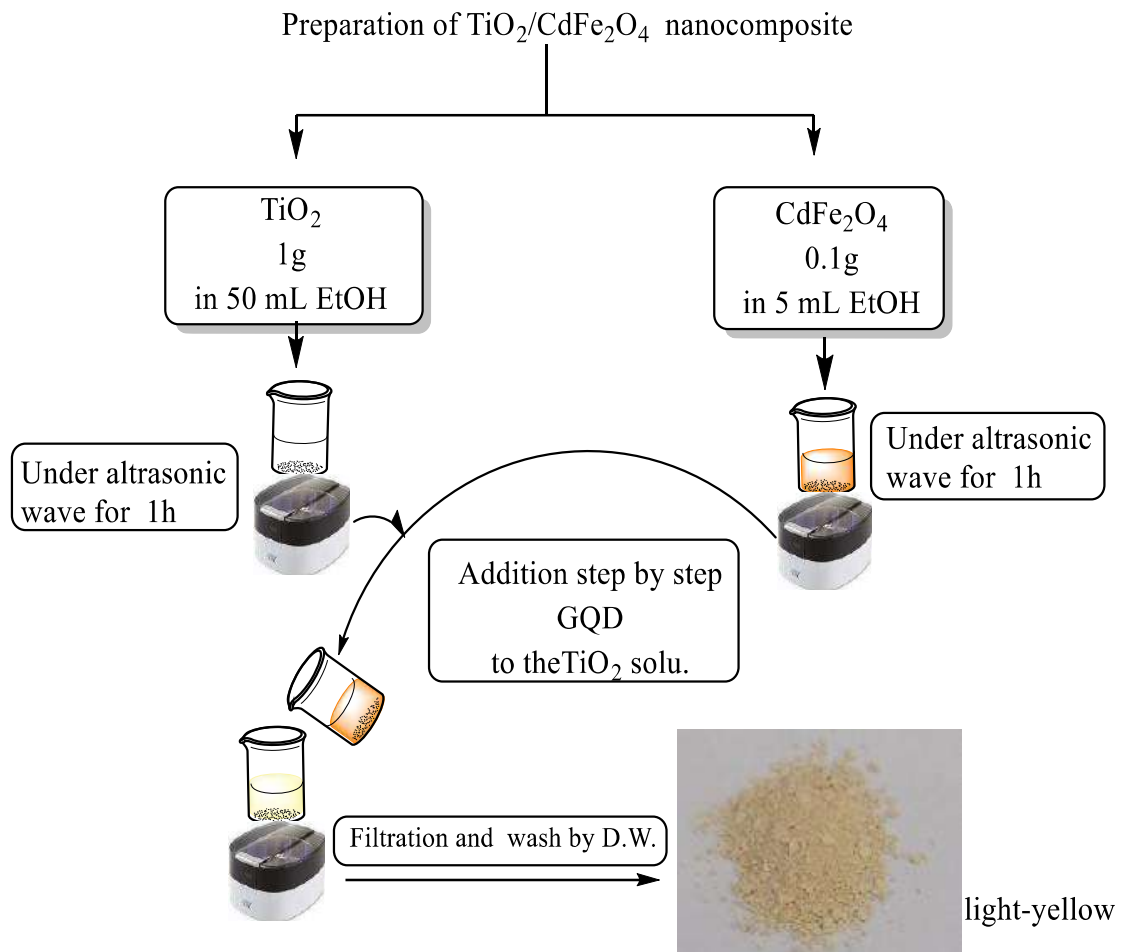
Figure (2-12): The schematic diagram of the steps of preparation of $TiO_2/CdFe_2O_4$ nanocomposite

2.8 Characterization of semiconductors

2.8.1 FT-IR Spectra

The semiconductor samples were subjected to Fourier Transform Infrared (FT-IR) spectroscopy using a Shimadzu instrument, with CsI powder utilized as the optical material. Spectral data were measured over the range of 250 to 4000 cm^{-1}.

2.8.2 X-Ray Diffraction Spectroscopy (XRD)

The average crystal sizes (L) of the semiconductor samples were determined using Scherrer's equation[198, 199]. X-ray diffraction (XRD) data were obtained using a Shimadzu Lab X XRD 6000 instrument, which employed

a copper (Cu) target source with a wavelength of 1.54060 Å, a voltage of 40.0 kV, and a current of 30 mA. The instrument operated at a speed of 12.0000 (deg/min), with the angle (2θ) range set between 20 and 80 degrees.

$$L = \frac{k.\lambda}{\beta.Cos\theta} \qquad ... (2-1)$$

In Scherrer's equation, Scherer's constant (k) was utilized with a value of 0.9 for a semi-spherical shape and 0.85 for a rod. The wavelength (λ) used for Cu kα was 0.15406 nm. The Bragg diffraction angle (θ) was employed in conjunction with the full-width half maximum (FWHM) measurement (in degrees, denoted as β) to calculate the crystal size) [199-205].

2.8.3 Field Emission Scan Electron Microscopes (FE-SEM)

Field Emission Scanning Electron Microscopy (FE-SEM) analysis was performed on all samples, including Graphene Quantum Dots (GQD), Cadmium Ferrite, and their composites. The FESEM instrument used was the Fei inspect f50, Dutch.

2.8.4 Energy Dispersive X-Rays (EDX)Analysis

To verify the elemental composition of the samples in terms of atomic percentages, Energy Dispersive X-ray Spectroscopy (EDX) spectra were obtained using FE-SEM instruments.

2.8.5 Bandgap Energy Measurements

The optical energy bandgaps (Eg) of all photocatalyst samples were calculated in electron volts (eV) using the Tauc equation [206, 207]. Equations 2-3 and 2-4 were utilized for this purpose.

$$(\alpha h\nu)^m = k(h\nu - Eg) \qquad ... (2-3)$$

$$\alpha = (2.3026A)/t \qquad ... (2-4)$$

The Tauc equation involves the following parameters: α (absorption coefficient), h (Planck's constant), v (light frequency), k (optical constant), t (thickness), A (absorbance), and m (a constant value of ½ or 2 for direct and indirect transitions, respectively).

2.9 Fabrication of Dye-Sensitized Solar Cells (DSSCs)

2.9.1 Preparation and Testing DSSCs

Fluorine-doped Tin Oxide (FTO) glass sheets were cleaned using an ultrasonic bath and washed with distilled water and ethanol. 3.0 g of TiO_2 or TiO_2/GQD or $TiO_2/CdFe_2O_4$ nanopowder were combined with 15 mL of ethanol, 2.5 mL of Triton X-100, and stirred TiO_2 or TiO_2/GQD or $TiO_2/CdFe_2O_4$. To create TiO_2 or TiO_2/GQD or $TiO_2/CdFe_2O_4$ paste, the mixture was agitated under moved using a tiny magnetic bar for 45 minutes. Using an eye dropper, the TiO_2 or TiO_2/GQD or $TiO_2/CdFe_2O_4$ paste was put onto the FTO glass sheet, where it was then applied using the doctor blade method to create a thin coating of TiO_2 or TiO_2/GQD or $TiO_2/CdFe_2O_4$ (0.5 cm^2 area). The glass sheet with the TiO_2 or TiO_2/GQD or $TiO_2/CdFe_2O_4$ layer was heated for 30 minutes at 70 °C before being sintered for 45 minutes at 400 ºC. The deposit TiO_2 or TiO_2/GQD or $TiO_2/CdFe_2O_4$ was submerged in the dye solution (0.001 M) for 5 hours after cooling. Gold was used to draw the counter electrode on a piece of another conducting glass (FTO). By sandwiching the TiO_2 or TiO_2/GQD or $TiO_2/CdFe_2O_4$ thin layer with dye and counter electrode with an I^-/I^{3-} redox electrolyte solution, a DSSC was created.

Fabricated solar cells were tested using a solar simulator equipped with a 450 W xenon light source (Osram XBO 450) and filter (Schott 113) for DSSCs. By employing a Si photodiode was employed as a reference, along with a KG^{-3} Schott color-matched filter, to minimize the mismatch in wavelength (350-750) nm between AM 1.5 and simulated light to less than 5%. The power of the solar simulator was regulated to the standard test of the DSSCs AM 1.5. To perform

JV characterization of the solar cells, a digital source meter (Keithley model 2400) was used to establish an 80 ms delay between voltage and current density.

2.9.2 Preparation of the Counter Electrode (CE)

A drop of iodine solution between two prepared electrodes was added. An iodine solution was prepared by combining (0.05M) of iodine(I_2) with (0.5M) of potassium iodide (KI) in the solvent of ethylene glycol and acetonitrile with a volume ratio of (4:1), respectively. The solution is then maintained in an opaque container after shaking the flask until the iodine has fully dissolved. In order to prevent the solution from leaking beyond the designated cell region, the counter electrode is then put on the working electrode and the solution is retained in an opaque container[208].

Figure (2-13) illustrates the steps involved in the fabrication of dye-sensitized solar cells (DSSCs): (A) starting with a cleaned FTO substrate was installed, (B) prepared of the anode part of cells has performed a mixture of TiO_2/GQD nanoparticles, ethanol, and Triton X-100 as a paste, (C) the TiO_2/GQD layer is annealed via heating by a heater, (D) the FTO substrate with the TiO_2/GQD layer is immersed in a dye solution, (E) a gold electrode is put onto the dye-coated substrate to be contacted, (F) the DSSC structure is completed, (G) the power output of the solar cell is applied, (H) a source meter (Keithley model 2400) is used for measuring the active signal[209].

A	B	C

D	E	F

G	H
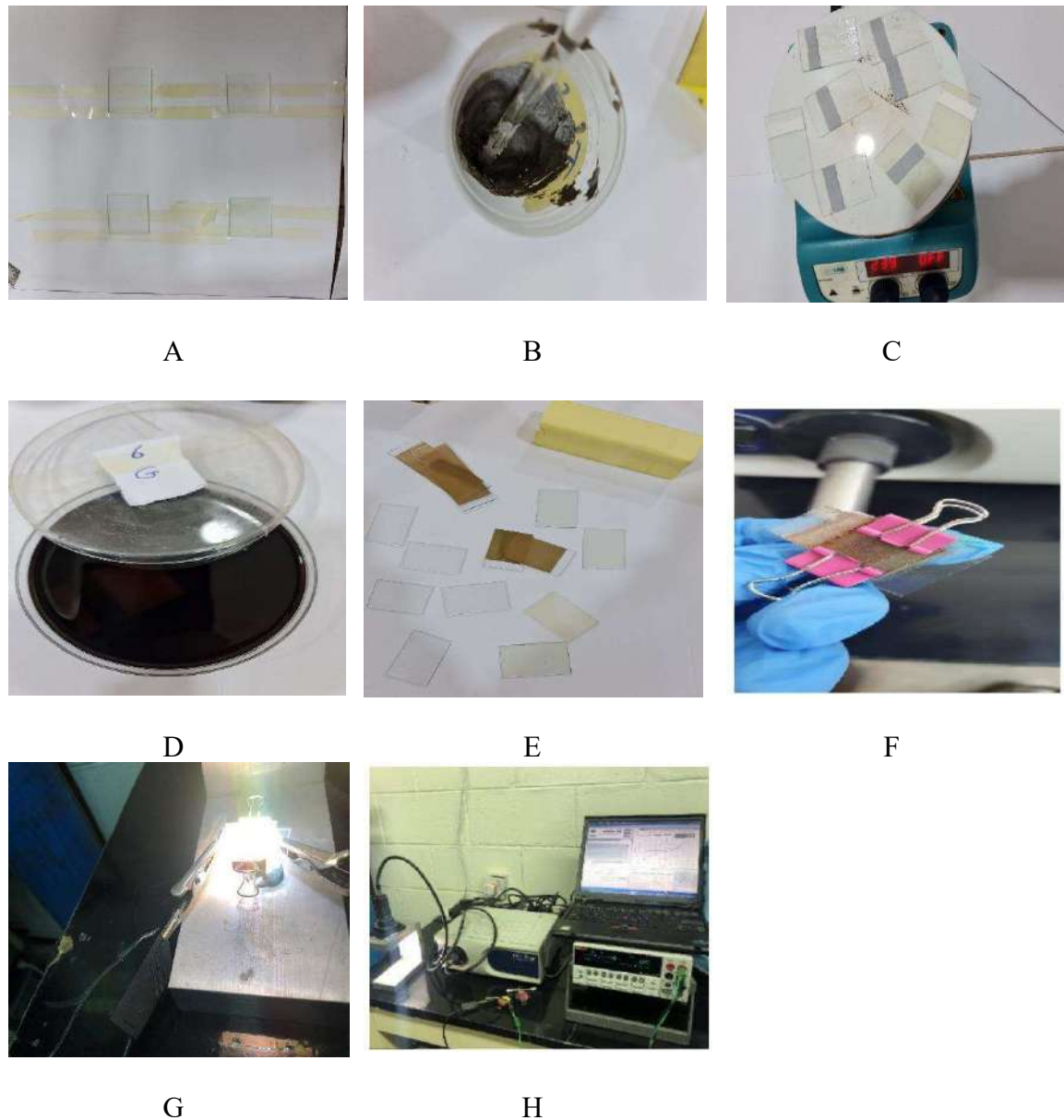
Figure (2-13): Steps of Fabrication DSSCs

2-10 Corrosion investigation of carbon steel

In this study, the used working electrodes are carbon steel specimens obtained from a Metal Sample Company, with a composition as specified in Table (2-3) [172]. The corrosive medium used was a 0.1 M hydrochloric acid solution, which was prepared by diluting analytical grade 37% HCl with double-distilled water. The dimensions of all carbon steel specimens used in this study were 25 mm in diameter and 3 mm in height, with an effective area of 1 cm^2. Before each run, the specimen surfaces were mechanically polished using fine-grade

emery paper (80/3000 grades), washed with double-distilled water, then degreased with acetone, dried, and stored in a desiccator.

Table 2-3. The chemical composition of the materials used in the carbon steel specimens[172].

Element	C	Si	Mn	S	P	Cu	Ni	Cr	Fe
%	0.42	0.30	1.40	0.05	0.05	0.50	0.20	0.20	96.88

Electrochemical reactions were monitored using a WENKING M Lab Bank Electronik-Intelligent controls GmbH potentiostat, which was connected to a computer using a RS 232 cable. The M Lab potentiostat/galvanostat has three operational modes for each channel: potentiostats, galvanostatic, and open circuit. However, for this experiment, potentiodynamic polarization was performed in a three-electrode glass cell with a water jacket, including a corrosion cell with three electrodes. The working electrodes were made of carbon steel, the counter electrode was made of platinum, and the reference electrode was made of silver-silver chloride. Two sets of experiments were conducted on the carbon steel specimens: one without the inhibitor and one with the inhibitor at a concentration of 0.5 mmol, with a temperature of 292K. Tafel polarization measurement was performed by applying a potential ranging from approximately 200 mV to the open circuit voltage (OCP). After immersing the working electrode in the solution for 30 minutes to reach steady state potential, the polarization curve experiments were started. Three measurements were performed, and only the average data were reported.

The corrosion potential (Ec) and corrosion current density (i_{corr}) values were determined for all corrosion parameters. Additionally, the Tafel slopes, "βa" and "βc," were calculated using the linear portion of the anodic and cathodic curves, respectively [210, 211]. The inhibitory efficiency (IE) from the polarization investigation was computed using Eq. (2-5) [212].

$$\%IE = \frac{i_{corr} - i_{corr,i}}{i_{corr}} \times 100 \quad \dots (2\text{-}5)$$

where i_{corr} and $i_{corr,\,i}$ are the corrosion current densities without and with the presence of porphyrin derivative, respectively.

CHAPTER THREE

Results &Discussion

3.1 Synthesis and Spectroscopic Characterization of the porphyrin derivatives

3.1.1 Compound 4,4',4'',4'''-(porphyrin-5,10,15,20-tetrayl) tetra benzoic acid

The product compound (3) was prepared through the reaction of pyrrole with substituted aldehyde (4-formyl benzoic acid) in the presence of propionic acid as shown in Equation (3-1)
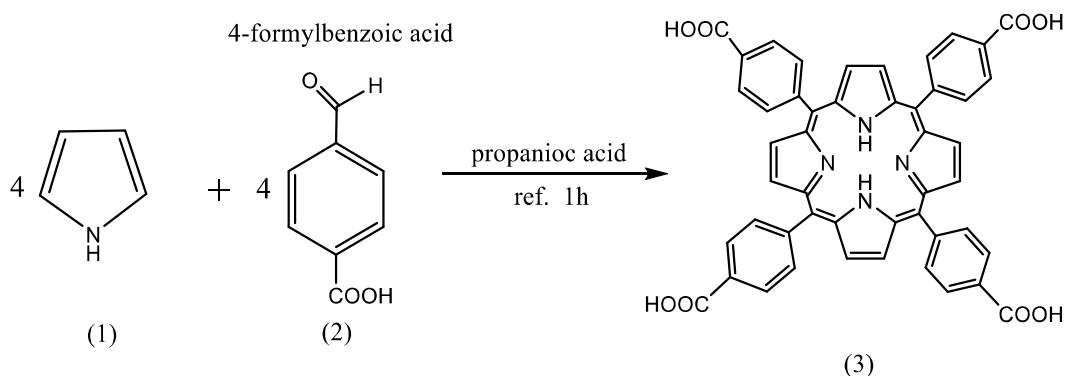
Equation (3-1): Synthesis of compound (3)

The proposed mechanism by the reference [213] for this reaction was shown in Scheme (3-1).
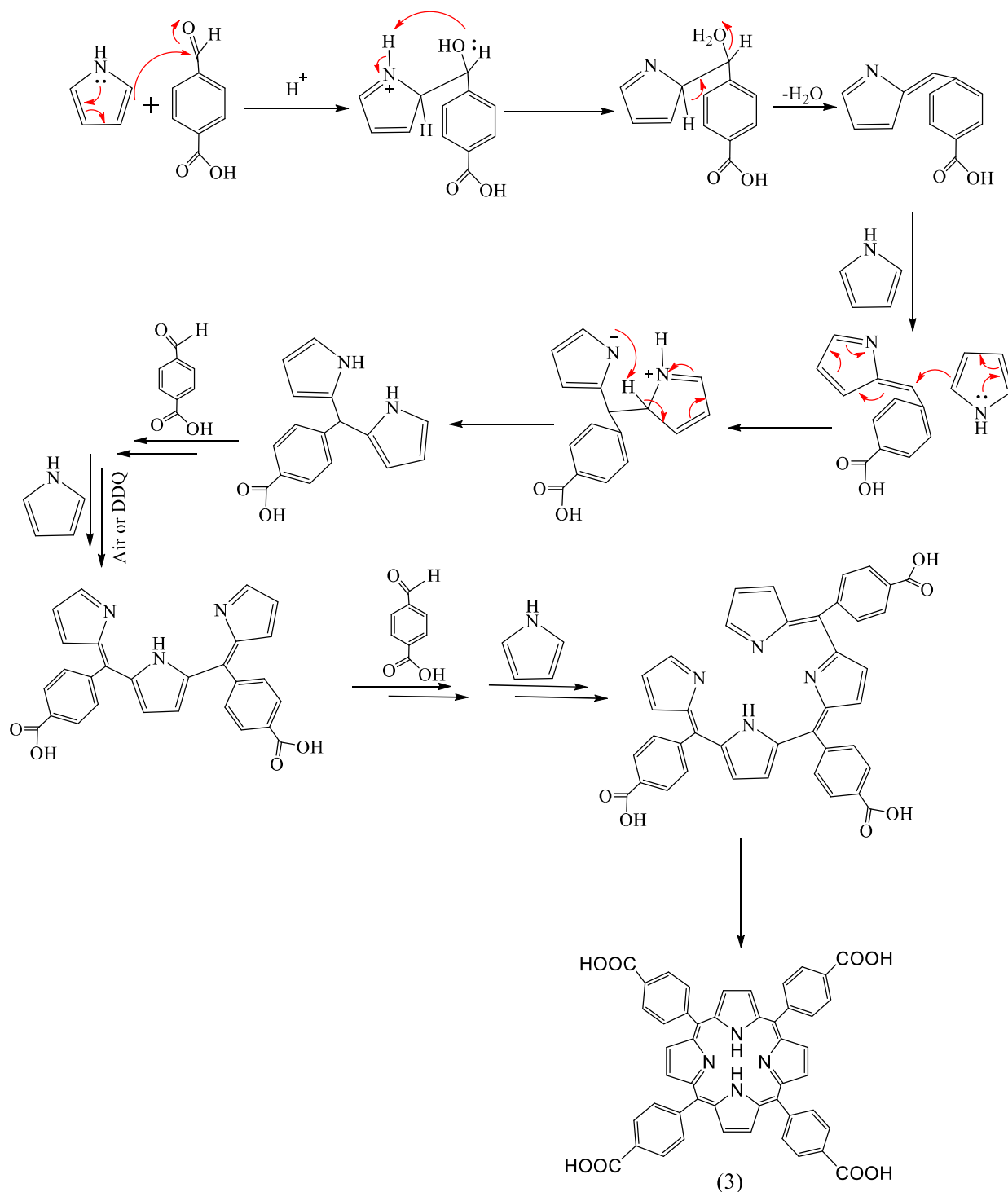
Scheme (3-1): Mechanism of formation of compound (3)

Compound (3) was diagnosed using the FT-IR by the appearance of NH, OH, and CO groups in carboxylic acid at radii of 3371, 3600-2400, and 1674 cm^{-1}, respectively. The ^{1}H-NMR spectrum of compound (3) showed a singlet signal at -2.29 (2H), which can be attributed to the N-H in the pyrrole group.

^{13}C-NMR was utilized to confirm the compound (3) structure which peak carboxylic acid carbonyl at (168.14) ppm and aromatic carbons in the range of (147.65-122.25) ppm. The Experimental part and appendix provide all of the porphyrin derivatives' complete spectrum information (ESI-MS, FT-IR, ^{1} H, and ^{13}C -NMR), as well as melting points.

3.1.2 Compounds 5a-f

The reaction of compound (3) with a variety of amines to obtain (5a-f), as explained in the Scheme (3-2).
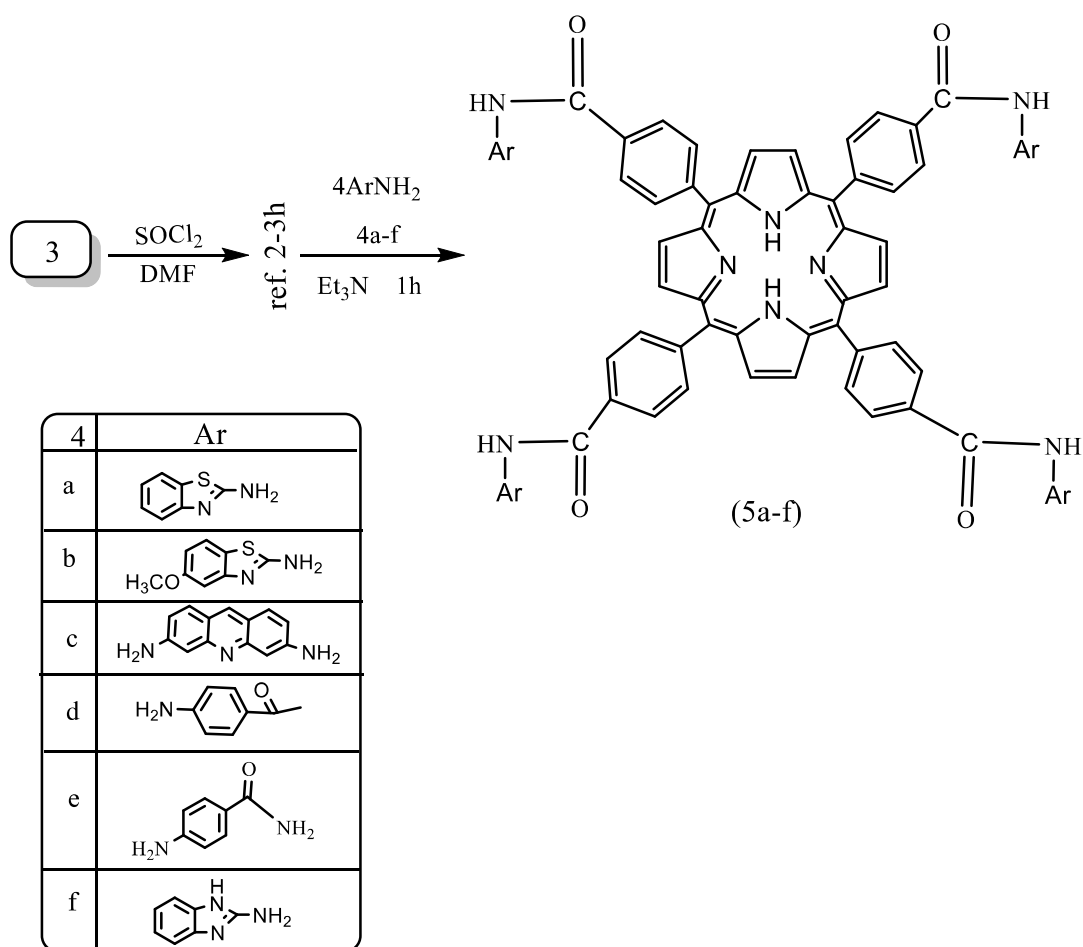
Scheme (3-2): Synthesis of compounds (5a-f)

These compounds were investigated using the FT-IR by disappearing the carbonyl group and appearing in the amide group. These compounds were identified by the disappearance of the OH in carboxylic acid (3600-2400) cm^{-1} and the appearance of the amide group 3420 cm^{-1}. The ^{1}H-NMR spectra of

compounds (5a-f) exhibited a singlet signal at the range of (10.69 - 9.84) (4H amide NH) and the disappearance of the OH group of carboxylic acid.^{13}C-NMR was utilized to confirm the compound (5a-f) structure which peak for amide carbonyl at the range of (166.95-16630) ppm and aromatic carbons in the range of (159.77-116.22) ppm. The Experimental section and appendix give comprehensive spectral data (ESI-MS, FT-IR, ^{1}H, and ^{13}C-NMR) and melting points for all the compounds (5a-f).

3.1.3 Compounds 6a-f

The study investigated the synthesis of porphyrin derivatives (6a-f) by reacting compound (3) with various amines, as depicted in the Scheme (3-3).
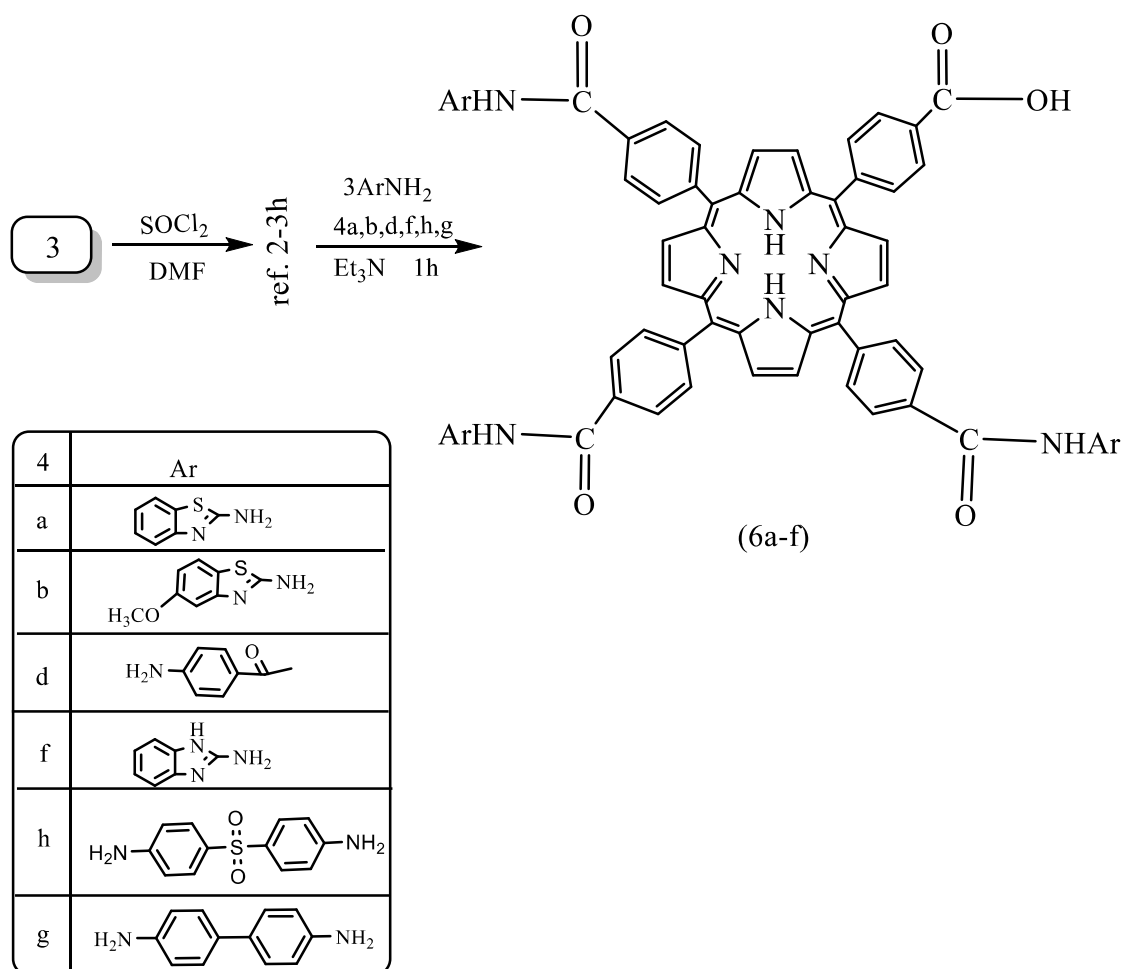
Scheme (3-3): Synthesis of compounds (6a-f)

The identification of these compounds was carried out using infrared spectroscopy, which showed the appearance of the amide group at 3420 cm^{-1}. the appearance of the amide group in the FT-IR spectra confirms the formation of the desired amide products. The ^{1}H-NMR spectra of compounds (6a-f) exhibited a singlet signal at the range of (10.68 - 9.63) (3H amide NH) and the disappearance of the OH group of carboxylic acid. ^{13}C-NMR was utilized to confirm the compound (6a-f) structure which peak for amide carbonyl at the range of (167.37-163.36) ppm and aromatic carbons in the range of (159.37-120.75) ppm. The results obtained from the experimental and appendix data confirm the successful synthesis of the porphyrin derivatives (6a-f) and provide useful information for their characterization.

3.1.4 Compound 8

The product compound 4-(10,15,20-tris(3-hydroxyphenyl)porphyrin-5-yl)benzoic acid (8) was prepared through the reaction of Pyrrole with a substituted aldehyde (4-formylbenzoic acid) and (3-hydroxybenzaldehyde) in propionic acid, as shown in Equation (3-2)
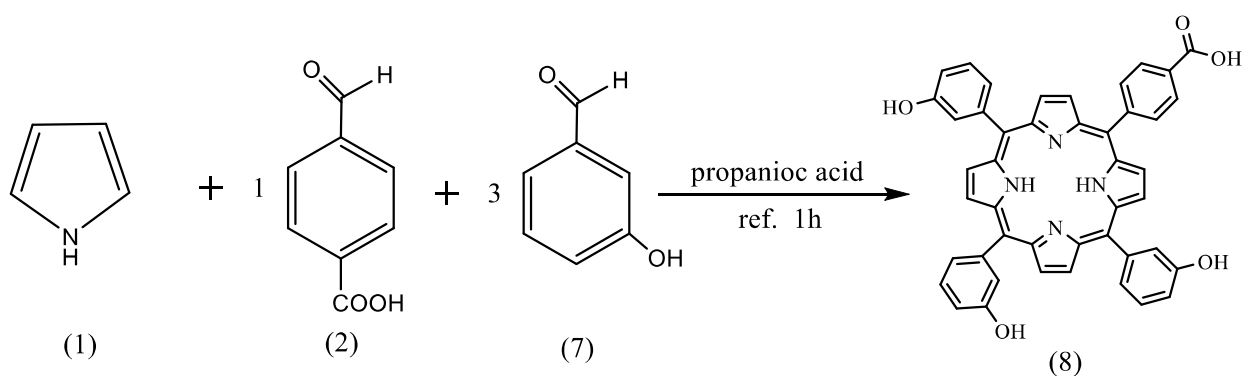
Equation (3-2): Synthesis of compound (8)

The product, compound (8), was identified by the appearance of OH and C=O groups in the carboxylic acid region of the infrared spectrum at 3600-2400 and 1708 cm^{-1}, respectively. The ^{1}H-NMR spectra of compound (8) exhibited a singlet signal at (-2.64 and -1.45) (2H), which corresponded to the N-H in the pyrrole group. ^{13}C-NMR was utilized to confirm the compound (8) structure which peaks for carboxylic acid carbonyl at about 169.36 ppm

aromatic carbons are in the range of (156.14-120.25) ppm and Carbon-bearing hydroxyl group is in 115.59 ppm. The compound was thoroughly characterized using various techniques, including FT-IR, ^{1}H-NMR, ^{13}C-NMR, and ESI-MS Spectroscopy. The results obtained from the experimental part and appendix confirm the successful synthesis of the porphyrin derivatives compound (8) and provide useful information for their characterization.

The proposed mechanism for reaction by the reference [213] compounds 8 and 12 was shown in Scheme (3-4).

8- $R_1,R_2,R_4=m$-OH , $R_3=P$-COOH
12- $R_2,R_4=m$-OH , R_1-$R_3=P$-COOH
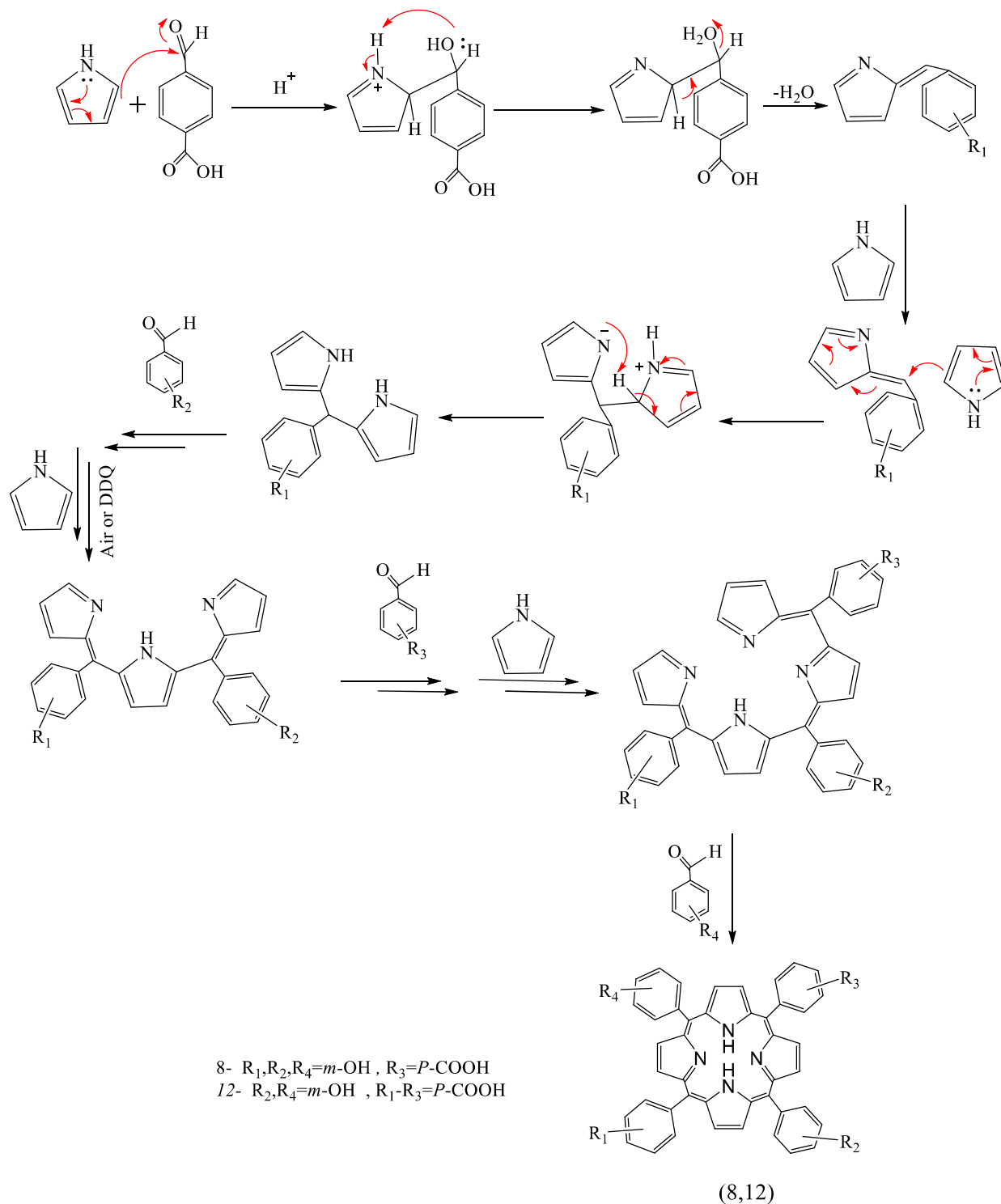
Scheme (3-4): Mechanism of formation of compounds (8,12)

3.1.5 Compounds (9a-d)

Synthesizing porphyrin derivatives compounds (9a-d) by reacting compound (8) with various amines, as illustrated in Scheme (3-5).
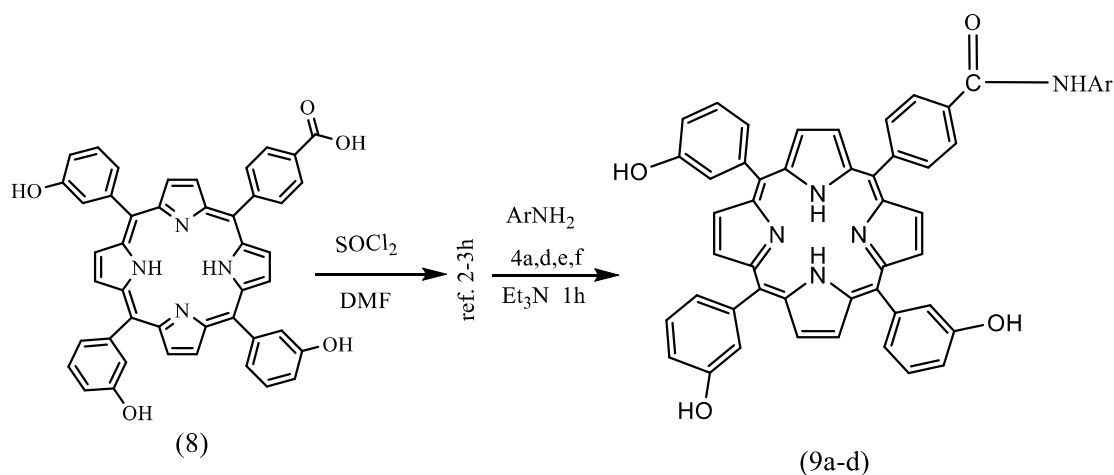
4	Ar
a	
d	
e	
f	

Scheme (3-5): Synthesis of compounds (9a-d)

The synthesized compounds were identified by FT-IR spectroscopy, which revealed the disappearance of the OH group in the carboxylic acid (at 3600-2400 cm^{-1}), and the emergence of the amide group (at 3410 cm^{-1}). The IR spectra of porphyrin derivatives compounds (9a-d) demonstrated the formation of the desired amide products by the carbonyl group's disappearance and the amide group's appearance. The ^{1}H-NMR spectra of compounds (9a-d) exhibited a singlet signal at about (10.80 - 9.26) (1H amide NH) and the disappearance of the OH group of carboxylic acid. The ^{13}C-NMR was utilized to confirm the compounds (9a-d) structure, which peaks for amide carbonyl at a range from (171.33- 168.41) ppm, and aromatic carbons are in the range of (159.79-119.57) ppm. The Carbon-bearing hydroxyl group is related to the benzene ring in about (116-97-115.34) ppm. The results obtained from the experimental part and appendix confirm the successful synthesis of the porphyrin derivatives compounds (9a-d) and provide useful information for their characterization.

3.1.6 Compounds (11a-e)

Synthesizing porphyrin derivatives (11a-e) by reacting (2mole) of compound (8) with various amines, as illustrated in Scheme (3-6).
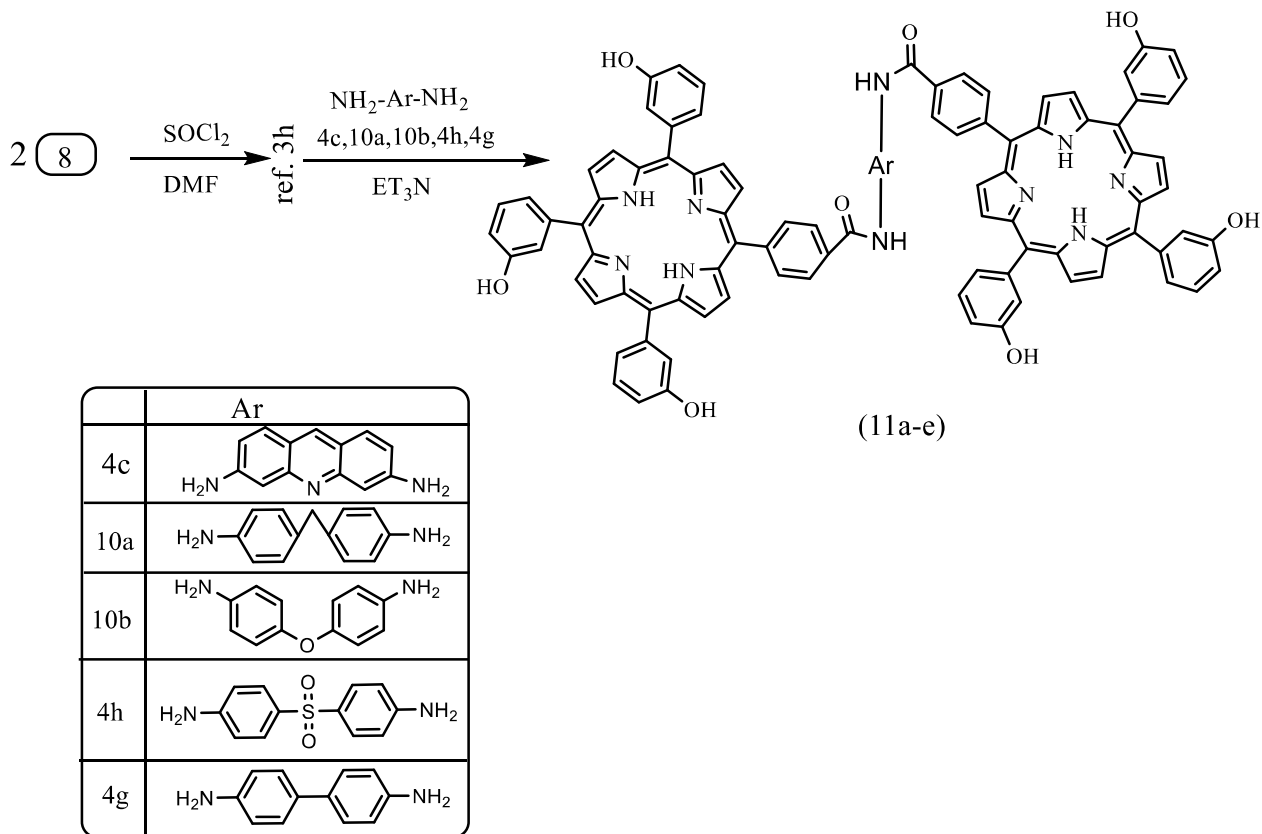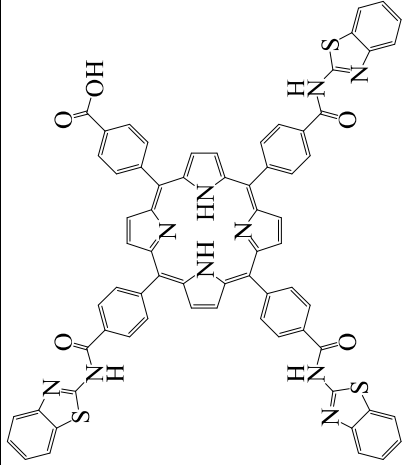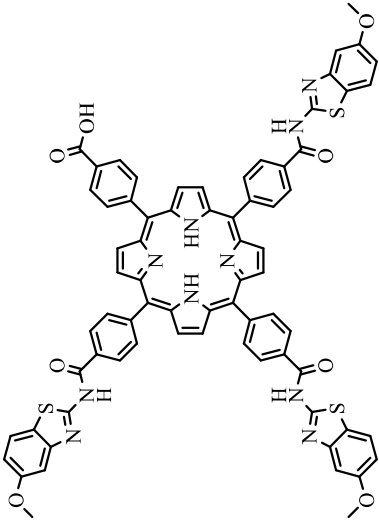

Scheme (3-6): Synthesis of compounds (11a-e)

The identification of the synthesized compounds (11a-e) was accomplished by FT-IR spectroscopy, which revealed the disappearance of the OH group in the carboxylic acid at 3600-2400 cm^{-1} and the emergence of the amide group at about 3410 cm^{-1}. The ^{1}H-NMR spectra of compounds (11a-e) exhibited a singlet signal at a range of (10.19 - 9.03) (1H amide NH) and the disappearance of the OH group of carboxylic acid. The experimental part and appendix data verified the successful synthesis of the porphyrin derivatives (11a-e) and provided valuable information for their characterization.

3.1.7 Compound (12)

The product compound 4,4'-(10,20-bis(3-hydroxyphenyl) porphyrin-5,15-diyl) di benzoic acid (12) was prepared through the reaction of Pyrrole with a substituted aldehyde (4-formylbenzoic acid) and (3-hydroxy benzaldehyde) in propionic acid, as shown in Equation (3-3).
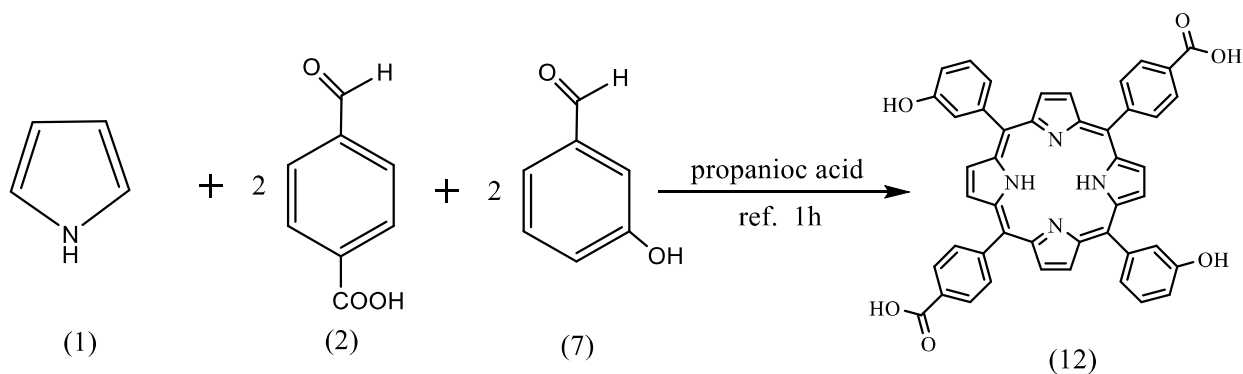
Equation (3-3): Synthesis of compound (12).

The product, compound (12), was identified by the appearance of OH and CO groups in the carboxylic acid region of the infrared spectrum at 3600-2400 and 1693cm^{-1}, respectively. The ^{1}H-NMR spectra of compound (12) exhibited a singlet signal at (-3.01) (2H), which corresponded to the N-H in the pyrrole group ^{13}C-NMR was utilized to confirm the compound (12) structure which peaks for carboxylic acid carbonyl at (165.14) ppm and aromatic carbons are in the range of (153.21-120.22) ppm and Carbon-bearing hydroxyl group related to the benzene ring is in (115.40) ppm. The results obtained from the experimental part and appendix confirm the successful synthesis compound (12) and provide useful information for their characterization.

The proposed mechanism for reaction compound 12 was shown in Scheme (3-4).

3.1.8 Compound (13a-f)

The study describes the synthesis of porphyrin derivatives (13a-f) by reacting compound (12) with various amines, as illustrated in the scheme (3-7).
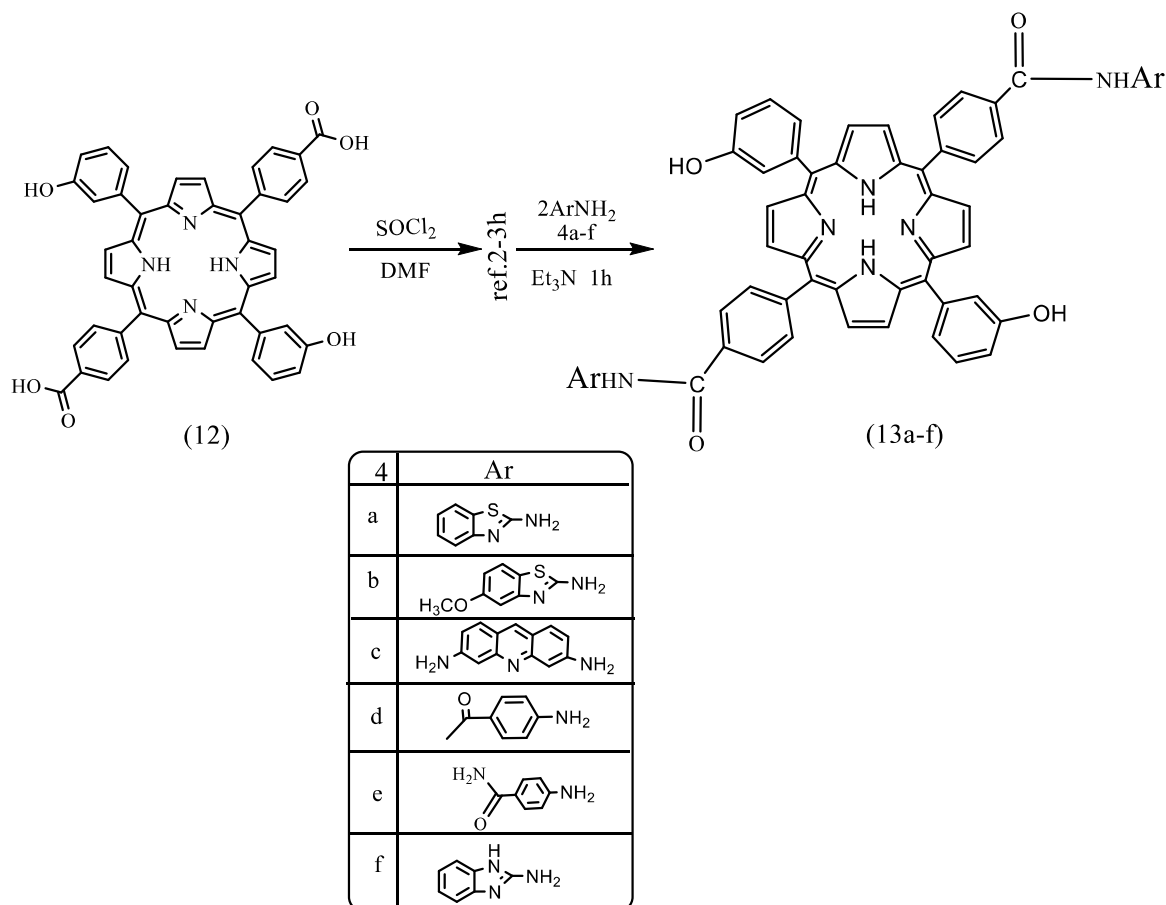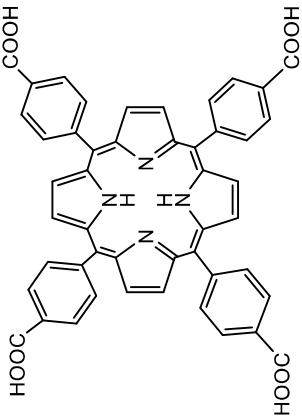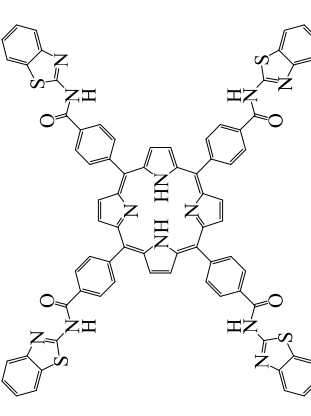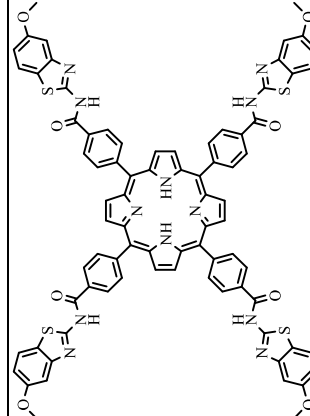
Scheme (3-7): Synthesis of compounds (13a-f).

The identification of the synthesized compounds was performed using infrared spectroscopy, which revealed the disappearance of the OH group in the carboxylic acid at (3600-2400 cm^{-1}), and the emergence of the amid group at approximately 3410 cm^{-1}. The complete spectrum information, including ESI-MS, FT-IR, ^{1}H, and ^{13}C-NMR, along with melting points for all synthesized porphyrin derivatives. The ^{1}H-NMR spectra of compounds (13a-f) exhibited a singlet signal at about (10.68 - 9.72) (2H amid NH) and the disappearance of the OH group of carboxylic acid. ^{13}C-NMR was utilized to confirm the compounds (13a-f) structure which peaks amid carbonyl at a range

from (172.63- 170.20) ppm and aromatic carbons are in the range of (160.25-120.16) ppm and Carbon-bearing hydroxyl group related to the benzene ring is in the range of (117.27-115.30) ppm. The results obtained from the experimental part and appendix confirm the successful synthesis of compounds (13a-f) and provide useful information for their characterization.

Results and Discussion

Table (3-1): Some of the physical properties of the synthesized dyes and mass data

Comp.no	Structure	Molecular formula	Color	M.Wt. g/mol	Mass Data (m/z) [M+]	Yield %	Rf
3		$C_{48}H_{30}N_4O_8$	Dark green	790.77	790.2	21	0.67 **n**-hexane: EtOAc 2: 3
5a		$C_{76}H_{46}N_{12}O_4S_4$	Black	1319.52	1318.20	80	0.7 **n**-hexane: EtOAc 2: 3
5b		$C_{80}H_{54}N_{12}O_8S_4$	Black	1439.63	-	83	0.65 **n**-hexane: EtOAc 2: 3

Results and Discussion
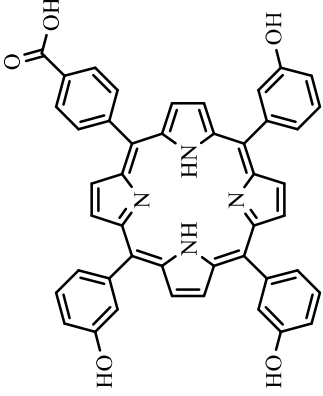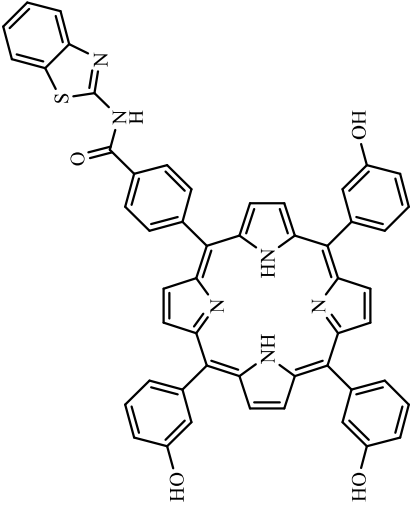
Comp.no	Structure	Molecular formula	Color	M.Wt. g/mol	Mass Data (m/z) [M+]	Yield %	Rf
5c		$C_{100}H_{66}N_{16}O_4$	Black	1555.74	1555.50	80	0.68 **n**-hexane: EtOAc 2: 3
5d		$C_{80}H_{58}N_8O_8$	Black	1259.39	-	82	0.67 **n**-hexane: EtOAc 2: 3

Comp.no	Structure	Molecular formula	Color	M.Wt. g/mol	Mass Data (m/z) [M+]	Yield %	Rf
5e		C$_{76}$H$_{54}$N$_{12}$O$_8$	Black	1263.34	-	84	0.7 **n**-hexane: EtOAc 2: 3
5f		C$_{76}$H$_{50}$N$_{16}$O$_4$	Black	1252.34	1250.38	82	0.64 **n**-hexane: EtOAc 2: 3

Results and Discussion
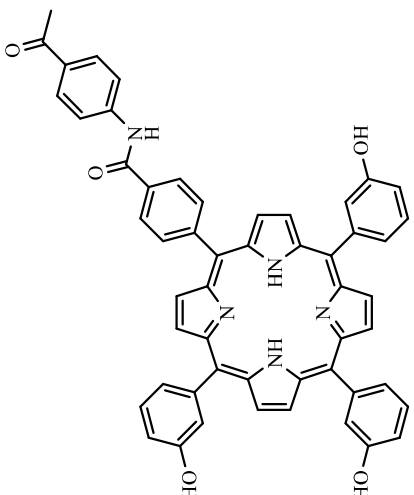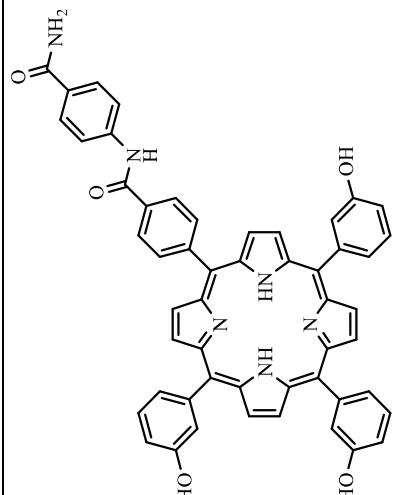
Comp.no	Structure	Molecular formula	Color	M.Wt. g/mol	Mass Data (m/z) [M+]	Yield %	Rf
6a		$C_{69}H_{42}N_{10}O_5S_3$	Black	1187.34	1186.20	75	0.55 **n**-hexane: EtOAc 2:3
6b		$C_{72}H_{48}N_{10}O_8S_3$	Black	1277.42	1276.21	65	0.6 **n**-hexane: EtOAc 2:3

Results and Discussion
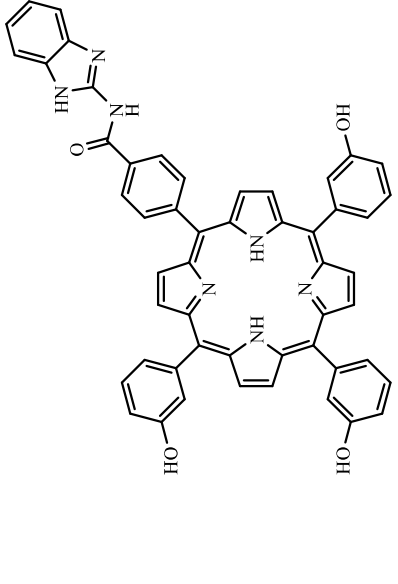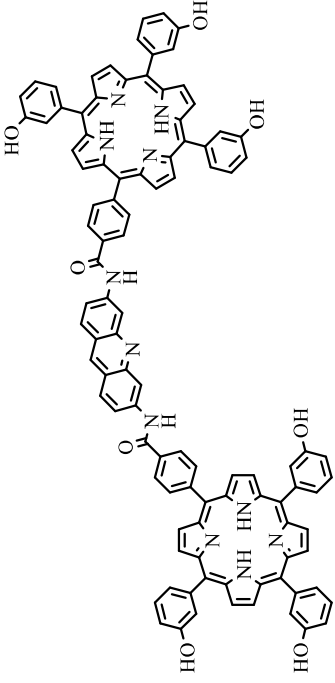
Comp.no	Structure	Molecular formula	Color	M.Wt. g/mol	Mass Data (m/z) [M+]	Yield %	Rf
6c		$C_{72}H_{51}N_7O_8$	Black	1142.24	1141.32	64	0.58 **n**-hexane: EtOAc 2: 3
6d		$C_{69}H_{45}N_{13}O_5$	Black	1136.21	1135.31	62	0.61 **n**-hexane: EtOAc 2: 3

Comp.no	Structure	Molecular formula	Color	M.Wt. g/mol	Mass Data (m/z) [M+]	Yield %	Rf
6e		$C_{84}H_{60}N_{10}O_{11}S_3$	Black	1481.64	1480.29	55	0.63 **n**-hexane: EtOAc 2: 3
6f		$C_{84}H_{60}N_{10}O_5$	Black	1289.47	1288.40	60	0.57 **n**-hexane: EtOAc 2: 3

Comp.no	Structure	Molecular formula	Color	M.Wt. g/mol	Mass Data (m/z) [M+]	Yield %	Rf
8		$C_{45}H_{30}N_4O_5$	Black	706.76	706.1	25	0.7 **n**-hexane: EtOAc 2: 3
9a		$C_{52}H_{34}N_6O_4S$	Black	838.94	838.2	65	0.64 **n**-hexane: EtOAc 2: 3

Results and Discussion
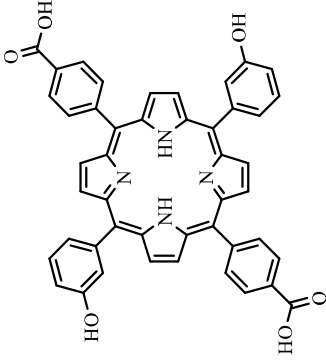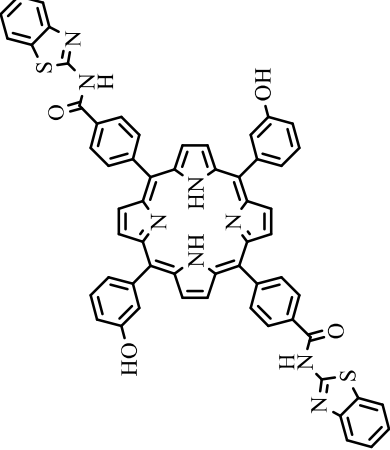
Comp.no	Structure	Molecular formula	Color	M.Wt. g/mol	Mass Data (m/z) [M+]	Yield %	Rf
9b		$C_{53}H_{37}N_5O_5$	Black	823.91	-	60	0.66 **n**-hexane: EtOAc 2: 3
9c		$C_{52}H_{36}N_6O_5$	Black	824.90	-	63	0.66 **n**-hexane: EtOAc 2: 3

Comp.no	Structure	Molecular formula	Color	M.Wt. g/mol	Mass Data (m/z) [M+]	Yield %	Rf
9d		$C_{52}H_{35}N_7O_4$	Black	821.90	-	66	0.62 **n**-hexane: EtOAc 2: 3
11a		$C_{103}H_{67}N_{11}O_8$	Black	1586.74	1586.51	60	0.72 **n**-hexane: EtOAc 2: 3

Comp.no	Structure	Molecular formula	Color	M.Wt. g/mol	Mass Data (m/z) [M+]	Yield %	Rf
11b		$C_{103}H_{72}N_{10}O_8$	Black	1575.75	1575.51	70	0.75 **n**-hexane: EtOAc 2: 3
11c		$C_{102}H_{68}N_{10}O_9$	Black	1577.73	1577.50	68	0.73 **n**-hexane: EtOAc 2: 3

Results and Discussion

Comp.no	Structure	Molecular formula	Color	M.Wt. g/mol	Mass Data (m/z) [M+]	Yield %	Rf
11d		$C_{102}H_{68}N_{10}O_{10}S$	Black	1625.79	1625.47	64	0.78 **n**-hexane: EtOAc 2: 3
11e		$C_{102}H_{68}N_{10}O_{8}$	Black	1561.73	1561.51	71	0.76 **n**-hexane: EtOAc 2: 3

Results and Discussion

Comp.no	Structure	Molecular formula	Color	M.Wt. g/mol	Mass Data (m/z) [M+]	Yield %	Rf
12		$C_{46}H_{30}N_4O_6$	Black	734.77	734.20	27	0.8 **n**-hexane: EtOAc 2:3
13a		$C_{60}H_{38}N_8O_4S_2$	Black	999.14	998.22	61	0.75 **n**-hexane: EtOAc 2:3

Results and Discussion

Comp.no	Structure	Molecular formula	Color	M.Wt. g/mol	Mass Data (m/z) [M+]	Yield %	Rf
13b		$C_{62}H_{42}N_8O_6S_2$	Black	1059.19	-	63	0.79 **n**-hexane: EtOAc 2: 3
13c		$C_{72}H_{48}N_{10}O_4$	Black	1117.24	-	55	0.78 **n**-hexane: EtOAc 2: 3

Comp.no	Structure	Molecular formula	Color	M.Wt. g/mol	Mass Data (m/z) [M+]	Yield %	Rf
13d		C₆₂H₄₄N₆O₆	Black	969.07	968.30	65	0.74 **n-**hexane: EtOAc 2: 3
13e		C₆₀H₄₂N₈O₆	Black	971.05	970.31	60	0.77 **n-**hexane: EtOAc 2: 3
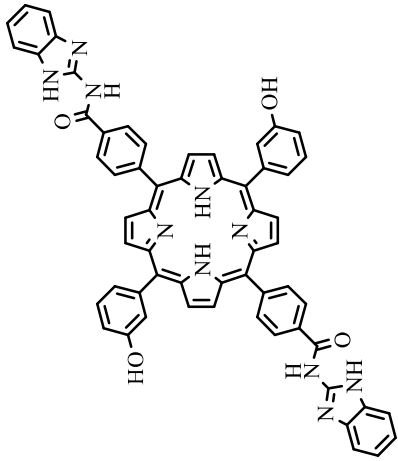
Comp.no	Structure	Molecular formula	Color	M.Wt. g/mol	Mass Data (m/z) [M+]	Yield %	Rf
13f		$C_{60}H_{40}N_{10}O_4$	Black	965.05	-	63	0.67 **n**-hexane: EtOAc 2: 3

Table (3-2): (C.H.N.S) Elementary Analysis

Com. no.	Calculated %				Found %			
	C	H	N	S	C	H	N	S
5a	69.18	3.51	12.74	9.72	68.21	3.32	11.48	9.52
5b	66.75	3.78	11.68	8.91	65.70	3.32	10.50	8.35
5c	76.41	4.05	13.22	-	77.20	4.28	14.41	-
5d	76.30	4.64	8.90	-	75.68	4.20	7.85	-
5e	72.26	4.31	13.30	-	71.80	4.15	12.57	-
5f	72.95	4.03	17.91	-	72.60	3.90	17.50	-
6a	69.80	3.57	11.80	8.10	69.25	3.35	11.33	7.83
6b	67.70	3.79	10.97	7.53	67.42	3.20	10.36	7.15
6c	75.71	4.50	8.58	-	75.15	4.40	8.19	-
6d	72.94	3.99	16.03	-	72.34	3.79	15.85	-
6e	68.09	4.08	9.45	6.49	67.75	3.90	8.85	6.18
6f	78.24	4.69	10.86	-	77.94	4.55	10.35	-
9b	77.26	4.53	8.50	-	76.80	4.32	8.05	-
9c	75.72	4.40	10.19	-	75.23	4.33	10.05	-
9d	75.99	9.29	11.93	-	75.59	9.20	11.54	-
13b	70.31	4.00	10.58	6.05	70.15	3.92	10.32	5.80
13c	77.40	4.33	12.54	-	77.15	4.13	12.34	-
13f	74.68	4.18	14.51	-	74.38	3.71	14.25	-

3.2 Characterization of graphene quantum dots

The graphene quantum dots nanoparticular were prepared for application in the one-pot synthesis of porphyrin derivative. Particularly, the graphene quantum dots nanoparticular were studied by FT-IR, XRD, Raman, FE-SEM, and EDX spectroscopy. The FT-IR spectrum of the graphene quantum dots nanoparticular was shown in Figure (3-1). The peak at about 1516 cm^{-1} is attributed to carbon-carbon double bonds in the sheets of graphene quantum dots. Moreover, other peaks at 3600-2400,3028,1701, and 1222 cm^{-1} could be assigned to hydrogen-oxygen, hydrogen-oxygen carboxylic acid (overlap),

carbon-hydrogen aromatic, carbonyl, and carbon-oxygen stretching modes of functional groups such as carboxylic and hydroxyl groups attached to graphene quantum dots, respectively.
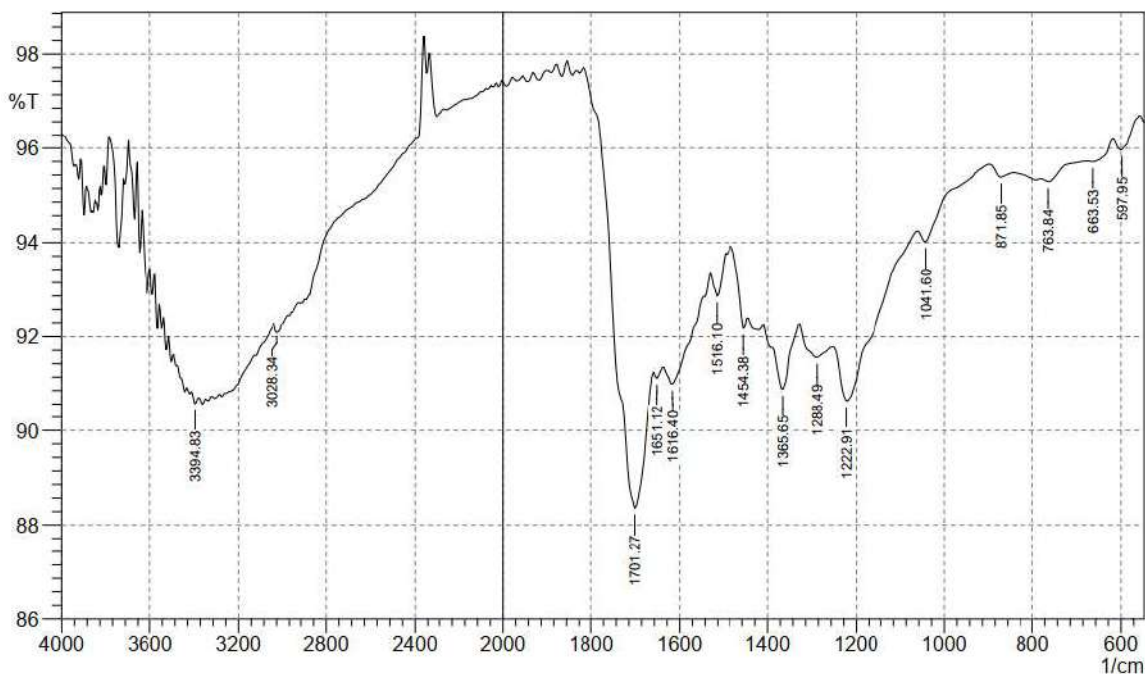
Figure (3-1): FT-IR spectrum of GQD

Figure (3-2) shows the results of the XRD analysis of the synthesized GQD's structure using a Lab X-XRD 6000-Shimadzu. The three crucial not-sharp peaks were seen in the XRD data of the GQD-synthesized powder, with diffraction patterns at $2\theta = 28.03°, 21.92°,$ and $12.38°$, using Scherer's equation (2-1)[198, 199, 202, 214, 215].

$$L = \frac{K.\lambda}{\beta.Cos\theta} \quad .... (2\text{-}1)$$

L represents the average size of the crystal, and it is calculated using the equation (1). The value of k, which is a Scherrer's constant that depends on the shape of the crystal, is set to 0.9 [214, 216, 217]. The wavelength of the X-ray radiation used for measurement is denoted by λ, which is 0.15406 nm for $Cu_{k\alpha}$. The full width of the half-maximum (FWHM) intensity expressed in radians is represented by β (originally in degrees, β is converted to radians by multiplying it by π/180). The diffraction (Bragg) angle is denoted by θ.

The mean crystallite size (L) in nm for graphene quantum dots nanoparticular was found to be 9.25 nm. The size ensures the generated graphene is quantum dots that seem to be nanoscale (less than 10 nm) [199-205].
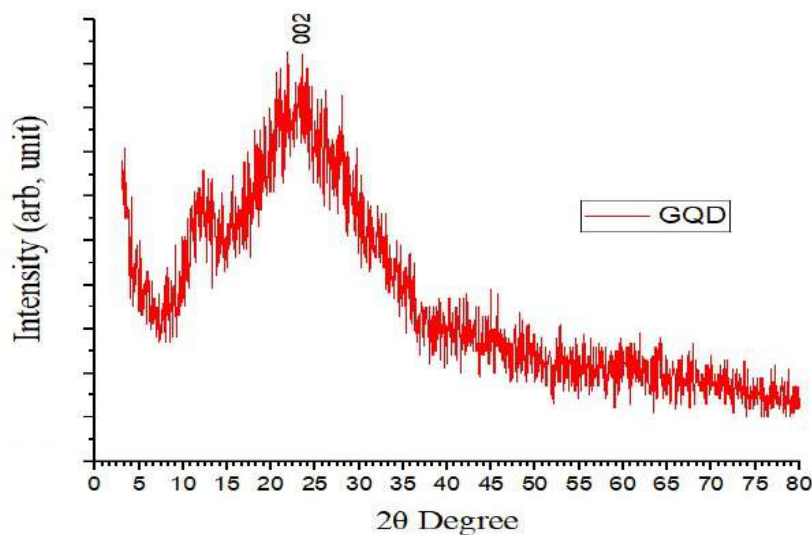
Figure (3-2): XRD analysis of GQD

To describe the graphene structure of the generated GQDs, Raman spectroscopy was also used. As shown in Figure (3-3), two Raman peaks for the GQDs may be attributed to well-ordered graphite (D-band) and disordered sp^2 carbon(G-band), at around 1352 and 1567 cm^{-1}, respectively. Moreover, the broadening in D-band may be attitude to the disorder/defects in the samples[218]. The fact that the G-band is more intense than the D-band suggests that the GQDs contain fewer lattice flaws[197]. The ratio D peak to G peak is less one that enhancement the amorphous and nanostructure of GQD.
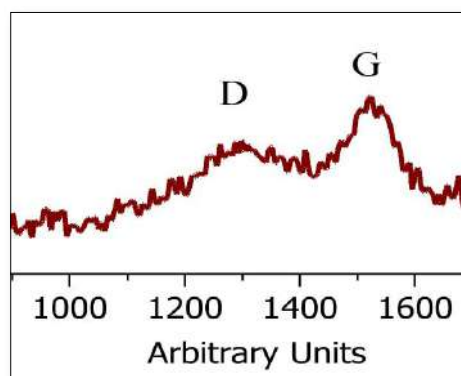
Figure (3-3): Raman spectrum of GQD

102

Graphene quantum dots' precise nanoscale structure is seen in Figure (3-4a). The FE-SEM image showed sheets of nanoparticular graphene quantum dots that were flat and network-like with range of particle sizes from 9.8 to 13 nm. The graphene quantum dots nanoparticles in particular are composed of aggregated and crumpled thin sheets, the surfaces of which also exhibit folds and wrinkles, with average particle size equal to 11.05 nm.

Element	Atomic %
C	68.5
O	31.5
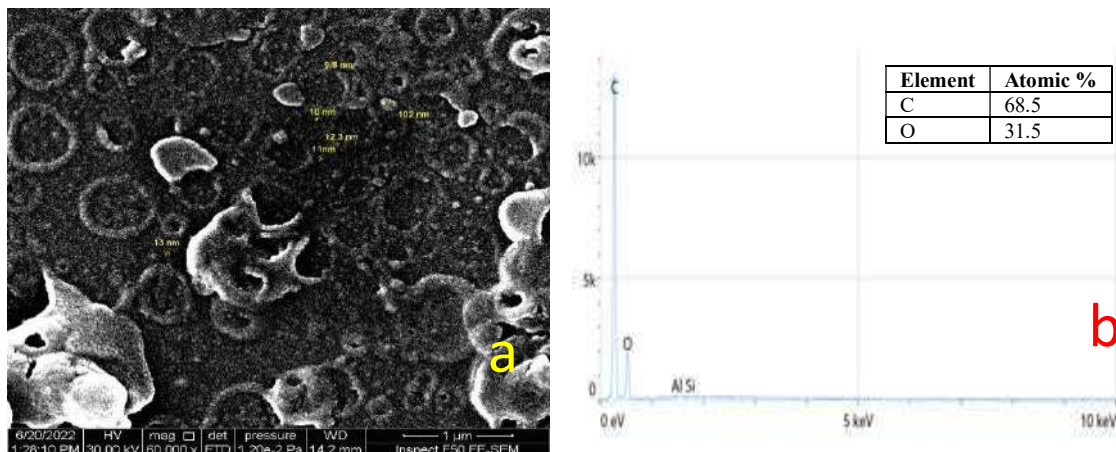
Figure (3-4): a- FE-SEM image and b- EDX spectrum of GQD

The sample's components were verified using the EDX spectrum, as shown in Figure (3-4 b), which revealed the presence of C and O from the nanoparticles and proved that no additional impurities were present[219].

The band gap energies of the investigated sample were determined using Tauc equation graphs[220, 221]. The indirect band gaps for the GQD in Figure (3-5) were equal to 0.70 eV.
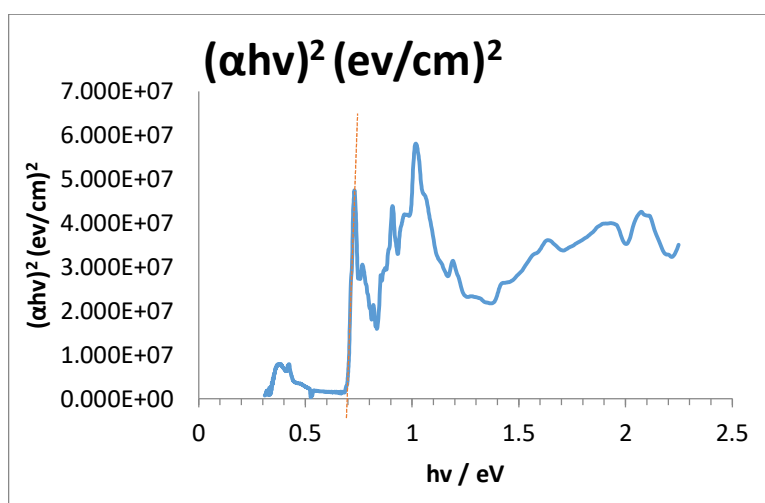
Figure (3-5): Band gap as an indirect of GQD

3.3 Characterization of TiO₂/GQD nanocomposite

The FT-IR spectrum of the composite TiO_2/GQD nanoparticular was shown in Figure (3-6). The prepared composites with broad absorption bands at 3600–3000 cm^{-1} are attributed to the O–H stretching vibrational absorptions bond. This suggests that there are numerous hydroxyl groups present on the surface of the TiO_2/GQD. The strong intensity peak at 1705 cm^{-1} is associated with the C=O stretching vibration in COOH. The edge of board peaks in TiO_2 ranged from 675 to 426 cm^{-1} shifts toward high frequency from 852 to 493 cm^{-1} after incorporated to formed a TiO_2/GQD composite. These spectra prove the prepared TiO_2/GQD contains COOH functional groups that will result in a good hydrophilic property and leads to enhanced photocatalysis[222].
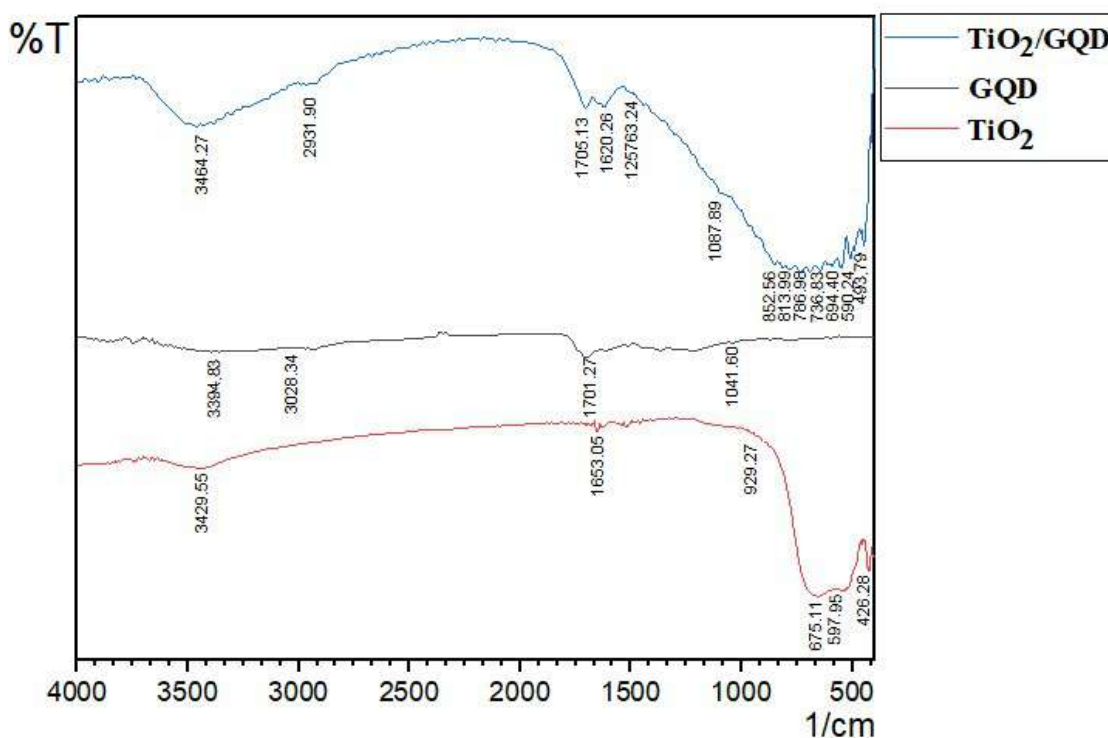
Figure (3-6): FT-IR spectrum of TiO₂/GQD, GQD, and TiO₂

The XRD patterns of pure TiO_2 nanoparticles, GQD, and TiO_2 nanoparticles loaded with GQDs are shown in Figure (3-7), respectively. Both anatase and rutile phases are indicated by TiO_2 in Figure (3-7), which corresponds to the patterns in JCPDS Nos. 88-1175 (anatase) and 84-1286 (rutile), respectively. Peaks in the anatase phase pattern may be seen at 25.2, 37.7, 48.0, 53.8, 55.0,

and 62.6°, which, respectively, correspond to the (101), (004), (200), (105), (211), and (204) planes. Furthermore, the (110), (101), (111), (210), and (220) planes, respectively, correspond to the rutile phase pattern's maxima at 27.4, 36.0, 41.2, 44.0, and 56.6°[223]. As shown in Figure (3-7), the diffraction pattern lacks any peaks from the carbon species. This may be a result of the GQDs' modest quantity and poor intensity. Additionally, the major peak of TiO$_2$ at (2θ = 25.2) may have protected the graphene peak (2θ = 24.7). The peak from the GQDs is often missing in the diffraction pattern of the TiO$_2$/GQD nanocomposites, which is similar to the XRD plots obtained by Gupta et al[224]. The sharp peak in TiO$_2$ at (101) and 25.2° shifts toward less 2thata 24.7° which refers to TiO$_2$ loading on GQD as TiO$_2$/ GQD composite. The mean crystallite size (L) in nm for TiO$_2$ was found to be 48.37 nm and this value decreased for TiO$_2$/ GQD composite to 34.39 nm. That is to the low value of the mean crystallite size of GQD.
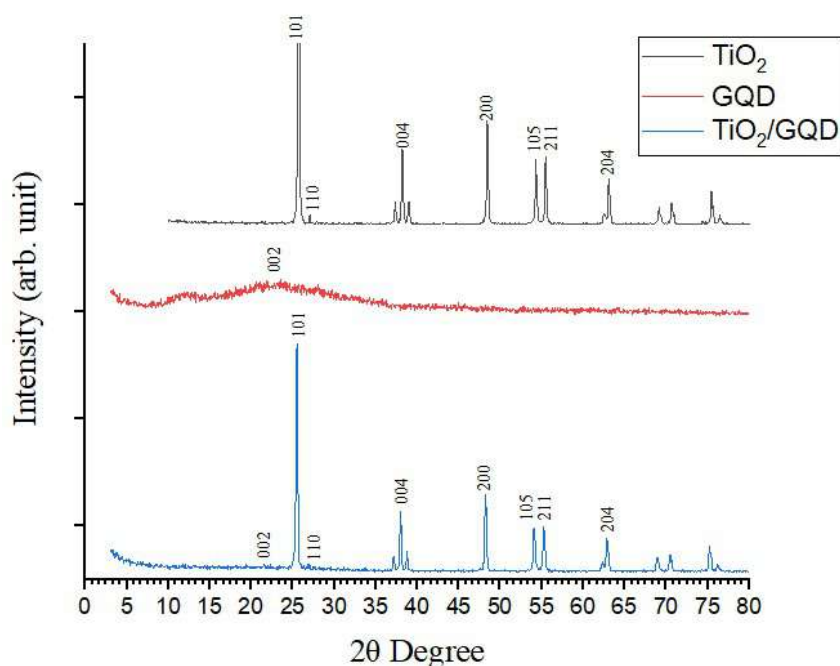
Figure (3-7): XRD analysis of TiO$_2$, GQD, TiO$_2$/GQD

Based on Figure (3-8), the shape of TiO$_2$ is elliptical with a micro scale, while the shape of the composite is semispherical cluster, with ranged of particle sizes from 60.98 to 79.47 nm and the average of it equal to 68.52 nm.
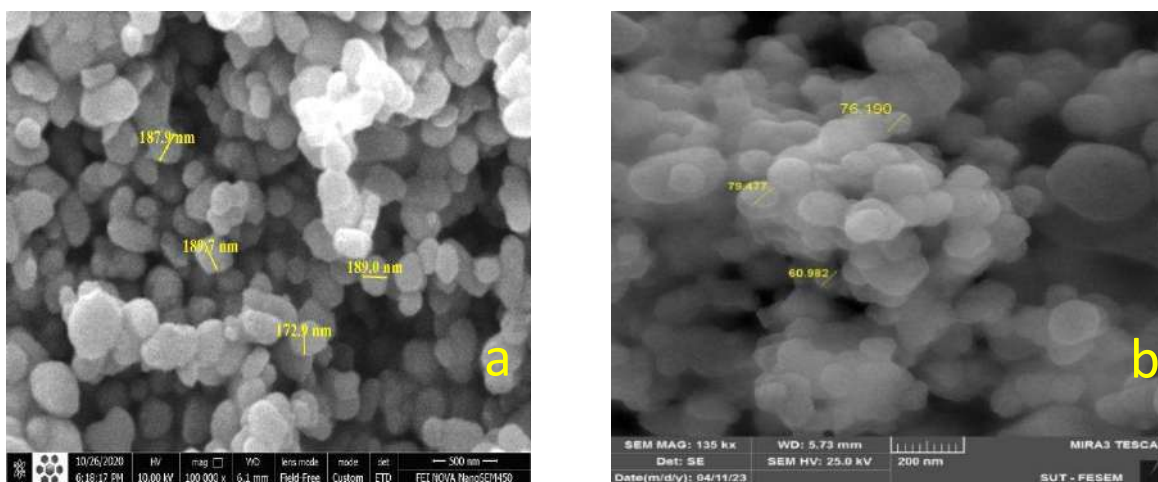
Figure (3-8): SEM image of a) TiO_2 and b) TiO_2/GQD

The calculations of the analyzed samples' band gap energies were made using Tauc equation graphs. For the photocatalysts TiO_2 and TiO_2/GQD, the indirect band gaps were 3.05 eV and 1.68 eV, respectively, in Figure (3-9). The band gap value of TiO_2 decreases after formed a composite, which ensures the interlayers between TiO_2 and GQD are generated.
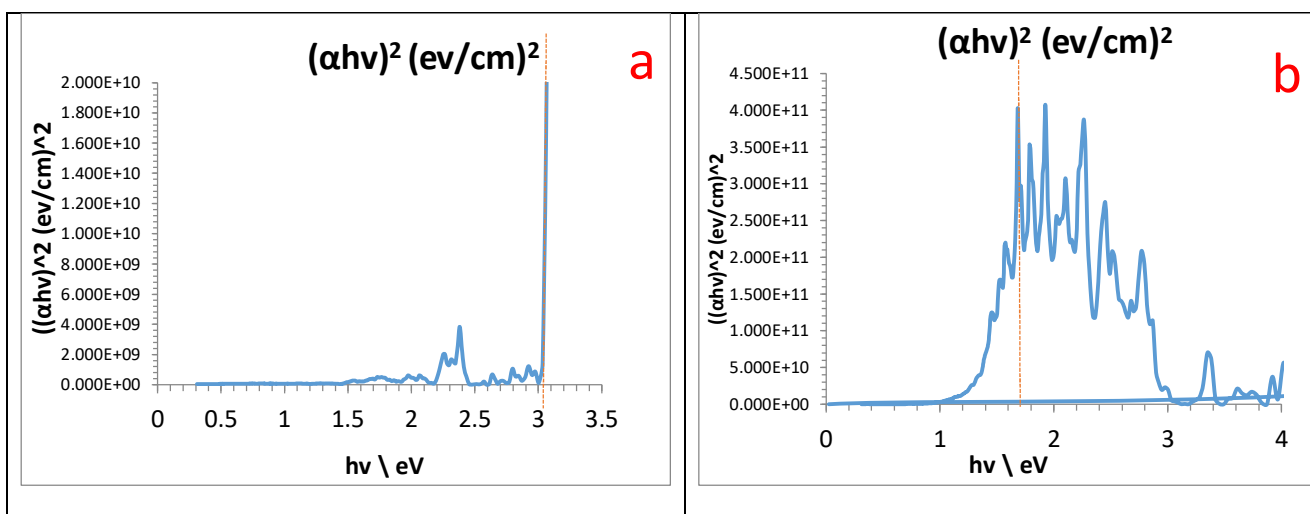
Figure (3-9): Band gap as an indirect of (a)TiO_2 and, (b) TiO_2/GQD

3.4 Characterization of Cadmium Ferrite Semiconductor

The FTIR spectra of normal spinal Cadmium Ferrite $(CdFe_2O_4)$ nanoparticles are shown in Figure (3-10) and were recorded in the range of 4000–400cm^{-1}. The bands at 3134 and 1662 cm^{-1} are caused by tensional stretching modes and H-O-H bending vibrations of free or absorbed water molecules[225]. There are

some weak absorption peaks at 2926 and 2854 cm^{-1} that were attributed to the stretching vibration mode of the C-H bond from the methanol [226]. The FT-IR spectrum observed two main sites: first band(v1) Fe-O (observed from 592 to 650 cm^{-1}); the higher frequency band corresponds to the intrinsic stretching vibrations of the tetrahedral site; and second, (v2) lower frequency band Cd-O (observed at 453 cm^{-1}), which is attributed to the intrinsic stretching vibration of octahedral site. The little variation in frequency between typical vibrations v1 and v2 can be explained by the large bond length of oxygen-metal ions in octahedral sites and the shorter bond length of oxygen-metal ions in tetrahedral sites. The resultant phase's high degree of crystallinity is connected with these bands' sharpness. Spinel ferrite ($CdFe_2O_4$) is characterized by two prominent sharp bands at 891 and 796 cm^{-1} [227-229].
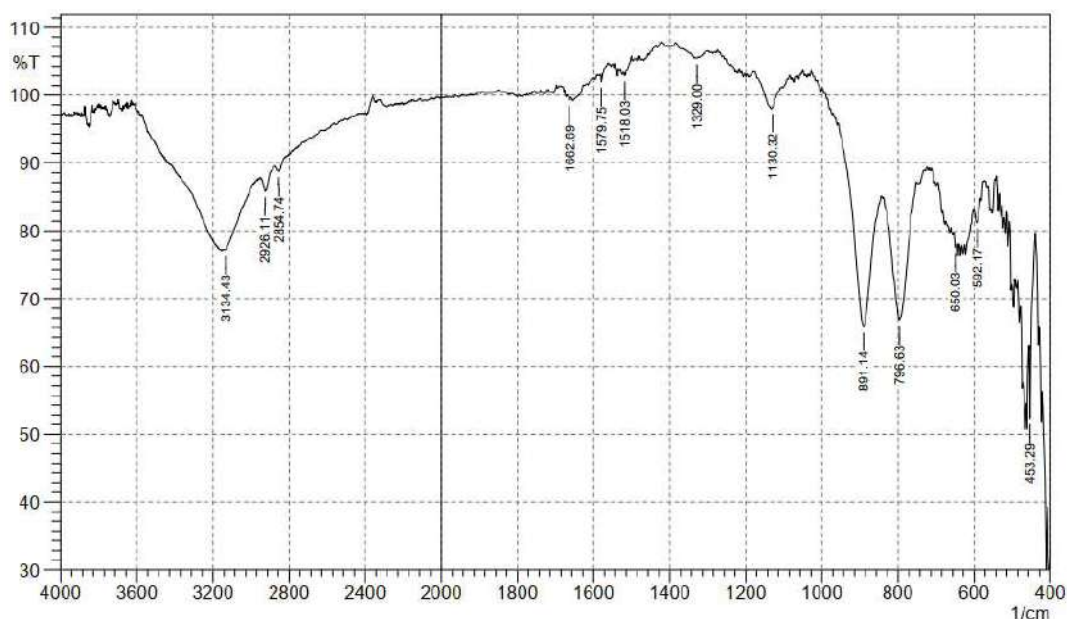
Figure (3-10): FT-IR spectrum of $CdFe_2O_4$

To determine the nanomaterial's crystalline state, X-ray diffraction (XRD) was performed. The outcomes for the produced cadmium ferrite (Spinel $CdFe_2O_4$) are given in Figure (3-11). The tetragonal phase structure may be indexed to all of the diffraction peaks. According to XRD pattern findings and comparison with XRD data files (JCPDS No. 35-0425), the diffraction peaks may be

assigned to (111), (220), (311), (400), (422), (511) and (440). These results support those from previous research [230], at $2\theta = 21.16°, 33.22°, 36.60°, 41.15°, 53.11°, 58.90°$, and $61.26°$, respectively.
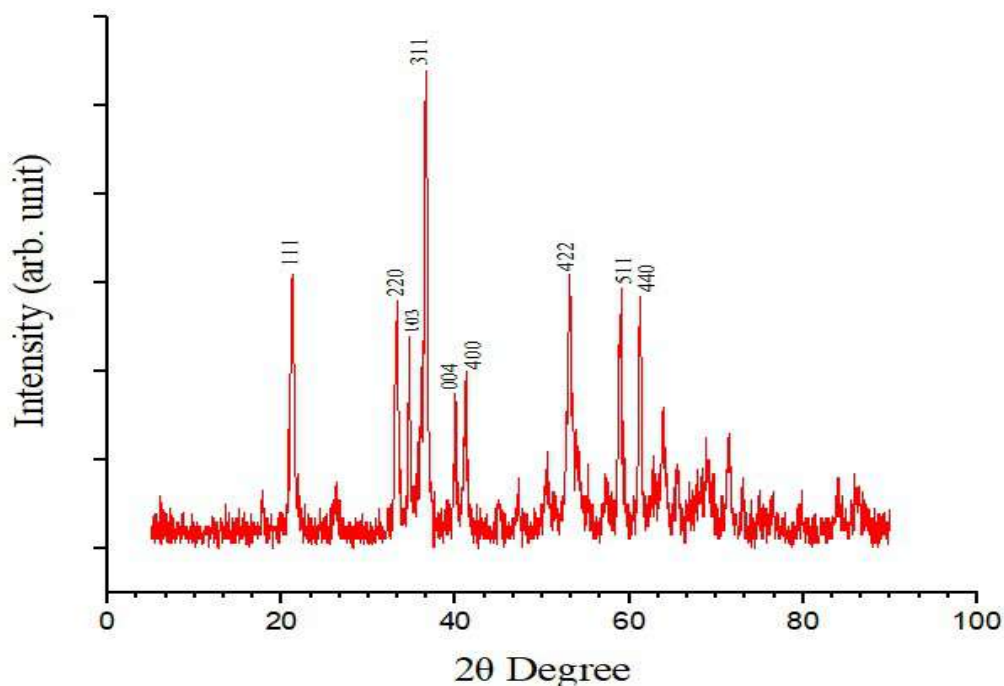
Figure (3-11): XRD analysis of $CdFe_2O_4$

Using the Debye-Scherer equation [231] (2-1), the mean crystal size of $CdFe_2O_4$ nanoparticles was carried out these peaks with a size equal to (21.07 nm).

The FE-SEM image of $CdFe_2O_4$ Nano particular as shown in Figure (3-12 a) revealed the rod were used to observe the morphology and size distribution of $CdFe_2O_4$ nanorods with particle size equal to 45.05 nm. However, the nanorods produced are thought to be single crystals that are free of defects and are oriented at random concerning the substrate surface [232]. The prepared $CdFe_2O_4$ is found to be poly-crystal because the particle size of $CdFe_2O_4$ is more than the mean crystal size of it.
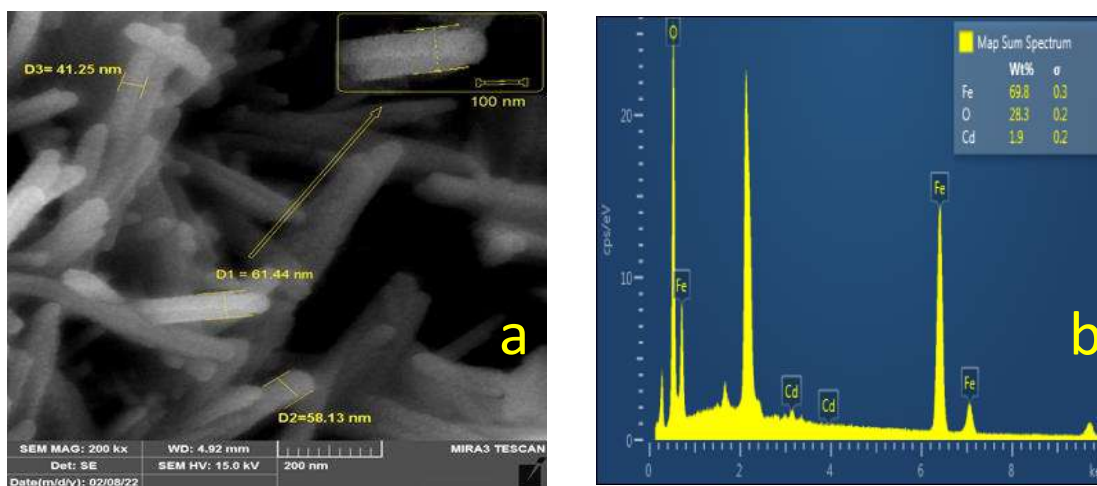
Figure (3-12): a) FE-SEM image and b) EDX spectrum of $CdFe_2O_4$

The sample's components were verified using the EDX spectrum, as shown in Figure (3-12 b), which revealed the presence of Cd, Fe, and O from the nanoparticles and proved that no additional impurities were present. Additionally, it is found that Fe is double the weight presence of Cd, which is in line with the stoichiometry preparation ratio of (2:1) that was used during preparation[233]. The band gap energies of the investigated sample were determined using Tauc equation graphs[220, 221]. The indirect band gaps for the photocatalyst $CdFe_2O_4$ in Figure (3-13) were equivalent to 2.60 eV.
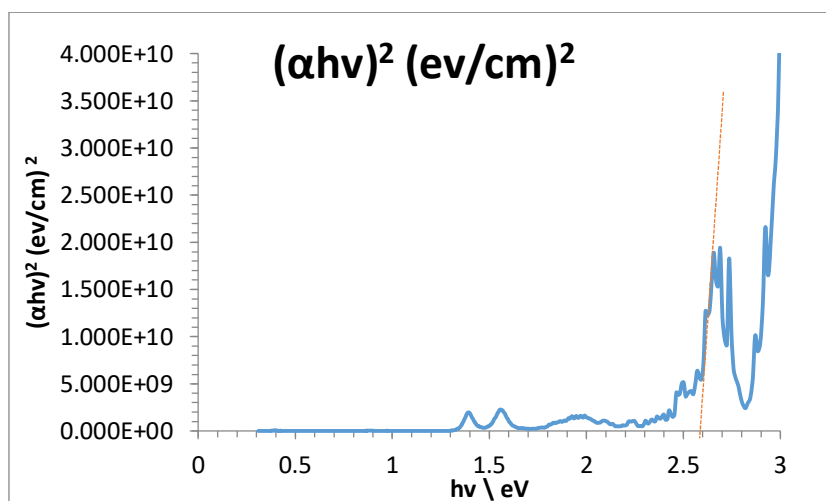
Figure (3-13): Band gap as an indirect of $CdFe_2O_4$

3.5 Characterization of TiO$_2$/CdFe$_2$O$_4$ nanocomposite

The synthetic nanocomposite (TiO$_2$/CdFe$_2$O$_3$) FTIR spectra, obtained in the 400–4000cm^{-1} range, are shown in the Figure (3-14). Peak patterns were seen in the TiO$_2$/CdFe$_2$O$_3$ nanocomposite areas at 3421 cm^{-1}, 1616 cm^{-1}, and 1080 cm^{-1} [226]. The O-H stretching vibrational absorptions bond is responsible for the produced composites' wide absorption bands at 3600–3000cm^{-1}. The C-O stretching vibration is what causes the peak to appear at 1080 cm^{-1}, and can be attitude to CTAB surfactant. Fe-O stretching mode is given to the strong band below 671 cm^{-1}. In the region of 671-474 cm^{-1}, metal oxide bands Ti-O and Ti-O-Ti stretching vibrations have been found. After incorporated CdFe$_2$O$_3$with TiO$_2$, the edge of TiO$_2$ band shifts toward more value from 929.27 to 1080.17 cm^{-1}, in addition to the sharp peak for Cd-O bond at 453.29 cm^{-1}in CdFe$_2$O$_4$ spectrum was moved to 474.5 cm^{-1}.
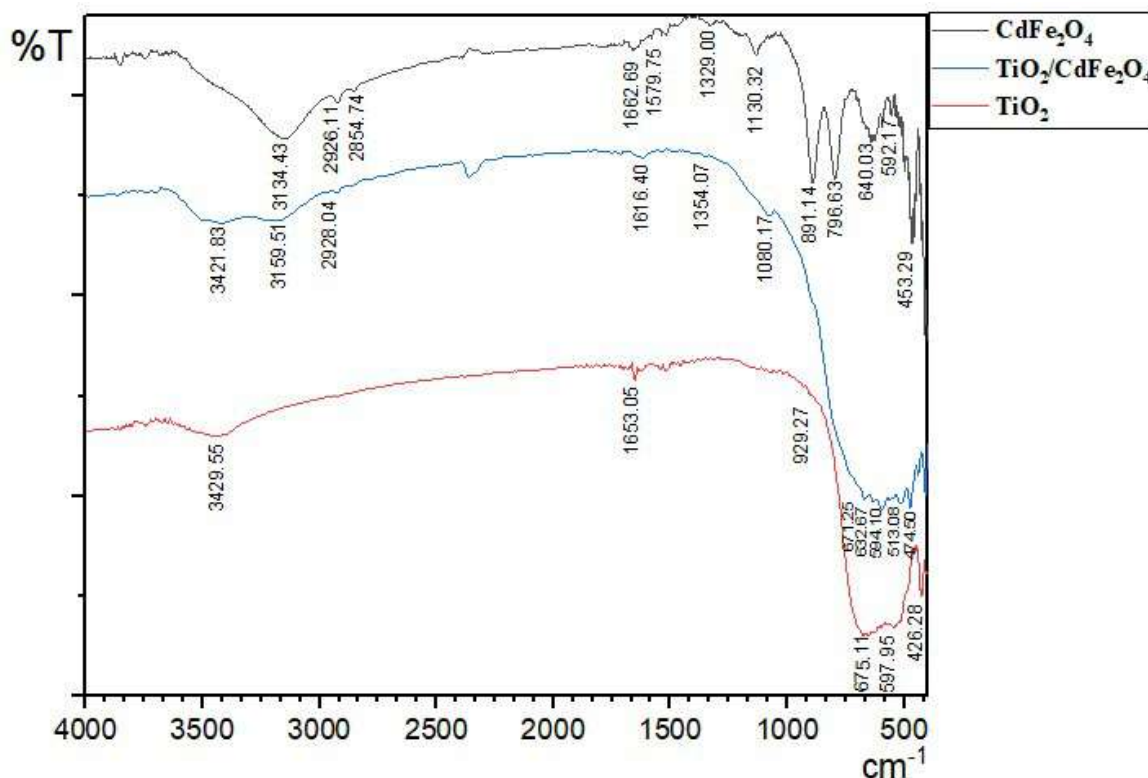
Figure (3-14): FT-IR spectrum of CdFe$_2$O$_4$, TiO$_2$/CdFe$_2$O$_4$. TiO$_2$

The XRD patterns of pure TiO$_2$ nanoparticles and TiO$_2$ nanoparticles loaded with GQDs are shown in Figure (3-15), respectively. The TiO$_2$ substrate may

be used to account for all of the diffraction peaks, according to the quantitative analysis Figure (3-12). The TiO_2 anatase phase is shown by the usual diffraction peak (101) centered at 25.15. (JCPDS no. 21-1272). The (101), (004), (200), (105), and (204), planes of the anatase phase with a tetragonal crystal structure and space group, are shown by the peaks. As shown in Figure (3-14), the diffraction pattern lacks any peaks from the carbon species. This may be a result of the $CdFe_2O_4$ modest quantity and poor intensity. Additionally, the major peak of anatase TiO_2 at ($2\theta = 25.15$) may have protected the $CdFe_2O_4$ peak ($2\theta = 24.80$). The peak from the $CdFe_2O_4$ is often missing in the diffraction pattern of the $TiO_2/CdFe_2O_4$ nanocomposites. The mean crystallite size in nm for TiO_2 was decreased for its composite $TiO_2/CdFe_2O_4$ from 48.37 nm to 36.96 nm. because the mean crystallite size of $CdFe_2O_4$ is low.
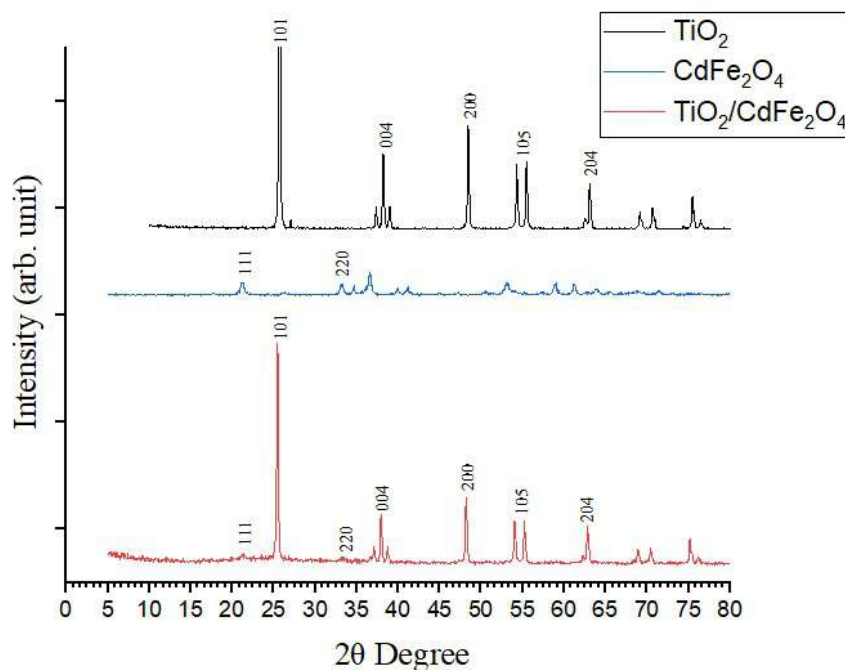
Figure (3-15): XRD analysis of TiO_2, $CdFe_2O_4$ and TiO_2-$CdFe_2O_4$

Based on Figure (3-16a), the shape of the composite is semispherical cluster that agglomerated on nanorod, with ranged of particle sizes from 41.42 to 75.79 nm and the average of it equal to 63.91 nm. The sample's components were

verified using the EDX spectrum, as shown in Figure (3-16b), which revealed the presence of Cd, Fe, Ti, and O from the nanoparticles and proved that no additional impurities were present.

Element	Atomic %
O	56.4
Ti	22.9
Fe	1.9
Cd	0.9
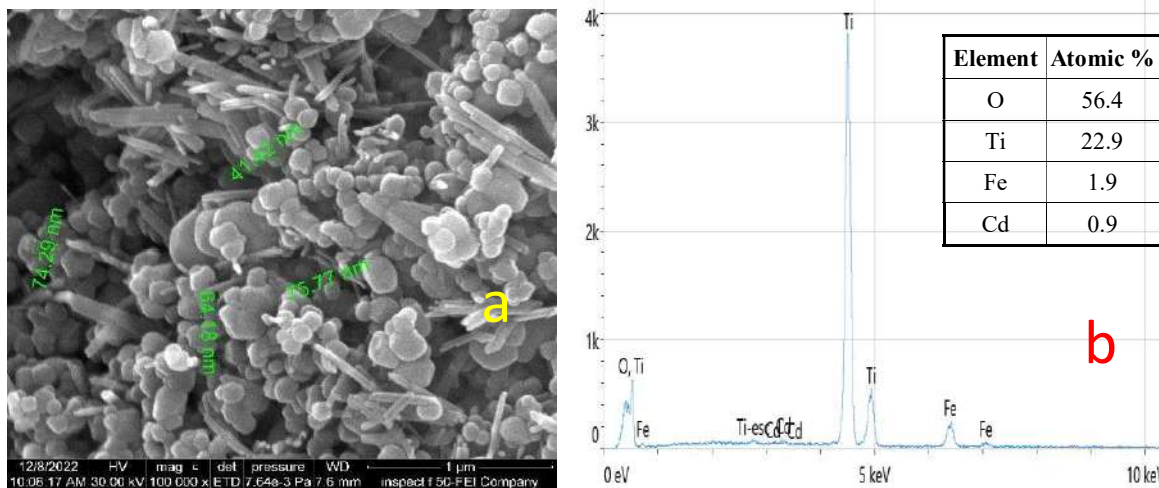
Figure (3-16): a) FE-SEM image and b) EDX spectrum of $TiO_2/CdFe_2O_4$

In Figure (3-17), the indirect band gap energies of analyzed samples' TiO_2 and $TiO_2/CdFe_2O_4$ were calculated using Tauc equation graphs, and found to be 3.03 eV and 2.47 eV, respectively. These compounds can be used as photocatalysts. The changed in band gap value of TiO_2 after formed a composite, ensure the interlayers have happened.
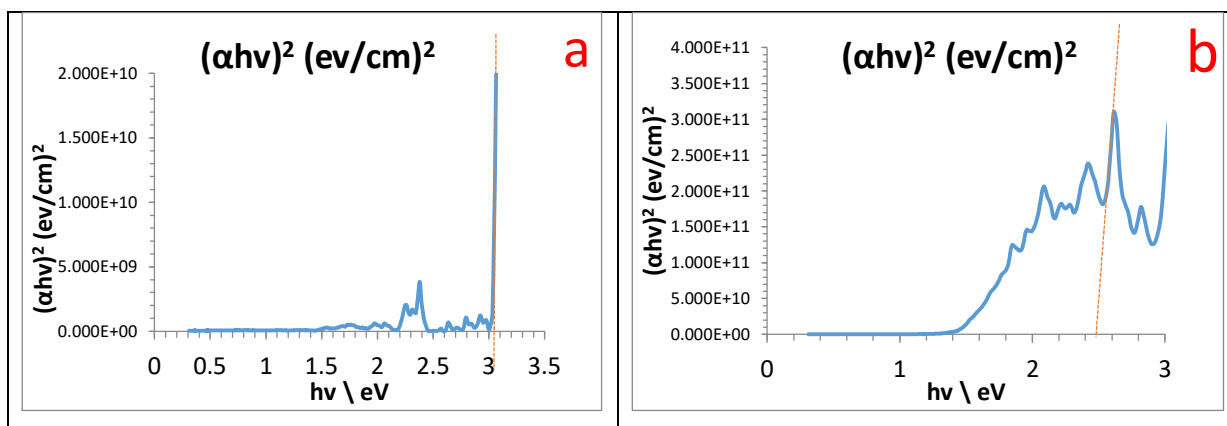
Figure (3-17): Band gaps as an indirect of (a)TiO_2, and, (b) $TiO_2/CdFe_2O_4$

3.6 Dye-Sensitized Solar Cells test

The J-V curve was used to compute the open-circuit voltage (V_{oc}) and short-circuit current (J_{sc}). The following equations were used to calculate the

solar cells' (photoelectrical conversion) efficiency ((η) or PCE) and fill factor (FF) [234], by the following equations

$$FF = \frac{J_{max}\, V_{max}}{J_{sc}\, V_{oc}} \qquad \text{... (3-1)}$$

$$\eta = \frac{J_{sc}\, V_{oc}\, FF}{I_o} \qquad \text{... (3-2)}$$

Where I_o is the total incident irradiance, V_{max} is the solar cell's maximum power point voltage, and J_{max} is the maximum power point current. J_{sc}, V_{oc}, FF, and PCE findings are shown in Figure (3-18 to 3-20) together with the J-V curves for all produced compounds Tables (3-3 to 3-5).

Table (3-3): The photoelectrical parameters of fabricated TiO_2 with dyes 3 and 8 as anode in DSSCs.

Dye	Jsc (mA.cm^{-2})	Voc (mV)	FF (%)	PCE (%)
3	1.55	0.750	78.9	1.29
8	1.65	0.775	79.3	1.41
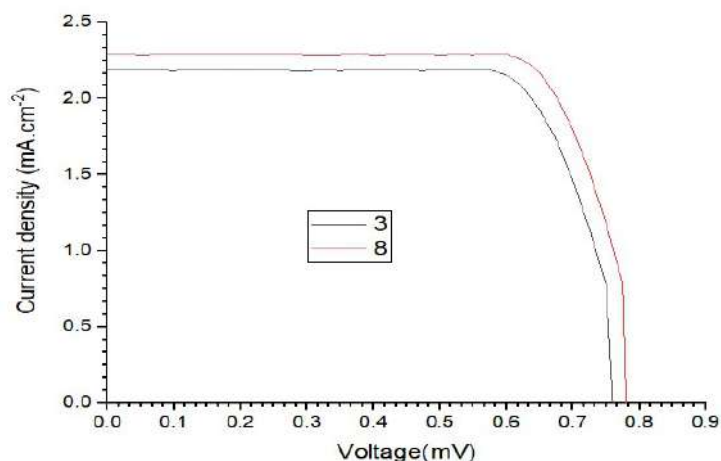
Figure (3-18): J-V curve of DSSCs sensitized TiO_2

The main studies to test the effectiveness of DSSCs' photoelectric conversion utilizing TiO_2 with prepared dyes 3 and 8 as anodes are shown in Table (3-3) and Figure (3-18). Because dye 3 has a substitution from -COOH, which is more active in solar cells, but dye 8 is give a maximum value that beyond to

the z.p.c for TiO_2 is ranged 5.8-6.8 therefor TiO_2 surface laver a liked with dye 8 which contain 3OH groups.

Table (3-4): The photoelectrical parameters of fabricated TiO_2 by GQD as composite with different dyes as anode in DSSCs.

Dye	Jsc (mA.cm^{-2})	Voc (mV)	FF (%)	PCE (%)
3	2.88	0.806	79.3	2.26
5d	2.01	0.775	70.9	1.45
6a	4.76	0.775	75.5	2.92
6b	5.47	0.777	76.6	3.35
6c	3.09	0.775	75.1	1.89
6d	4.69	0.775	74.6	2.88
6e	3.25	0.780	76.5	1.99
6f	4.09	0.765	74.6	2.51
8	2.5	0.852	67.6	1.82
9b	1.60	0.775	77.3	1.34
9d	1.39	0.703	79.7	1.14
11c	2.28	0.821	77.3	1.86
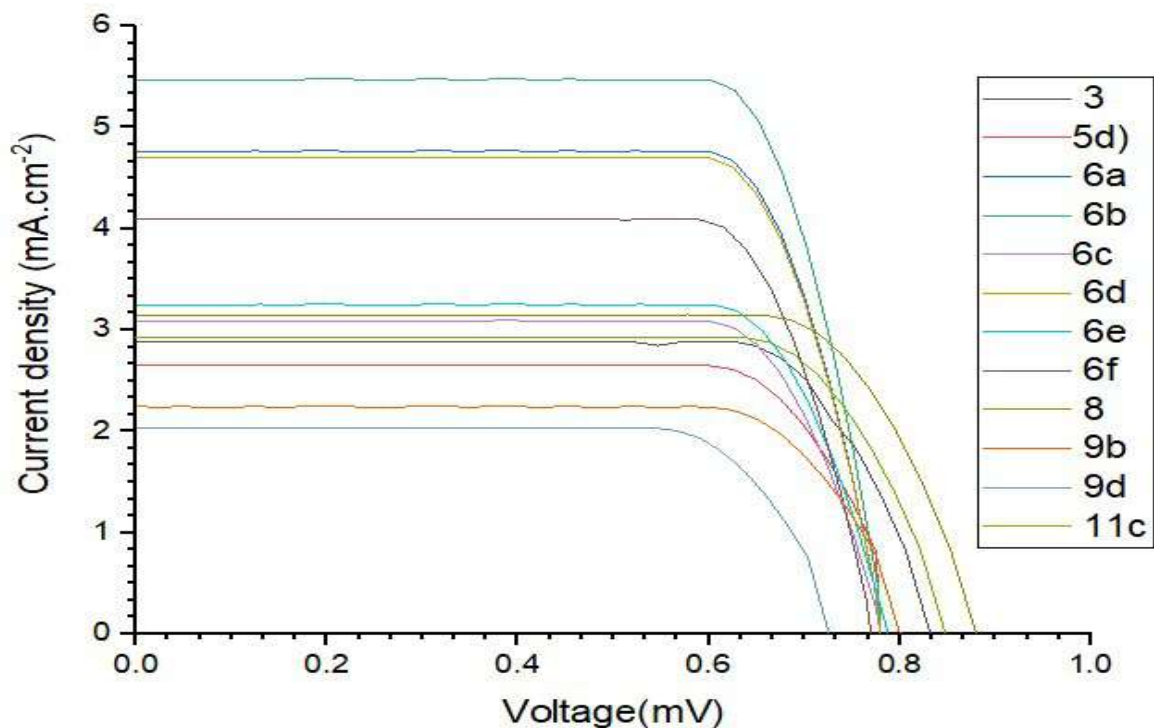
Figure (3-19): J-V curve of DSSCs sensitized TiO_2/GQD

Table (3-5): The photoelectrical parameters of fabricated TiO_2 by $CdFe_2O_4$ as composite with different dyes as anode in DSSCs.

Dye	Jsc (mA.cm^{-2})	Voc (mV)	FF (%)	PCE (%)
3	2.77	0.776	76.5	1.69
6a	5.22	0.777	76.1	3.20
6b	5.99	0.785	76.8	3.67
6c	3.58	0.750	76.5	2.19
6d	5.05	0.775	75.5	3.09
6e	3.86	0.775	76.5	2.36
6f	4.75	0.750	75.1	2.92
8	2.90	0.778	76.5	1.77
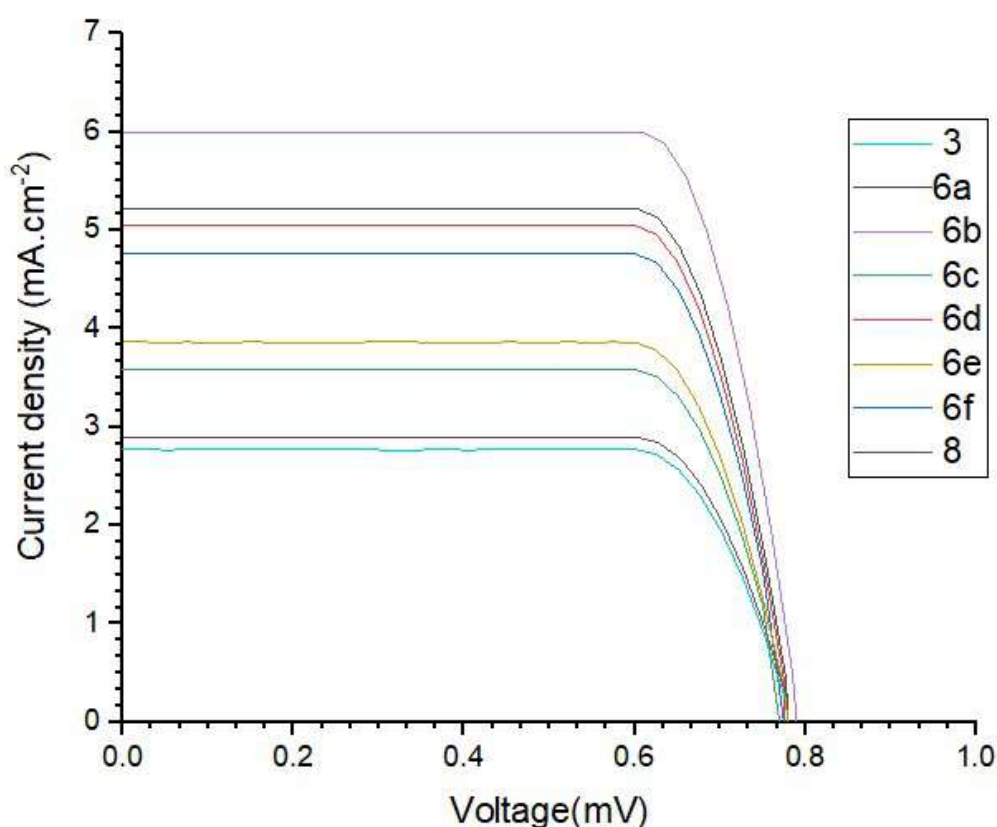
Figure (3-20): J-V curve of DSSCs sensitized TiO_2/ $CdFe_2O_4$

The results in Tables (3-4) and (3-5) showed the values PCE% when using different preparation dyes with surface of TiO_2/$CdFe_2O_4$ composite as an anode in sensitized of DSSCs are mainly higher than the values when using most prepared dye with TiO_2/GQD as an anode. This may be because $CdFe_2O_4$ has a nanorod shape, which disperses the crystal of TiO_2 on its surface and

decreases its agglomeration. If The agglomeration, occurs, will result in poor loading of the produced dye and increased resistance to electron mobility across the photoanode film [235, 236].

Additionally, the light-yellow color of $TiO_2/CdFe_2O_4$ composite is superior to the deep grey color of TiO_2/GQD in terms, will improve the photon absorption associated with penetration light and improve the light scattering[199]. This is because the deep color of a composite has an impact on the reach of light to a photo semiconductor to activate it this is called screen effect. Although the bandgap of the composite $TiO_2/CdFe_2O_4$ is greater than that of TiO_2/GQD, it is nevertheless appropriate for use as an anode in DSSCs because it exhibits less recombination and has good charge separation (excitons) that are produced when the prepared dye interacts with photons constantly. Consequently, any dye can act as a good sensitizer when it generates a significant free charge that is converted to current as it approaches the electrodes[237, 238].

3.7 Potentiodynamic Polarization

A carbon steel sample submerged in a corrosive media in the absence and presence of the compounds (5c, b) and (13c, b) at a temperature of 292 K as shown in Figure (3-21) polarization curves. There is a discernible difference in the Tafel area of the polarization curves and a linear connection between the potential and the logarithm of the current density was discovered. Numerous electrochemical kinetic parameters for the corrosion process, including the corrosion potential (E_{corr}), corrosion current density (I_{corr}), and both cathodic and anodic Tafel slopes (c, a), were calculated by extrapolating the anodic and cathodic areas of the Tafel lines. Table (3) has a list of these parameters.

Table (3-6): Measurements of corrosion parameters for carbon steel using a Tafel scan in the presence and absence of compounds (5c, b) and (13c, b) at temperature (292 K).

Solution Mg	T (K)	-E_{corr} (mV)	Δ E_{corr} (mV)	Icorr (mA/cm^2)	βc (mV/dec)	βa (mV/dec)	C.R (mm/y)	Rp (Ω/cm^2)	IE%
Blank	292	465.7	-	0.3255	140	121	3.781	43.36	-
5c	292	429.1	36.6	0.0846	185	76	0.9829	138.7	74.00
5b	292	409.3	56.4	0.1038	234	72	1.206	115.6	68.11
13c	292	430.6	35.1	0.2637	293	124	3.062	71.85	18.98
13b	292	381.8	83.8	0.1785	360	85	2.073	83.97	45.16

Table (3-6) shows that the addition of compounds (3a, b and 5a, b) had a significant impact on the corrosion process compared to the blank solution. The difference in the ΔE_{corr} values for the prepared compounds was calculated using equation (3-3) [239, 240] and demonstrated that all values are less than 85 mV, hence the inhibitor can be classified as an inhibitor mixture from cathodic or anodic inhibitors [240].

$$\Delta E_{corr.} = E_{corr., \text{without inhibitor}} - E_{corr., \text{with inhibitor}} \quad \dots (3\text{-}3)$$

Generally, the corrosion current density (which is directly proportional to the corrosion rate) of the sample decreased significantly after the addition of compounds (5c, b, and 13c, b). At 292 K, the corrosion current density of the blank solution was 0.3255 mA cm^{-2} and depressed after the addition of the prepared compounds to range 0.0846 mA cm^{-2} - 0.2637 mA cm^{-2}. When adding compound 5c, the maximum depression in this value has occurred with a maximum value of % IE. This case is an attitude to include compound 5c on four substituted aromatic amine groups in its structure symmetry compound). This aromatic amine group acts as an essential positive charge in organic inhibitors to control corrosion in an acidic medium[241]. Moreover, the addition of compounds 5b and 13b gives the medium value of % IE 68.11 % and 45.16 %, respectively. This is because both contain heteroatoms in their

structures such as nitrogen, sulfur, and oxygen. These atoms include free pairs of electrons that supported the link on the metal surface (mostly Fe, Cu…) of carbon steel by the adsorption method to produce a thin film layer. The formed thin film layer will act as a barrier to separate the metal from the corrosive medium and blocks their active sites for acidic medium[242-244]. On the contrary, the addition of 13c compound as anticorrosion involved less value of % IE, which may be an attitude to the big and asymmetric molecule, so, its adsorption on Carbon Steel is weak in the spirit of contains two amine group substituted. Furthermore, the corrosion rate (CR) also declined with using prepared compounds.
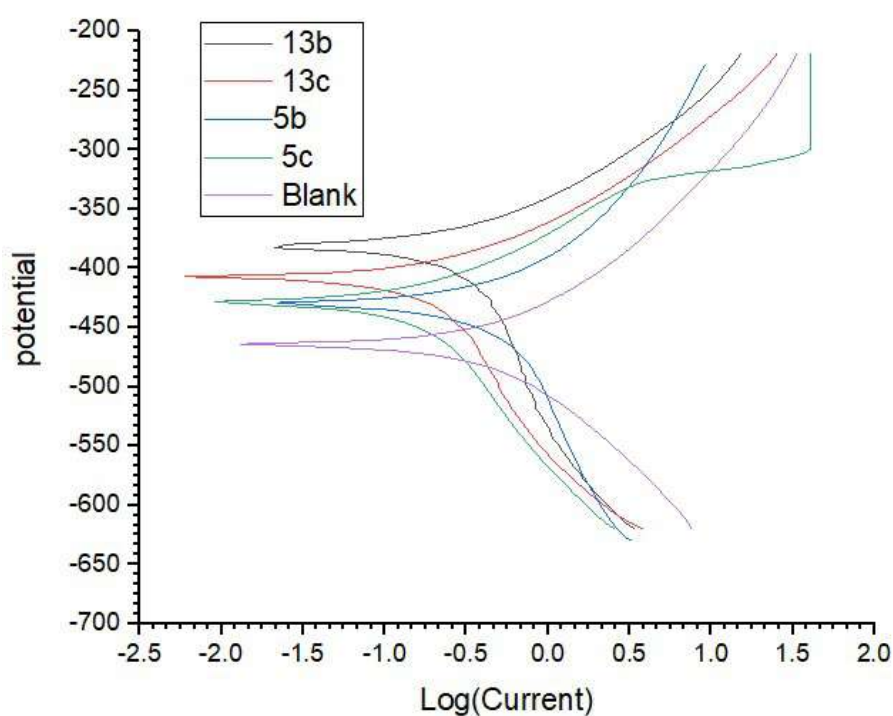
Figure (3-21): Polarization curves of carbon steel corrosion in the absence and presence of compounds (5b,5c,13band13c)

In Figure (3-21), overall, the polarization results indicate that the compounds (5c, b and 13c, b) are effective in reducing the corrosion rate of carbon steel in the tested conditions. The peak intensity for the blank is depressed after the addition of the prepared compounds and shifted the polarization curves towards a positive side during formed a thin layer onto the surface of the steel[245].

3.8 Mechanism of inhibition

In terms of the inhibition process, it is commonly accepted that the initial stage of the inhibitors' action mechanism in hostile acid media is their adsorption at the metal solution interface. The porphyrin derivatives' ability to inhibit C-steel in HCl solution may be explained in terms of adsorption. At the metal-solution interface, organic molecules may adsorb in one of four ways [246]:

(i)   Through electrostatic attraction between charged molecules and the metal.

(ii)   Through interactions between electrons and the metal.

(iii)   Through interactions between uncharged electron pairs within the molecule and the metal.

(iv)   or through a combination of the above

The significant delocalization of the electrons in the porphyrin molecule, the unoccupied d-orbitals of the iron surface atoms, and the lone pairs of the heteroatoms make it clear that the direct adsorption of these compounds on the Fe surface might take place [247]. Additionally, the electron density on the heterocyclic ring is increased by the presence of the electron-releasing additional NH_2 groups in the molecules. These substances may exist as protonated species in acidic solutions. These protonated species may adhere to the cathodic sites on the surface of the C-steel and reduce hydrogen evolution. These substances' N atoms, heterocyclic rings, and aromatic rings all electron-donating groups allow them to adhere to anodic surfaces. These substances may lessen the anodic breakdown of C-steel by adhering to anodic sites. Two distinct methodologies were utilized to examine the inhibitory impact of the various chemicals used in this experiment. It is possible for heteroatoms with lone pairs of electrons to transfer their lone pairs of electrons into the d-orbitals of the surface iron atoms, which results in chemisorption.[248] Further oxidation of the surface iron atoms produces

electrons that are consumed by NH-H$^+$, causing the adsorbed cationic inhibitor molecules to return to their neutral form as shown in equations (3-4) and (3-5). Stronger chemical interactions are between the surface and inhibitor as shown in the Figure (3-21) [249].

$$Fe(H_2O)n_{ads} + 2Cl^- \Longleftrightarrow Fe\left[(H_2O)_n(Cl)_2\right]_{ads}^{-2} \quad ...(3\text{-}4)$$

$$Fe\left[(H_2O)_n(Cl)_2\right]_{ads}^{-2} + NH\text{-}H^+ \longrightarrow Fe\left[(H_2O)_n(Cl)_2NH\text{-}H\right]_{ads}^{-} \quad ...(3\text{-}5)$$
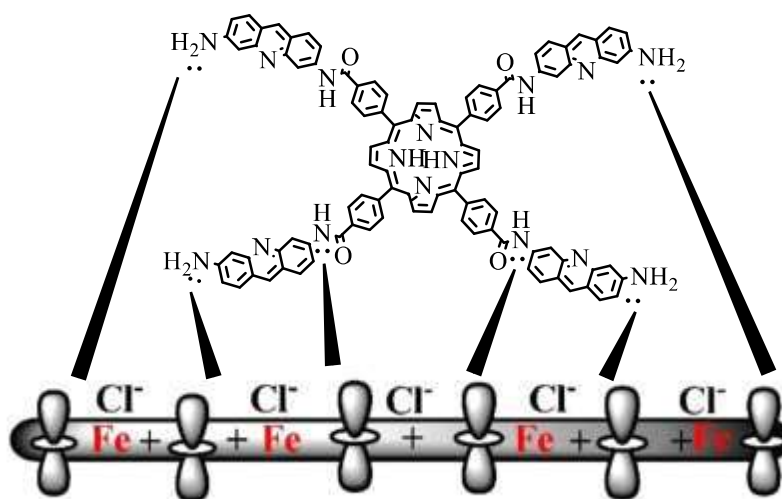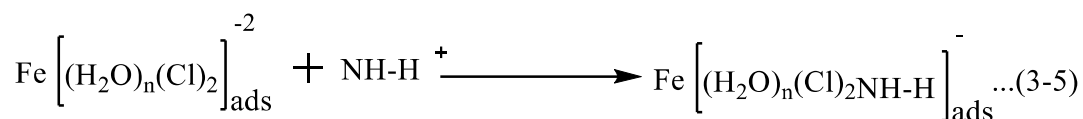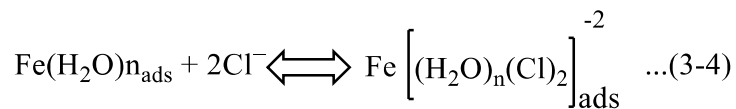
Figure (3-22): Diagrammatic illustration of the adsorptions of organic corrosion inhibitors compound 5c.

3.9 Conclusions

1- Preparation many porphyrin derivatives were successfully performed.

2- Graphene Quantum Dot (GQD) was prepared as a net-layered using hydrothermal method.

3- Cd ferrite nano-rod was prepared using the precipitation method in the presence of CTAB as positive surfactant, this method assisted with solve-thermal method.

4- Composites of graphene quantum dot and Cd ferrite nano-rod were prepared with commercial Titanium dioxide clusters using indirect ultra-sonication waves.

5- Most prepared porphyrin derivatives are used as a sensitizer of solar cells.

6- Most prepared porphyrin derivatives are used as an anti-corrosion.

3.10 Future Works

1. Synthesis of different porphyrin via a condensation reaction with other primary amines which could be used as precursors for the synthesis.

2. Synthesis of new porphyrin derivatives with new substituent groups as a donor and acceptor.

3. Preparation of some porphyrin derivatives with metals like (Co or Ni or Cu) as macro-complexes.

4. Using various types of surfactants can be negative and non-polar during preparing of $CdFe_2O_4$ to controlling on the shape and size of its crystal.

5. Preparation of different metal ferrite nanostructures using other metals such as Co and Cu.

6. Supporting the experimental part with a theoretical study to know the appropriate dyes for application in dye-sensitized solar cells.

7. Application these catalysts as a sensor.

References

References

[1]   K. Kadish, R. Guilard, and K. M. Smith, *The Porphyrin Handbook: Phthalocyanines: Properties and Materials*: Elsevier,vol,7, 2012.

[2]   N. M. Moura, C. J. Monteiro, A. C. Tomé, M. G. P. Neves, and J. A. Cavaleiro, "Synthesis of chlorins and bacteriochlorins from cycloaddition reactions with porphyrins," *Arkivoc*, no. part ii, pp. 0-0, 2022.

[3]   W. Caughey, G. Smythe, D. O'Keeffe, J. Maskasky, and M. Smith, "Heme A of cytochrome c oxicase. Structure and properties: comparisons with hemes B, C, and S and derivatives," *Journal of Biological Chemistry,* vol. 250, no. 19, pp. 7602-7622, 1975.

[4]   V. Luzgina, E. Filippovich, and R. Evstigneeva, "Hematoporphyrin IX," *Pharmaceutical Chemistry Journal,* vol. 11, no. 5, pp. 613-620, 1977.

[5]   J. M. Scott, and A. M. Molloy" ,The discovery of vitamin B12," *Annals of Nutrition and Metabolism,* vol. 61, no. 3, pp. 239-245, 2012.

[6]   K. M. Kadish, K. M. Smith, and R. Guilard, "Handbook of Porphyrin Science (Volumes 21-25)," World Scientific, 2012.

[7]   D. Kusch, and F.-P. Montforts, "Enantioselective synthesis of hematoporphyrin stereoisomers," *Tetrahedron: Asymmetry,* vol. 6, no. 4, pp. 867-870, 1995.

[8]   D. Drabkin, "Philadelphia Oxford Press," *London, England*, 1958.

[9]   W. W. Kalisch, and M. O. Senge, "Facile meso functionalization of porphyrins by nucleophilic substitution with organolithium reagents," *Angewandte Chemie International Edition,* vol. 37, no. 8, pp. 1107-1109, 1998.

[10]   K. Kadish, K. Smith, and R. Guilard, "The Porphyrin Handbook: Inorganic, organometallic and coordination chemistry, vol. 3," Elsevier, 2000.

[11]   M. da GH Vicente, and K. M Smith, "Syntheses and functionalizations of porphyrin macrocycles," *Current organic synthesis,* vol. 11, no. 1, pp. 3-28, 2014.

[12]   F. v. Figueira, and M. Pereira, "P.; Silva ,S.; AS Cavaleiro, J.; PC Tome," *J. Porphyrins and Phthalocyanines Decorated with Dendrimers: Synthesis and Biomedical Applications. Current Organic Synthesis,* vol. 11, pp. 110-126, 2014.

[13]   E. Alves, M. A. Faustino, M. G. Neves, A. Cunha, H. Nadais, and A. Almeida, "Potential applications of porphyrins in photodynamic inactivation beyond the medical scope," *Journal of Photochemistry and Photobiology C: Photochemistry Reviews,* vol. 22, pp. 34-57, 2015.

[14]   H. Lu, and X. P. Zhang, "Catalytic C–H functionalization by metalloporphyrins: recent developments and future directions," *Chemical Society Reviews,* vol. 40, no. 4, pp. 1899-1909, 2011.

[15] E. Vogel, M. Köcher, H. Schmickler, and J. Lex, "Porphycene—a novel porphin isomer," *Angewandte Chemie International Edition in English,* vol. 25, no. 3, pp. 257-259, 1986.

[16] P. J. Chmielewski, L. Latos-Grażyński, K. Rachlewicz, and T. Glowiak, "Tetra-p-tolylporphyrin with an Inverted Pyrrole Ring: A Novel Isomer of Porphyrin," *Angewandte Chemie International Edition in English,* vol. 33, no. 7, pp. 779-781, 1994.

[17] H. Furuta, T. Asano, and T. Ogawa, "" N-Confused Porphyrin": A New Isomer of Tetraphenylporphyrin," *Journal of the American Chemical Society,* vol. 116, no. 2, pp. 767-768, 1994.

[18] E. Pacholska ,L. Latos-Grażyński, L. Szterenberg, and Z. Ciunik, "Pyrrole-inverted isomer of 5, 10, 15, 20-tetraaryl-21-selenaporphyrin," *The Journal of Organic Chemistry,* vol. 65, no. 24, pp. 8188-8196, 2000.

[19] Y. Saegusa, T. Ishizuka, K. Komamura, S. Shimizu, H. Kotani, N. Kobayashi, and T. Kojima, "Ring-fused porphyrins: extension of π-conjugation significantly affects the aromaticity and optical properties of the porphyrin π-systems and the Lewis acidity of the central metal ions," *Physical Chemistry Chemical Physics,* vol. 17, no. 22, pp. 15001-15011, 2015.

[20] R. L. Luck, "A Review of:"Phthalocyanine Materials Synthesis, Structure and Function" By Neil B. McKeown," Taylor & Francis, 1999.

[21] Ö. Bekaroğlu, *Functional phthalocyanine molecular materials*: Springer Science & Business Media, 2010.

[22] A. v. Braun, and J. Tcherniac, "Über die produkte der einwirkung von acetanhydrid auf phthalamid," *Berichte der deutschen chemischen Gesellschaft,* vol. 40, no. 2, pp. 2709-2714, 1907.

[23] R. A. Sheldon, *Metalloporphyrins in catalytic oxidations*: CRC Press, 1994.

[24] J. Merritt, and K. Loening, "Nomenclature of tetrapyrroles," *Pure & Appl. Chem,* vol. 51, pp. 2251-2304, 1979.

[25] S. Okada, and H. Segawa, "Substituent-control exciton in J-aggregates of protonated water-insoluble porphyrins," *Journal of the American Chemical Society,* vol. 125, no. 9, pp. 2792-2796, 2003.

[26] P. J. Brothers, "Boron complexes of porphyrins and related polypyrrole ligands: unexpected chemistry for both boron and the porphyrin," *Chemical communications*, no. 18, pp. 2090-2102, 2008.

[27] D. K. Lavallee, "A Review of:"Coordination Compounds of Porphyrins and Phthalocyanines, BD Berezin, John Wiley & Sons, Chichester, New York, Brisbane, Toronto, 1981; Xiii+ 286 pp, $53.95 (cloth)"," Taylor & Francis, 1982.

[28] T. D. Lash, S. A. Jones, and G. M. Ferrence, "Synthesis and characterization of tetraphenyl-21, 23-dideazaporphyrin: The best evidence yet that porphyrins really are the [18] annulenes of nature,"

Journal of the American Chemical Society, vol. 132, no. 37, pp. 12786-12787, 2010.

[29] P. Zucca, C. M. Neves, M. M. Simões, M. d. G. P. Neves, G. Cocco, and E. Sanjust, "Immobilized lignin peroxidase-like metalloporphyrins as reusable catalysts in oxidative bleaching of industrial dyes ",*Molecules,* vol. 21, no. 7, pp. 964, 2016.

[30] A. Osuka, and S. Saito, "Expanded porphyrins and aromaticity," *Chemical Communications,* vol. 47, no. 15, pp. 4330-4339, 2011.

[31] Y. Zeng, F. Feng, H. Medová, J. Dean, and M. Koblížek, "Functional type 2 photosynthetic reaction centers found in the rare bacterial phylum Gemmatimonadetes," *Proceedings of the National Academy of Sciences,* vol. 111, no. 21, pp. 7795-7800, 2014.

[32] D. A. Bryant, A. M. G. Costas, J. A. Maresca, A. G. M. Chew, C. G. Klatt, M. M .Bateson, L. J. Tallon, J. Hostetler, W. C. Nelson, and J. F. Heidelberg, "Candidatus Chloracidobacterium thermophilum: an aerobic phototrophic acidobacterium," *Science,* vol. 317, no. 5837, pp. 523-526, 2007.

[33] G. de la Torre, C. G. Claessens, and T .Torres, "Phthalocyanines: The need for selective synthetic approaches," *European Journal of Organic Chemistry,* vol. 2000, no. 16, pp. 2821-2830, 2000.

[34] M. L. Embleton, S. P. Nair, W. Heywood, D. C. Menon, B. D. Cookson, and M. Wilson, "Development of a novel targeting system for lethal photosensitization of antibiotic-resistant strains of Staphylococcus aureus," *Antimicrobial agents and chemotherapy,* vol. 49, no. 9, pp. 3690-3696, 2005.

[35] E. X. S. Pinto, and N. Handayani, "Analisis Faktor–Faktor yang Berpengaruh Terhadap Ketepatan Waktu Penyampaian Laporan Keuangan," *Jurnal Ilmu dan Riset Akuntansi (JIRA),* vol. 5, no. 1, 2016.

[36] L. C. Makola, "Photodynamic antimicrobial chemotherapy against Staphylococcus aureus and Escherichia coli sensitized using indium (III) cationic porphyrins linked to core-shell magnetic nanoparticles," Rhodes University, 2020.

[37] P. Rothemund, "Formation of porphyrins from pyrrole and aldehydes," *Journal of the American Chemical Society,* vol. 57, no. 10, pp. 2010-2011.1935 ,

[38] P. Rothemund, and A. R. Menotti, "Porphyrin Studies. IV. 1 The Synthesis of α, β, γ, δ-Tetraphenylporphine," *Journal of the American Chemical Society,* vol. 63, no. 1, pp. 267-270, 1941.

[39] A. D. Adler, F. R. Longo, and W. Shergalis, "Mechanistic investigations of porphyrin syntheses. I. Preliminary studies on ms-tetraphenylporphin," *Journal of the American Chemical Society,* vol. 86, no. 15, pp. 3145-3149, 1964.

[40] A. Adler, F. Longo, J. Finarelli, and J. Goldmacher, "Assour J and Korsakoff L," *J. Org. Chem.,* vol. 1967, pp. 32, 1967.

[41] R. G. Little, J. A. Anton, P. A. Loach, and J. A. Ibers, "The synthesis of some substituted tetraarylporphyrins," *Journal of Heterocyclic Chemistry,* vol. 12, no. 2, pp. 343-349, 1975.

[42] J. S. Lindsey" ,The synthesis of meso-substituted porphyrins," *Metalloporphyrins Catalyzed Oxidations*, pp. 49-86: Springer, 1994.

[43] F. L. Carter, *Molecular electronic devices*: M. Dekker, 1982.

[44] M. Taniguchi, H. Du, and J. S. Lindsey, "Virtual libraries of tetrapyrrole macrocycles. Combinatorics, isomers, product distributions, and data mining," *Journal of chemical information and modeling,* vol. 51, no. 9, pp. 2233-2247, 2011.

[45] J. S. Lindsey, I. C. Schreiman, H. C. Hsu, P. C. Kearney, and A. M. Marguerettaz, "Rothemund and Adler-Longo reactions revisited: synthesis of tetraphenylporphyrins under equilibrium conditions," *The Journal of Organic Chemistry,* vol. 52, no. 5, pp. 827-836, 1987.

[46] G. Nishida, and R. F. Labbe, "Heme biosynthesis on the incorporation of iron into protoporphyrin," *Biochimica et Biophysica Acta,* vol. 31, no. 2, pp. 519-524, 1959.

[47] M. Yaseen, M. Ali, M. NajeebUllah, M. Ali Munawar, and I. Khokhar, "Microwave-assisted synthesis, metallation, and duff formylation of porphyrins," *Journal of Heterocyclic Chemistry,* vol. 46, no. 2, pp. 251-255, 2009.

[48] B. F. Nascimento, M. Pineiro, A. M. d. A. Rocha Gonsalves, M. Ramos Silva, A. Matos Beja, and J. A. Paixão, "Microwave-assisted synthesis of porphyrins and metalloporphyrins: a rapid and efficient synthetic method," *Journal of Porphyrins and Phthalocyanines,* vol. 11, no. 02, pp. 77-84, 2007.

[49] B. F. Nascimento, A. M. d. A. R. Gonsalves, and M. Pineiro, "MnO2 instead of quinones as selective oxidant of tetrapyrrolic macrocycles," *Inorganic Chemistry Communications,* vol. 13, no. 3, pp. 395-398, 2010.

[50] R. Lucas, J. Vergnaud, K. Teste, R. Zerrouki, V. Sol, and P. Krausz, "A facile and rapid iodine-catalyzed meso-tetraphenylporphyrin synthesis using microwave activation," *Tetrahedron Letters,* vol. 49, no. 38, pp. 5537-5539, 2008.

[51] B. Boëns, P.-A. Faugeras, J. Vergnaud, R. Lucas, K. Teste, and R. Zerrouki, "Iodine-catalyzed one-pot synthesis of unsymmetrical meso-substituted porphyrins," *Tetrahedron,* vol. 66, no. 11, pp. 1994-1996 , .2010

[52] Y. Vignaud, R. Granet, and P. Krausz, "An expeditious, solvent-free synthesis of meso-arylporphyrins using activated charcoal as a catalyst," *Journal of Porphyrins and Phthalocyanines,* vol. 10, no. 07, pp. 937-941, 2006.

[53] M. Gouterman, "Spectra of porphyrins," *Journal of Molecular Spectroscopy,* vol. 6, pp. 138-163, 1961.

[54] R. Giovannetti, "The use of spectrophotometry UV-Vis for the study of porphyrins," *Macro to nano spectroscopy*, pp. 87-108, 2012.

[55] R. Yang, K. a. Li, K. Wang, F. Zhao, N. Li, and F. Liu, "Porphyrin assembly on β-cyclodextrin for selective sensing and detection of a zinc ion based on the dual emission fluorescence ratio," *Analytical chemistry,* vol. 75, no. 3, pp. 612-621, 2003.

[56] K. M. Smith, "Development of porphyrin syntheses," *New Journal of Chemistry,* vol. 40, no. 7, pp. 5644-5649, 2016.

[57] U. Noomnarm, and R. M. Clegg, "Fluorescence lifetimes: fundamentals and interpretations," *Photosynthesis research,* vol. 101, pp. 181-194, 2009.

[58] Q. X. Zhou, W. H. Lei ,J. R. Chen, C. Li, Y. J. Hou, X. S. Wang, and B. W. Zhang, "A new heteroleptic ruthenium (II) polypyridyl complex with long-wavelength absorption and high singlet-oxygen quantum yield," *Chemistry–A European Journal,* vol. 16, no. 10, pp. 3157-3165, 2010.

[59] F. Ricchelli, "Photophysical properties of porphyrins in biological membranes," *Journal of Photochemistry and Photobiology B: Biology,* vol. 29, no. 2-3, pp. 109-118, 1995.

[60] K. Lang, P. Kubát, P. Lhoták, J. Mosinger, and D. M. Wagnerová, "Photophysical Properties and Photoinduced Electron Transfer Within Host–Guest Complexes of 5, 10, 15, 20-Tetrakis (4-N-methylpyridyl) porphyrin with Water-soluble Calixarenes and Cyclodextrins¶," *Photochemistry and Photobiology,* vol. 74, no. 4, pp. 558-565, 2001.

[61] Y. Li, "Solvent effects on photophysical properties of copper and zinc porphyrins," *Chinese Science Bulletin,* vol. 53, no. 23, pp. 3615-3619, 2008.

[62] J. Hulla, S. Sahu, and A. Hayes, "Nanotechnology: History and future," *Human & experimental toxicology,* vol. 34, no. 12, pp. 1318-1321, 2015.

[63] I. Khan, K. Saeed, and I. Khan, "Review nanoparticles: properties, applications and toxicities," *Arab J Chem,* vol. 12, no. 2, pp. 908-931, 2019.

[64] A. Gnach, T. Lipinski, A. Bednarkiewicz, J. Rybka, and J. A. Capobianco, "Upconverting nanoparticles: assessing the toxicity," *Chemical Society Reviews,* vol. 44, no. 6, pp. 1561-1584, 2015.

[65] S. Bayda, M. Adeel, T. Tuccinardi, M. Cordani, and F. Rizzolio, "The history of nanoscience and nanotechnology: from chemical–physical applications to nanomedicine," *Molecules,* vol. 25, no. 1, pp. 112, 2019.

[66] R. Aversa, M. H. Modarres, S. Cozzini, R. Ciancio, and A. Chiusole, "The first annotated set of scanning electron microscopy images for nanoscience," *Scientific data,* vol. 5, no. 1, pp. 1-10, 2018.

[67] B.-W. Shiau, C.-H. Lin, Y.-Y. Liao, Y.-R. Lee, S.-H. Liu, W.-C. Ding, and J.-R. Lee, "The characteristics and mechanisms of Au nanoparticles processed by functional centrifugal procedures," *Journal of Physics and Chemistry of Solids,* vol. 116, pp. 161-167, 2018.

[68] P. Pimpang, R. Sumang, and S. Choopun, "Effect of concentration of citric acid on size and optical properties of fluorescence graphene quantum dots prepared by tuning carbonization degree," *Chiang Mai J. Sci,* vol. 45, no. 5, pp. 2005, 2018.

[69] M. Bacon, S. J. Bradley, and T. Nann, "Graphene quantum dots," *Particle & Particle Systems Characterization,* vol. 31, no. 4, pp. 415-428, 2014.

[70] P. Tian, L. Tang, K. Teng, and S. Lau, "Graphene quantum dots from chemistry to applications," *Materials today chemistry,* vol. 10, pp. 221-258, 2018.

[71] H. Sun, L. Wu, W. Wei, and X. Qu, "Recent advances in graphene quantum dots for sensing," *Materials today,* vol. 16, no. 11, pp. 433-442, 2013.

[72] P. K .Ang, W. Chen, A. T. S. Wee, and K. P. Loh, "Solution-gated epitaxial graphene as pH sensor," *Journal of the American Chemical Society,* vol. 130, no. 44, pp. 14392-14393, 2008.

[73] M. Hasanzadeh, A. Karimzadeh, S. Sadeghi, A. Mokhtarzadeh, N. Shadjou, and A. Jouyban, "Graphene quantum dot as an electrically conductive material toward low potential detection: a new platform for interface science," *Journal of Materials Science: Materials in Electronics,* vol. 27, no. 6, pp. 6488-6495, 2016.

[74] P. Das, S. Ganguly, S. Banerjee, and N. C. Das, "Graphene based emergent nanolights: a short review on the synthesis, properties and application," *Research on Chemical Intermediates,* vol. 45, no. 7, pp. 3823-3853, 2019.

[75] C. Wang, Y. Li, Q. Lv, H. Zheng, G. Zhu, X .Xu, and Y. Wang, "Te4+/Bi3+ Co-Doped Double Perovskites with Tunable Dual-Emission for Contactless Light Sensor, Encrypted Information Transmission and White Light Emitting Diodes," *Chemical Engineering Journal,* vol. 431, pp. 134135, 2022.

[76] M. Yu, X .Wei, X. Min, A. Yuan, and J. Xu, "Graphene Quantum Dot Surface Coating for Improving the Electrochemical Performance of Li-Rich Li1. 2Mn0. 54Ni0. 13Co0. 13O2," *Energy & Fuels*, 2022.

[77] M. P. More, P. H. Lohar, A. G. Patil, P. O. Patil, and P. K. Deshmukh, "Controlled synthesis of blue luminescent graphene quantum dots from carbonized citric acid: Assessment of methodology, stability, and fluorescence in an aqueous environment," *Materials Chemistry and Physics,* vol. 220, pp. 11-22, 2018.

[78] W. Kwon ,Y.-H. Kim, C.-L. Lee, M. Lee, H. C. Choi, T.-W. Lee, and S.-W. Rhee, "Electroluminescence from graphene quantum dots prepared by amidative cutting of tattered graphite," *Nano letters,* vol. 14, no. 3, pp. 1306-1311, 2014.

[79] D. Pan, J. Zhang, Z. Li, and M. Wu, "Hydrothermal route for cutting graphene sheets into blue-luminescent graphene quantum dots," *Advanced materials,* vol. 22, no. 6, pp. 734-738, 2010.

[80] W. Gao, "Graphene Oxide Reduct," *Recipes, Spectrosc. Appl,* vol. 61, 2015.

[81] Y. Dong, R. Wang, H. Li, J. Shao, Y. Chi, X. Lin, and G. Chen, "Polyamine-functionalized carbon quantum dots for chemical sensing," *Carbon,* vol. 50, no. 8, pp. 2810-2815, 2012.

[82] J. P. Naik, P. Sutradhar, and M. Saha, "Molecular scale rapid synthesis of graphene quantum dots (GQDs)," *Journal of Nanostructure in Chemistry,* vol. 7, no. 1, pp. 85-89, 2017.

[83] M. V. Davydov, A. N. Osipov, S. Y. Kilin, V. A. Kulchitsky, and B. Stepanov, "Neural Network Structures: Current and Future States, "*Open semantic technologies for designing intelligent systems,* no. 8, pp. 259-265, 2018.

[84] V. Bressi, A. Ferlazzo, D. Iannazzo, and C. Espro, "Graphene quantum dots by eco-friendly green synthesis for electrochemical sensing: Recent advances and future perspectives," *Nanomaterials,* vol. 11, no. 5, pp. 1120, 2021.

[85] O. Vozniuk, T. Tabanelli, N. Tanchoux, J.-M. M. Millet, S. Albonetti, F. Di Renzo, and F. Cavani, "Mixed-oxide catalysts with spinel structure for the valorization of biomass: The chemical-loop reforming of bioethanol," *Catalysts,* vol. 8, no. 8, pp. 332, 2018.

[86] G. Pilania, V. Kocevski, J. A. Valdez, C. R. Kreller, and B. P. Uberuaga, "Prediction of structure and cation ordering in an ordered normal-inverse double spinel," *Communications Materials,* vol ,1 .no. 1, pp. 84, 2020.

[87] O. Silva, and P. Morais, "Investigation of anisotropy in cadmium ferrite-based ionic magnetic fluid using magnetic resonance," *Journal of magnetism and magnetic materials,* vol. 289, pp. 136-138, 2005.

[88] T. Sato, T. Iijima ,M. Seki, and N. Inagaki, "Magnetic properties of ultrafine ferrite particles," *Journal of Magnetism and Magnetic Materials,* vol. 65, no. 2-3, pp. 252-256, 1987.

[89] G. Albanese, A. Deriu, G. Calestani, F. Leccabue, and B. Watts, "Formation of cadmium-containing W-type hexagonal ferrite," *Journal of materials science,* vol. 27, pp. 6146-6150, 1992.

[90] D. Ravinder, S. S. Rao, and P. Shalini, "Room temperature electric properties of cadmium-substituted nickel ferrites," *Materials Letters,* vol. 57, no. 24 ,25-pp. 4040-4042, 2003.

[91]   M. G. Naseri, E. B. Saion, H. A. Ahangar, M. Hashim, and A. H. Shaari, "Simple preparation and characterization of nickel ferrite nanocrystals by a thermal treatment method," *Powder Technology,* vol. 212, no. 1, pp. 80-88, 20.11

[92]   M. Cernea, S.-G. Sandu, C. Galassi, R. Radu, and V. Kuncser, "Magnetic properties of BaxSr1− xFe12O19 (x= 0.05–0.35) ferrites prepared by different methods," *Journal of alloys and compounds,* vol. 561, pp. 121-128, 2013.

[93]   W. Onreabroy, K. Papato, G. Rujijanagul, K. Pengpat, and T. Tunkasiri, "Study of strontium ferrites substituted by lanthanum on the structural and magnetic properties," *Ceramics International,* vol. 38, pp. S415-S419, 2012.

[94]   D.-l. Fang, C.-s. Chen, and A. J. Winnubst, "Preparation and electrical properties of FexCu0. 10Ni0. 66Mn2. 24− xO4 (0≤ x≤ 0.90) NTC ceramics," *Journal of alloys and compounds,* vol. 454, no. 1-2, pp. 286-291, 2008.

[95]   J. L. Arias, M. A. Ruiz, V. Gallardo, and Á. V. Delgado, "Tegafur loading and release properties of magnetite/poly (alkylcyanoacrylate)(core/shell) nanoparticles," *Journal of controlled release,* vol. 125, no. 1, pp. 50-58, 2008.

[96]   D.-L. Zhao, Q. Lv, and Z.-M. Shen, "Fabrication and microwave absorbing properties of Ni–Zn spinel ferrites," *Journal of Alloys and Compounds,* vol. 480, no. 2, pp. 634-638, 2009.

[97]   A. R. Bueno, M. L. Gregori, and M. C. Nobrega, "Microwave-absorbing properties of Ni0. 50–xZn0. 50− xMe2xFe2O4 (Me= Cu, Mn, Mg) ferrite–wax composite in X-band frequencies," *Journal of Magnetism and Magnetic Materials,* vol. 320, no. 6, pp. 864-870, 2008.

[98]   C. Chinnasamy, A. Narayanasamy, N. Ponpandian, R. J. Joseyphus, K. Chattopadhyay, K. Shinoda, B. Jeyadevan, K. Tohji, K. Nakatsuka, and H. Guerault, "Structure and magnetic properties of nanocrystalline ferrimagnetic CdFe2O4 spinel," *Scripta materialia,* vol. 44, no. 8-9, pp. 1411-1415, 2001.

[99]   F. Miao, Z. Deng, X. Lv, G. Gu, S. Wan, X. Fang, Q. Zhang, and S. Yin, "Fundamental properties of CdFe2O4 semiconductor thin film," *Solid state communications,* vol. 150, no. 41-42, pp. 2036-2039, 2010.

[100] W. Shi, X. Liu, T. Zhang, Q. Wang, and L. Zhang, "Magnetic nano-sized cadmium ferrite as an efficient catalyst for the degradation of Congo red in the presence of microwave irradiation," *RSC Advances,* vol. 5, no. 63, pp. 51027-51034, 2015.

[101] A. Lozhkomoev, A. Pervikov, A. Chumaevsky, E. Dvilis, V. Paygin, O. Khasanov, and M. Lerner, "Fabrication of Fe-Cu composites from electroexplosive bimetallic nanoparticles by spark plasma sintering," *Vacuum,* vol. 170, pp. 108980, 2019.

[102] Y. Oh, J. Lee, and M. Lee, "Fabrication of Ag-Au bimetallic nanoparticles by laser-induced dewetting of bilayer films," *Applied Surface Science,* vol. 434, pp. 1293-1299, 2018.

[103] R. M. Abozaid ,Z. Ž. Lazarević, I. Radović, M. Gilić, D. Šević, M. S. Rabasović, and V. Radojević, "Optical properties and fluorescence of quantum dots CdSe/ZnS-PMMA composite films with interface modifications," *Optical Materials,* vol. 92, pp. 405-410, 2019.

[104] A .S. Abdulhameed, A.-T. Mohammad, and A. H. Jawad, "Application of response surface methodology for enhanced synthesis of chitosan tripolyphosphate/TiO2 nanocomposite and adsorption of reactive orange 16 dye," *Journal of Cleaner Production,* vol. 232, pp. 4.2019 ,56-3

[105] H. L. Parker, A. J. Hunt, V. L. Budarin, P. S. Shuttleworth, K. L. Miller, and J. H. Clark, "The importance of being porous: polysaccharide-derived mesoporous materials for use in dye adsorption," *RSC advances,* vol. 2, no. 24, pp. 8992-8.2012 ,997

[106] P. H. C. Camargo, K. G. Satyanarayana, and F. Wypych, "Nanocomposites: synthesis, structure, properties and new application opportunities," *Materials Research,* vol. 12, pp. 1-39, 2009.

[107] K. S. Ahmad, S. N. Naqvi, and S. B. Jaffri, "Systematic review elucidating the generations and classifications of solar cells contributing towards environmental sustainability integration," *Reviews in inorganic chemistry,* vol. 41, no. 1, pp. 21-39, 2021.

[108] M. Tao, "Roadblocks to Terawatt Solar Photovoltaics," *Terawatt Solar Photovoltaics*, pp. 61-79: Springer, 2014.

[109] J. Jean, P. R. Brown, R. L. Jaffe, T. Buonassisi, and V. Bulović, "Pathways for solar photovoltaics," *Energy & Environmental Science,* vol. 8, no. 4, pp. 1200-1219, 2015.

[110] J .M. Gordon, T. Fasquelle, E. Nadal, and A. Vossier, "Providing large-scale electricity demand with photovoltaics and molten-salt storage," *Renewable and Sustainable Energy Reviews,* vol. 135, pp. 110261, 2021.

[111] V. M. Fthenakis, "Life cycle impact analysis of cadmium in CdTe PV production," *Renewable and Sustainable Energy Reviews,* vol. 8, no. 4, pp. 303-334, 2004.

[112] J. Hutchison, N. Kiselev, E. Krinichnaya, A. Krestinin, R. Loutfy, A. Morawsky, V. Muradyan, E. Obraztsova, J. Sloan, and S. Terekhov , "Double-walled carbon nanotubes fabricated by a hydrogen arc discharge method," *Carbon,* vol. 39, no. 5, pp. 761-770, 2001.

[113] H. Huang, H. Kajiura, S. Tsutsui, Y. Murakami, and M. Ata, "High-quality double-walled carbon nanotube super bundles grown in a hydrogen-free atmosphere," *The journal of physical chemistry B,* vol. 107, no. 34, pp. 8794-8798, 2003.

[114] B.-J. Kim, S.-H. Han, and J.-S. Park, "Properties of CNTs coated by PEDOT: PSS films via spin-coating and electrophoretic deposition

methods for flexible transparent electrodes," *Surface and Coatings Technology,* vol. 271, pp. 22-26, 2015.

[115] Z. I. Alferov, V. Andreev, and V. Rumyantsev, "Solar photovoltaics: Trends and prospects," *Semiconductors,* vol. 38, no. 8, pp. 899-908, 2004.

[116] S. William, "Electrons and Holes in Semiconductors with applications to transistor electronics," *D. Van nortrand vompany, inc*, 1950.

[117] O. Shevaleevskiy, "The future of solar photovoltaics: A new challenge for chemical physics," *Pure and Applied Chemistry* ,vol. 80, no. 10, pp. 2079-2089, 2008.

[118] C. Sun, K. Vezzù, G. Pagot, A. Nale, Y. H. Bang, G. Pace, E. Negro, C. Gambaro, L. Meda, and T. A. Zawodzinski, "Elucidation of the interplay between vanadium species and charge-discharge processes in VRFBs by Raman spectroscopy," *Electrochimica Acta,* vol. 318, pp. 913-921, 2019.

[119] M. Alipour, H. Salim, R. A. Stewart, and O. Sahin, "Residential solar photovoltaic adoption behaviour: End-to-end review of theories, methods and approaches," *Renewable Energy,* vol. 170, pp. 471-486, 2021.

[120] R. Sun, D. Deng, J. Guo, Q. Wu, J. Guo, M. Shi, K. Shi, T. Wang, L. Xue, and Z. Wei, "Spontaneous open-circuit voltage gain of fully fabricated organic solar cells caused by elimination of interfacial energy disorder," *Energy & Environmental Science,* vol. 12, no. 8, pp. 2518-2528, 2019.

[121] B. Zaidi, "Introductory chapter: Introduction to photovoltaic effect," *Solar Panels and Photovoltaic Materials*, pp. 1-8, 2018.

[122] A. Nogueira, C. Longo, and M.-A. De Paoli, "Polymers in dye sensitized solar cells: overview and perspectives," *Coordination Chemistry Reviews,* vol. 248, no. 13-14, pp. 1455-1468, 2004.

[123] J. Z. Chen, Y. C. Yan, and K. J. Lin, "Effects of Carbon Nanotubes on Dye-Sensitized Solar Cells," *Journal of the Chinese Chemical Society,* vol. 57, no. 5B, pp. 1180-1184, 2010.

[124] D. M. Chapin, C. S. Fuller, and G. L. Pearson, "A new silicon p-n junction photocell for converting solar radiation into electrical power," *Journal of applied physics,* vol. 25, no. 5 ,pp. 676-677, 1954.

[125] A. Drygała, L. Dobrzański, M. Pawlyta, M. Szindler, M. Prokopiuk vel Prokopowicz, and K. Lukaszkowicz, "Carbon nanotubes counter electrode for dye-sensitized solar cells application," *Archives of Metallurgy and Materials*, no. 2, 2.016

[126] K. I. Jayawardena, L. J. Rozanski, C. A. Mills, M. J. Beliatis, N. A. Nismy, and S. R. P. Silva, "'Inorganics-in-Organics': recent developments and outlook for 4G polymer solar cells," *Nanoscale,* vol. 5, no. 18, pp. 8411-8427, 2013.

[127] J. Gong, J. Liang, and K. Sumathy, "Review on dye-sensitized solar cells (DSSCs): fundamental concepts and novel materials," *Renewable and Sustainable Energy Reviews,* vol. 16, no. 8, pp. 5848-5860, 2012.

[128] J. B. Baxter, and E. S. Aydil, "Nanowire-based dye-sensitized solar cells," *Applied physics letters,* vol. 86, no. 5, pp. 053114, 2005.

[129] A. A. Mohammed, A. S. S. Ahmad, and W. A. Azeez, "Fabrication of dye sensitized solar cell based on titanium dioxide (TiO 2)," *Advances in Materials Physics and Chemistry,* vol. 5, no. 09, pp. 361, 2015.

[130] V. K. Manam, and A. K. Nakkella, "NaNotechNology iN eNergy aNd eNviroNmeNt," *Frontiers In Nanotechnology*, pp. 1.

[131] J.-W. Shiu, Y.-C. Chang, C.-Y. Chan, H.-P. Wu, H.-Y. Hsu, C.-L. Wang, C.-Y. Lin, and E. W-.G. Diau, "Panchromatic co-sensitization of porphyrin-sensitized solar cells to harvest near-infrared light beyond 900 nm," *Journal of Materials Chemistry A,* vol. 3, no. 4, pp. 1417-1420, 2015.

[132] K. Ladomenou, T. Kitsopoulos, G. Sharma, and A. Coutsolelos, "The importance of various anchoring groups attached on porphyrins as potential dyes for DSSC applications," *Rsc Advances,* vol. 4, no. 41, pp. 21379-21404, 2014.

[133] X. Shi, and K. Xu, "Properties of fluorine-doped tin oxide films prepared by an improved sol-gel process," *Materials Science in Semiconductor Processing,* vol. 58, pp. 1-7, 2017.

[134] A. Way, J. Luke, A. D. Evans, Z. Li, J.-S. Kim, J. R. Durrant, H. K. Hin Lee, and W. C. Tsoi, "Fluorine doped tin oxide as an alternative of indium tin oxide for bottom electrode of semi-transparent organic photovoltaic devices," *AIP Advances,* vol. 9, no. 8, pp. 085220, 2019.

[135] T. Markvart, and L. Castaner, "Practical handbook of photovoltaics: fundamentals and applications," *Solar cells,* vol. 5, pp .I1, 2003.

[136] M. K. Nazeeruddin, A. Kay, I. Rodicio, R. Humphry-Baker, E. Müller, P. Liska, N. Vlachopoulos, and M. Grätzel, "Conversion of light to electricity by cis-X2bis (2, 2'-bipyridyl-4, 4'-dicarboxylate) ruthenium (II) charge-transfer sensitizers (X= Cl-, Br-, I-, CN-, and SCN-) on nanocrystalline titanium dioxide electrodes," *Journal of the American Chemical Society,* vol. 115, no. 14, pp. 6382-6390, 1993.

[137] E. Krysiak, A. Wypych-Puszkarz, K. Krysiak, G. Nowaczyk, M. Makrocka-Rydzyk, S. Jurga, and J. Ulanski, "Core–shell system based on titanium dioxide with elevated value of dielectric permittivity: Synthesis and characterization," *Synthetic Metals,* vol. 209, pp. 150-157, 2015.

[138] N. Robertson, "Optimizing dyes for dye-sensitized Solar Cells," *Angewandte Chemie International Edition,* vol. 45, no. 15, pp. 2338-2345, 2006.

[139] M. Grätzel, "Recent advances in sensitized mesoscopic solar cells," *Accounts of chemical research,* vol. 42, no. 11, pp. 1788-1798, 2009.

[140] M. Winter, and R. J .Brodd, "What are batteries, fuel cells, and supercapacitors?," *Chemical reviews,* vol. 104, no. 10, pp. 4245-4270, 2004.

[141] K. E. Jasim, "Dye sensitized solar cells-working principles, challenges and opportunities," *Solar Cells-Dye-Sensitized Devices* ,vol. 8, pp. 172Ā210, 2011.

[142] U. Mehmood, S.-u. Rahman, K. Harrabi, I. A. Hussein, and B. Reddy, "Recent advances in dye sensitized solar cells," *Advances in Materials Science and Engineering,* vol. 2014, 2014.

[143] Z. Yu, N. Vlachopoulos, M. Gorlov, and L. Kloo, "Liquid electrolytes for dye-sensitized solar cells," *Dalton transactions,* vol. 40, no. 40, pp. 10289-10303, 2011.

[144] J. N. de Freitas, A. F. Nogueira, and M.-A. De Paoli, "New insights into dye-sensitized solar cells with polymer electrolytes," *Journal of Materials Chemistry,* vol. 19, no. 30, pp. 5279-5294, 2009.

[145] K. Rokesh, A. Pandikumar, and K. Jothivenkatachalam, "Dye sensitized solar cell: a summary." In: *Materials Science Forum*. Trans Tech Publications Ltd, p. 1-24. 2014.

[146] A. N. B. Zulkifili, T. Kento, M. Daiki, and A. Fujiki, "The basic research on the dye-sensitized solar cells (DSSC)," *Journal of Clean Energy Technologies,* vol. 3, no. 5, pp. 382-387, 2015.

[147] S. Thomas, T. Deepak, G. Anjusree, T. Arun, S. V. Nair, and A. S. Nair, "A review on counter electrode materials in dye-sensitized solar cells," *Journal of Materials Chemistry A,* vol. 2, no. 13, pp. 4474-4490, 2014.

[148] G. Jerkiewicz, "Applicability of Platinum as a Counter-Electrode Material in Electrocatalysis Research," *ACS Catalysis,* vol. 12, no. 4, pp. 2661-2670, 2022.

[149] N. Shahzad, T. Perveen, D. Pugliese, S. Haq, N. Fatima, S. M. Salman, A. Tagliaferro, and M. I. Shahzad, "Counter electrode materials based on carbon nanotubes for dye-sensitized solar cells," *Renewable and Sustainable Energy Reviews,* vol. 159, pp.2022 ,112196 .

[150] A. Subramanian, C.-Y. Ho, and H. Wang, "Investigation of various photoanode structures on dye-sensitized solar cell performance using mixed-phase TiO_2," *Journal of alloys and compounds,* vol. 572, pp. 11-16, 2013.

[151] A. Shah, G. Saha, and M. Mahato, "Parameters Involved in CVD Growth of CNT: A Review," *Tailored Functional Materials*. *Select Proceedings of MMETFP 2021*, pp. 185-198, 2022.

[152] M. Salman Naeem, "Synthesis and Characterization of Molybdenum Disulfide and Lignocellulose Fibre-based Composites for Working

Electrode in Dye Sensitized Solar Cell," Physics COMSATS University Islamabad Lahore Campus, 2022.

[153] S. S. Cell, "A Numerical Model and a Code Development for Photogeneration Rate Calculation for a Dye Sensitized Solar Cell". In: *2022 IEEE 16th International Symposium on Applied Computational Intelligence and Informatics (SACI)*. IEEE, p. 000341-000346. 2022

[154] L. Chen, Y. Zhou, W .Tu, Z. Li, C. Bao, H. Dai, T. Yu, J. Liu, and Z. Zou, "Enhanced photovoltaic performance of a dye-sensitized solar cell using graphene–TiO$_2$ photoanode prepared by a novel in situ simultaneous reduction-hydrolysis technique," *Nanoscale,* vol. 5, no. 8, pp. 3481-3485, 2013.

[155] B. O'Sullivan, S. O'Sullivan, T. Narayan, H. Shao, B. Patella, I. Seymour, R. Inguanta, and A. O'Riordan, "A direct comparison of 2D versus 3D diffusion analysis at nanowire electrodes: A finite element analysis and experimental study," *Electrochimica Acta,* vol. 408, pp. 139890, 2022.

[156] H.-H. Wang, C. Su, C.-Y. Wu, H.-B. Tsai, C.-Y. Li, and W.-R. Li, "Preparation of composite light-scattering layer for dye sensitized solar cells," *Thin Solid Films,* vol. 529, pp. 15-18, 2013.

[157] B.-K. Koo, D.-Y. Lee, H.-J. Kim, W.-J. Lee, J.-S. Song, and H.-J. Kim, "Seasoning effect of dye-sensitized solar cells with different counter electrodes," *Journal of Electroceramics,* vol. 17, no. 1, pp. 79-82, 2006.

[158] Y. Fang, P. Ma, H. Cheng, G .Tan, J. Wu, J. Zheng, X. Zhou, S. Fang, Y. Dai, and Y. Lin, "Synthesis of Low-Viscosity Ionic Liquids for Application in Dye-Sensitized Solar Cells," *Chemistry–An Asian Journal,* vol. 14, no. 23, pp. 4201-4206, 2019.

[159] D. Rangel, J. C. Gallegos, S. Vargas, F. García, and R. Rodríguez, "Optimized dye-sensitized solar cells: A comparative study with different dyes, mordants and construction parameters," *Results in Physics,* vol. 12, pp. 2026-2037, 2019.

[160] E. T. Hashim, and A. A. Abbood, "Temperature Effect on Power Drop of Different Photovoltaic Modules," *Journal of Engineering,* vol. 22, no. 5, pp. 129-143, 2016.

[161] K. Ansari, M. Quraishi, and A. Singh, "Schiff's base of pyridyl substituted triazoles as new and effective corrosion inhibitors for mild steel in hydrochloric acid solution," *Corrosion science,* vol. 79, pp. 5-15, 2014.

[162] J. Arjomandi, H. Moghanni-Bavil-Olyaei, M. H. Parvin, J. Y. Lee, K. C. Ko, M. Joshaghani, and K. Hamidian, "Inhibition of corrosion of aluminum in alkaline solution by a novel azo-schiff base: Experiment and theory," *Journal of Alloys and Compounds,* vol. 746, pp. 185-193, 2018.

[163] P. Atkins, "De Paula J. Keeler J.:'Atkins' physical chemistry'," Oxford University Press, Oxford, England, UK, 2018.

[164] J. Aljourani, M. Golozar, and K. Raeissi, "The inhibition of carbon steel corrosion in hydrochloric and sulfuric acid media using some benzimidazole derivatives," *Materials chemistry and physics,* vol. 121, no. 1-2, pp. 320-325, 2010.

[165] A. Fouda, H. Megahed, N .Fouad, and N. Elbahrawi, "Corrosion inhibition of carbon steel in 1 M hydrochloric acid solution by aqueous extract of Thevetia peruviana," *Journal of Bio-and Tribo-Corrosion,* vol. 2, pp. 1-13, 2016.

[166] G. Badr, "The role of some thiosemicarbazide derivatives as corrosion inhibitors for C-steel in acidic media," *Corrosion Science,* vol. 51, no. 11, pp. 2529-2536, 2009.

[167] D. Dwivedi, K. Lepková, and T. Becker, "Carbon steel corrosion: a review of key surface properties and characterization methods ",*RSC advances,* vol. 7, no. 8, pp. 4580-4610, 2017.

[168] J. Aljourani, K. Raeissi, and M. Golozar, "Benzimidazole and its derivatives as corrosion inhibitors for mild steel in 1M HCl solution," *Corrosion science,* vol. 51, no. 8, pp. 1836-1843, 2009.

[169] K. Zhang, B. Xu, W. Yang, X. Yin, Y. Liu, and Y. Chen, "Halogen-substituted imidazoline derivatives as corrosion inhibitors for mild steel in hydrochloric acid solution," *Corrosion Science,* vol. 90, pp. 284-295, 2015.

[170] L. T. Popoola, A. S. Grema, G .K. Latinwo, B. Gutti, and A. S. Balogun, "Corrosion problems during oil and gas production and its mitigation," *International Journal of Industrial Chemistry,* vol. 4, pp. 1-15, 2013.

[171] I. B. Onyeachu, M. M. Solomon, S. A. Umoren, I. B. Obot, and A. A . Sorour, "Corrosion inhibition effect of a benzimidazole derivative on heat exchanger tubing materials during acid cleaning of multistage flash desalination plants," *Desalination,* vol. 479, pp. 114283, 2020.

[172] S. S. Al-Najjar, and A. Y. Al-Baitai, "Synthesized of Novel Imidazole-derived Schiff Base as a Corrosion Inhibitor of Carbon Steel in Acidic Medium Supported by Electrochemical and DFT Studies," *Physical Chemistry Research,* vol. 10, no. 2, pp. 179-194, 2022.

[173] R. G. M. de Araújo Macedo, N .do Nascimento Marques, J. Tonholo, and R. de Carvalho Balaban, "Water-soluble carboxymethylchitosan used as corrosion inhibitor for carbon steel in saline medium," *Carbohydrate polymers,* vol. 205, pp. 371-376, 2019.

[174] W. Wei, S. Geng, D. Xie, and F. Wang, "High temperature oxidation and corrosion behaviours of Ni–Fe–Cr alloys as inert anode for aluminum electrolysis," *Corrosion Science,* vol. 157, pp. 382-391, 2019.

[175] A. O. Ijaola, P. K. Farayibi, and E. Asmatulu, "Superhydrophobic coatings for steel pipeline protection in oil and gas industries: A

comprehensive review," *Journal of Natural Gas Science and Engineering,* vol. 83, pp. 103544, 2020.

[176] A. C. Fonseca, I. M. Lopes, J. F. Coelho, and A. C. Serra, "Synthesis of unsaturated polyesters based on renewable monomers: Structure/properties relationship and crosslinking with 2-hydroxyethyl methacrylate," *Reactive and Functional Polymers,* vol. 97, pp. 1-11, 2015.

[177] K. R. Ansari, D. S. Chauhan, A. Singh, V. S. Saji, and M. A. Quraishi, "Corrosion inhibitors for acidizing process in oil and gas sectors," *Corrosion Inhibitors in the Oil and gas Industry*, pp. 151-176, 2020.

[178] M. Migahed, M. El-Rabiei, H. Nady, H. Gomaa, and E. Zaki, "Corrosion inhibition behavior of synthesized imidazolium ionic liquids for carbon steel in deep oil wells formation water," *Journal of Bio-and Tribo-Corrosion,* vol. 3, pp. 1-20, 2017.

[179] I. Ahamad, R. Prasad, and M. Quraishi, "Thermodynamic, electrochemical and quantum chemical investigation of some Schiff bases as corrosion inhibitors for mild steel in hydrochloric acid solutions," *Corrosion Science,* vol. 52, no. 3, pp. 933-942, 2010.

[180] M. E. Mashuga, L. O. Olasunkanmi, A. S. Adekunle, S. Yesudass, M. M. Kabanda, and E. E. Ebenso, "Adsorption, thermodynamic and quantum chemical studies of 1-hexyl-3-methylimidazolium based ionic liquids as corrosion inhibitors for mild steel in HCl," *Materials,* vol. 8, no. 6, pp. 3607-3632, 2015.

[181] F. R. Longo, *Porphyrins as Corrosion Inhibitors*, DREXEL UNIV PHILADELPHIA PA DEPT OF CHEMISTRY, 1984.

[182] K. S. Lokesh, M. D. Keersmaecker, and A. Adriaens, "Self assembled films of porphyrins with amine groups at different positions: Influence of their orientation on the corrosion inhibition and the electrocatalytic activity," *Molecules,* vol. 17, no. 7, pp. 7824-7842, 2012.

[183] M. Biesaga, K. Pyrzyńska, and M. Trojanowicz, "Porphyrins in analytical chemistry. A review," *Talanta,* vol. 51, no. 2, pp. 209-224, 2000.

[184] J. Xiao, and M. E. Meyerhoff, "Retention behavior of amino acids and peptides on protoporphyrin-silica stationary phases with varying metal ion centers," *Analytical chemistry,* vol. 68, no. 17, pp. 2818-2825, 1996.

[185] Z. Guan, H. Li, Z. Wei, N. Shan, Y. Fang, Y. Zhao, L. Fu, Z. Huang, M. G. Humphrey, and C. Zhang, "Enhanced nonlinear optical performance of perovskite films passivated by porphyrin derivatives," *Journal of Materials Chemistry C,* vol. 11, no. 4, pp. 1509-1521, 2023.

[186] S. Hettiarachchi, Y. Chan, R. Wilson Jr, and V. Agarwala, "Macrocyclic corrosion inhibitors for steel in acid chloride environments," *Corrosion,* vol. 45, no. 1, pp. 30-34, 1989.

[187] S. L. d. A. Maranhão, I. C. Guedes, F. J. Anaissi, H. E. Toma, and I. V. Aoki, "Electrochemical and corrosion studies of poly (nickel-tetraaminophthalocyanine) on carbon steel," *Electrochimica Acta,* vol. 52, no. 2, pp. 519-526, 2006.

[188] K. S. Lokesh, M. De Keersmaecker, A. Elia, D. Depla, P. Dubruel, P. Vandenabeele, S. Van Vlierberghe, and A. Adriaens, "Adsorption of cobalt (II) 5, 10, 1-20 ,5tetrakis (2-aminophenyl)-porphyrin onto copper substrates: Characterization and impedance studies for corrosion inhibition," *Corrosion science,* vol. 62, pp. 73-82, 2012.

[189] I. Benmahammed, T. Douadi, S. Issaadi, M. Al-Noaimi, and S. Chafaa, "Heterocyclic Schiff bases as corrosion inhibitors for carbon steel in 1 M HCl solution: hydrodynamic and synergetic effect," *Journal of Dispersion Science and Technology*, 2019.

[190] I. Fratilescu, A. Lascu, B. O. Taranu, C. Epuran, M. Birdeanu, A.-M. Macsim ,E. Tanasa, E. Vasile, and E. Fagadar-Cosma, "One A3B porphyrin structure Three successful applications," *Nanomaterials,* vol. 12, no. 11, pp. 1930, 2022.

[191] G. K. Jayaprakash, B. K. Swamy, S. Rajendrachari, S. Sharma, and R. Flores-Moreno, "Dual descriptor analysis of cetylpyridinium modified carbon paste electrodes for ascorbic acid sensing applications," *Journal of Molecular liquids,* vol. 334, pp. 116348, 2021.

[192] A. Wolfram, Q. Tariq, C. C. Fernández, M. Muth, M. Gurrath, D. Wechsler, M. Franke ,F. J. Williams, H.-P. Steinrück, and B. Meyer, "Adsorption energies of porphyrins on MgO (100): An experimental benchmark for dispersion-corrected density-functional theory," *Surface Science,* vol. 717, pp. 121979, 2022.

[193] A. Singh, Y. Lin, M. A. Quraishi, L. O. Olasunkanmi, O. E. Fayemi, Y. Sasikumar, B. Ramaganthan, I. Bahadur, I. B. Obot, and A. S. Adekunle, "Porphyrins as corrosion inhibitors for N80 steel in 3.5% NaCl solution: electrochemical, quantum chemical, QSAR and Monte Carlo simulations studies," *Molecules,* vol. 20, no. 8, pp. 15122-15146, 2015.

[194] M. T. Jaafar, L. M. Ahmed, and R. T. Haiwal, "Synthesis of Novel Porphyrin Derivatives and Investigate their Application in Sensitized Solar Cells," *Iraqi Journal of Chemical and Petroleum Engineering,* vol. 24, no. 2, pp. 113-122, 2023.

[195] A. Leggio, E. Belsito, G. De Luca, M. L. Di Gioia, V. Leotta, E. Romio, C. Siciliano, and A. Liguori, "One-pot synthesis of amides from carboxylic acids activated using thionyl chloride," *Rsc Advances,* vol. 6, no. 41, pp. 34468-34475, 2016.

[196] D. Li, P. Li, Z. Jiang, and L. Guo, "Enhanced Tumor Targeting and Photocytotoxicity of Folate–Poly (ethylene glycol)–Chlorin Photo sensitizer Mediated by Folate Receptor," *Chemistry letters,* vol. 42, no. 2, pp. 1.2013 ,131-30

[197] W. Chen, D. Li, L. Tian, W. Xiang, T. Wang, W. Hu, Y. Hu, S. Chen, J. Chen, and Z. Dai, "Synthesis of graphene quantum dots from natural polymer starch for cell imaging," *Green Chemistry,* vol. 20, no. 19, pp. 4438-4442, 2018.

[198] S .Jassim, A. Abbas, M. AL-Shakban, and L. Ahmed, "Chemical Vapour Deposition of CdS Thin Films at Low Temperatures from Cadmium Ethyl Xanthate," *Egyptian Journal of Chemistry,* vol. 64, no. 5, pp. 2533-2538, 2021.

[199] L. M. Ahmed, I. Ivanova, F. H. Hussein ,and D. W. Bahnemann, "Role of platinum deposited on TiO_2 in photocatalytic methanol oxidation and dehydrogenation reactions," *International Journal of Photoenergy,* vol. 2014, 2014.

[200] R. K. Mohammad, and A. Elttayef, "Structural properties of Ag-CuO thin films on silicon prepared via DC magnetron sputtering," *Egyptian Journal of Chemistry,* vol. 65, no. 4, pp. 685-691, 2022.

[201] D. C. Ghosh, and R. Biswas, "Theoretical calculation of absolute radii of atoms and ions. Part2. The ionic radii," *International Journal of Molecular Sciences,* vol. 4, no. 6, pp. 379-407, 2003.

[202] L. M. Ahmed, A. F. Alkaim, A. F. Halbus, and F. H. Hussein, "Photocatalytic hydrogen production from aqueous methanol solution over metallized TiO_2," *Int. J. ChemTech Res,* vol ,9 .no. 10, pp. 90-98, 2016.

[203] L. M. Ahmed, F. H. Hussein, and A. A. Mahdi, "Photocatalytic dehydrogenation of aqueous methanol solution by naked and platinized TiO_2 nanoparticles," *Asian Journal of Chemistry,* vol. 24, no. 12, pp. 5564, 2012.

[204] H .Kadhim, L. Ahmed, and M. AL-Hachamii, "Facile Synthesis of Spinel $CoCr_2O_4$ and Its Nanocomposite with ZrO_2: Employing in Photo-catalytic Decolorization of Fe(II)-(luminol-Tyrosine) Complex," *Egyptian Journal of Chemistry,* vol. 65, no. 1, pp. 481-488, 202.2

[205] H. M. Mohammad, S. I. Saeed, and L. M. Ahmed, "Broccoli–like Iron Oxide Nanoparticles Synthesis in Presence of Surfactants and Using Them in the Removal of Water-Colored Contamination," *Journal of Nanostructures,* vol. 12, no. 4, pp. 1034-1048, 20.22

[206] T. M. Jawad, and L. M. Ahmed, "Direct Ultrasonic Synthesis oF WO_3/TiO_2 Nanocomposites and Applying Them in the Photodecolorization of Eosin Yellow Dye," *Periódico Tchê Química,* vol. 17, no. 34, 2020.

[207] M. K. Hayawi, M. M. Kareem, And L. M .Ahmed, "Synthesis Of Spinel Mn_3O_4 and Spinel Mn_3O_4/ZrO_2 Nanocomposites AND Using Them in Photo-Catalytic Decolorization oF Fe(II)-(4,5-Diazafluoren-9-ONE 11) Complex," *Periódico Tchê Química,* vol. 17, no. 34, 2020.

[208] S. M. Abdalhadi, A. Y. Al-Baitai, and H. A. Al-Zubaidi, "Synthesis and characterization of 2, 3-diaminomaleonitrile derivatives by one-pot schiff base reaction and their application in dye synthesized Solar cells," *Indonesian Journal of Chemistry,* vol. 21, no. 2, pp. 443-451, 20.20

[209] N. Chander, and V. K. Komarala, "Fabrication and characterization of dye sensitized solar cells: A photographic guide," 2017.

[210] E. McCafferty, "Validation of corrosion rates measured by the Tafel extrapolation method," *Corrosion science,* vol ,47 .no. 12, pp. 3202-3215, 2005.

[211] M. Deyab, G. Mele, A. Al-Sabagh, E. Bloise, D. Lomonaco, S. E. Mazzetto, and C. D. Clemente, "Synthesis and characteristics of alkyd resin/M-Porphyrins nanocomposite for corrosion protection application," *Progress in Organic Coatings,* vol. 105, pp. 286-290, 2017.

[212] W. Yang, Q. Wang, K. Xu, Y. Yin, H. Bao, X. Li, L. Niu, and S. Chen, "Enhanced corrosion resistance of carbon steel in hydrochloric acid solution by Eriobotrya japonica Thunb. leaf extract: Electrochemical study," *Materials,* vol. 10, no. 8, pp. 956, 2017.

[213] A. A. Fadda, R. E. El-Mekawy, A. El-Shafei, H. S. Freeman, D. Hinks, and M. El-Fedawy, "Design, synthesis, and pharmacological screening of novel porphyrin derivatives," *Journal of Chemistry* ,vol. 2013, 2013.

[214] S. Ali, M. Ali, and L. Ahmed, "Hybrid Phosphotungstic acid-Dopamine (PTA-DA) Like-flower Nanostructure Synthesis as a Furosemide Drug Delivery System and Kinetic Study of Drug Releasing," *Egyptian Journal of Chemistry,* vol. 64, no ,10 .pp. 5547-5553, 2021.

[215] E. N. Alkhafaji, N. A. Oda, and L. M. Ahmed, "Characterization of silver nanohybrid with layers double hydroxide and demonstration inhibition of antibiotic-resistance Staphylococcus aureus," *Egyptian Journal of Chemistry,* vol. 65, no. 6, pp. 1-2, 2022.

[216] S. M. H. Ali, M. M. M. A. Alali, and L. M. Ahmed, "Flower-like hierarchical nanostructures synthesis of polyoxometalate-dopamine and loading furosemide on its surface and aging them using microwave technique." p. 040010.

[217] A. Obaid, and L. Ahmed, "One-step hydrothermal synthesis of α-MoO3 nano-belts with ultrasonic assist for incorporating TiO_2 as a nano composite," *Egyptian Journal of Chemistry,* vol. 64, no. 10, pp. 5725-5734, 2021.

[218] A. Kaniyoor, and S. Ramaprabhu, "A Raman spectroscopic investigation of graphite oxide derived graphene," *Aip Advances,* vol. 2, no. 3, 2012.

[219] M. J. Deka, A. Dutta, and D. Chowdhury, "Tuning the wettability and photoluminescence of graphene quantum dots via covalent modification ",*New Journal of Chemistry,* vol. 42, no. 1, pp. 355-362, 2018.

[220] S. T. Fardood, R. Forootan, F. Moradnia, Z. Afshari, and A. Ramazani, "Green synthesis, characterization, and photocatalytic activity of cobalt chromite spinel nanoparticles," *Materials Research Express,* vol. 7, no. 1, p. 015086, 2020.

[221] S. Sharifi, A. Yazdani, and K. Rahimi, "Incremental substitution of Ni with Mn in NiFe2O4 to largely enhance its supercapacitance properties," *Scientific reports,* vol. 10, no. 1, pp. 10916, 2020.

[222] P. F. Lim, K. H. Leong, L. C. Sim, A. Abd Aziz, and P. Saravanan, "Amalgamation of N-graphene quantum dots with nanocubic like TiO 2: an insight study of sunlight sensitive photocatalysis," *Environmental Science and Pollution Research,* vol. 26, pp. 3.2019 ,3464-455

[223] J. Jitputti, Y. Suzuki, and S. Yoshikawa, "Synthesis of TiO_2 nanowires and their photocatalytic activity for hydrogen evolution," *Catalysis Communications,* vol. 9, no. 6, pp. 1265-1271, 2008.

[224] B. K. Gupta, G. Kedawat, Y. Agrawal ,P. Kumar, J. Dwivedi, and S. Dhawan, "A novel strategy to enhance ultraviolet light driven photocatalysis from graphene quantum dots infilled TiO_2 nanotube arrays," *RSC Advances,* vol. 5, no. 14, pp. 10623-10631, 2015.

[225] G. Singh, I. Kapoor, R. Dubey, and P. Srivastava, "Preparation, characterization and catalytic behavior of $CdFe_2O_4$ and Cd nanocrystals on AP, HTPB and composite solid propellants, Part: 79," *Thermo chimica Acta,* vol. 511, no. 1-2, pp. 112-118, 2010.

[226] A. El Nahrawy, A. Soliman, E .Sakr, and H. El Attar, "sodium-cobalt ferrite nanostructure study: sol-gel synthesis, characterization, and magnetic properties," *Journal of Ovonic Research,* vol. 14, no. 3, 2018.

[227] M. Naseri, "Optical and magnetic properties of monophasic cadmium ferrite (CdFe2O4) nanostructure prepared by thermal treatment method," *Journal of magnetism and magnetic materials,* vol. 392, pp. 107-113, 2015.

[228] S. Sagadevan, K. Pal, Z. Z. Chowdhury, and M. E. Hoque, "Structural, optical and dielectric investigation of CdFe2O4 nanoparticles," *Materials Research Express,* vol. 4, no. 7, pp. 075025, 2017.

[229] R. Anusa, C. Ravichandran, T. Rajendran, M. Arularasu, and E. Sivakumar, "comparative investigation of cobalt ferrite (cofe 2 o 4) and cadmium ferrite (cdfe 2 o (4 nanoparticles for the structural, optical properties and antibacterial activity," *Digest Journal of Nanomaterials & Biostructures (DJNB),* vol. 14, no. 2, 2019.

[230] R. B. Jimaa, Z. H. Mahmoud, and F. K. Ali, "Evaluation the efficiency of $CuFe_2O_4$ prepared photolysis by OSD and photo degradation," *Entomol. Appl. Sci. Lett,* vol. 5, no. 2, p. 91-100, 2018.

[231] H. Kaur, J. Singh, and B. Randhawa, "Essence of superparamagnetism in cadmium ferrite induced by various organic fuels via novel solution

combustion method," *Ceramics International,* vol. 40, no. 8, pp. 12235-12243, 2014.

[232] M. Cross, and W. Varhue, "Radiative melting of crystalline ruthenium oxide nanorods," *Nanotechnology,* vol. 19, no. 43, pp. 435705, 2008.

[233] M. A. Golsefidi, "Influence of the surfactant, capping agent and reductant agent on the morphology and size of $CdFe_2O_4$ nanoparticles," *Journal of Materials Science: Materials in Electronics,* vol. 28, pp. 6345-6351, 2017.

[234] S. Umale, V. Sudhakar, S. M. Sontakke, K. Krishnamoorthy, and A. B. Pandit, "Improved efficiency of DSSC using combustion synthesized TiO2," *Materials Research Bulletin,* vol. 109, pp. 222-226, 2019.

[235] S.-L. Chung, and C.-M. Wang, "Solution combustion synthesis of TiO2 and its use for fabrication of photoelectrode for dye-sensitized solar cell," *Journal of Materials Science & Technology,* vol. 28, no. 8, pp. 713-722, 2012.

[236] H. Deepa, G. Madhu, and B. K. Swamy, "Evaluation of performance characteristics of nano TiO2 and TiO_2-ZnO composite for DSSC applications and electrochemical determination of potassium ferrocyanide using cyclic voltammetry," *Materials Research Express,* vol. 8, no. 12, pp. 125004, 2021.

[237] A. Bakhshayesh, M. Mohammadi, H. Dadar, and D. Fray, "Improved efficiency of dye-sensitized solar cells aided by corn-like TiO_2 nanowires as the light scattering layer," *Electrochimica Acta,* vol. 90, pp. 302-308, 2013.

[238] D. Darwis, "Dye Sensitized Solar Cells Fabricated Using Natural Dyes from Traditional Indonesian Plant as Sanitizers," *Natural Science: Journal of Science and Technology,* vol. 9, no. 3, pp. 63-66, 2020.

[239] D. K. Verma, E. E. Ebenso, M. Quraishi, and C. Verma, "Gravimetric, electrochemical surface and density functional theory study of acetohydroxamic and benzohydroxamic acids as corrosion inhibitors for copper in 1 M HCl," *Results in Physics,* vol. 13, pp. 102194, 2019.

[240] O. Dagdag, A. El Harfi, O. Cherkaoui, Z. Safi, N. Wazzan, L. Guo, E. Akpan, C. Verma, E. Ebenso, and R. T. Jalgham, "Rheological, electrochemical ,surface, DFT and molecular dynamics simulation studies on the anticorrosive properties of new epoxy monomer compound for steel in 1 M HCl solution," *RSC advances,* vol. 9, no. 8, pp. 4454-4462, 2019.

[241] P. R. Roberge, *Handbook of corrosion engineering* :Mcgraw-hill New York, 2000.

[242] P. D. Desai, C. B. Pawar, M. S. Avhad, and A. P. More, "Corrosion inhibitors for carbon steel: A review," *Vietnam Journal of Chemistry,* vol. 61, no. 1, pp. 15-42, 2023.

[243] A. Lgamri, H. Abou El Makarim, A. Guenbour, A .B. Bachir, L. Aries, and S. El Hajjaji, "Electrochemical study of the corrosion behaviour of iron in presence of new inhibitor in 1 M HCl," *Progress in organic coatings,* vol. 48, no. 1, pp. 63-70, 2003.

[244] M. Vinutha, and T. Venkatesha, "Review on mechanistic action of inhibitors on steel corrosion in acidic media," *Portugaliae Electrochimica Acta,* vol. 34, no. 3, pp. 157-184, 2016.

[245] H. F. Alesary, H. K. Ismail, N. M. Shiltagh, R. A. Alattar, L. M. Ahmed, M. J. Watkins, and K. S. Ryder, "Effects of additives on the electrodeposition of ZnSn alloys from choline chloride/ethylene glycol-based deep eutectic solvent," *Journal of Electroanalytical Chemistry,* vol. 874, pp. 114517, 2020.

[246] G. Elewady, "Pyrimidine derivatives as corrosion inhibitors for carbon-steel in 2M hydrochloric acid solution," *International Journal of Electrochemical Science,* vol. 3, no. 10, pp. 1149-1161, 2008.

[247] S. Muralidharan, M. Quraishi, and S. Iyer, "The effect of molecular structure on hydrogen permeation and the corrosion inhibition of mild steel in acidic solutions," *Corrosion Science,* vol. 37, no. 11, pp. 1739-1750, 1995.

[248] C. Verma, H. Lgaz, D. Verma, E. E. Ebenso, I. Bahadur, and M. Quraishi, "Molecular dynamics and Monte Carlo simulations as powerful tools for study of interfacial adsorption behavior of corrosion inhibitors in aqueous phase: a review," *Journal of Molecular Liquids,* vol. 260, pp. 99-120, 2018.

[249] L. Chen, D. Lu, and Y. Zhang, "Organic compounds as corrosion inhibitors for carbon steel in HCl solution: a comprehensive review," *Materials,* vol. 15, no. 6, pp. 2023, 2022.

Appendix

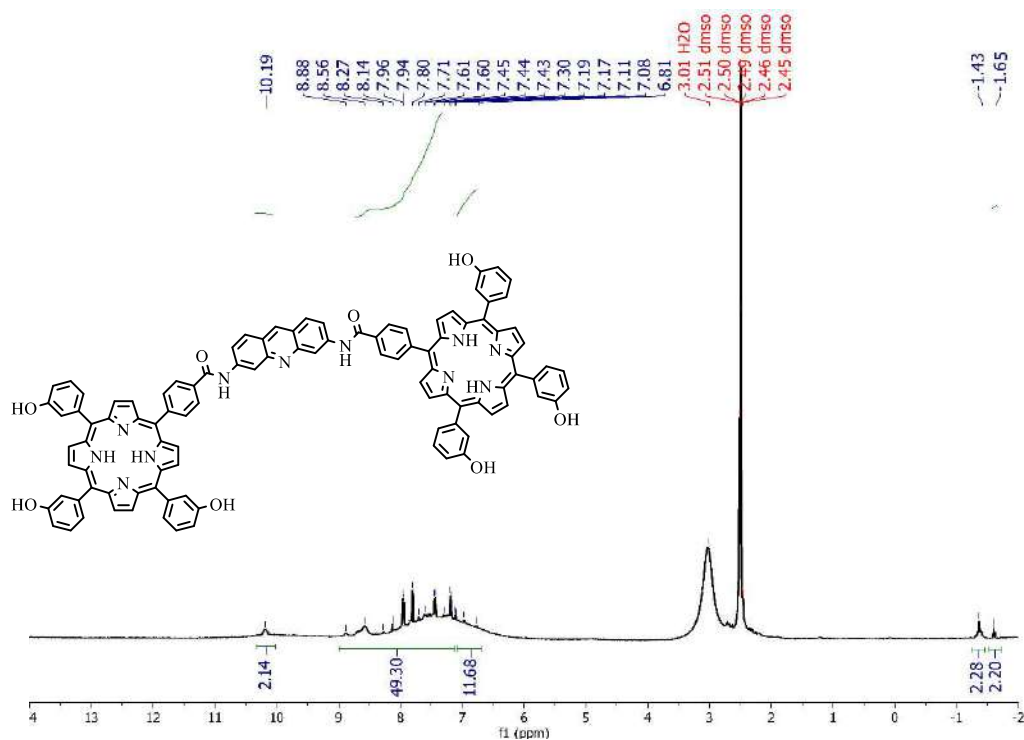**Figure 1:** FT-IR spectrum of compound (3)

Figure 2: ^{1}HNMR spectrum of compound (3)
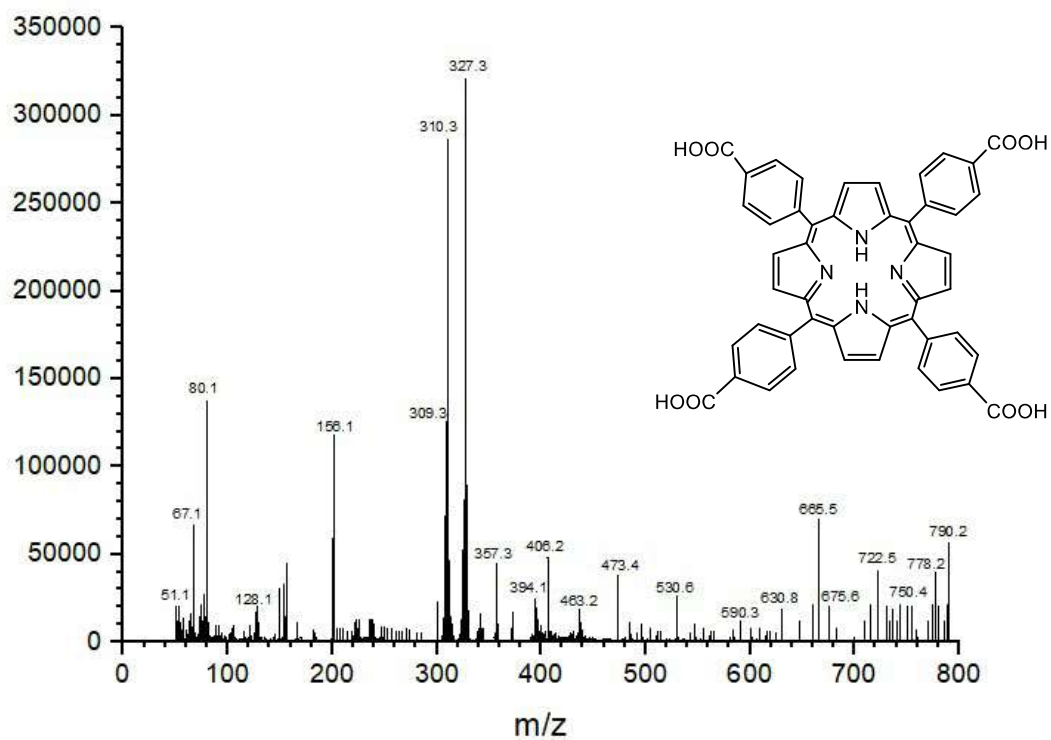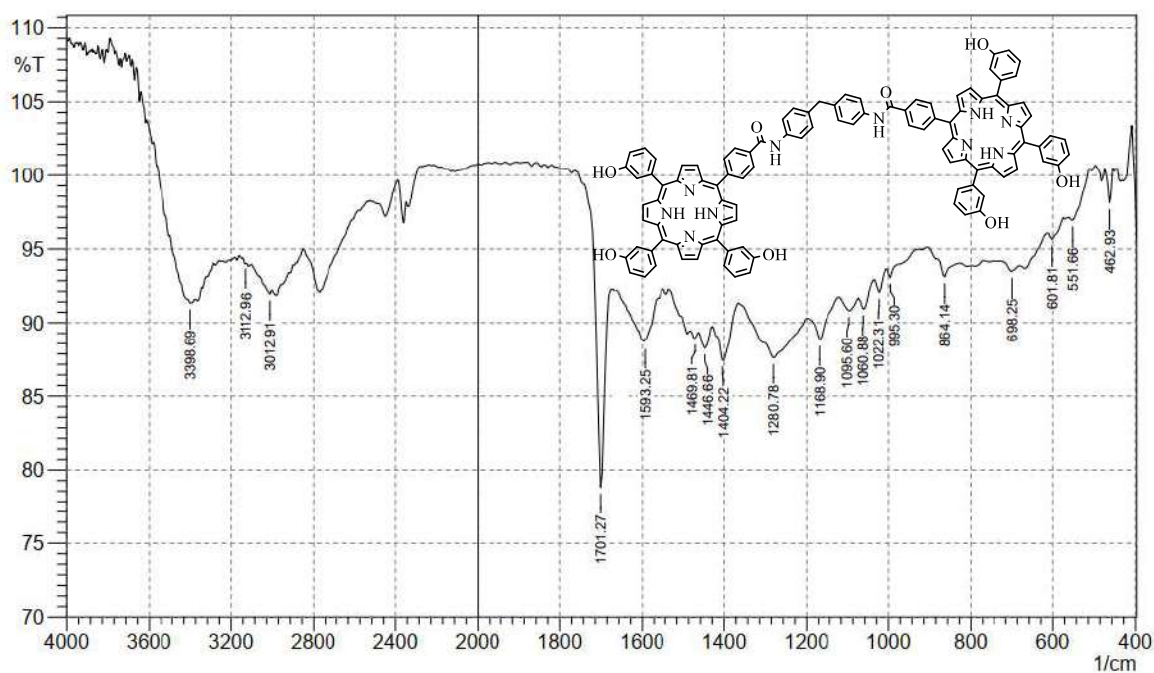
Figure 3: Mass spectrum of compound (3)
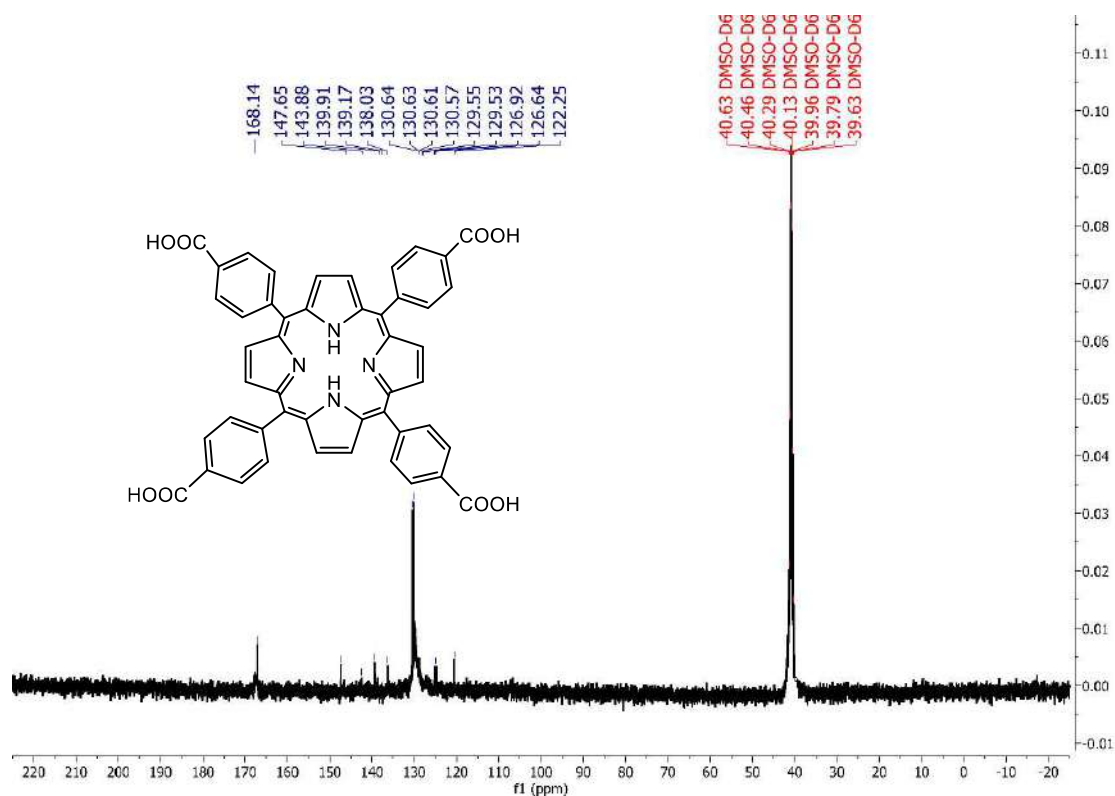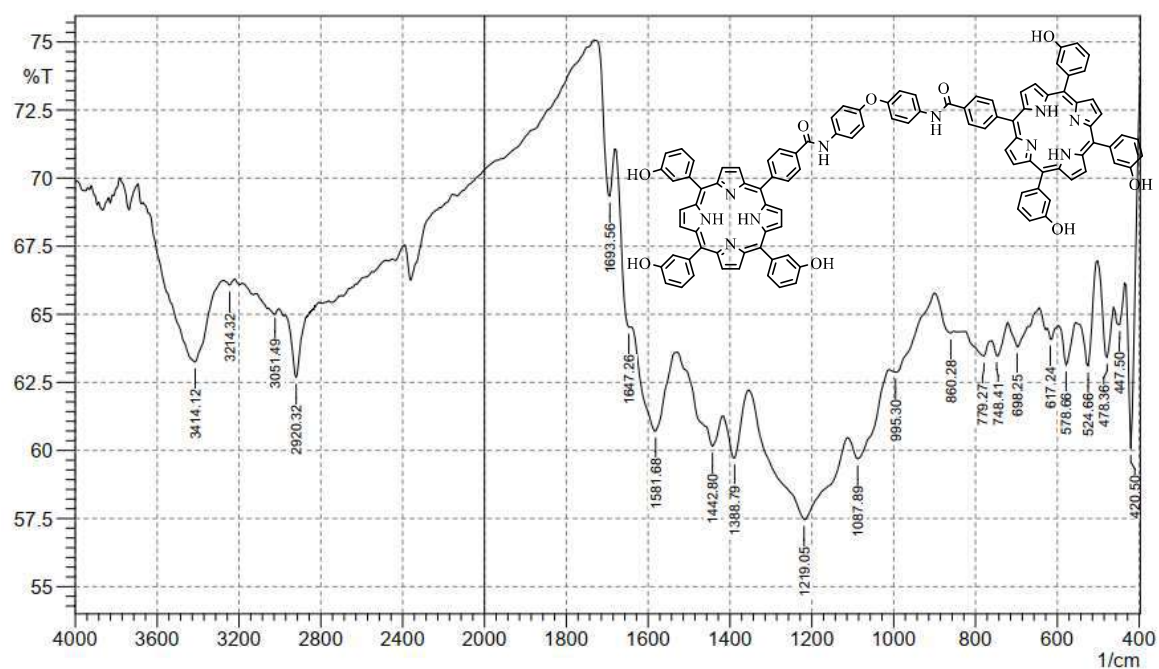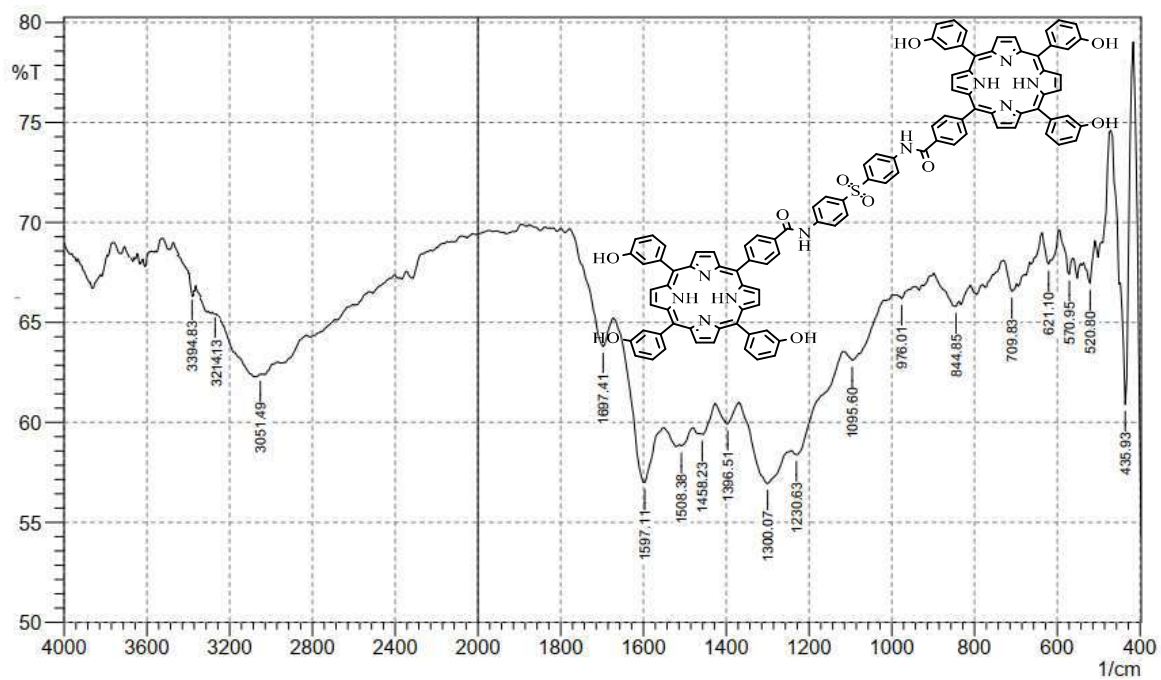

Figure 4: ^{13}CNMR spectrum of compound (3)
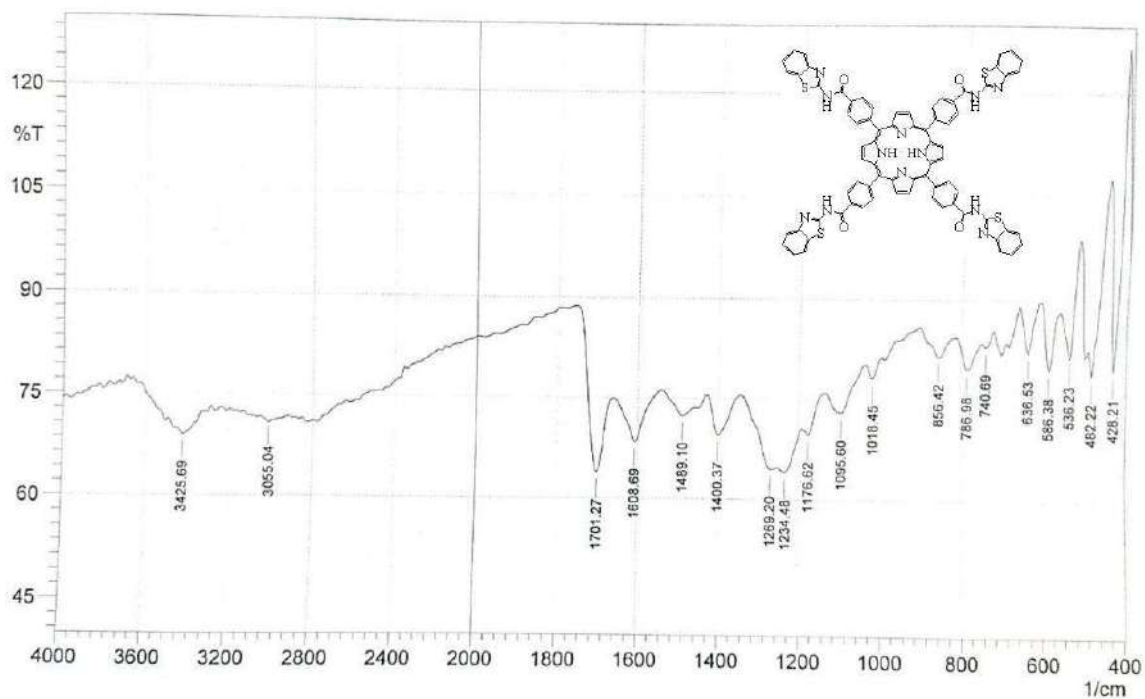
Figure 5: FT-IR spectrum of compound (5a)
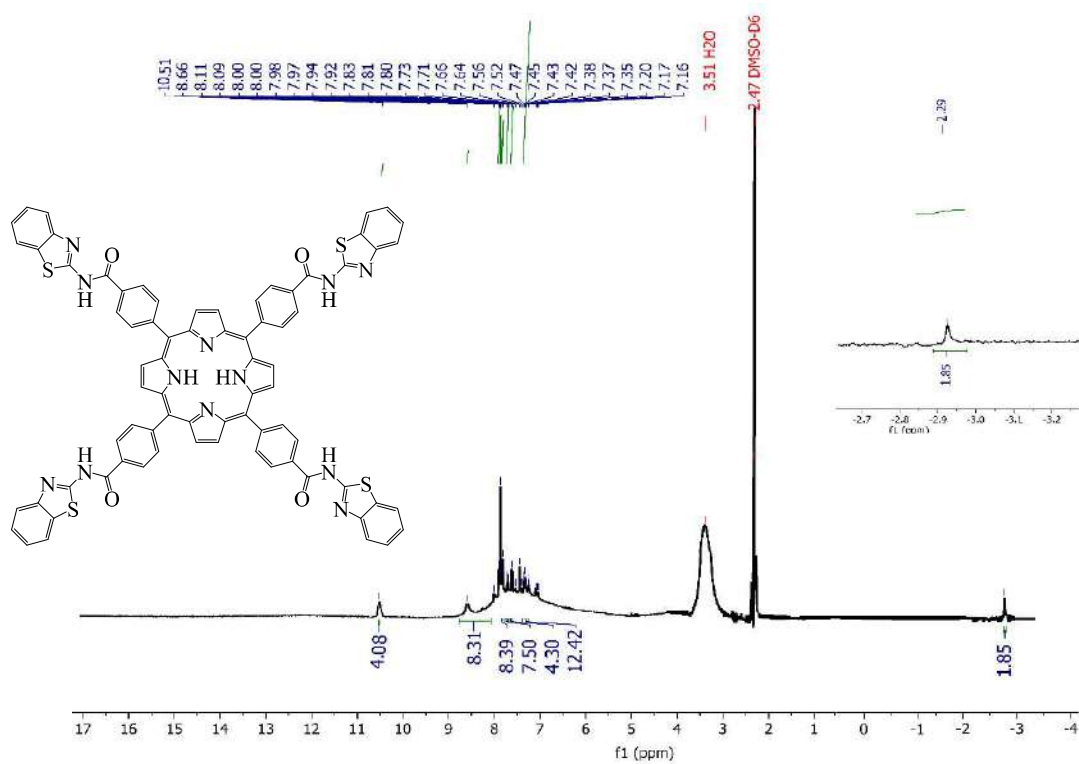
Figure 6: ¹HNMR spectrum of compound (5a)
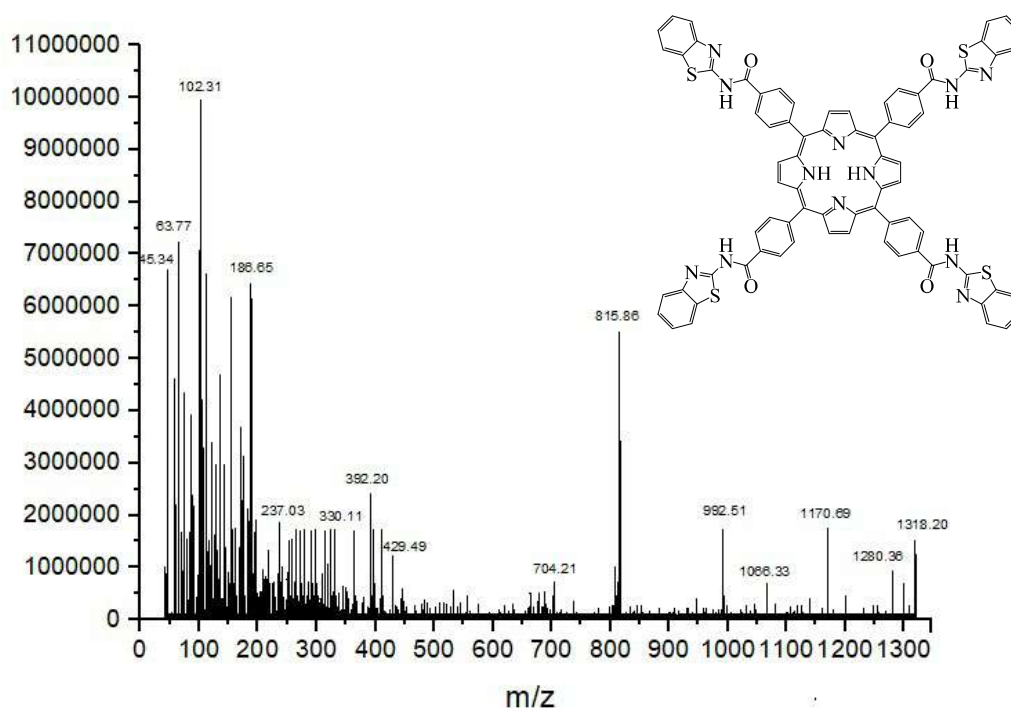
Figure 7: Mass spectrum of compound (5a)
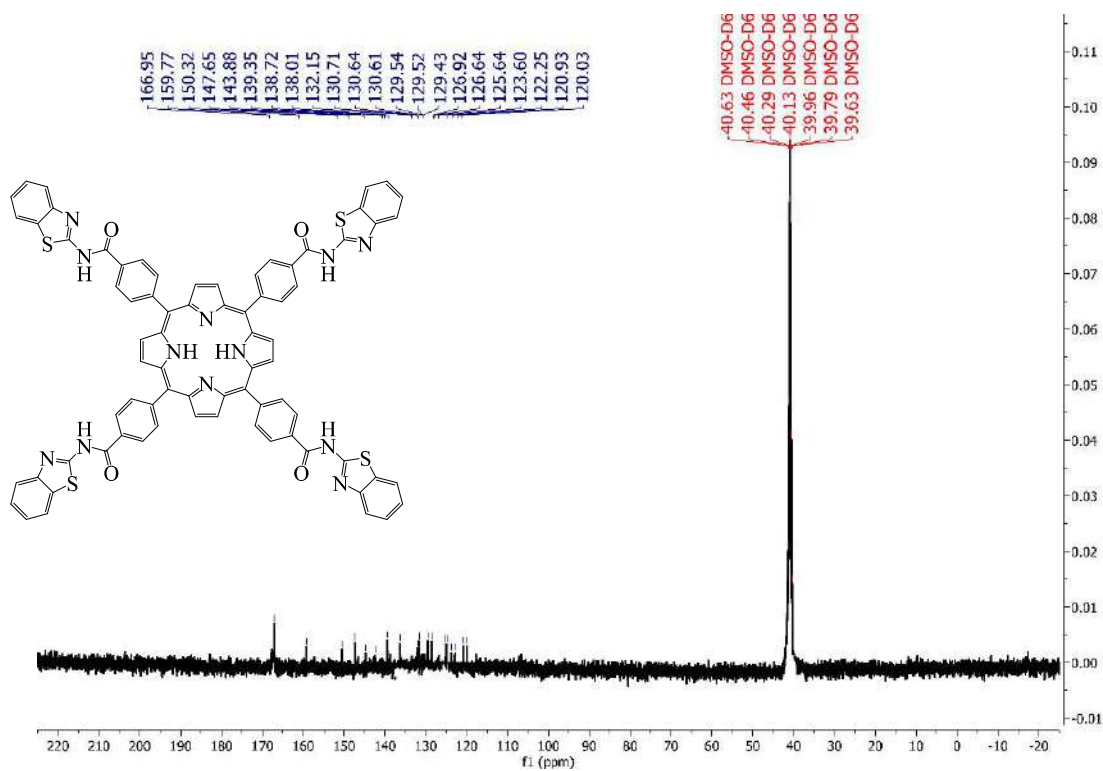
Figure 8: ^{13}CNMR spectrum of compound (5a)
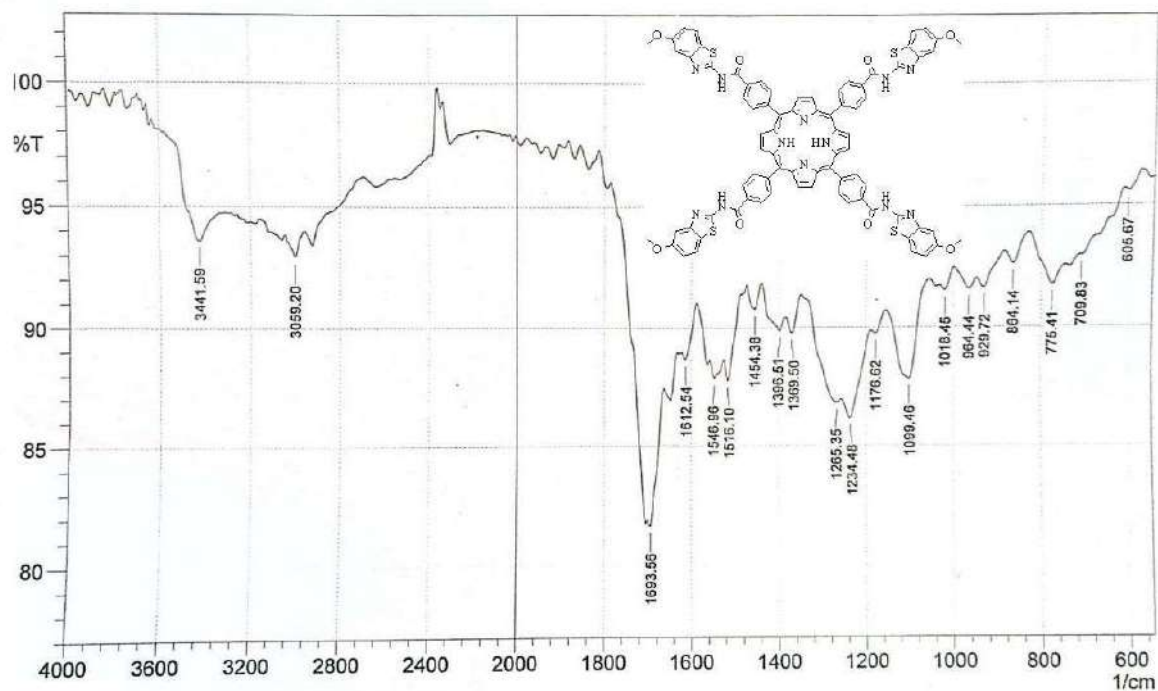
Figure 9: FT-IR spectrum of compound (5b)
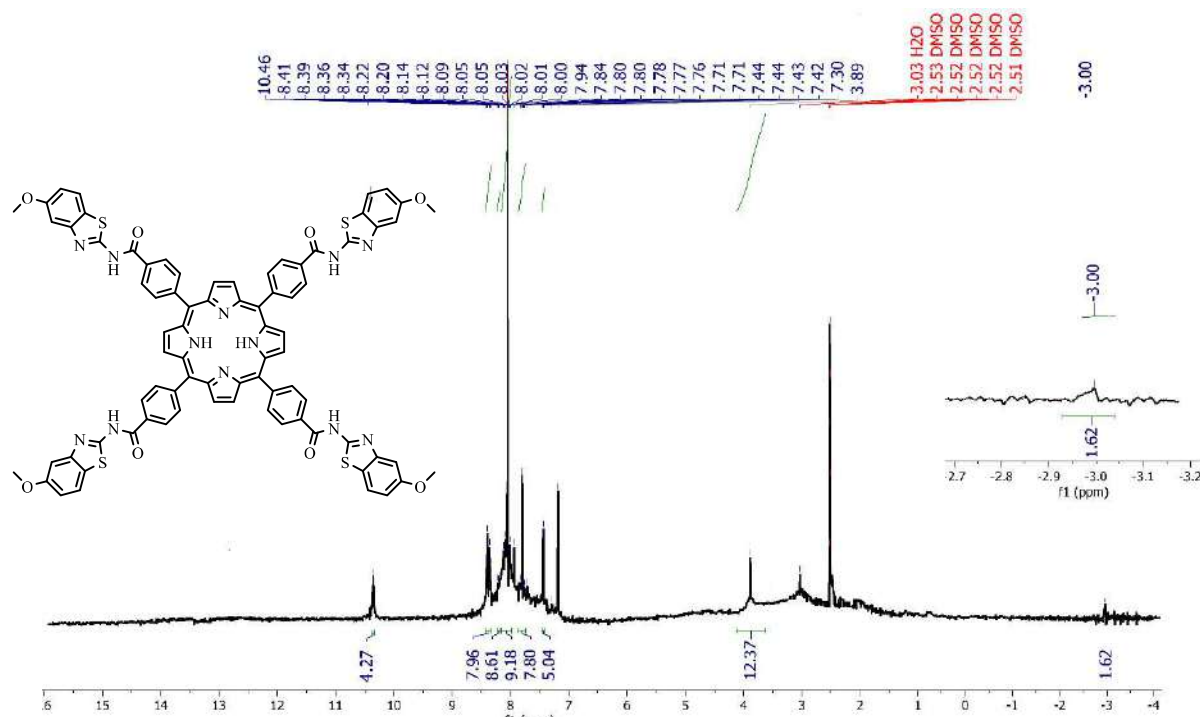
Figure 10: ^{1}HNMR spectrum of compound (5b)
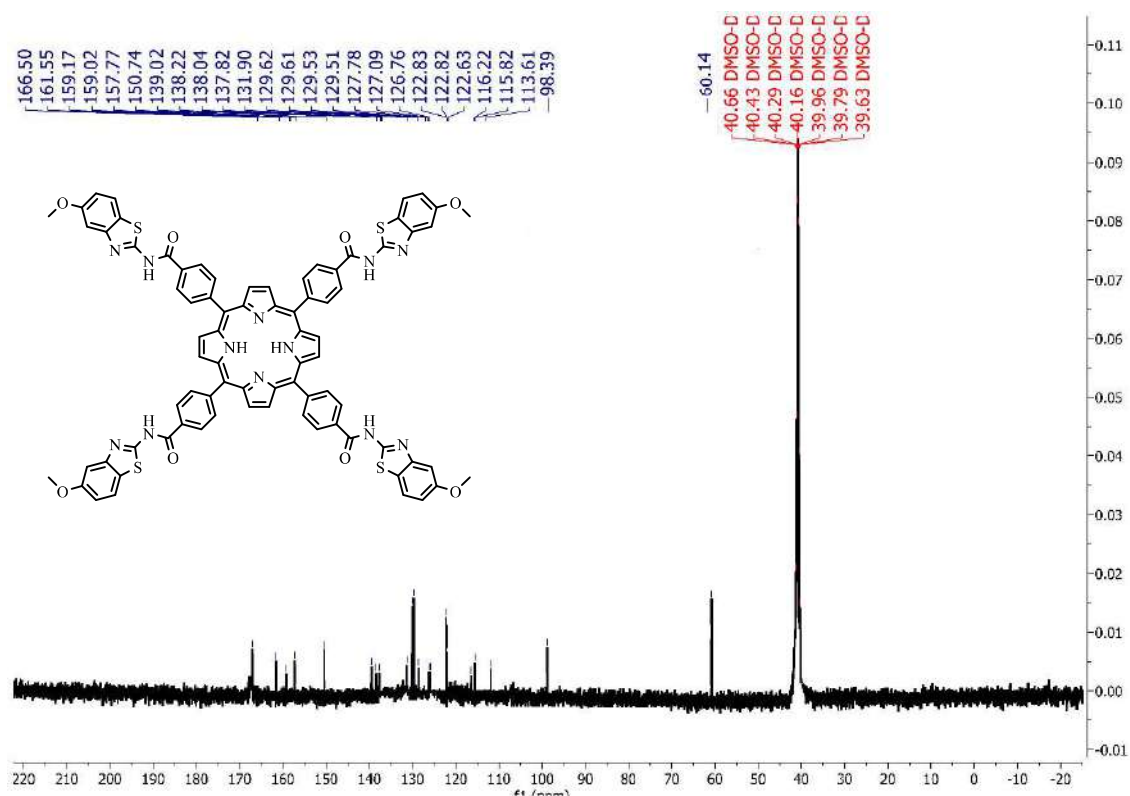
Figure 11: ^{13}CNMR spectrum of compound (5b)
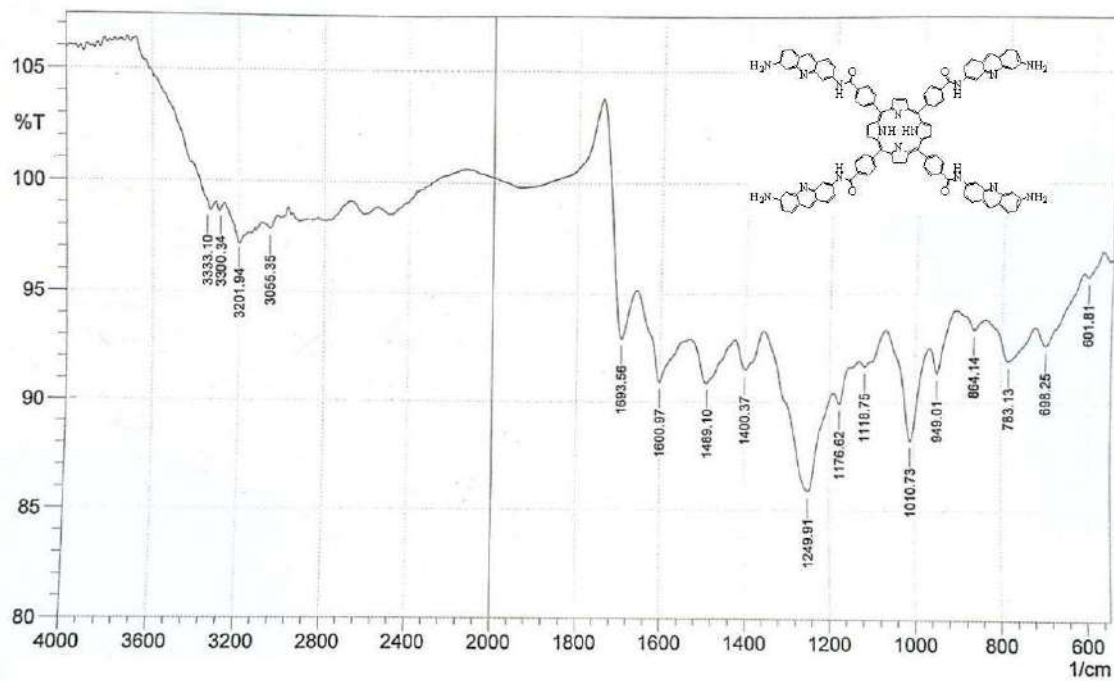
Figure 12: FT-IR spectrum of compound (5c)
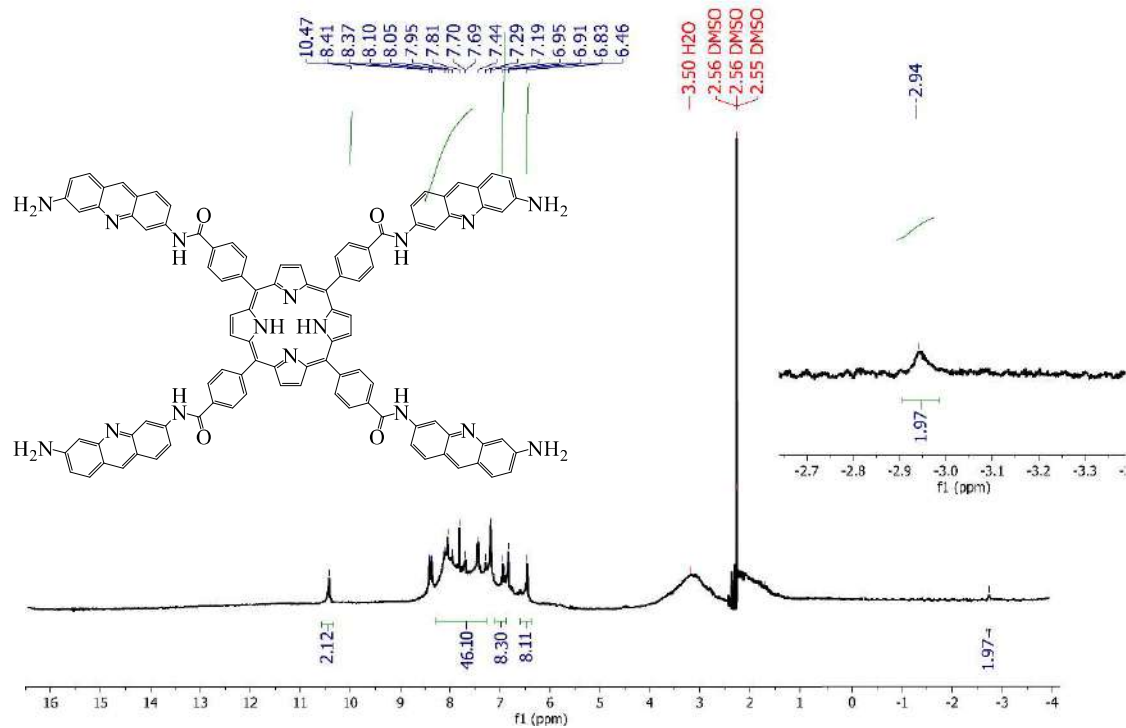
Figure 13: ^{1}HNMR spectrum of compound (5c)
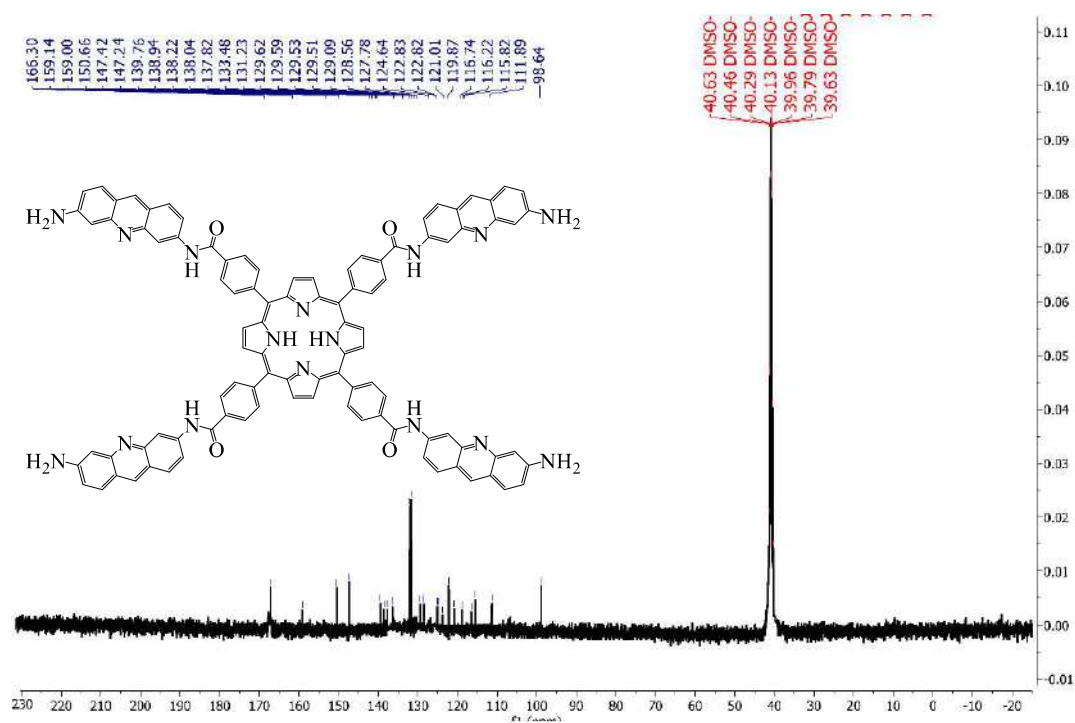
Figure 14: ^{13}CNMR spectrum of compound (5c)
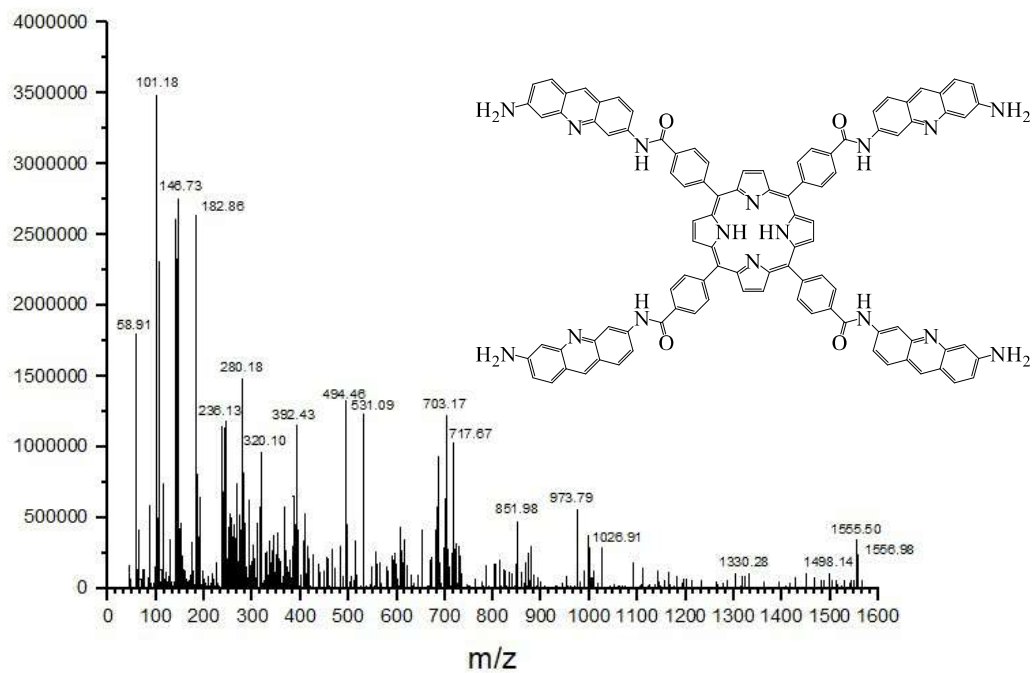
Figure 15: Mass spectrum of compound (5c)
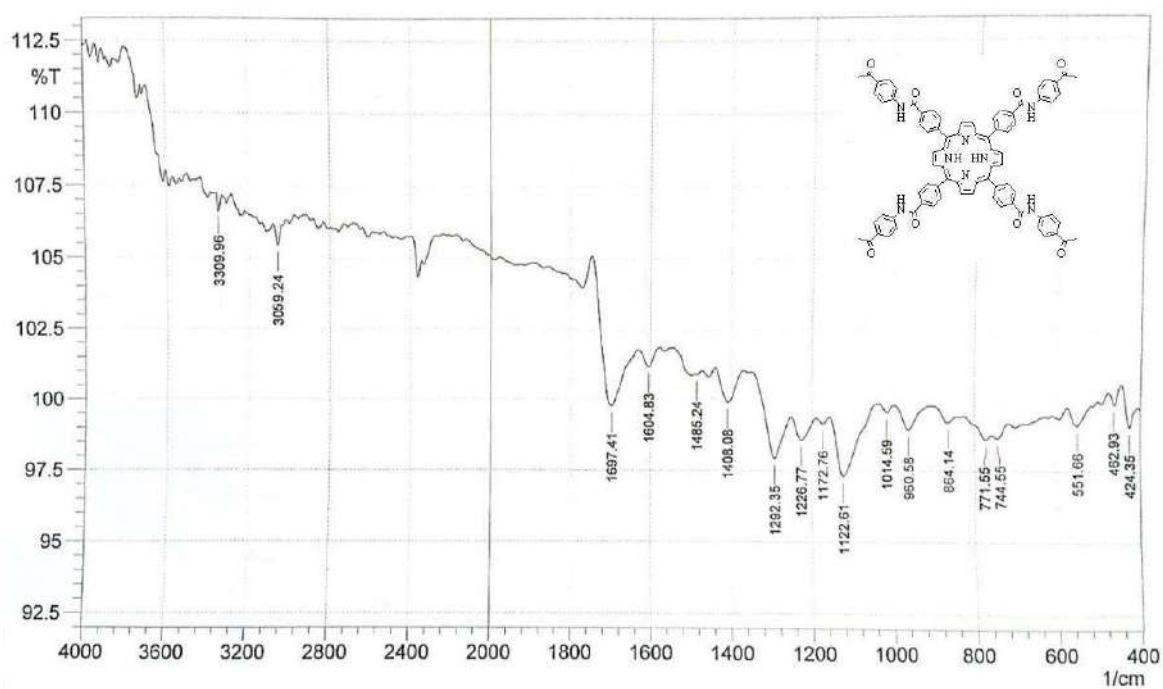
Figure 16: FT-IR spectrum of compound (5d)
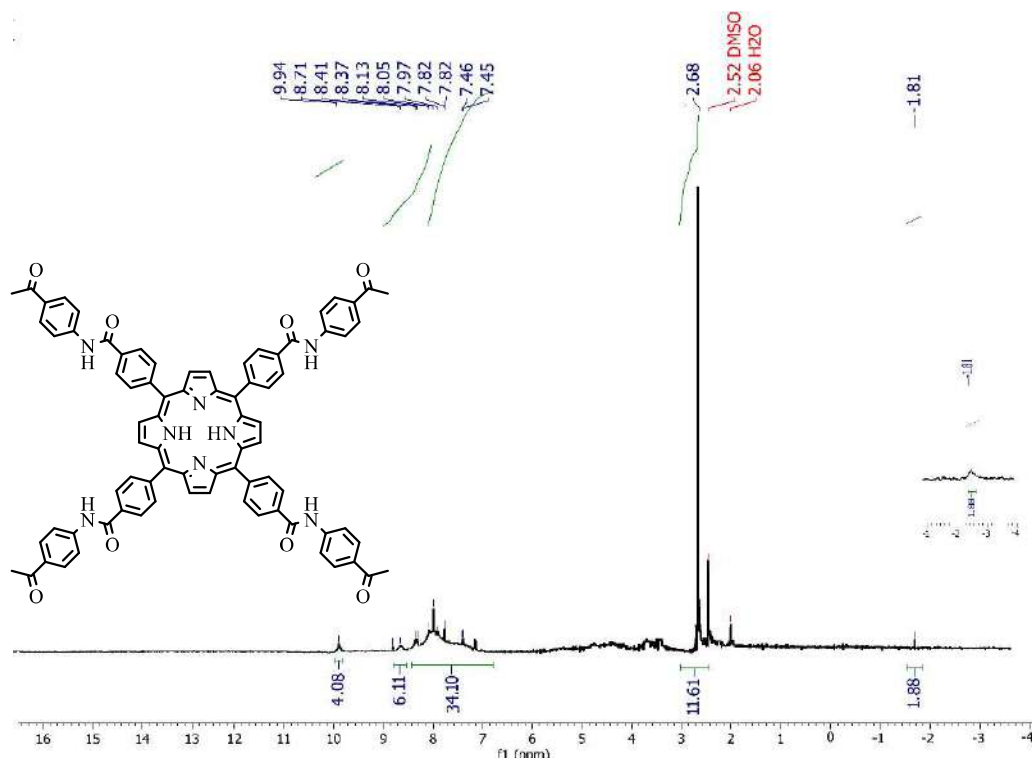
Figure 17: ^{1}HNMR spectrum of compound (5d)
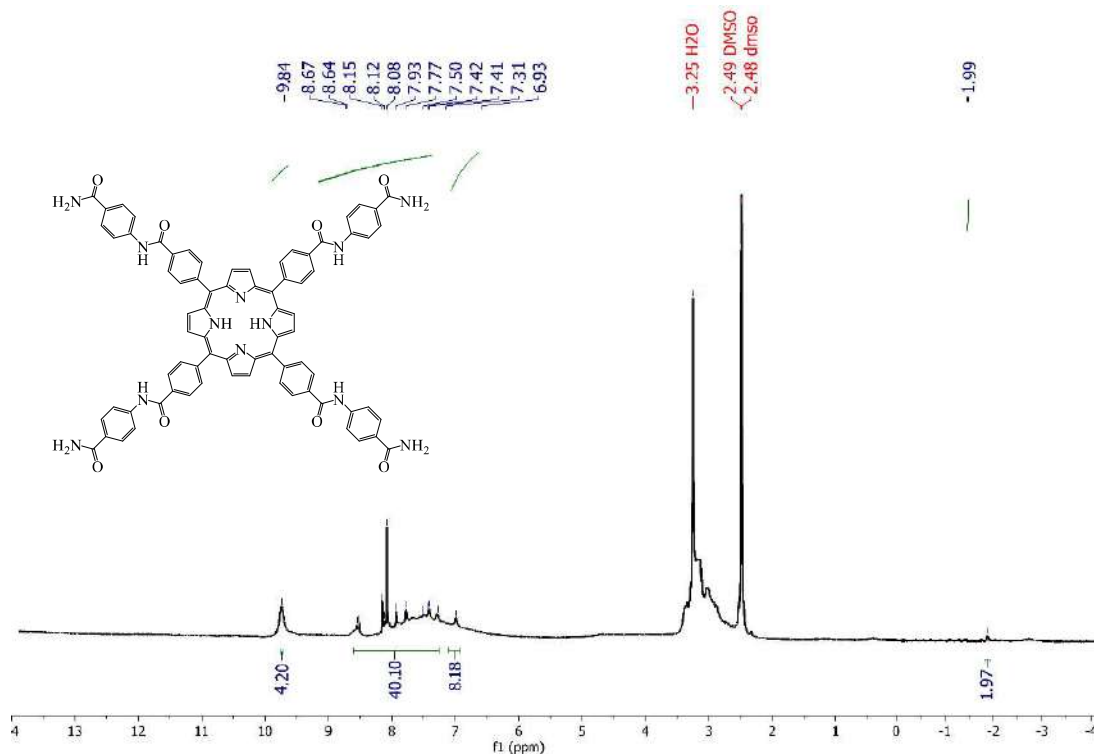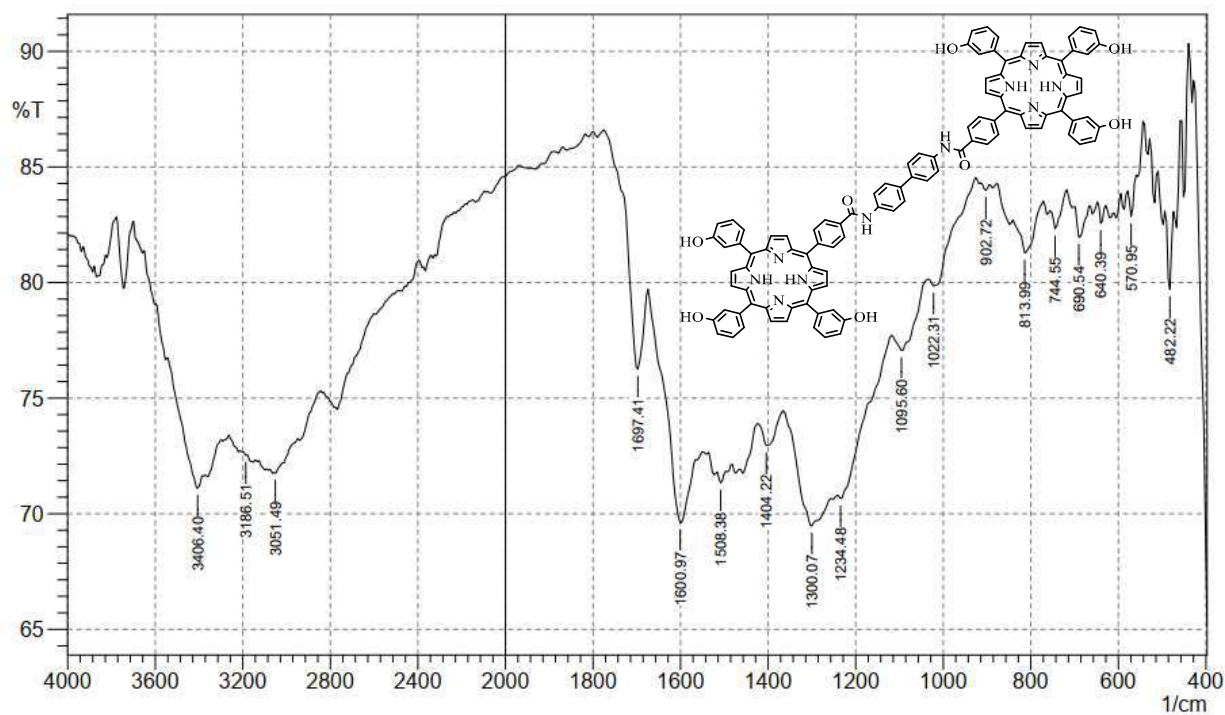

Figure 18: ^{1}HNMR spectrum of compound (5e)
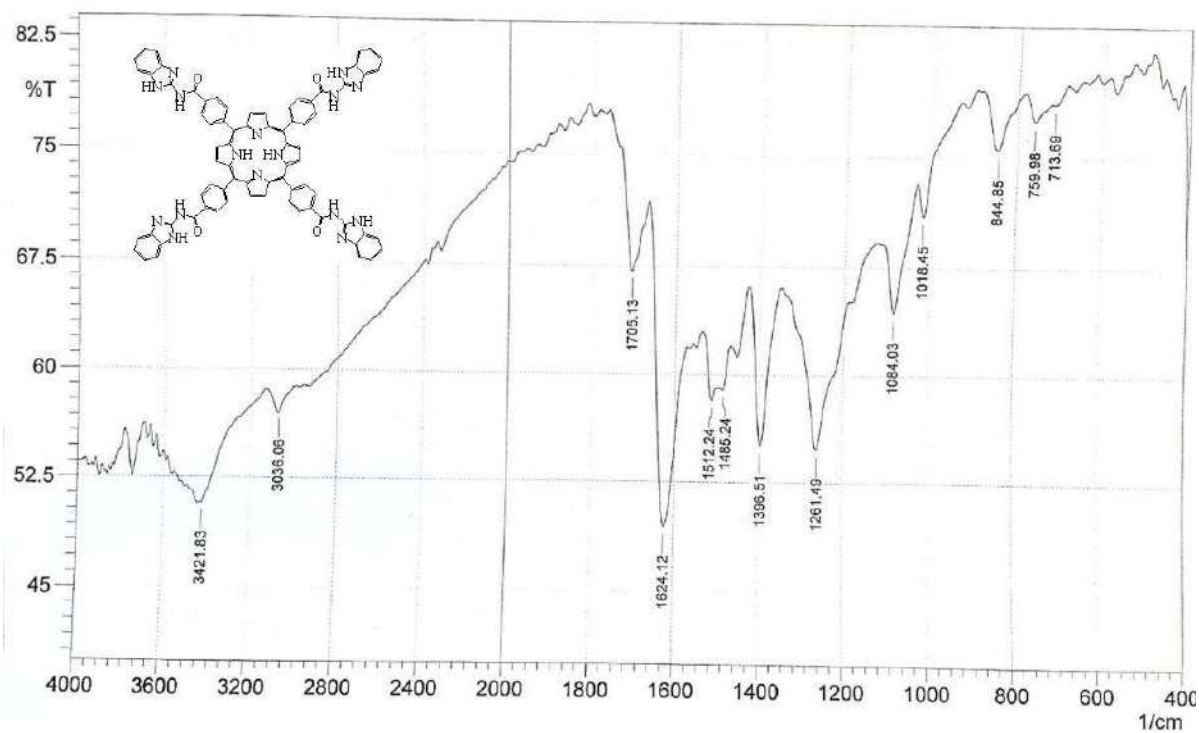
Figure 19: FT-IR spectrum of compound (5f)
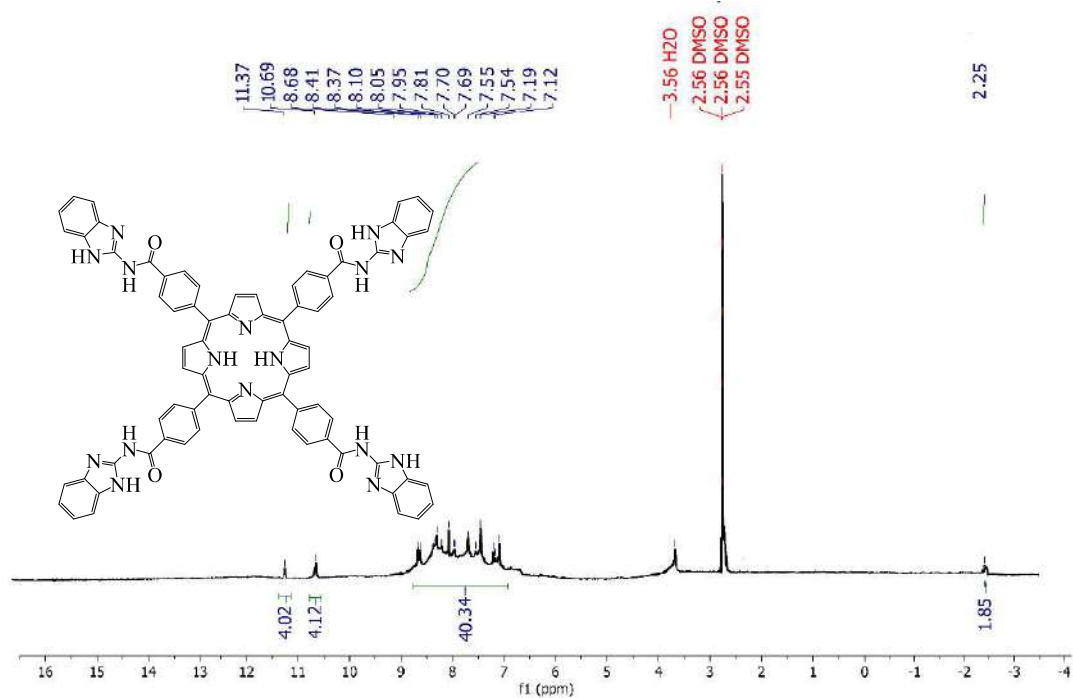
Figure 20: ¹HNMR spectrum of compound (5f)
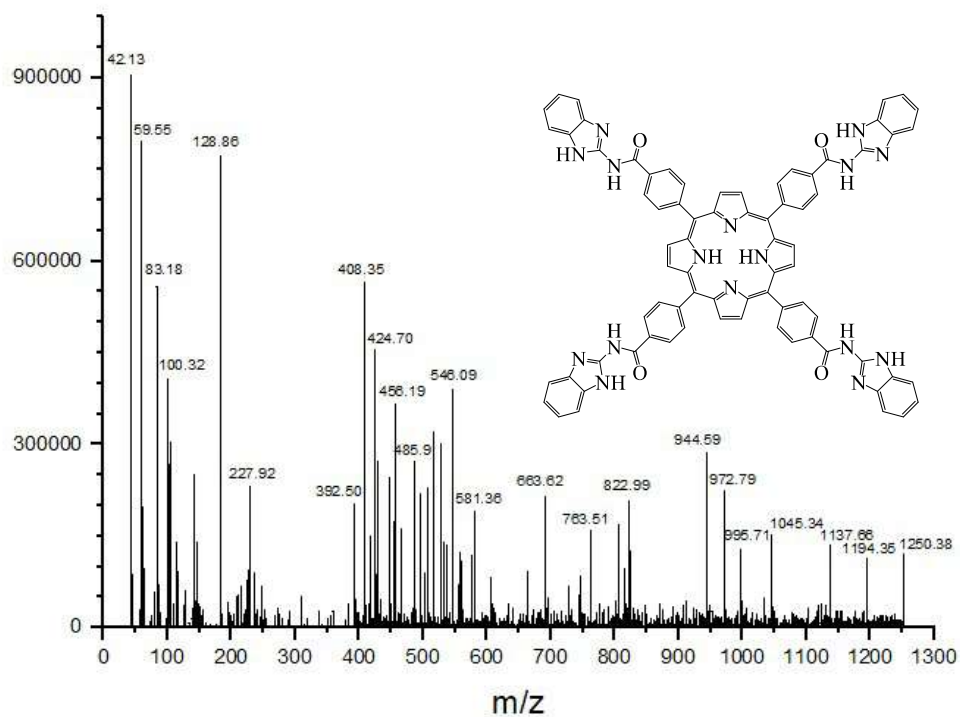
Figure 21: Mass spectrum of compound (5f)
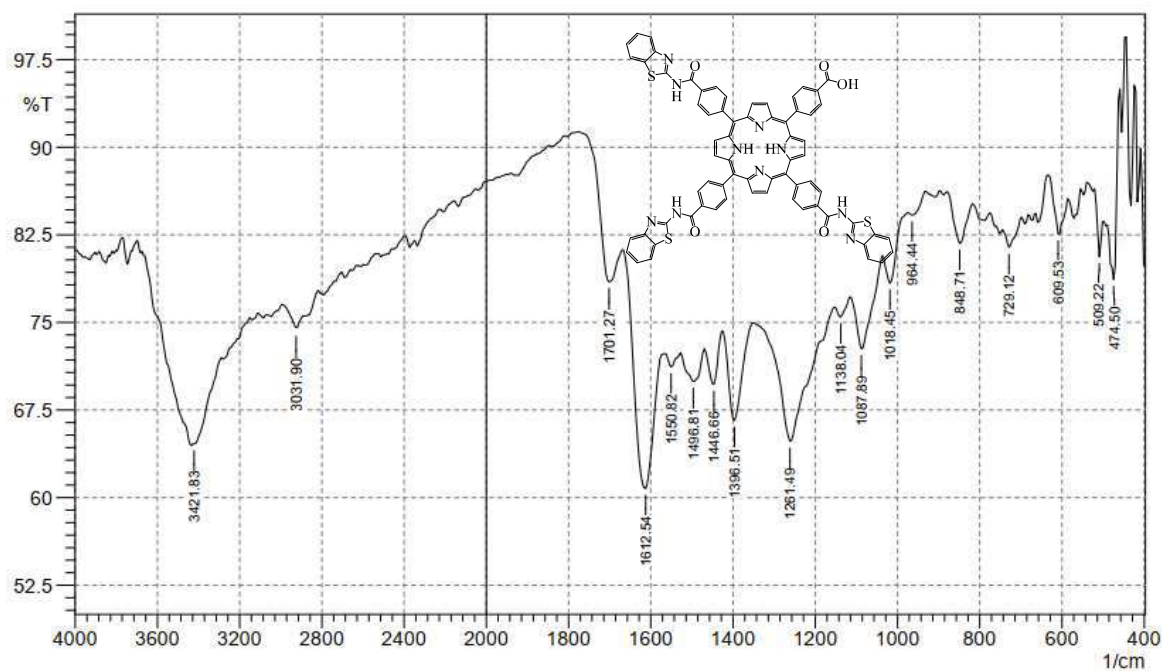
Figure 22: FT-IR spectrum of compound (6a)
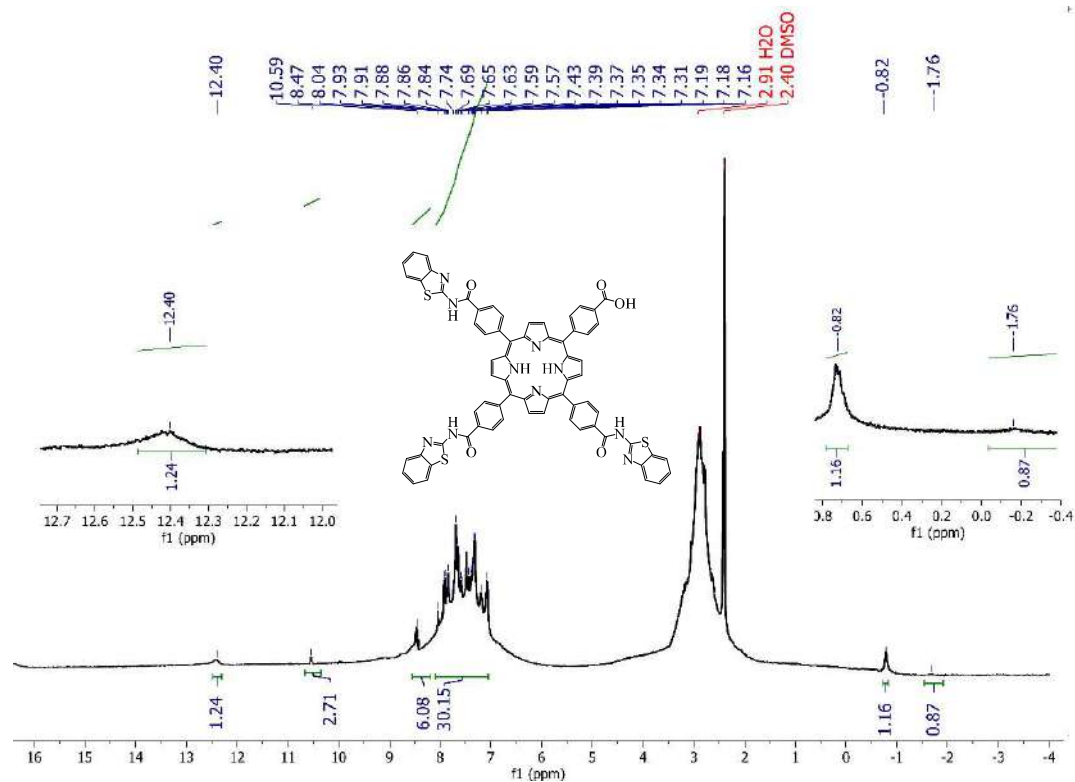
Figure 23: ^{1}HNMR spectrum of compound (6a)
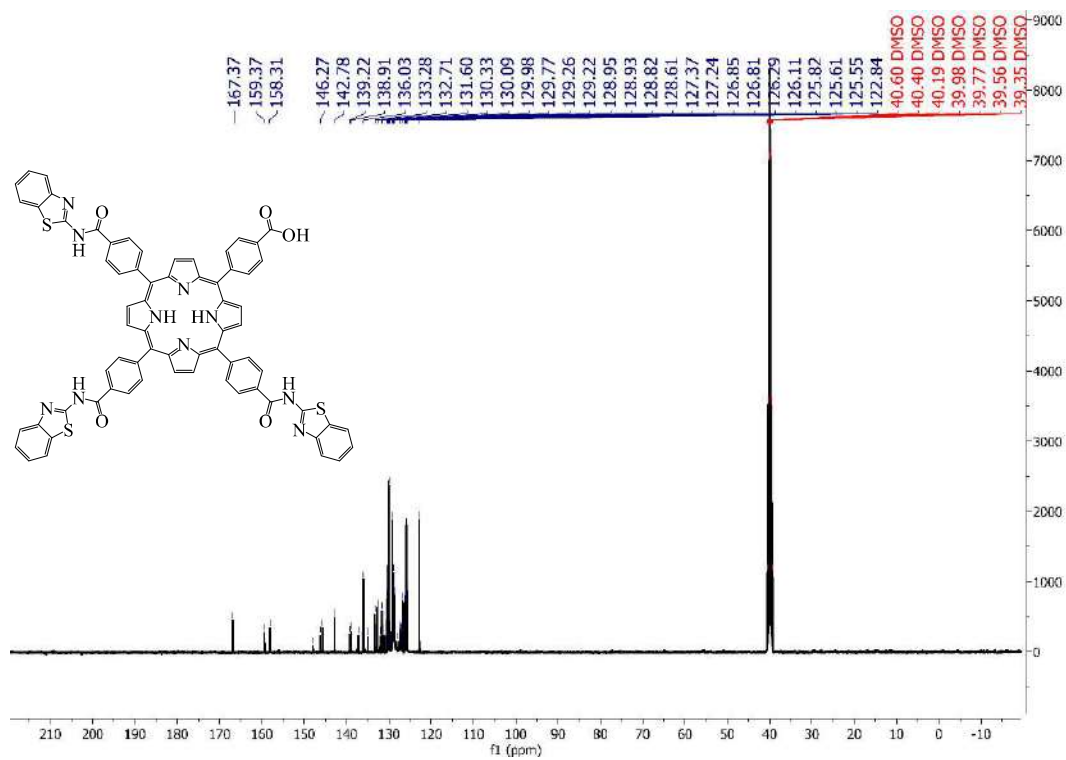
Figure 24: ^{13}CNMR spectrum of compound (6a)
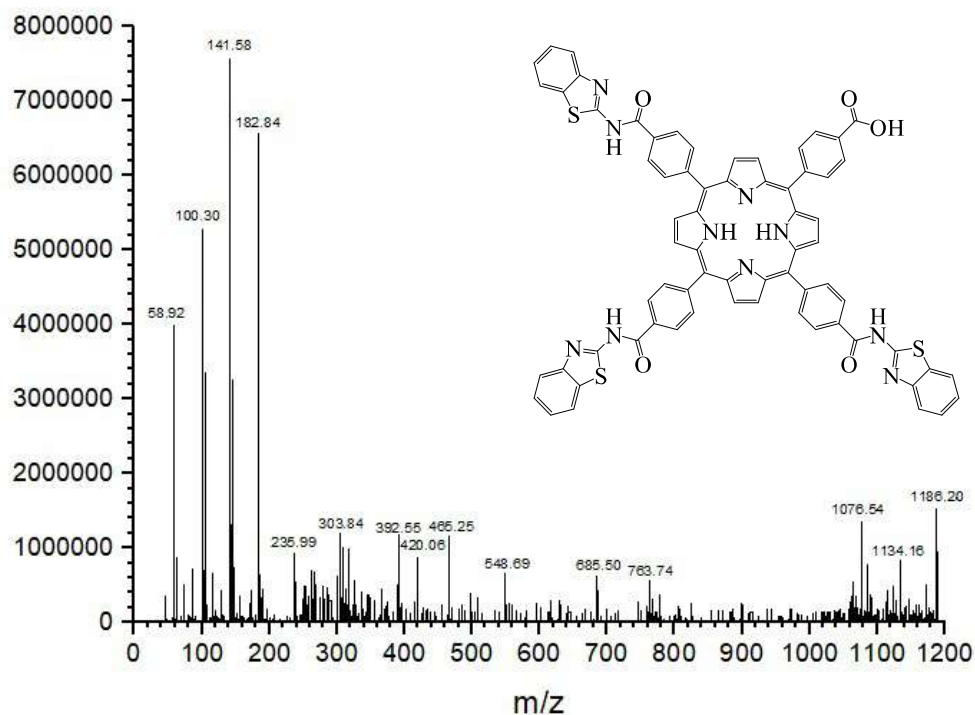
Figure 25: Mass spectrum of compound (6a)
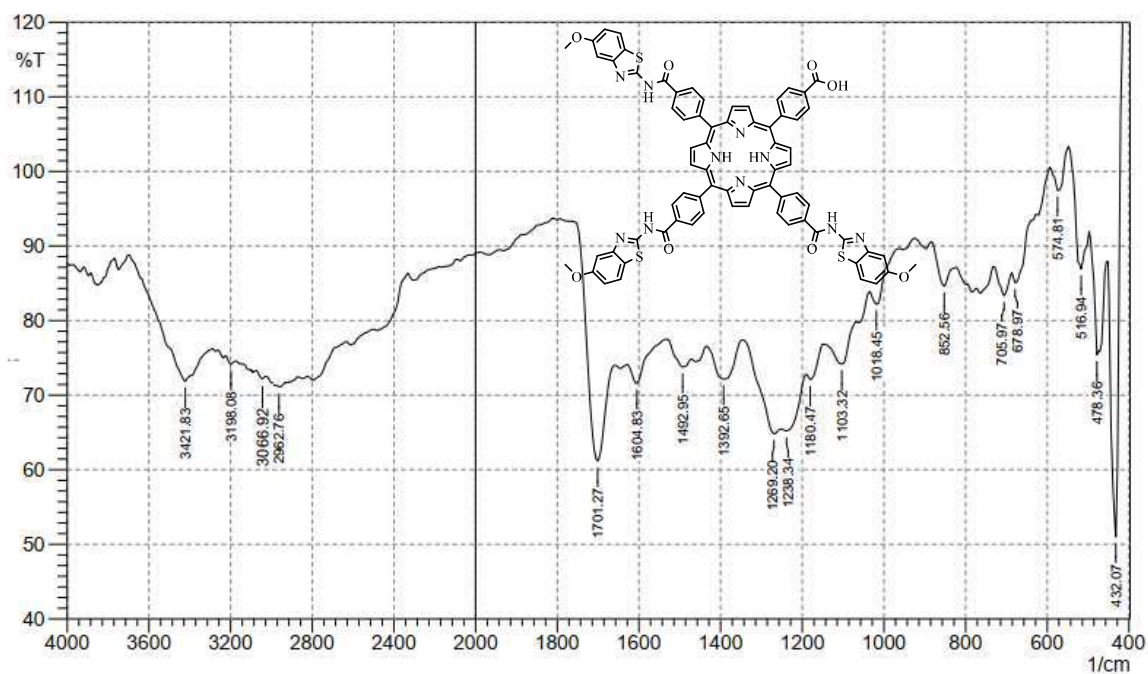
Figure 26: FT-IR spectrum of compound (6b)
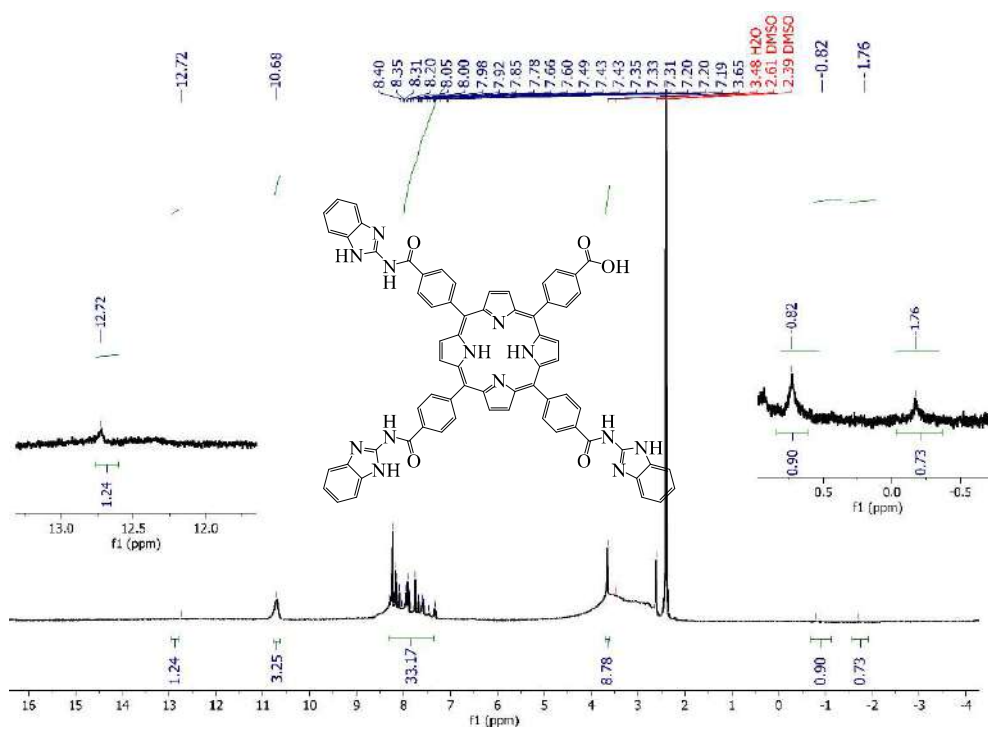
Figure 27: ^{1}HNMR spectrum of compound (6b)
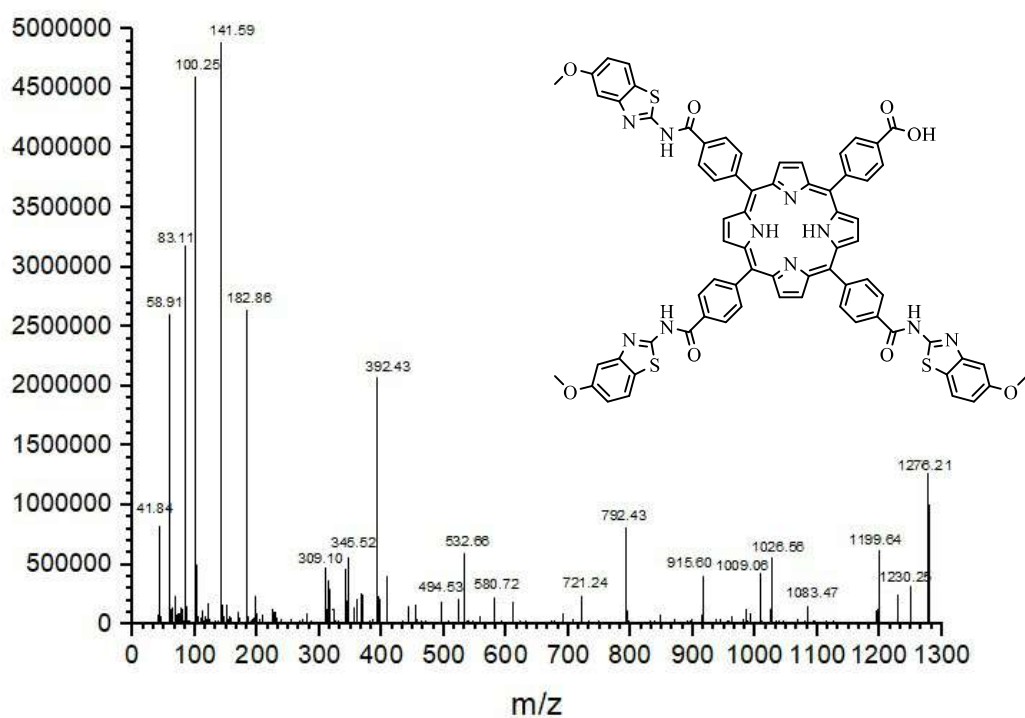
Figure 28: Mass spectrum of compound (6b)
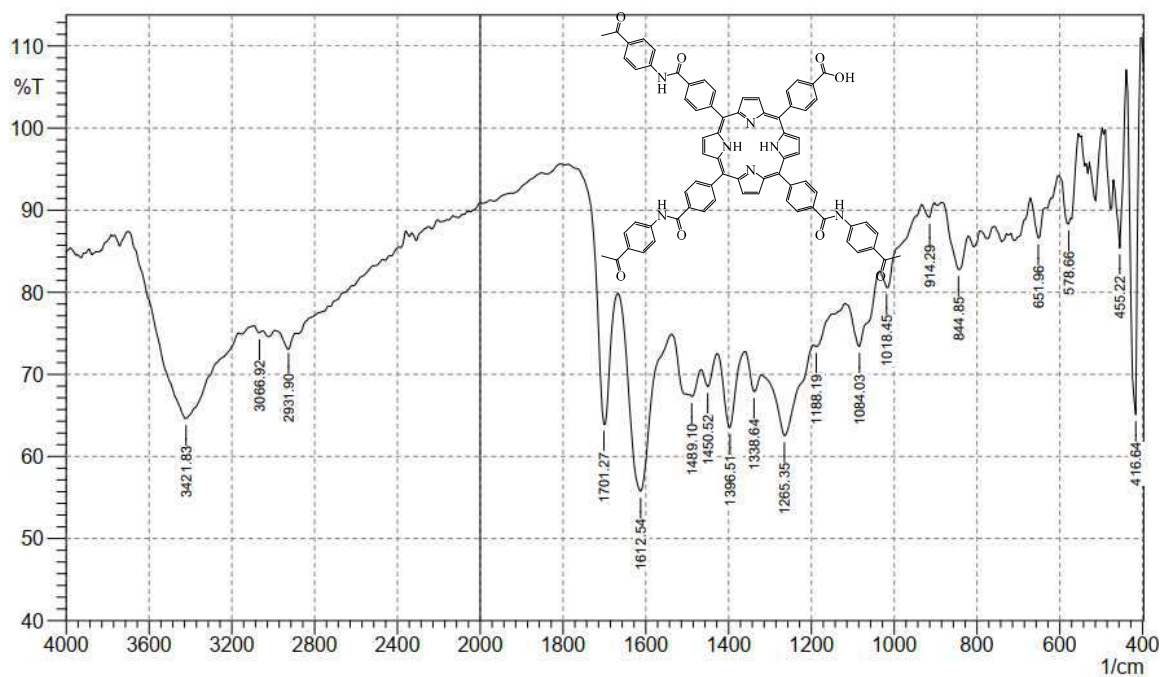
Figure 29: FT-IR spectrum of compound (6c)
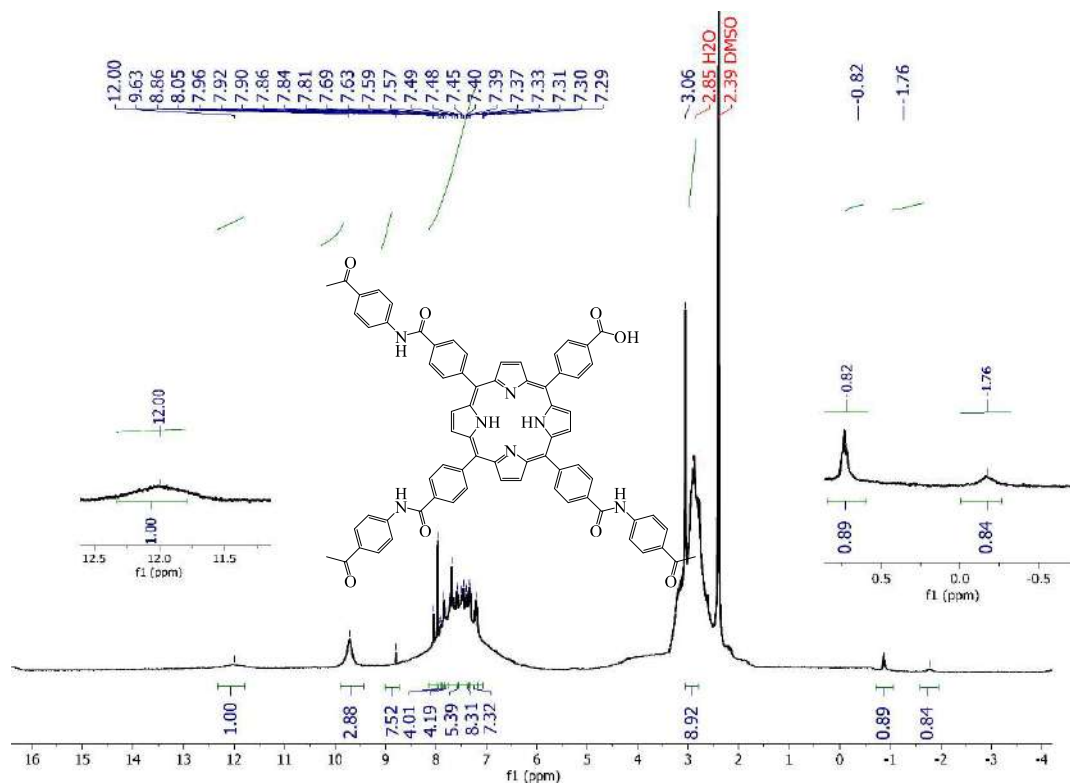
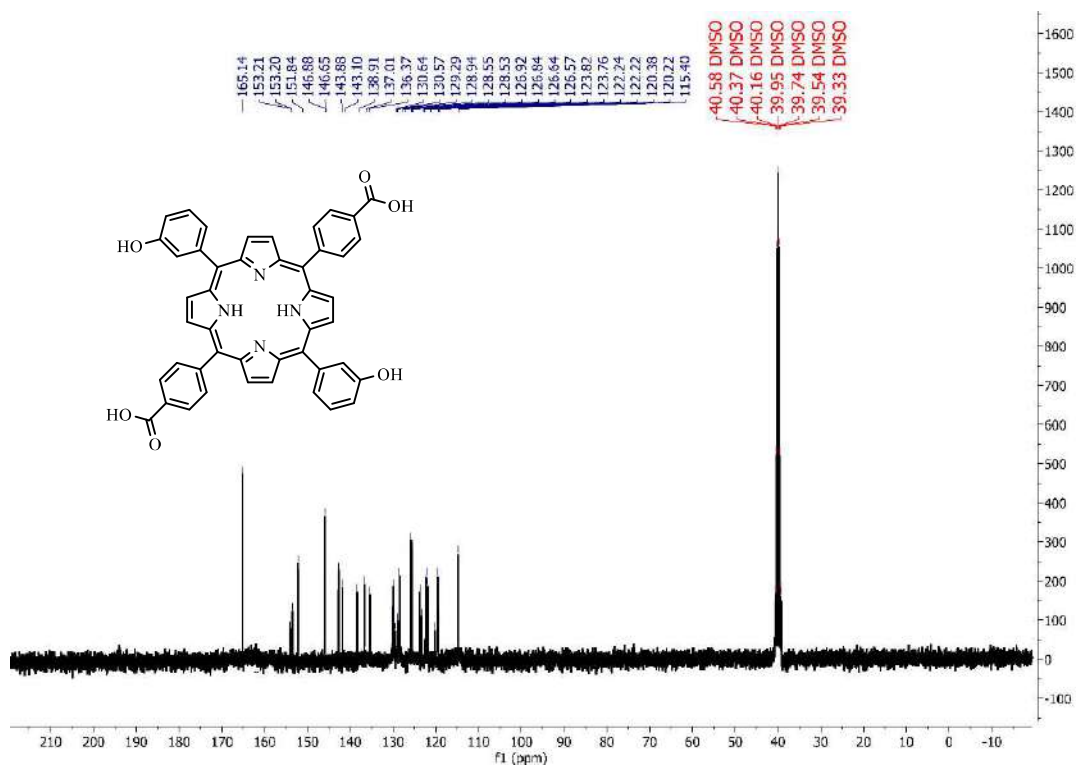**Figure 30:** ¹HNMR spectrum of compound (6c)
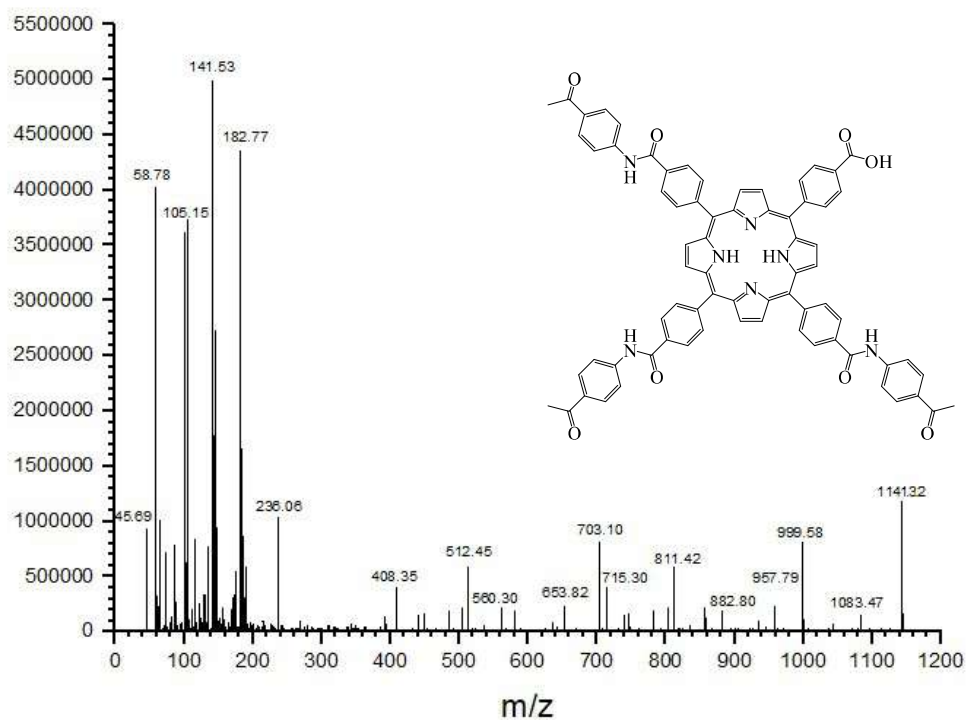
Figure 31: Mass spectrum of compound (6c)
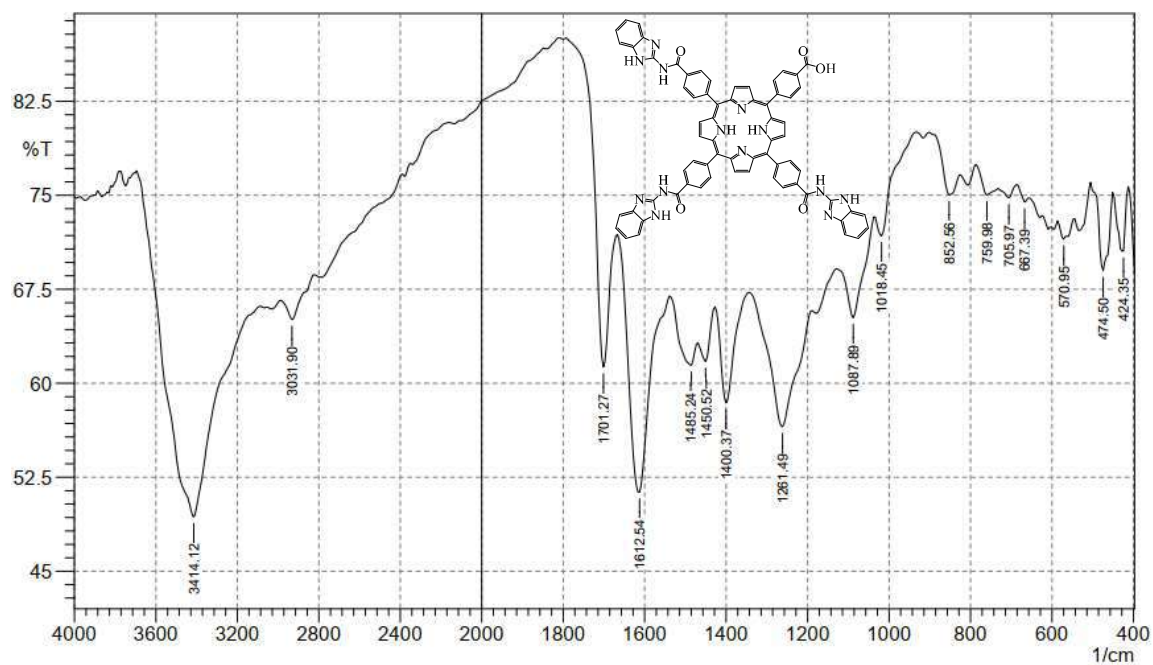
Figure 32: FT-IR spectrum of compound (6d)
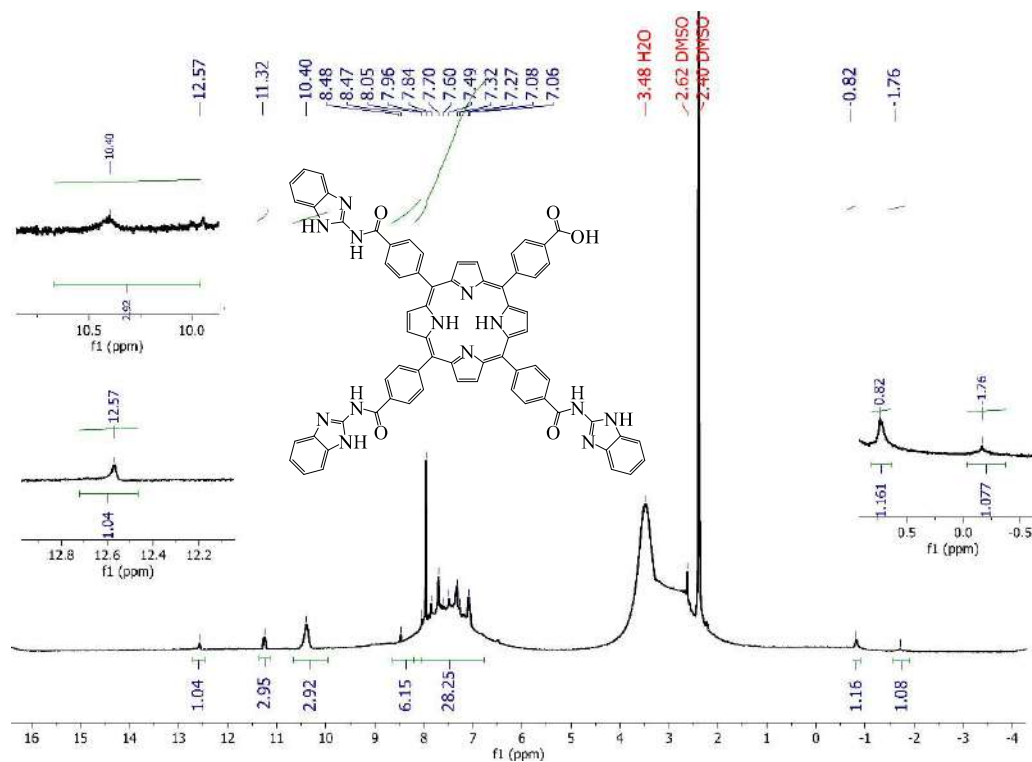
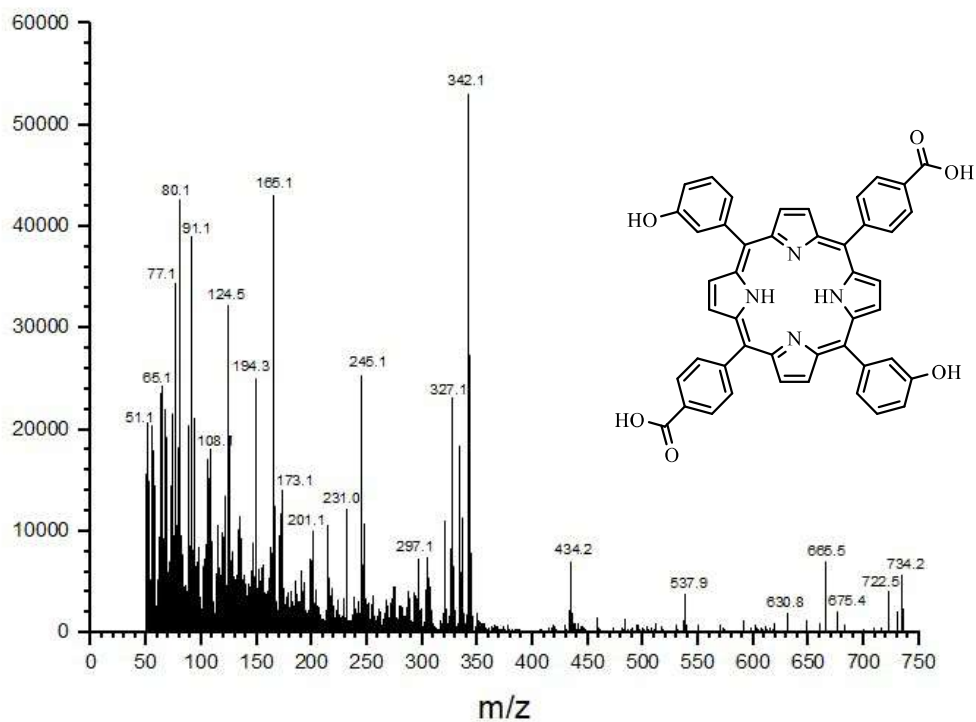**Figure 33:** ^{1}HNMR spectrum of compound (6d)
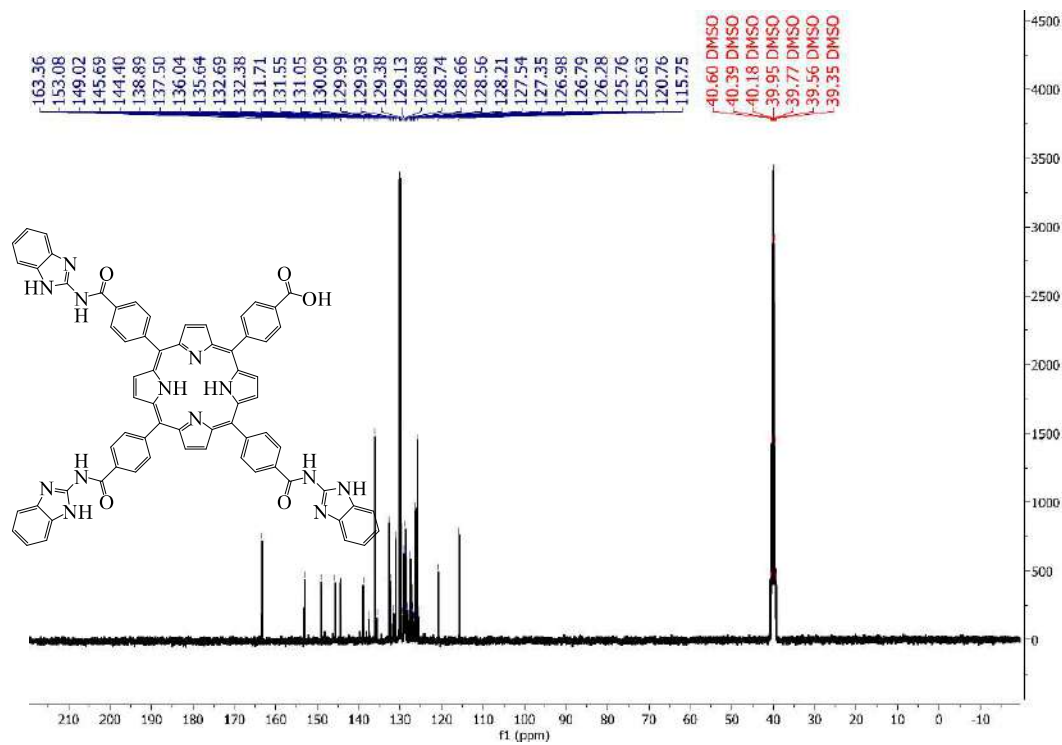
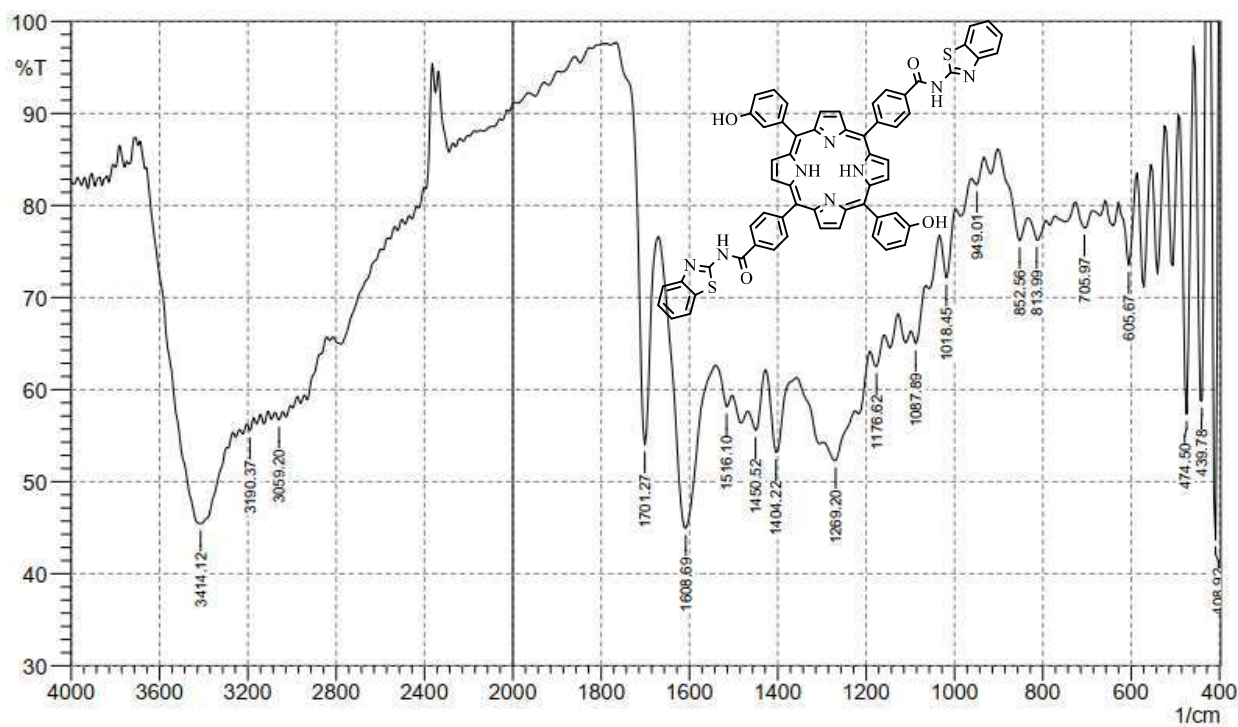**Figure 34:** ^{13}CNMR spectrum of compound (6d)
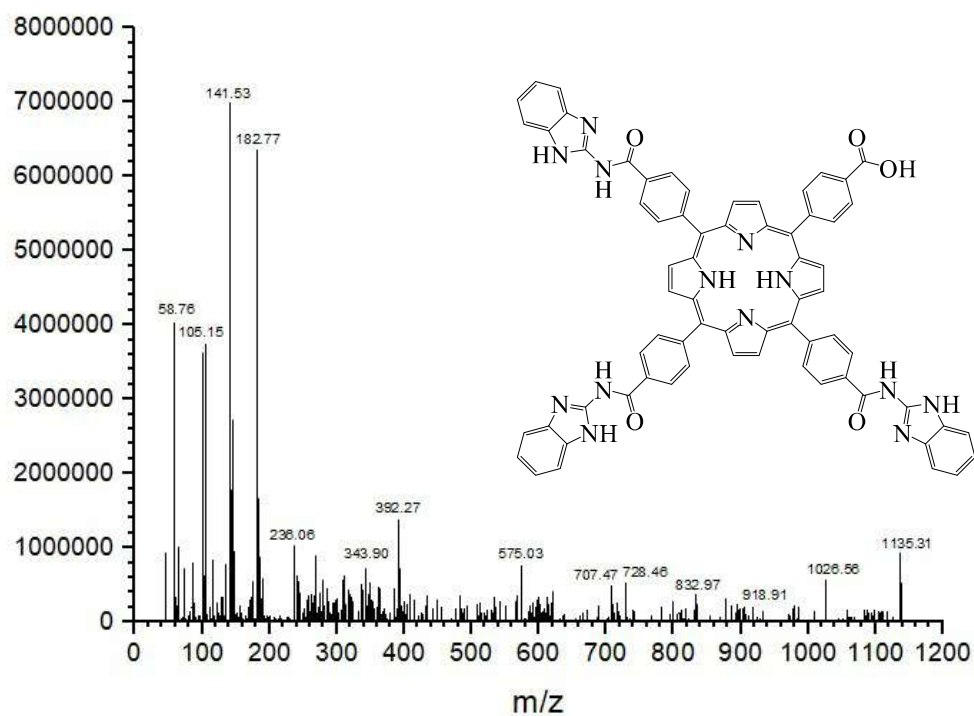
Figure 35: Mass spectrum of compound (6d)
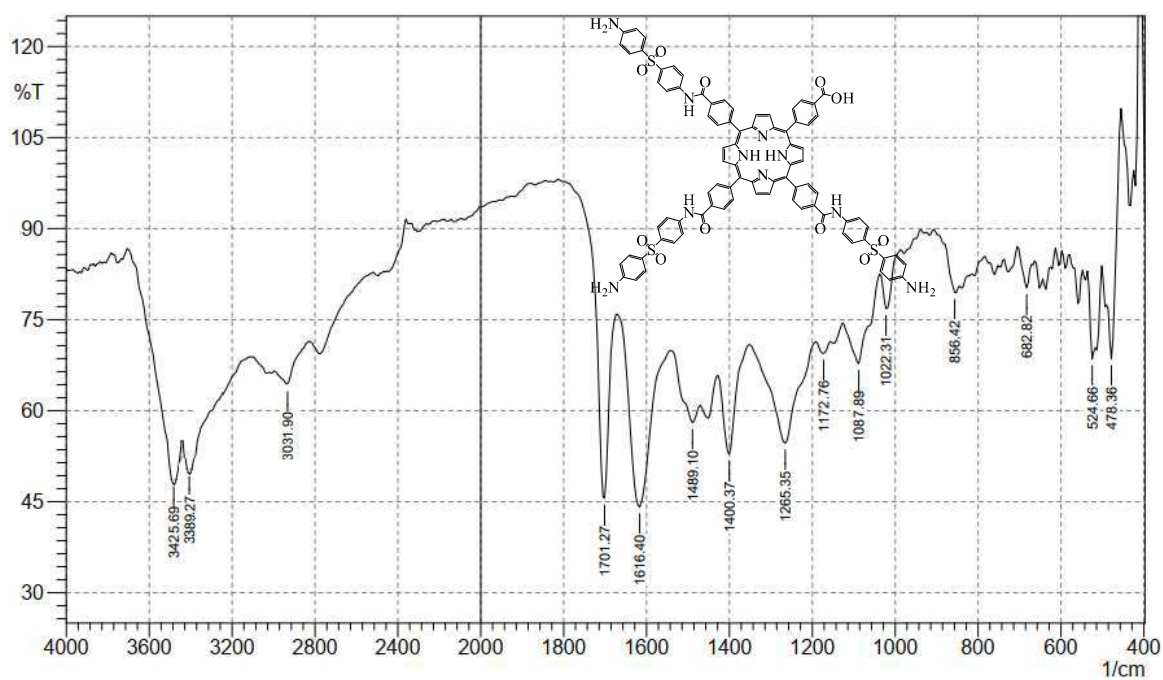
Figure 36: FT-IR spectrum of compound (6e)
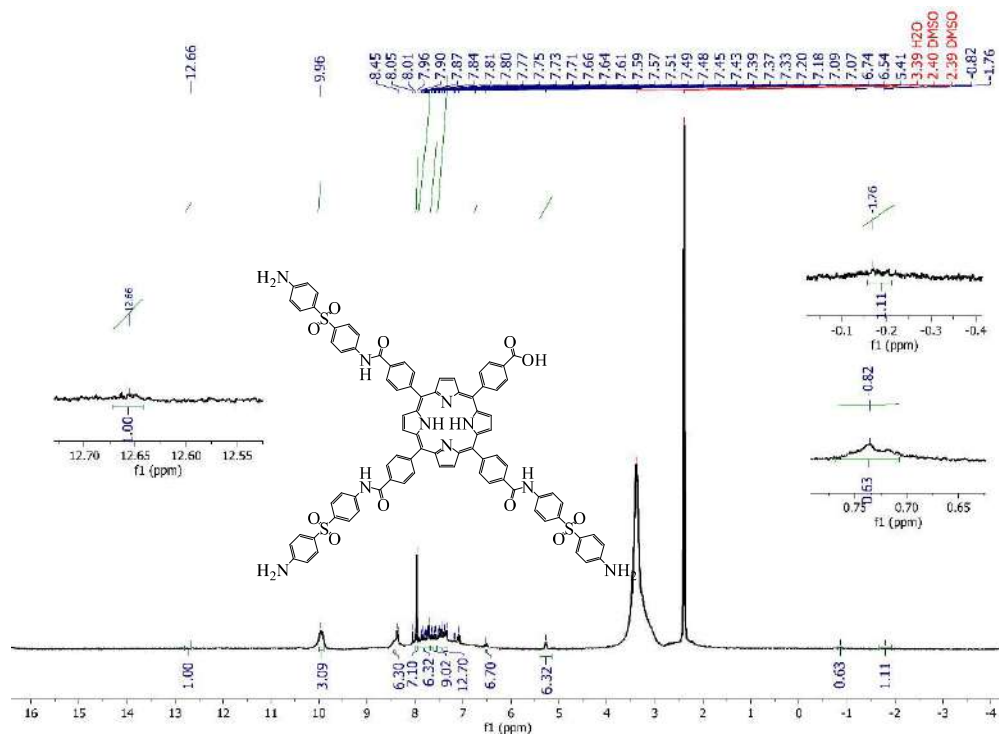
Figure 37: ^{1}HNMR spectrum of compound (6e)
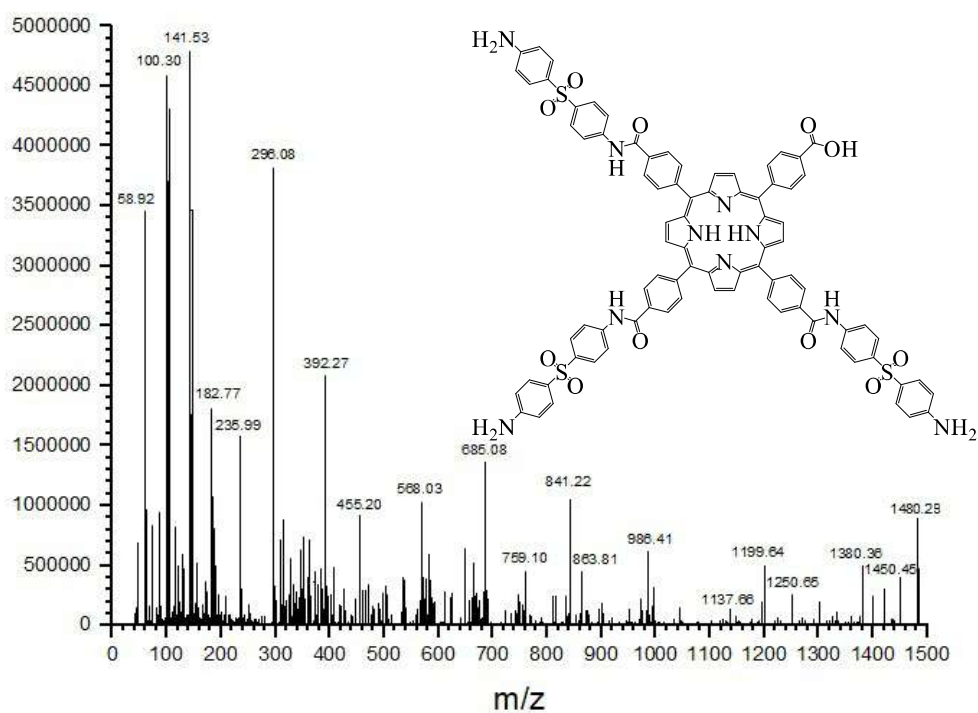
Figure 38: Mass spectrum of compound (6e)
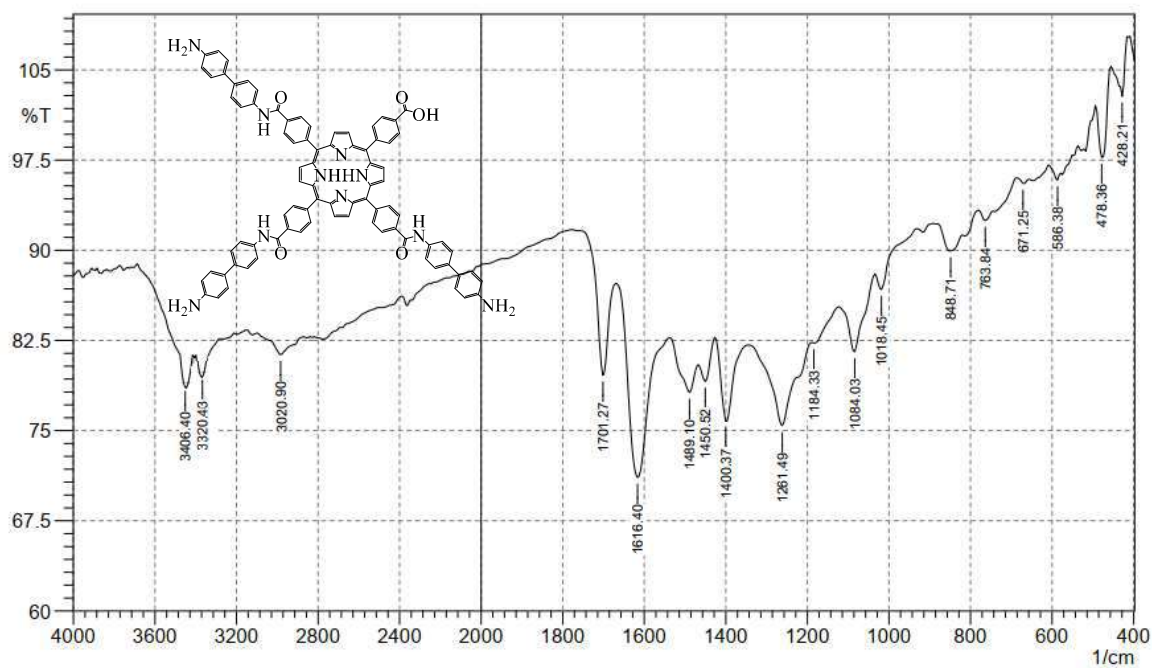
Figure 39: FT-IR spectrum of compound (6f)
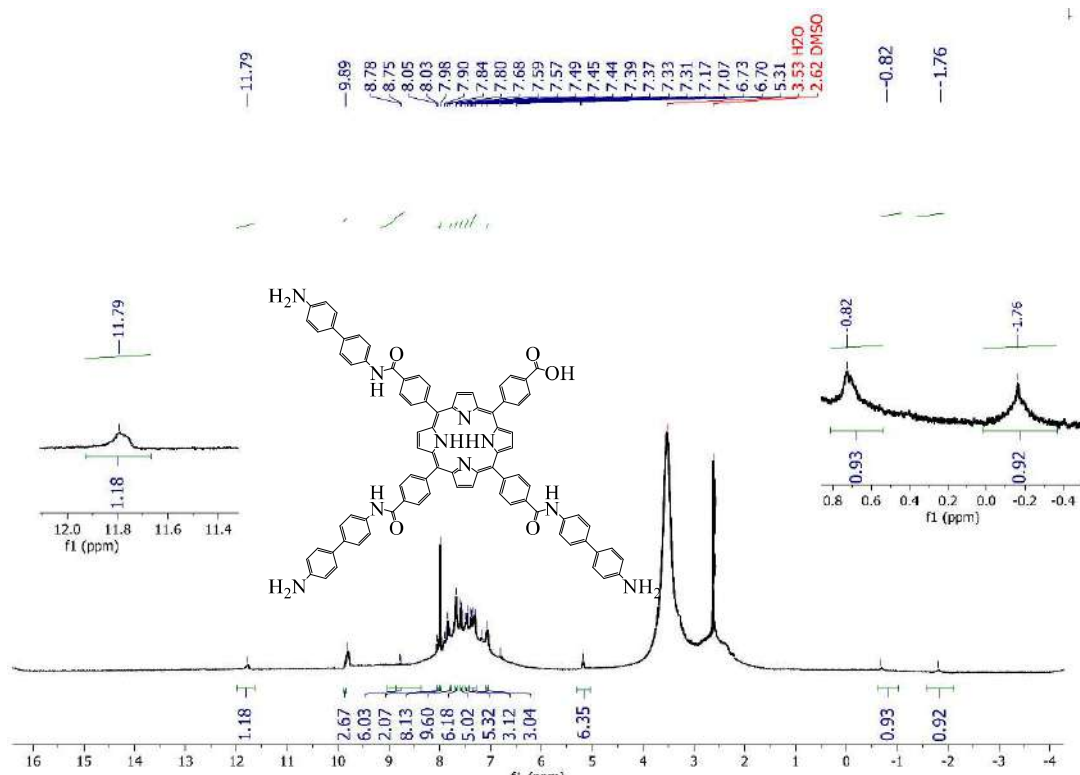
Figure 40: ^{1}HNMR spectrum of compound (6f)
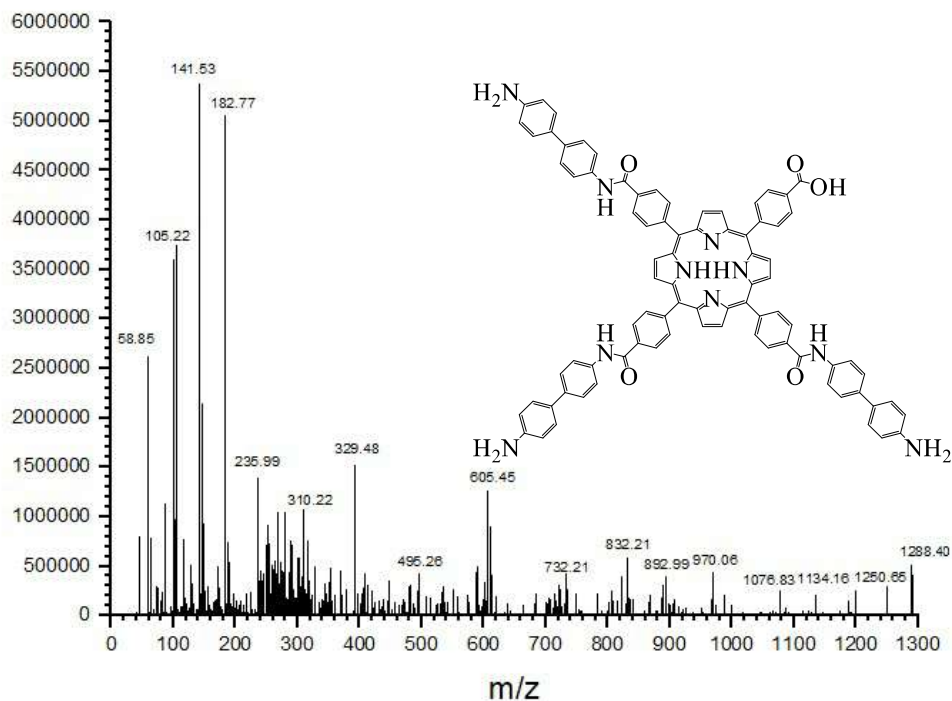
Figure 41: Mass spectrum of compound (6f)
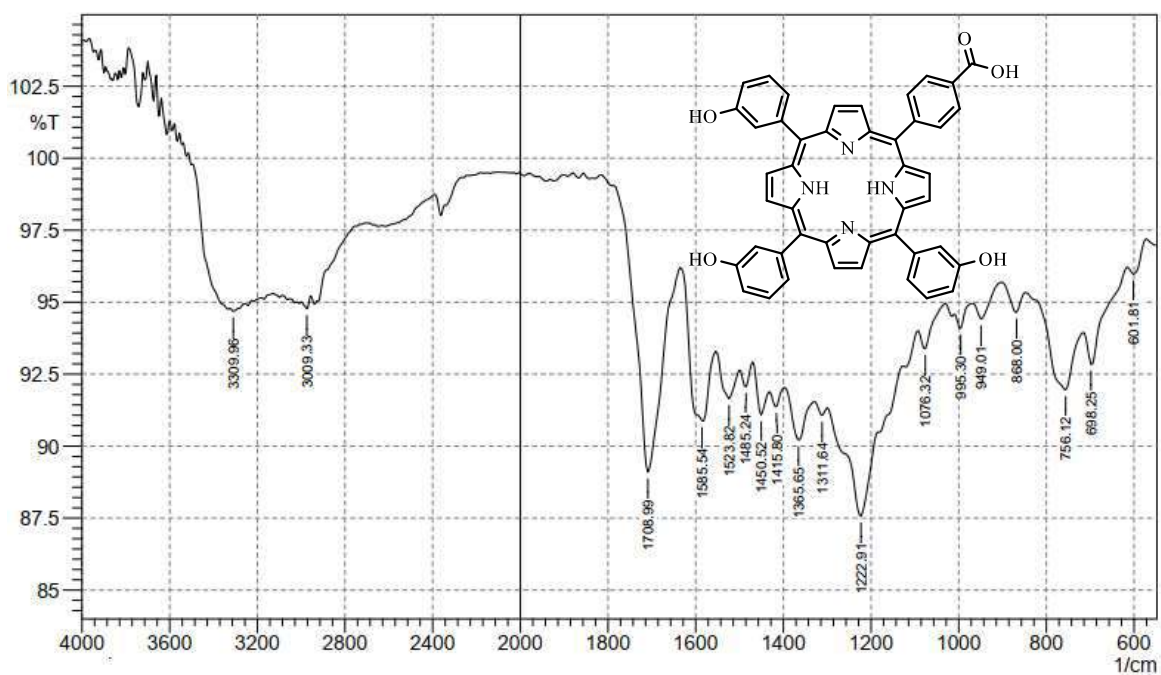
Figure 42: FT-IR spectrum of compound (8)
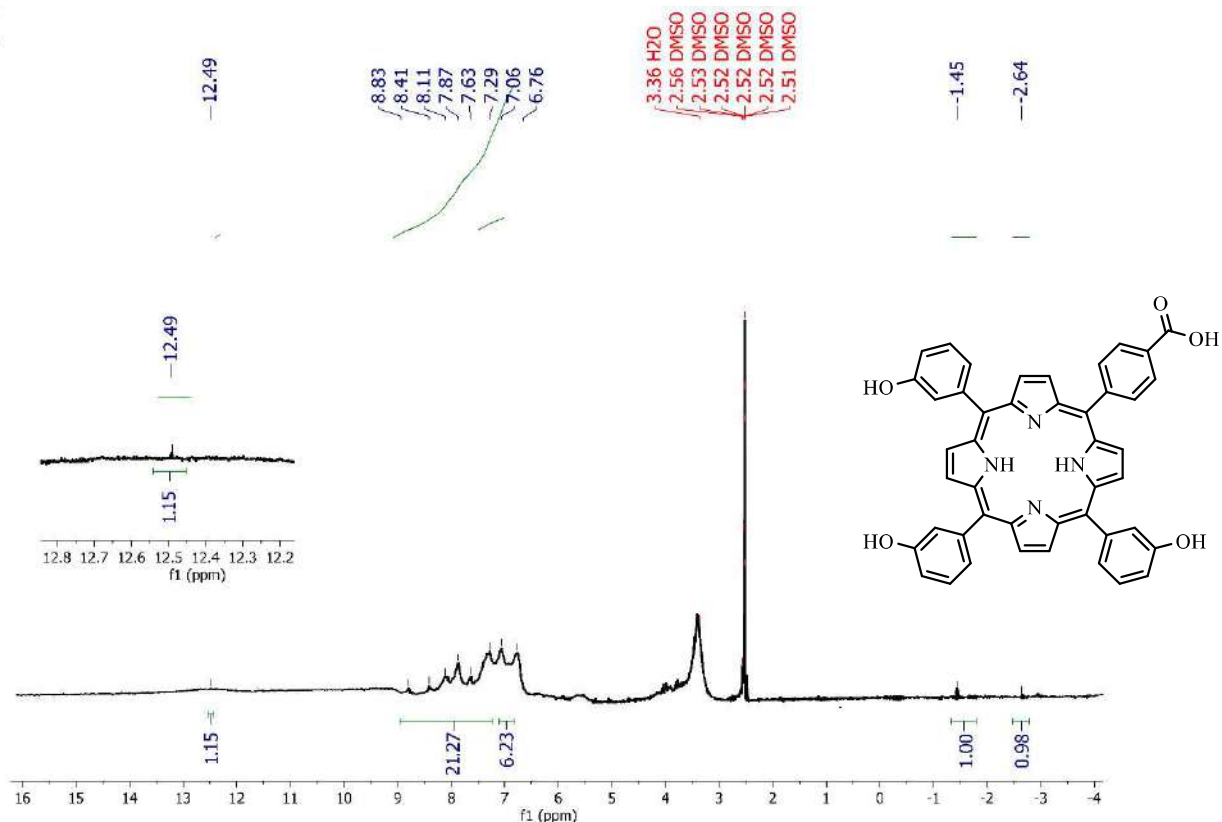
Figure 43: ^{1}HNMR spectrum of compound (8)
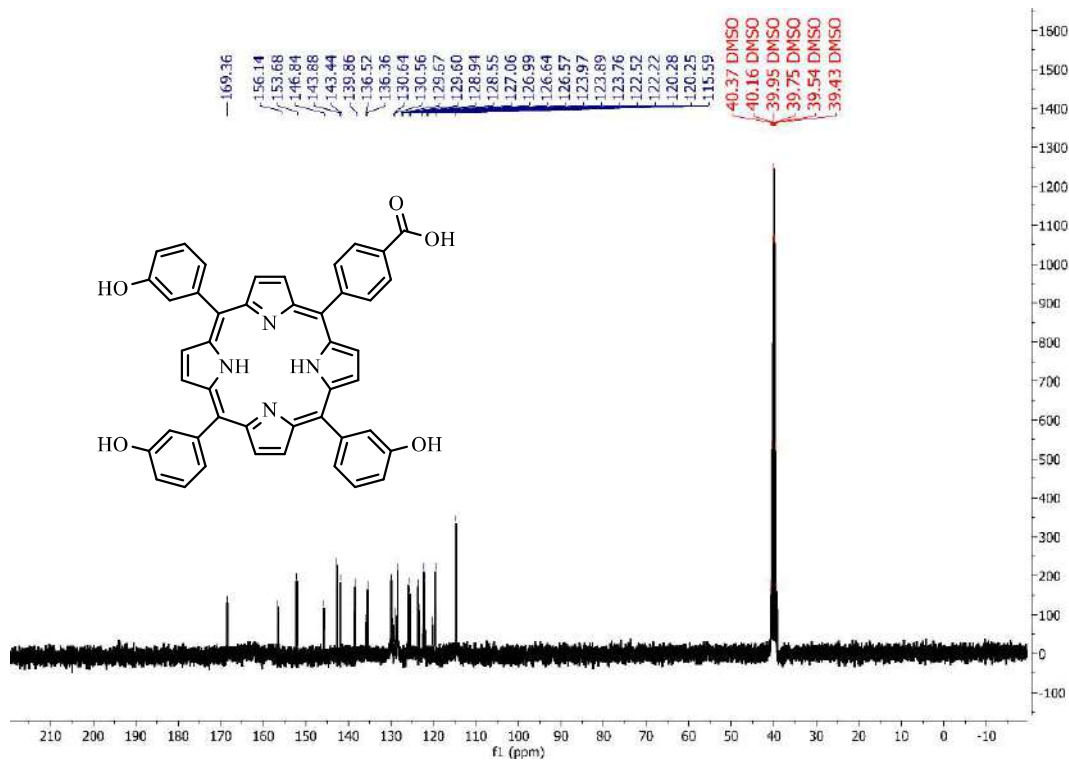
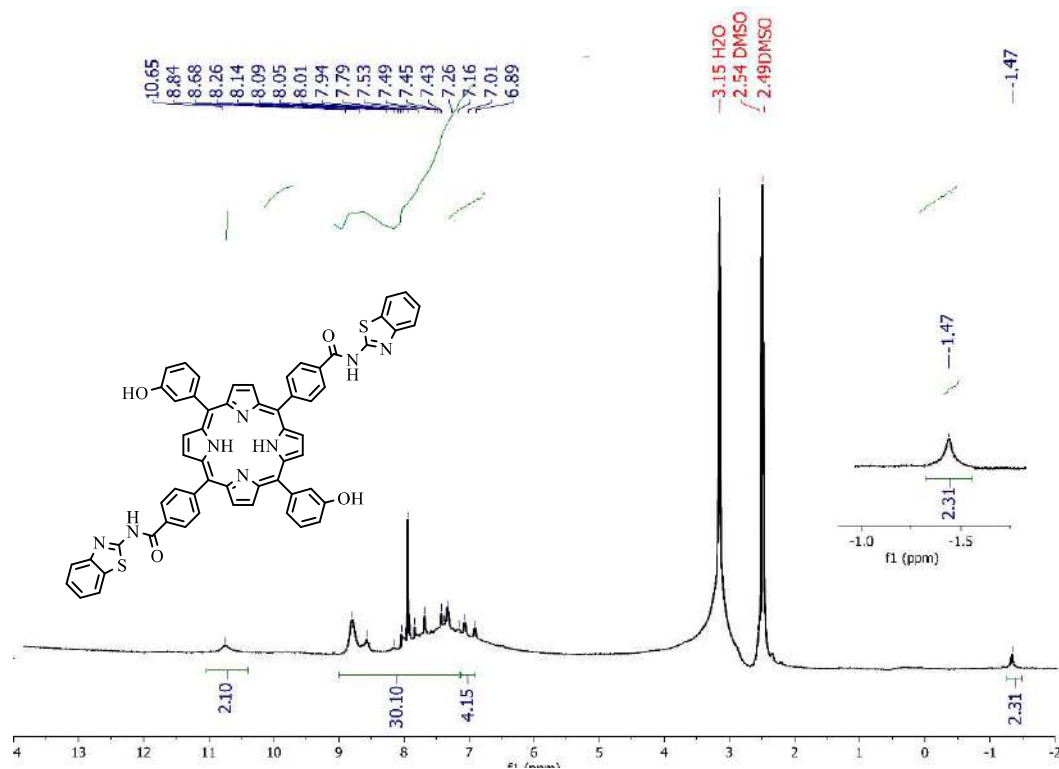**Figure 44:** ^{13}CNMR spectrum of compound (8)
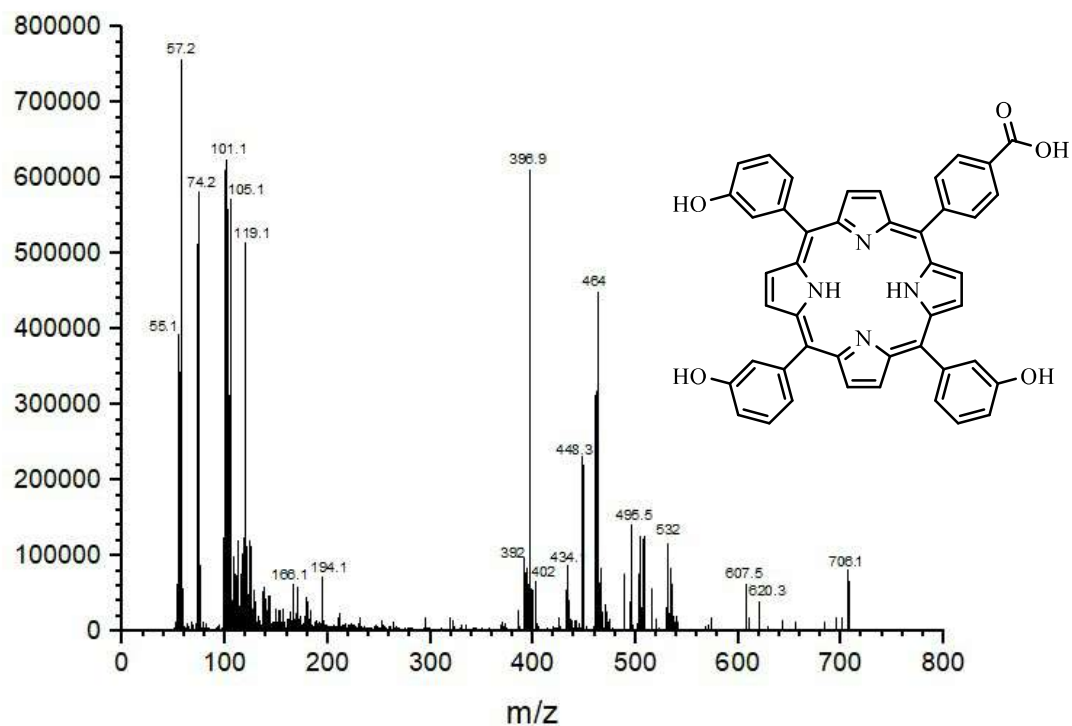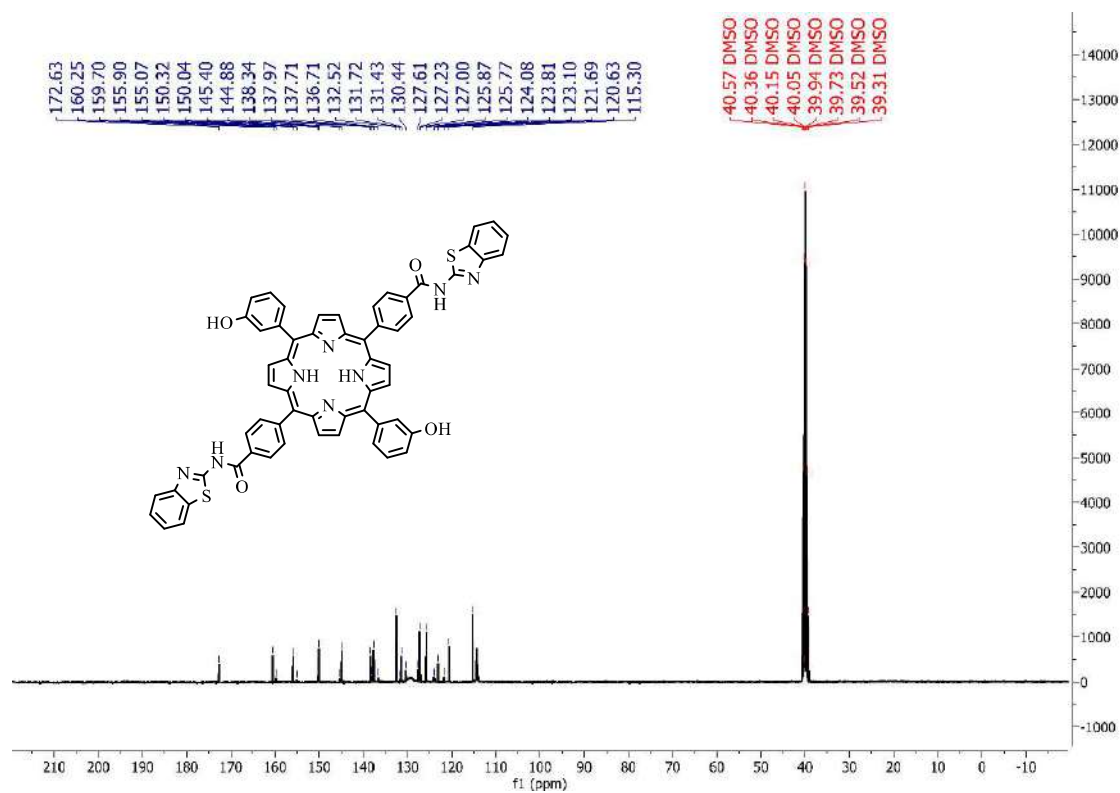
Figure 45: Mass spectrum of compound (8)
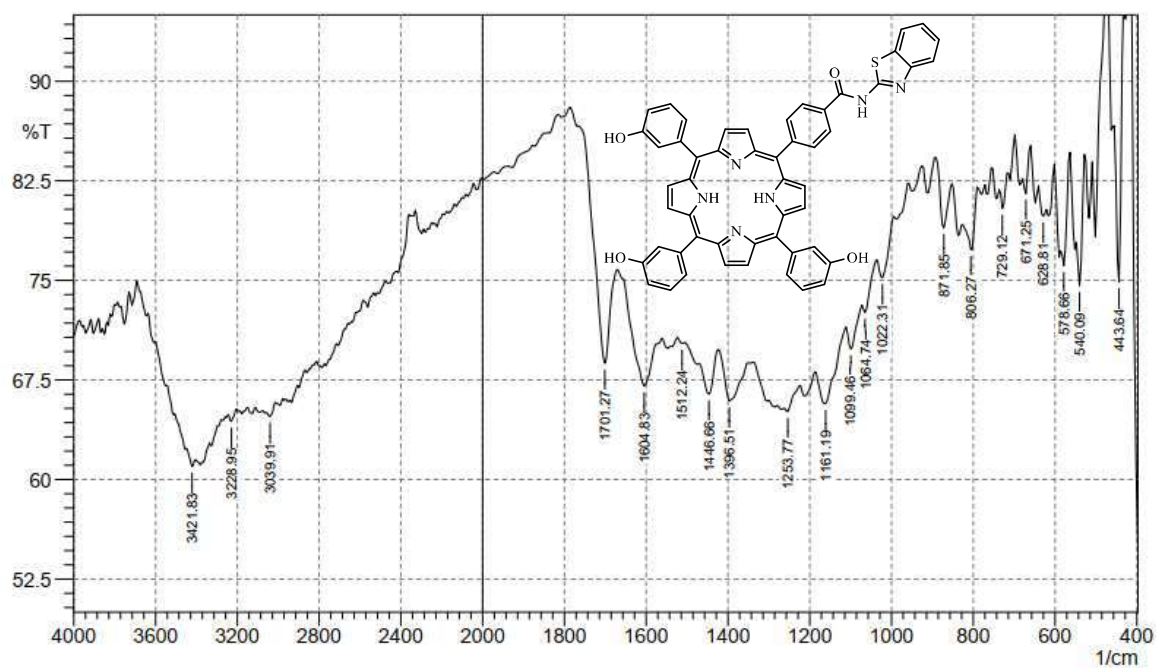
Figure 46: FT-IR spectrum of compound (9a)
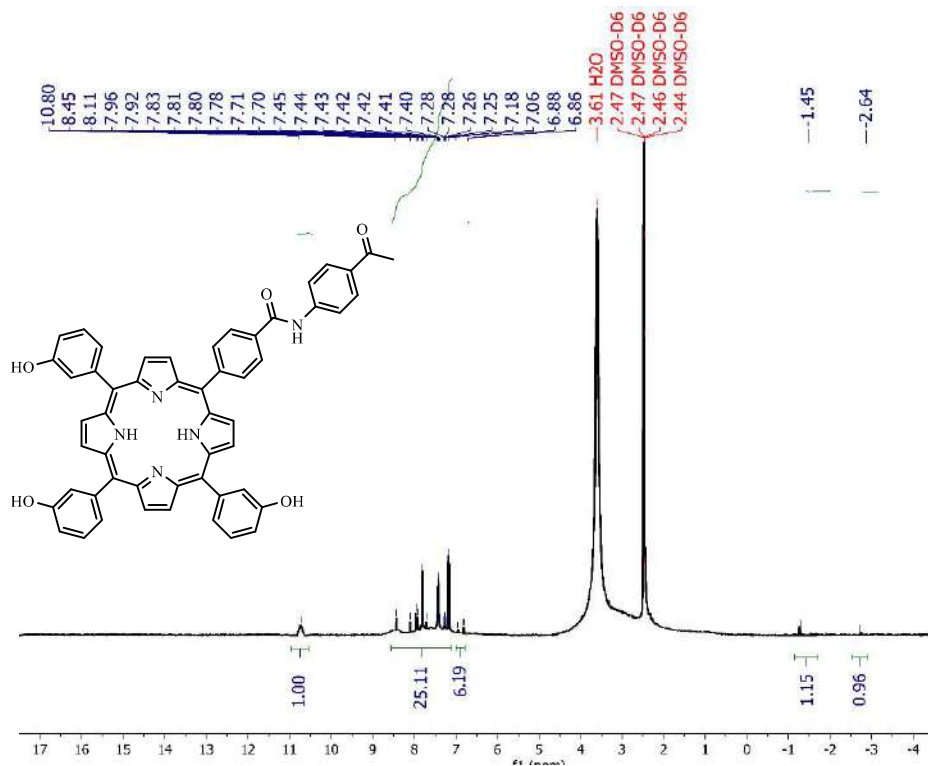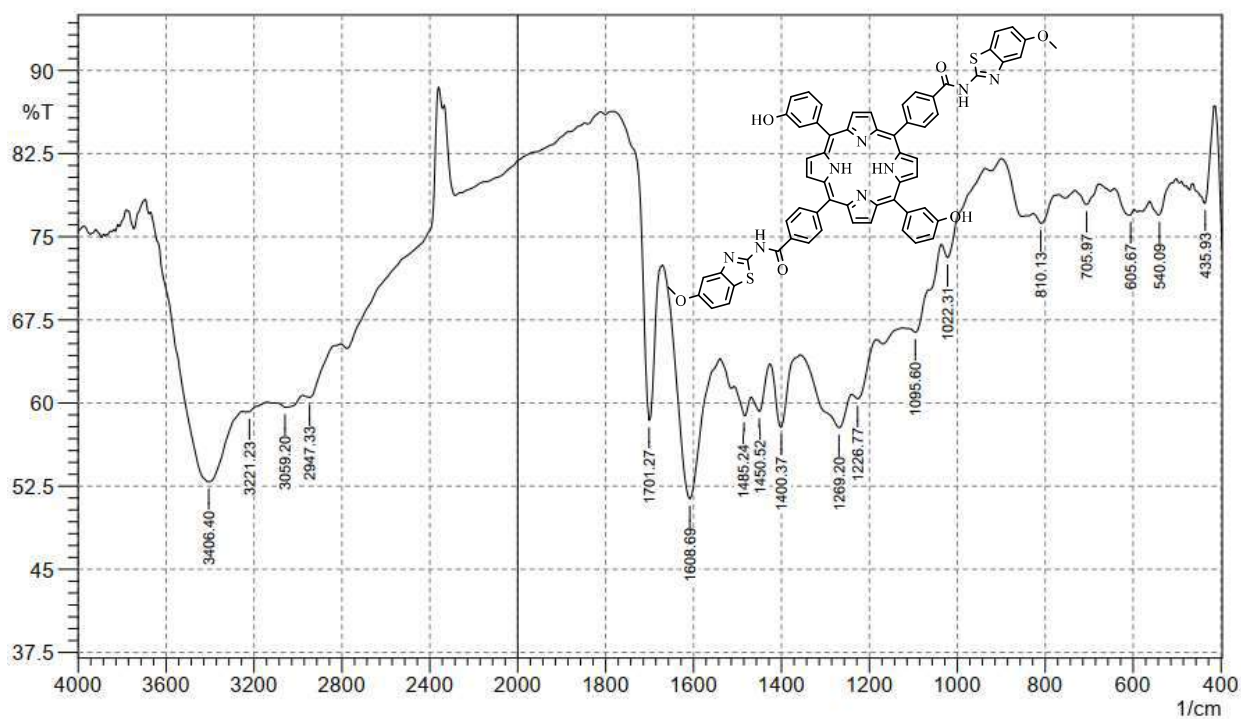
Figure 47: ^{1}HNMR spectrum of compound (9a)
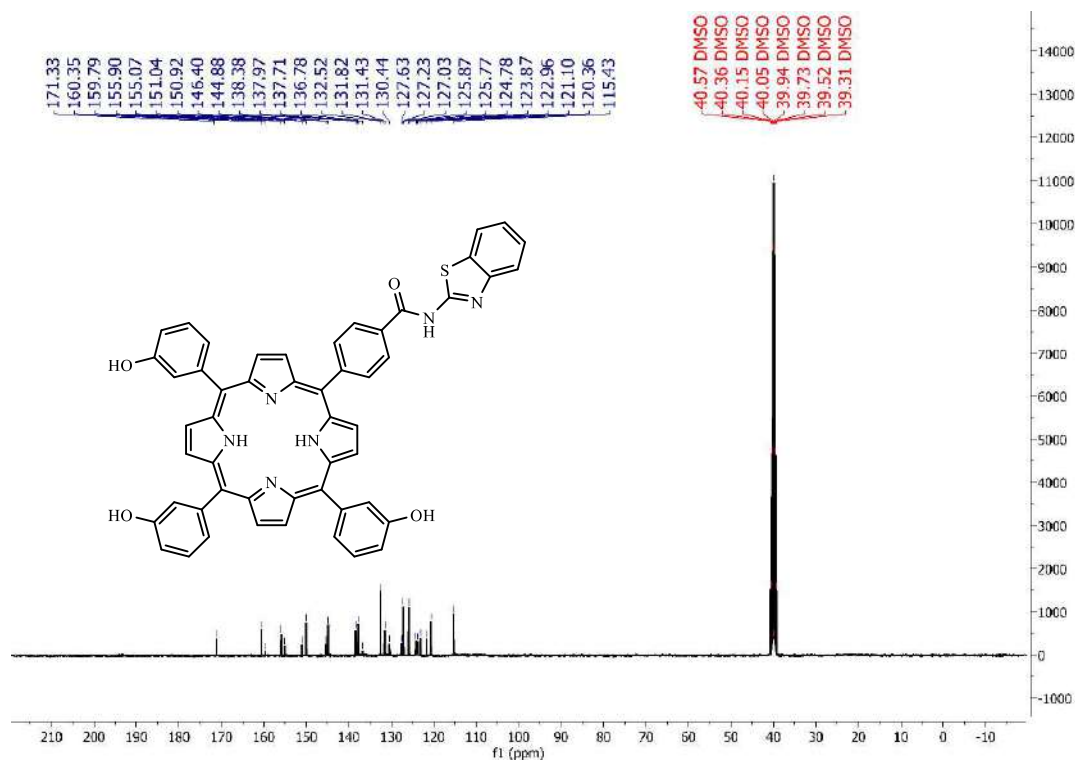
Figure 48: ^{13}CNMR spectrum of compound (9a)
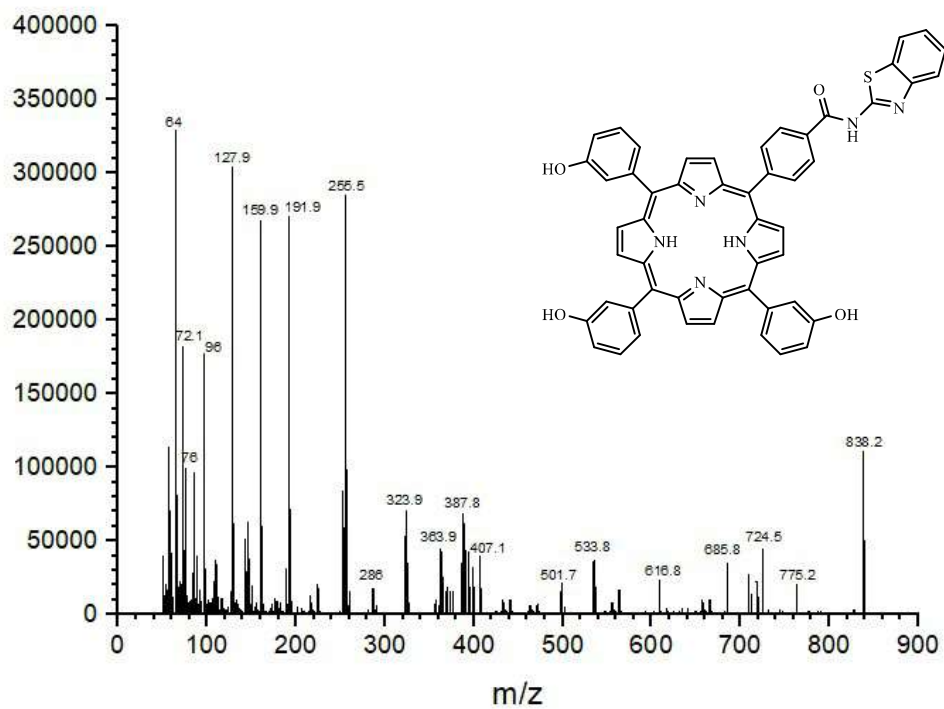
Figure 49: Mass spectrum of compound (9a)
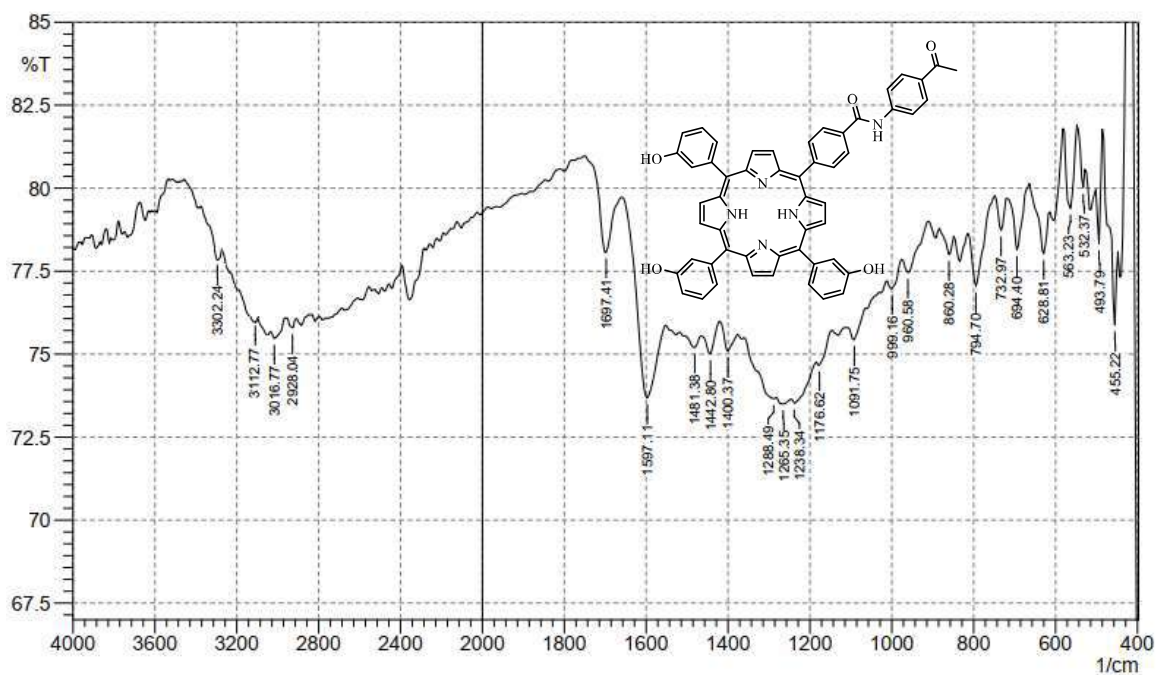
Figure 50: FT-IR spectrum of compound (9b)
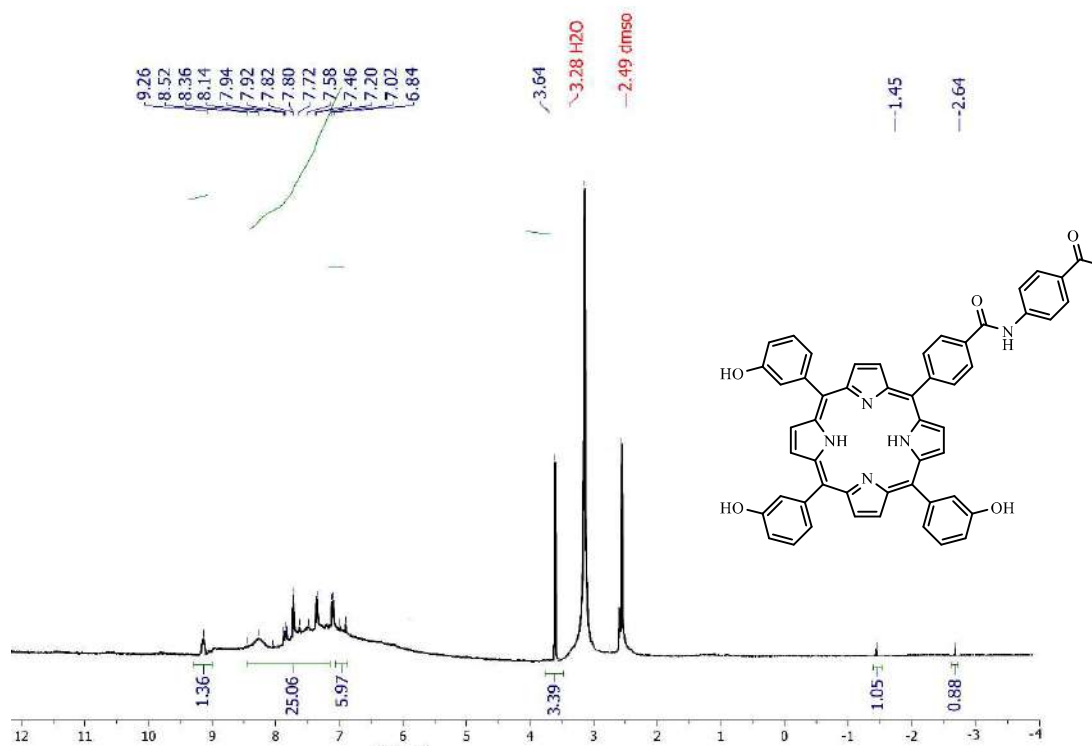
Figure 51: ^{1}HNMR spectrum of compound (9b)
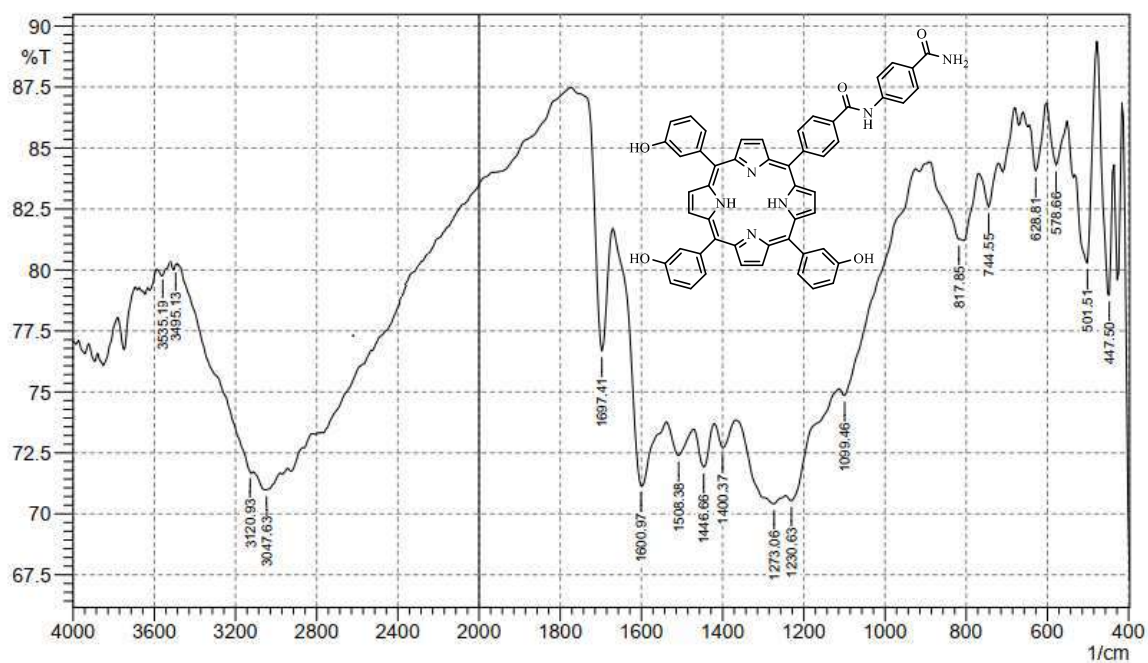
Figure 52: FT-IR spectrum of compound (9c)
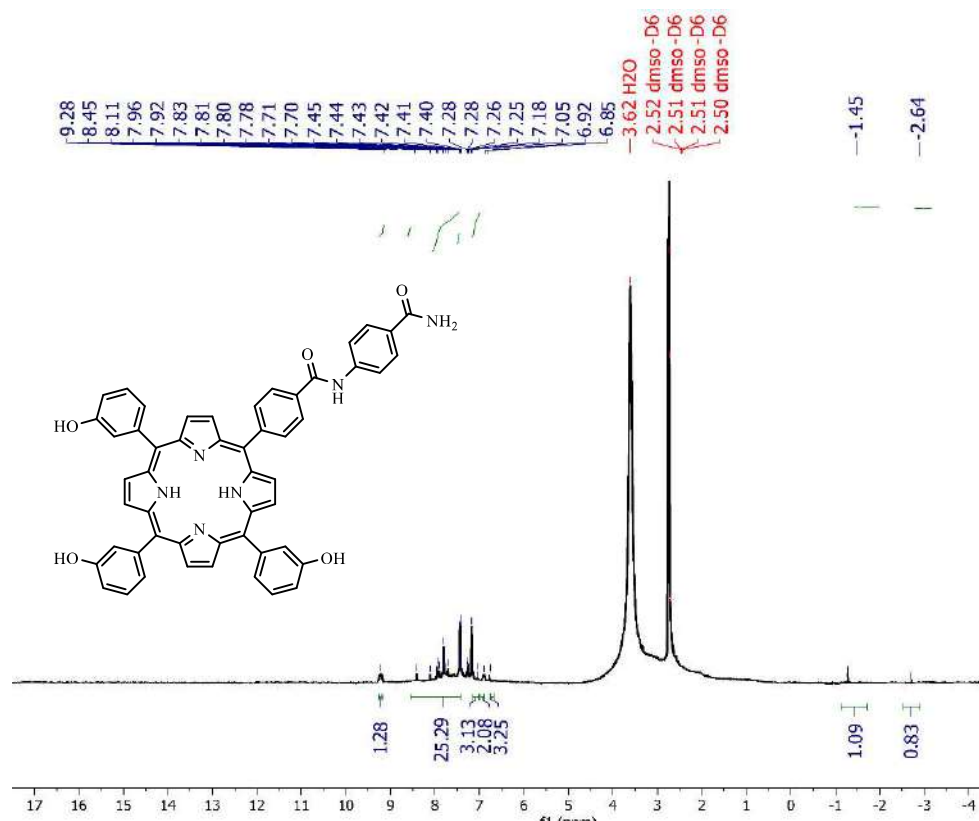
Figure 53: ^{1}HNMR spectrum of compound (9c)
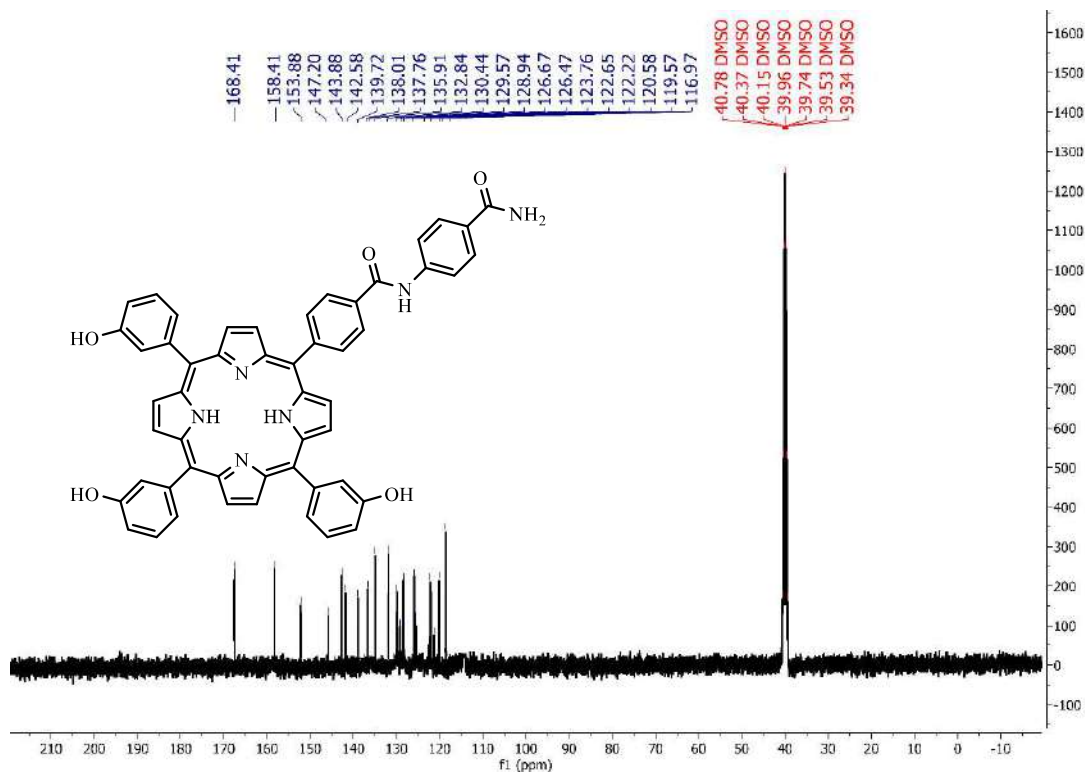
Figure 54: ^{13}CNMR spectrum of compound (9c)
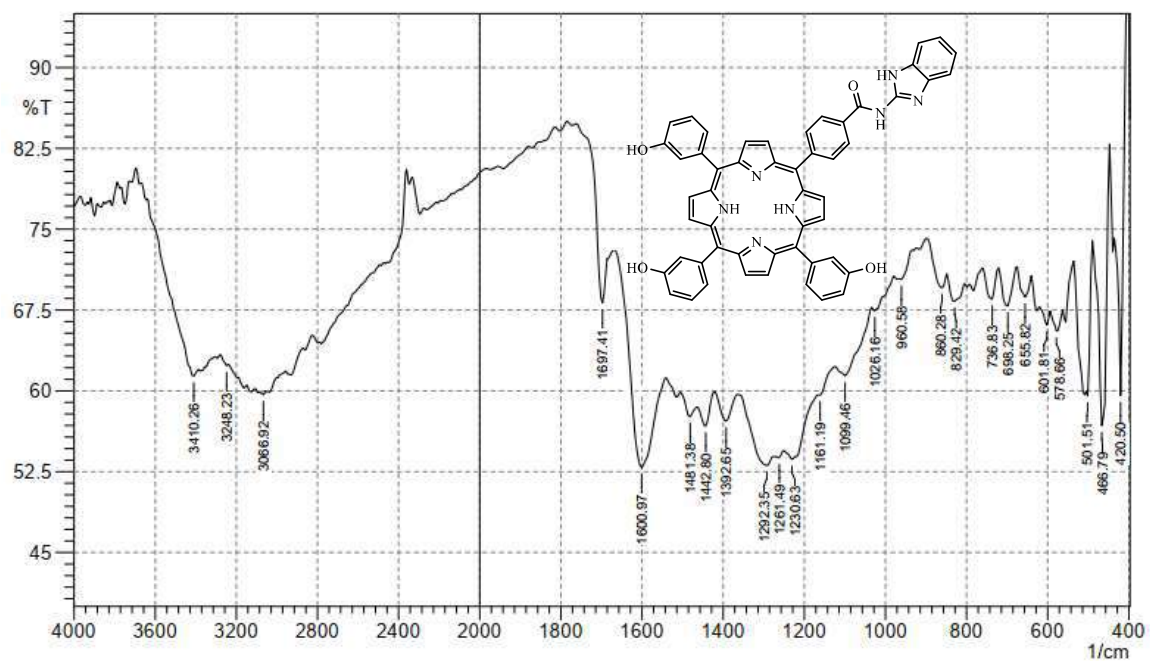
Figure 55: FT-IR spectrum of compound (9d)
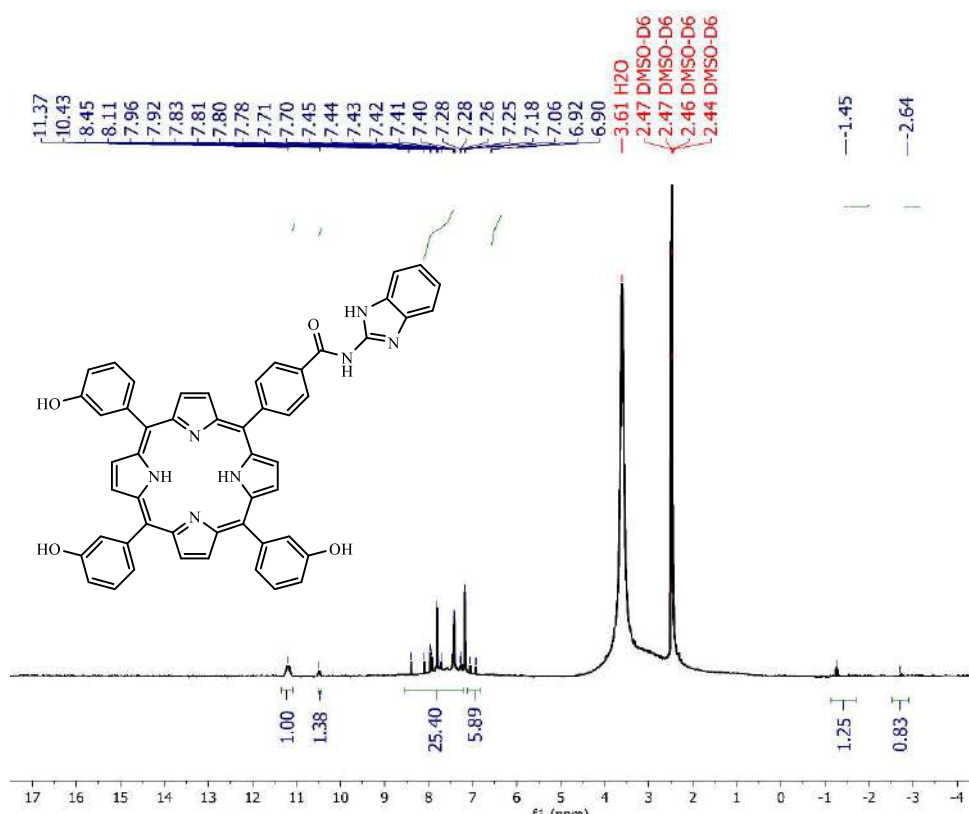
Figure 56: ^{1}HNMR spectrum of compound (9d)
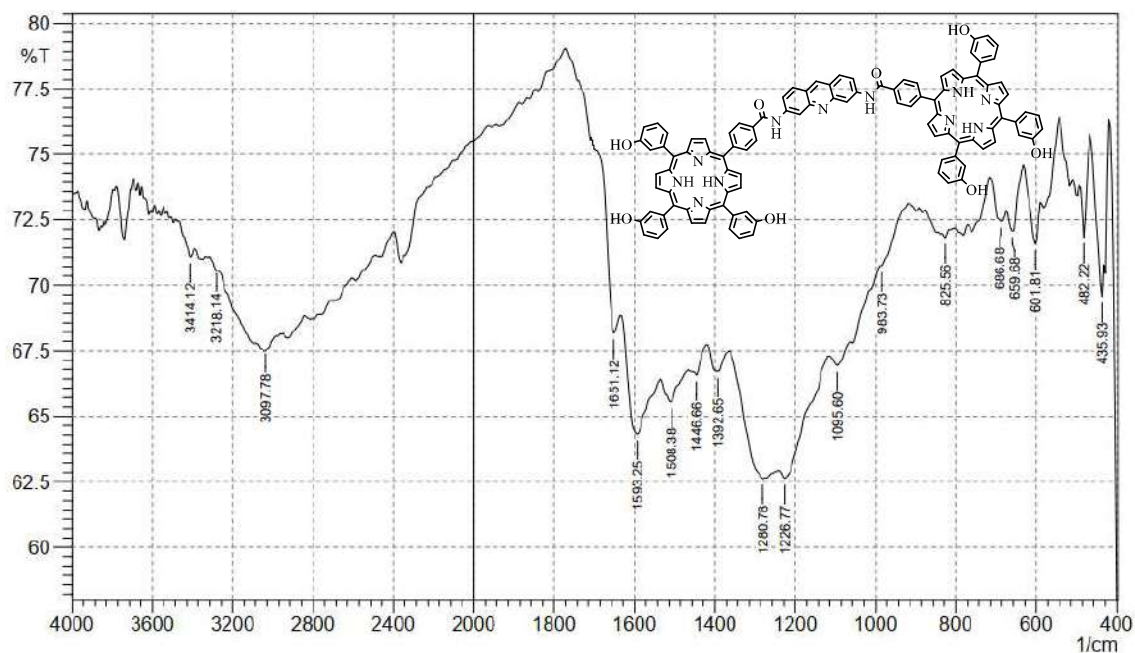
Figure 57: FT-IR spectrum of compound (11a)
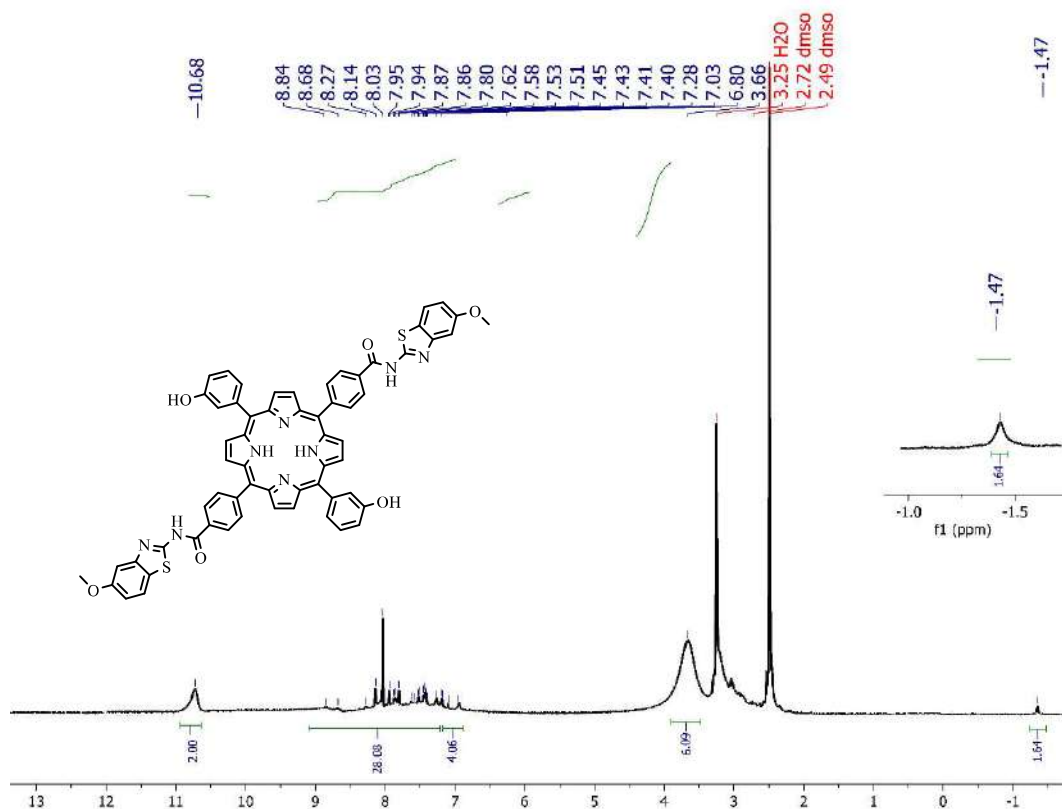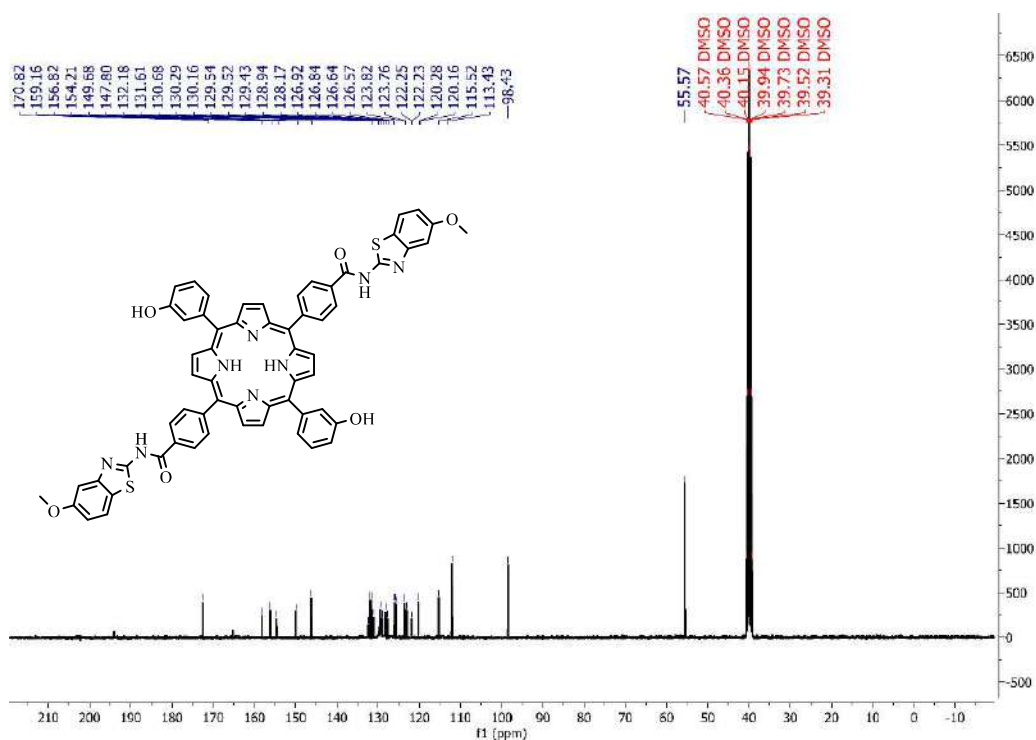

Figure 58: ^{1}HNMR spectrum of compound (11a)
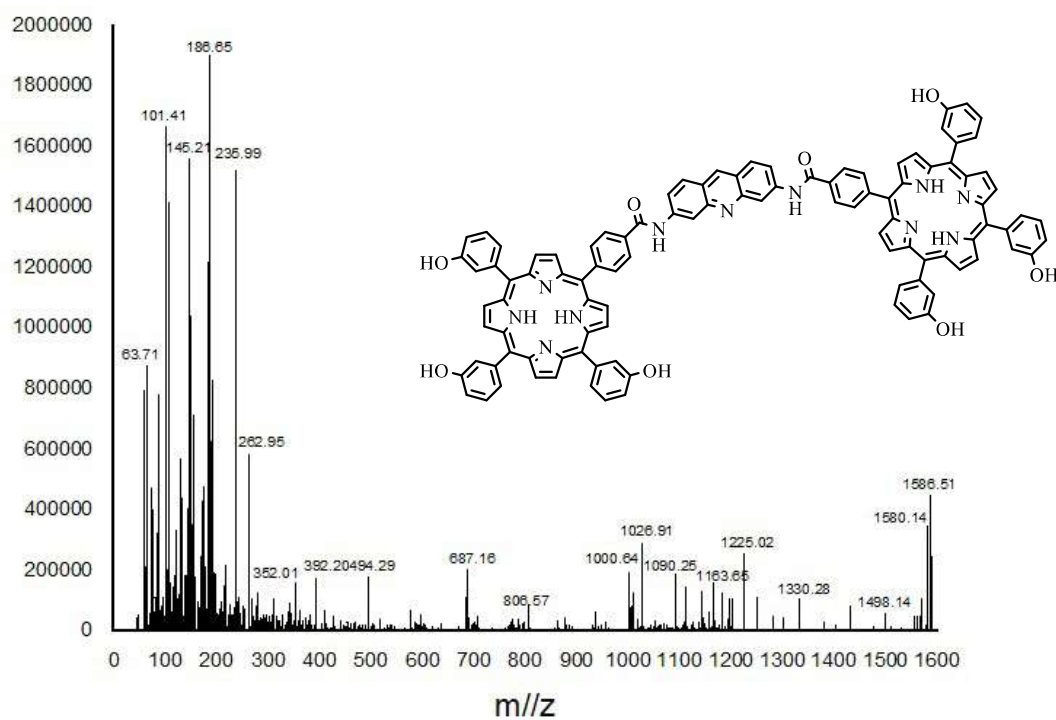
Figure 59: Mass spectrum of compound (11a)

Figure 60: FT-IR spectrum of compound (11b)
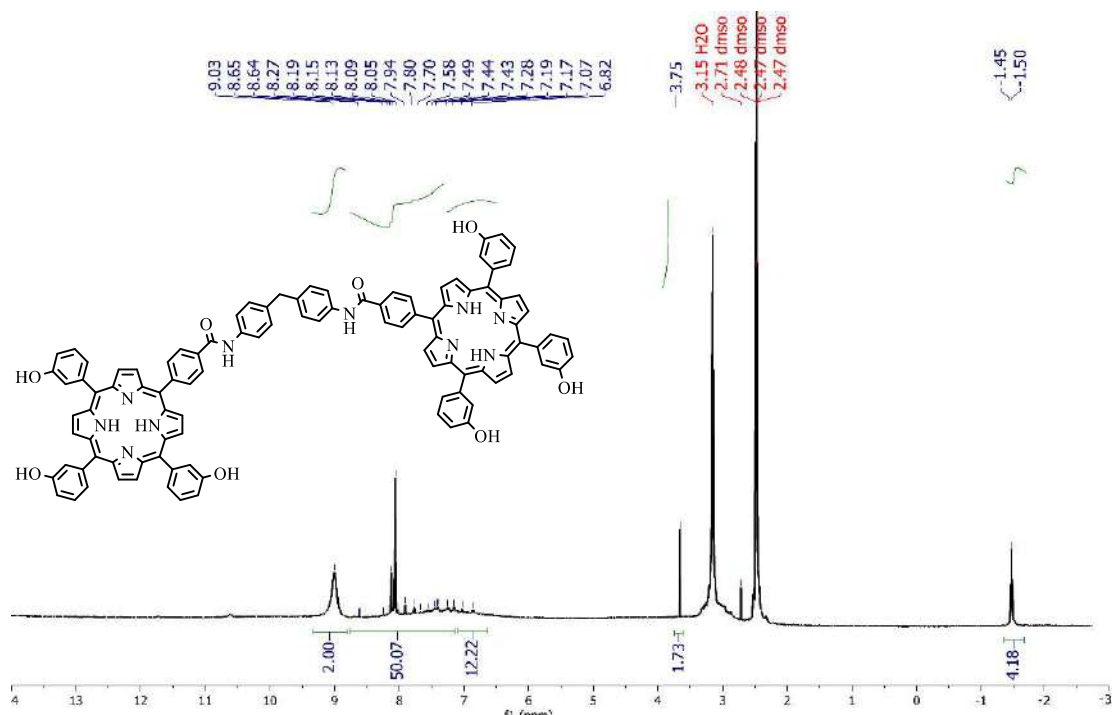
Figure 61: ^{1}HNMR spectrum of compound (11b)
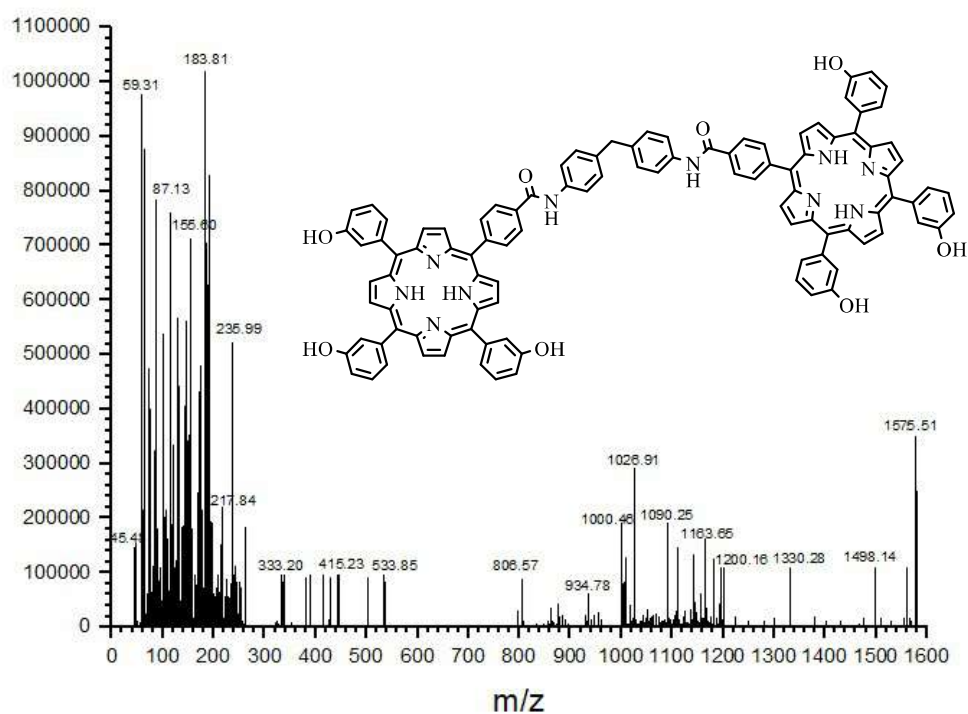
Figure 62: Mass spectrum of compound (11b)

Figure 63: FT-IR spectrum of compound (11c)
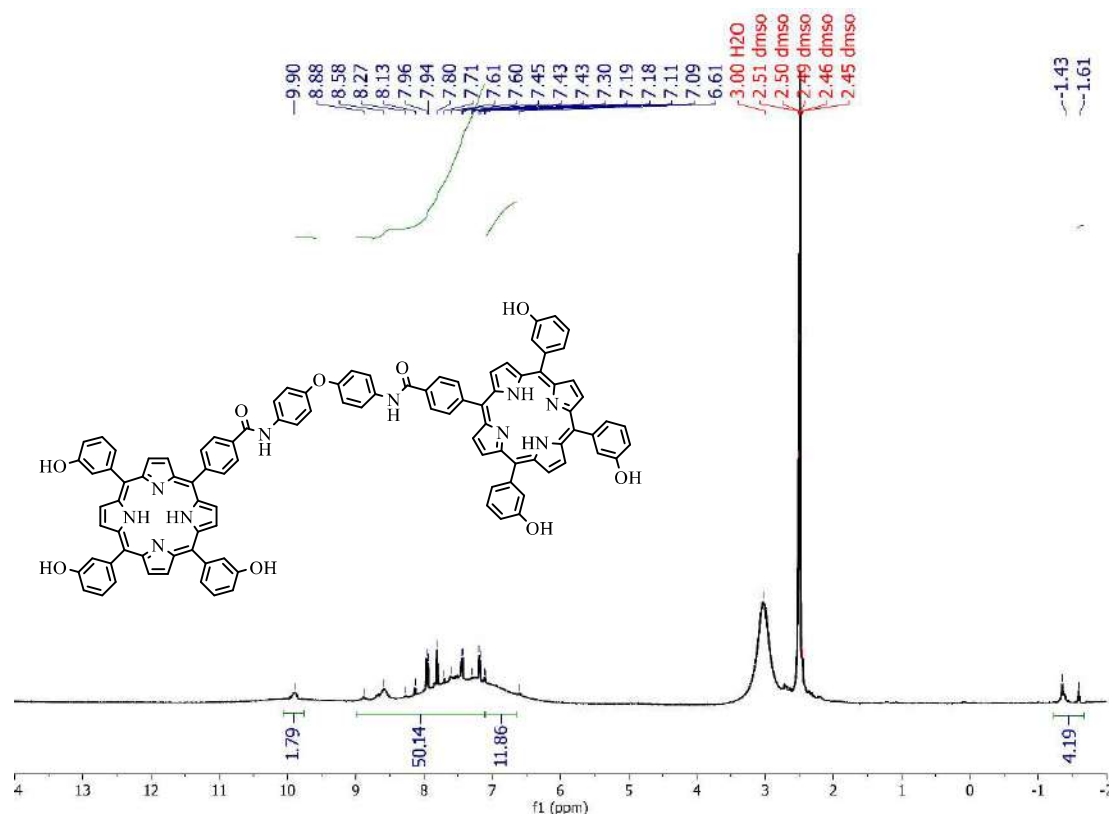
Figure 64: ^{1}HNMR spectrum of compound (11c)
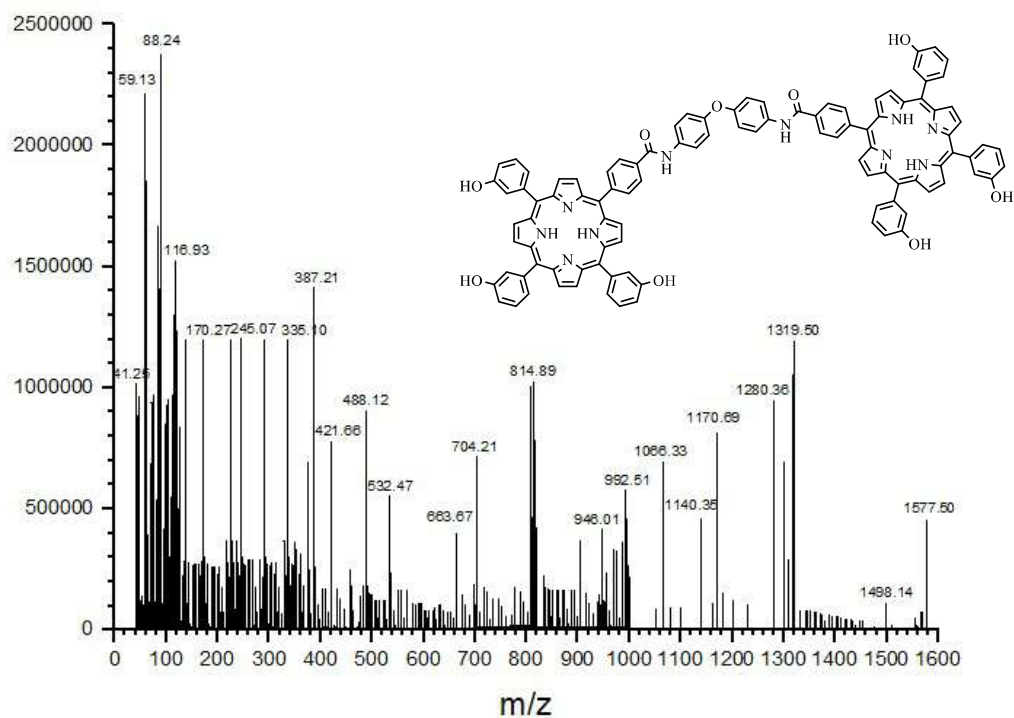
Figure 65: Mass spectrum of compound (11c)

Figure 66: FT-IR spectrum of compound (11d)
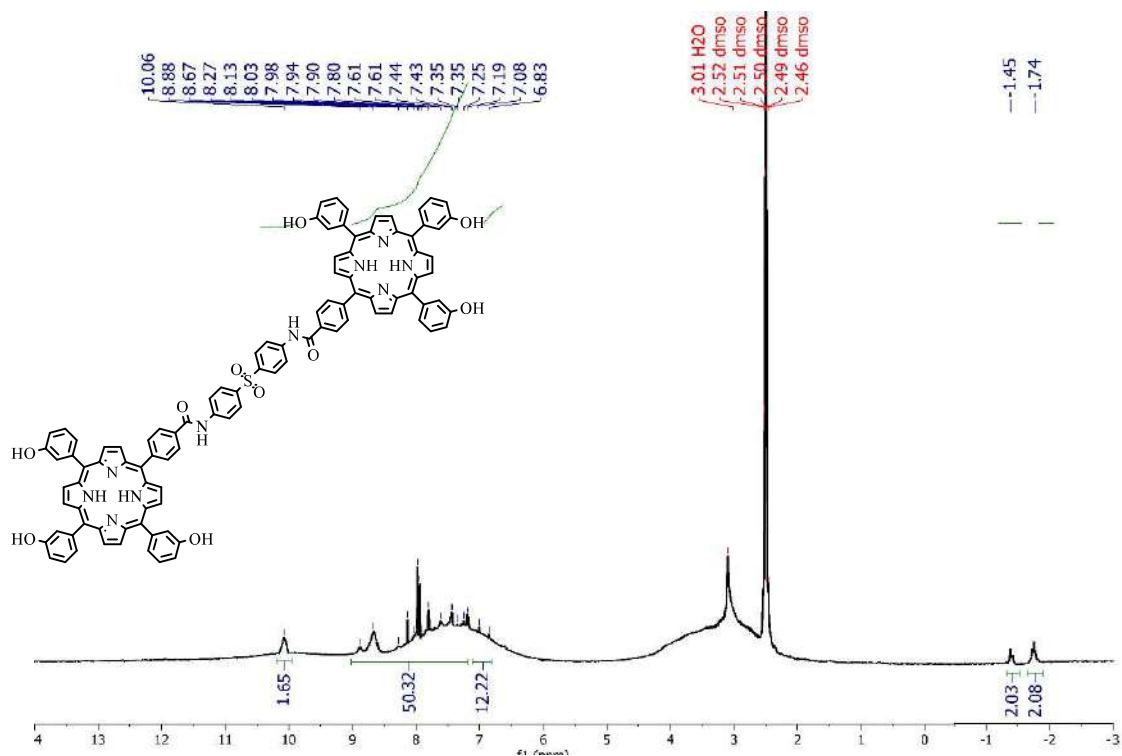
Figure 67: ^{1}HNMR spectrum of compound (11d)
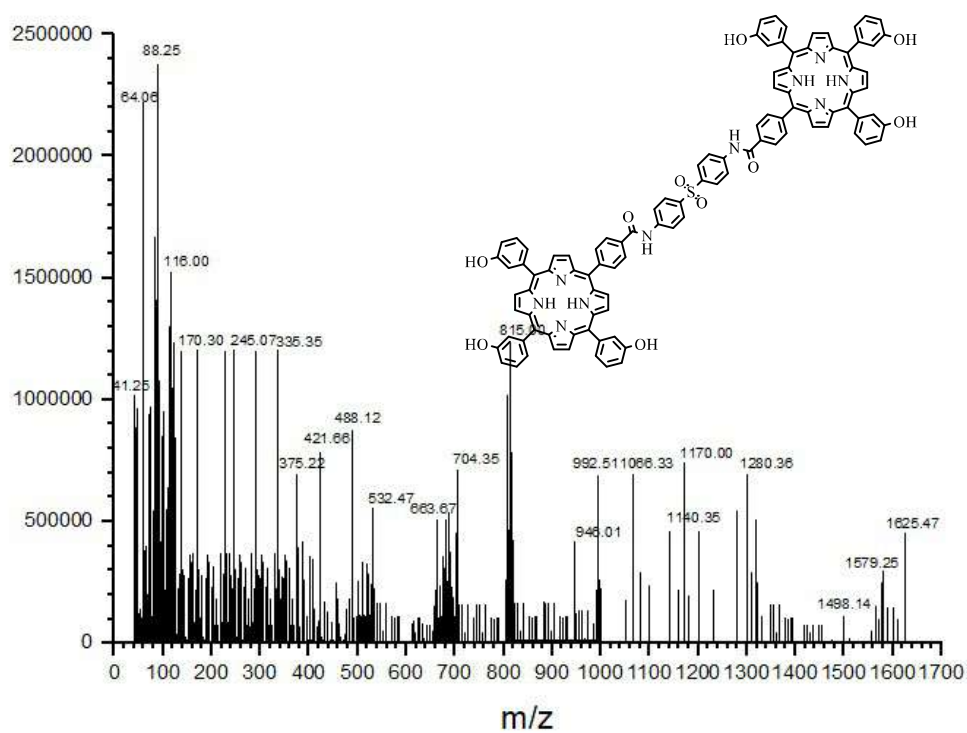
Figure 68: Mass spectrum of compound (11d)

Figure 69: FT-IR spectrum of compound (11e)
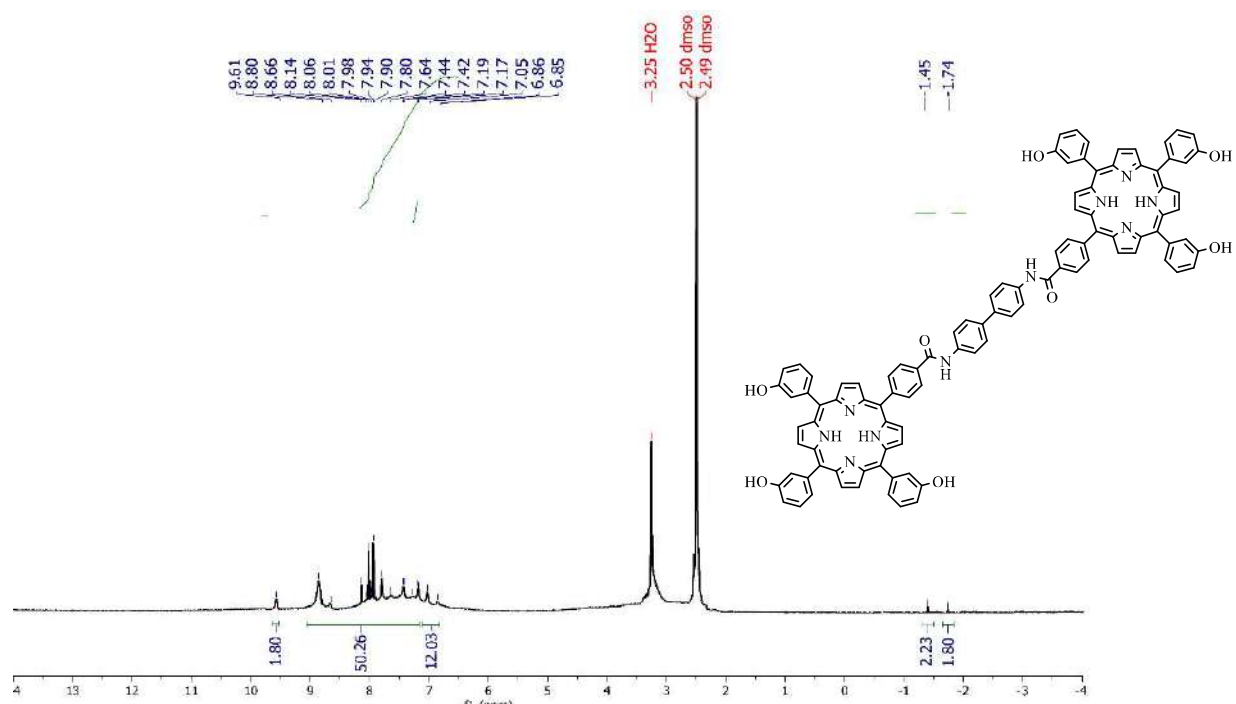
Figure 70: ¹HNMR spectrum of compound (11e)
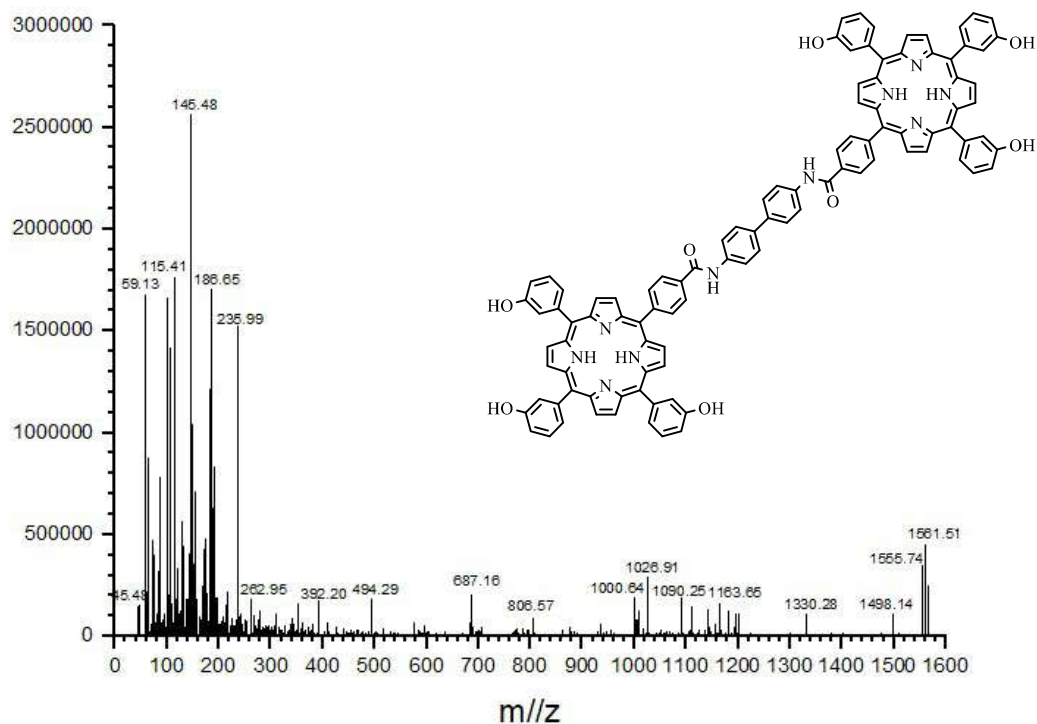
Figure 71: Mass spectrum of compound (11e)
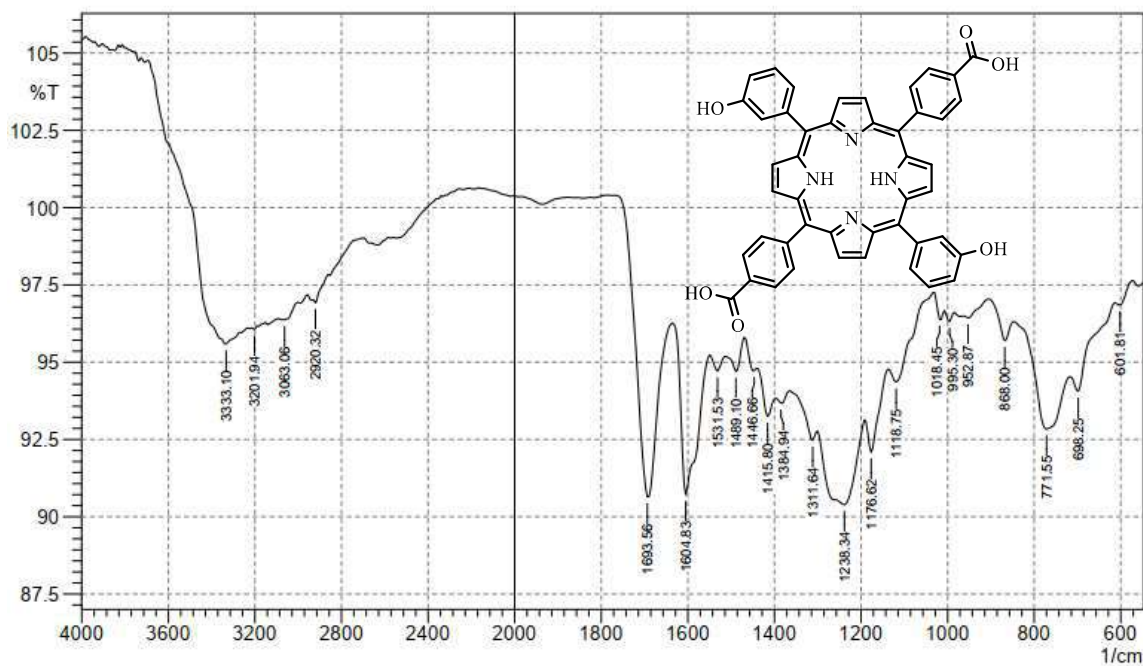
Figure 72: FT-IR spectrum of compound (12)
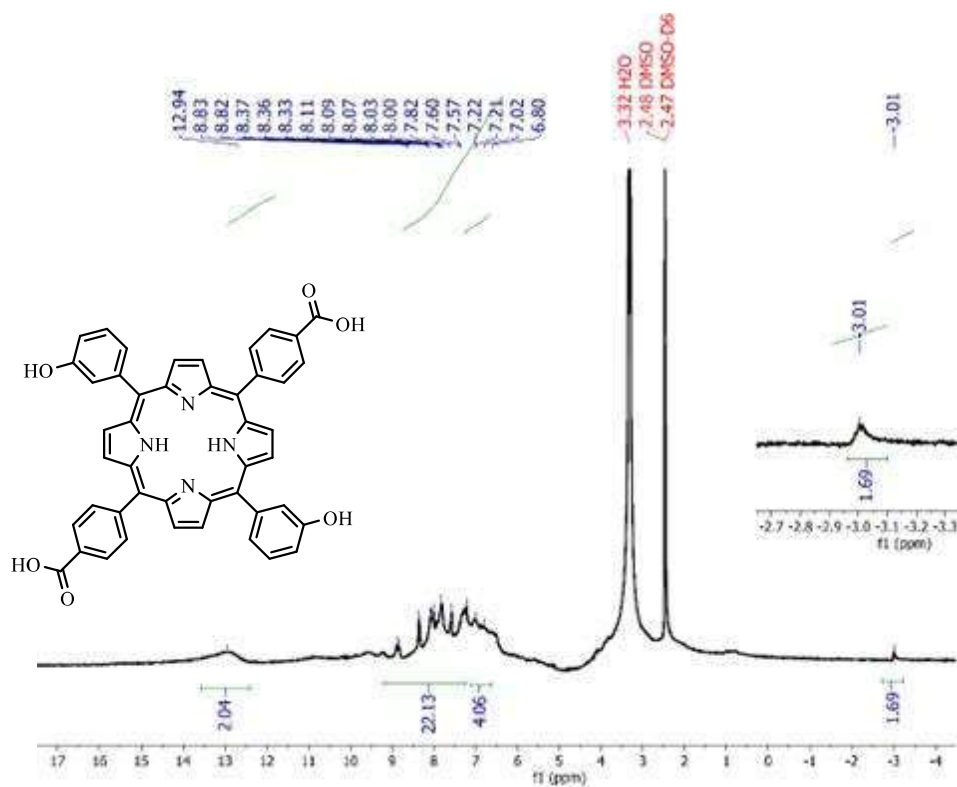
Figure 73: ^{1}HNMR spectrum of compound (12)

Figure 74: ^{13}CNMR spectrum of compound (12)

Figure 75: Mass spectrum of compound (12)

Figure 76: FT-IR spectrum of compound (13a)

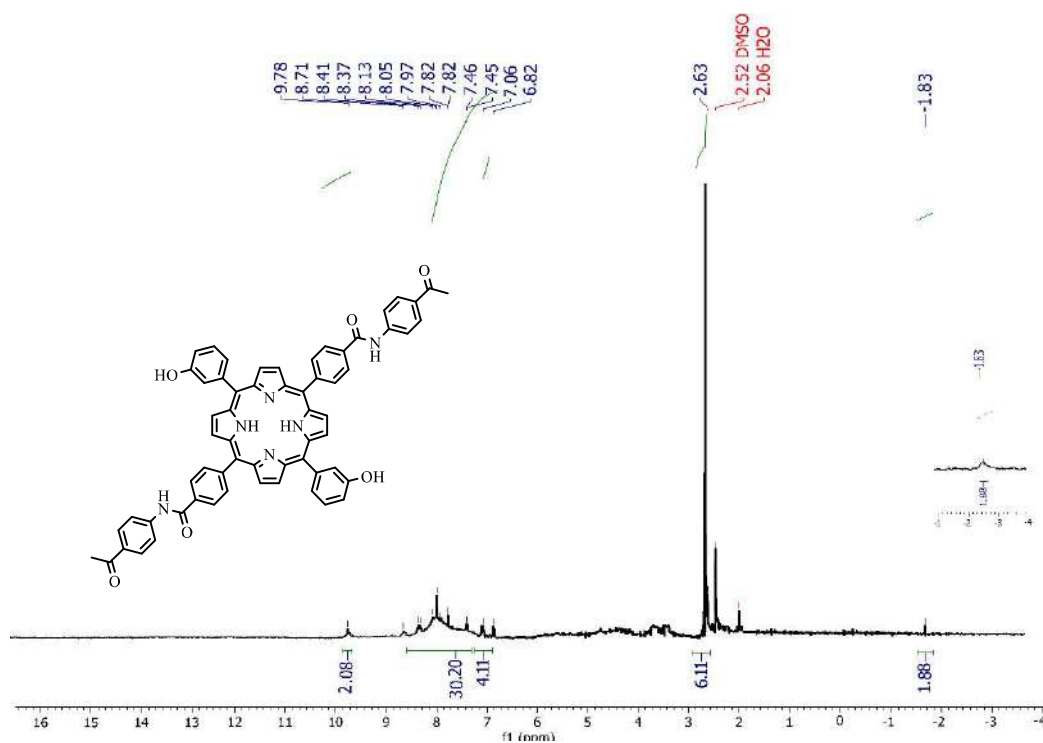**Figure 77:** ^{1}HNMR spectrum of compound (13a)

Figure 78: ^{13}CNMR spectrum of compound (13a)
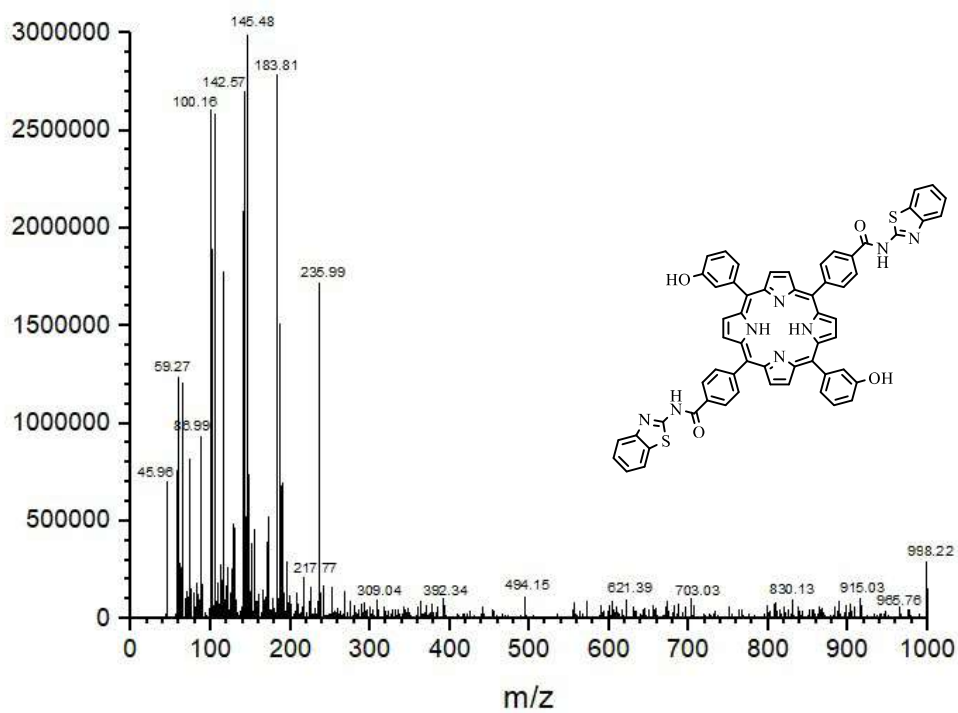
Figure 79: Mass spectrum of compound (13a)

Figure 80: FT-IR spectrum of compound (13b)

Figure 81: ^{1}HNMR spectrum of compound (13b)

Figure 82: ^{13}CNMR spectrum of compound (13b)
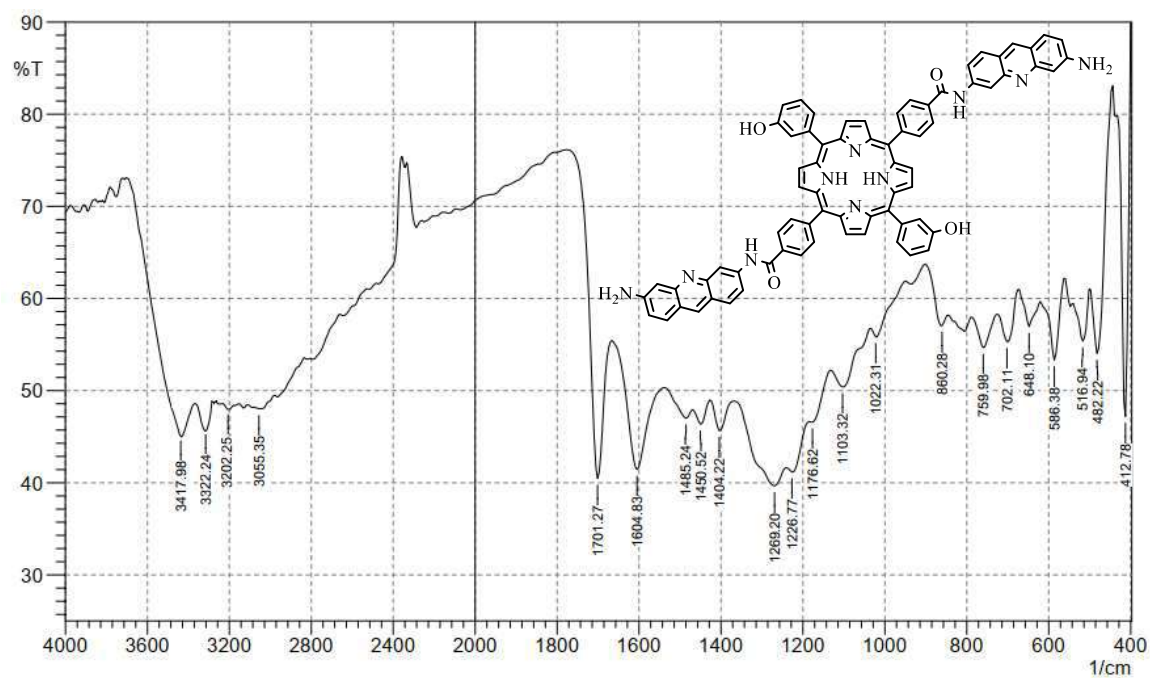
Figure 83: FT-IR spectrum of compound (13c)
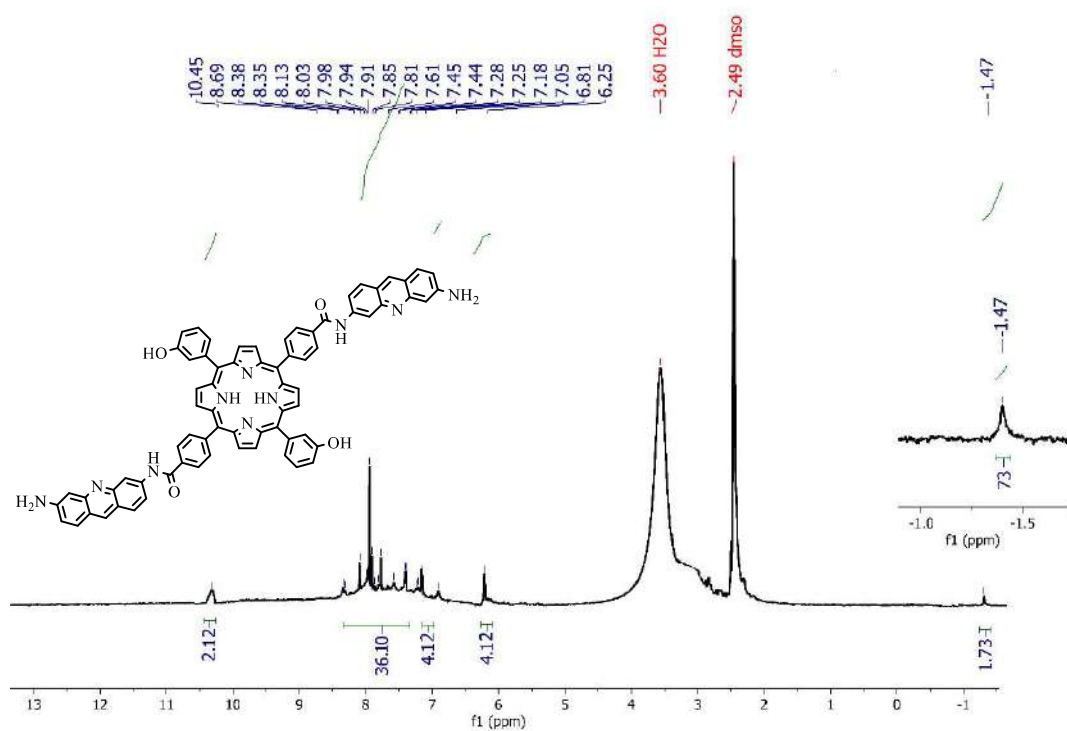
Figure 84: ^{1}HNMR spectrum of compound (13c)
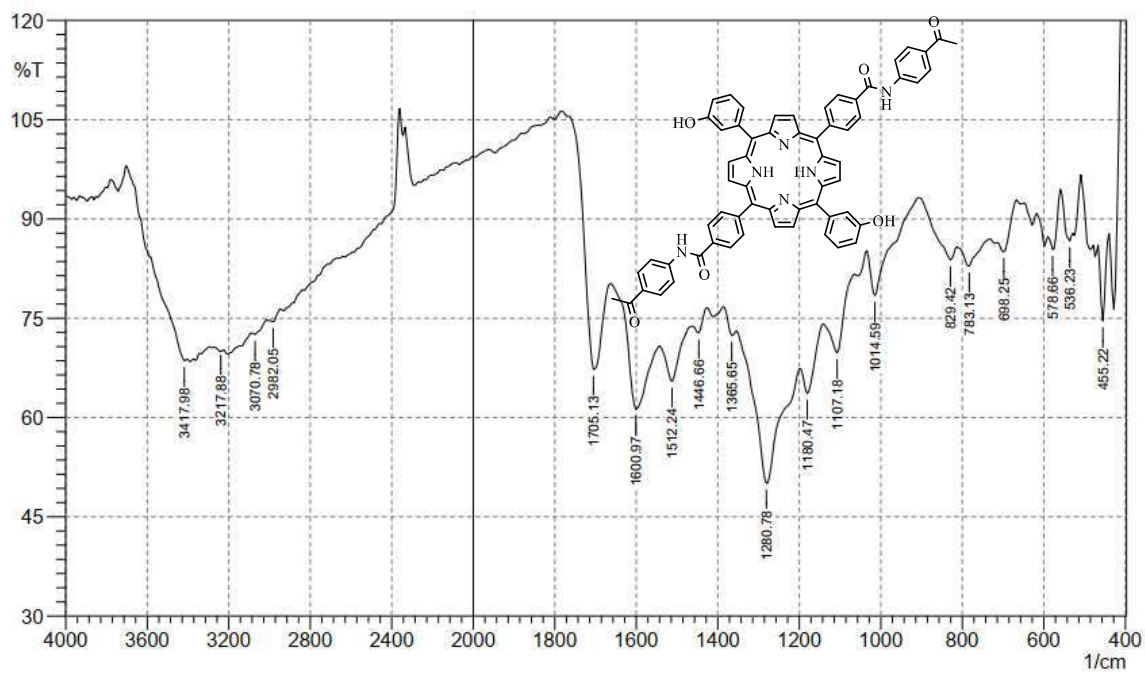
Figure 85: FT-IR spectrum of compound (13d)
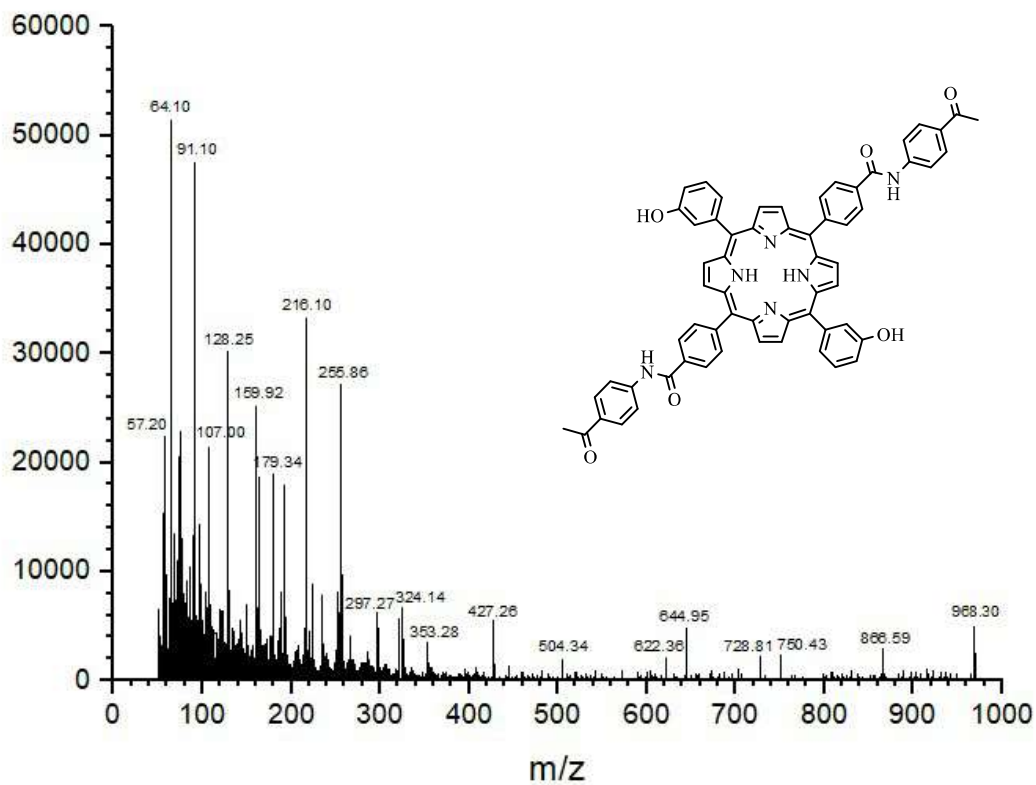

Figure 86: ^{1}HNMR spectrum of compound (13d)
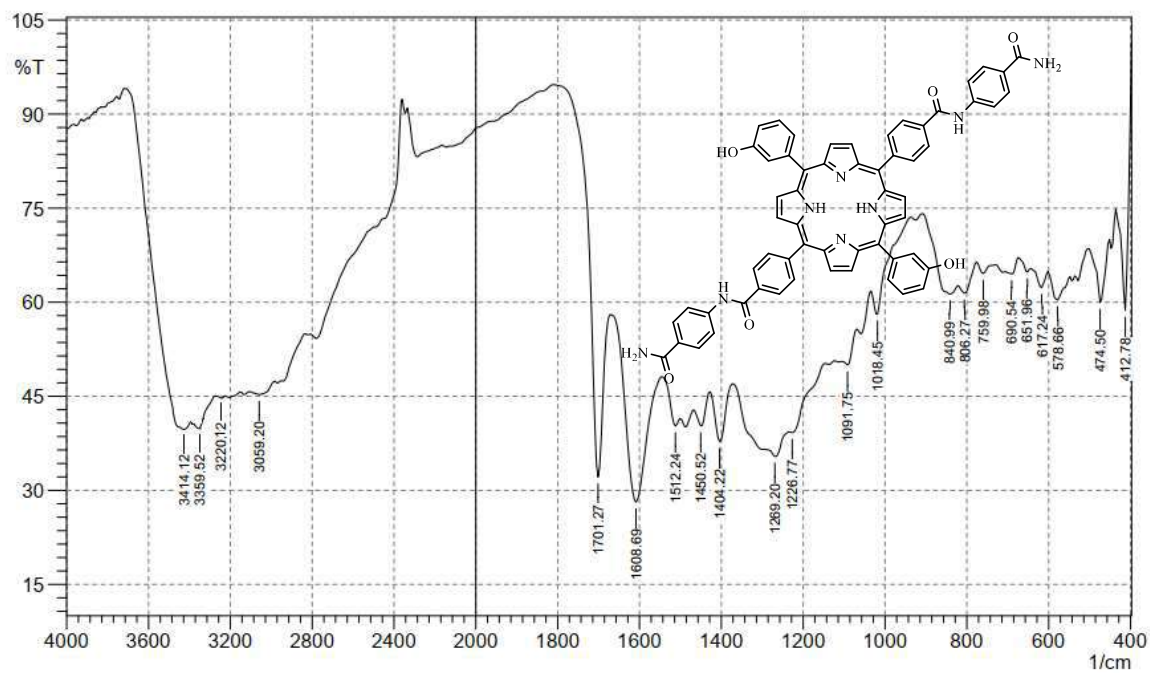
Figure 87: Mass spectrum of compound (13d)
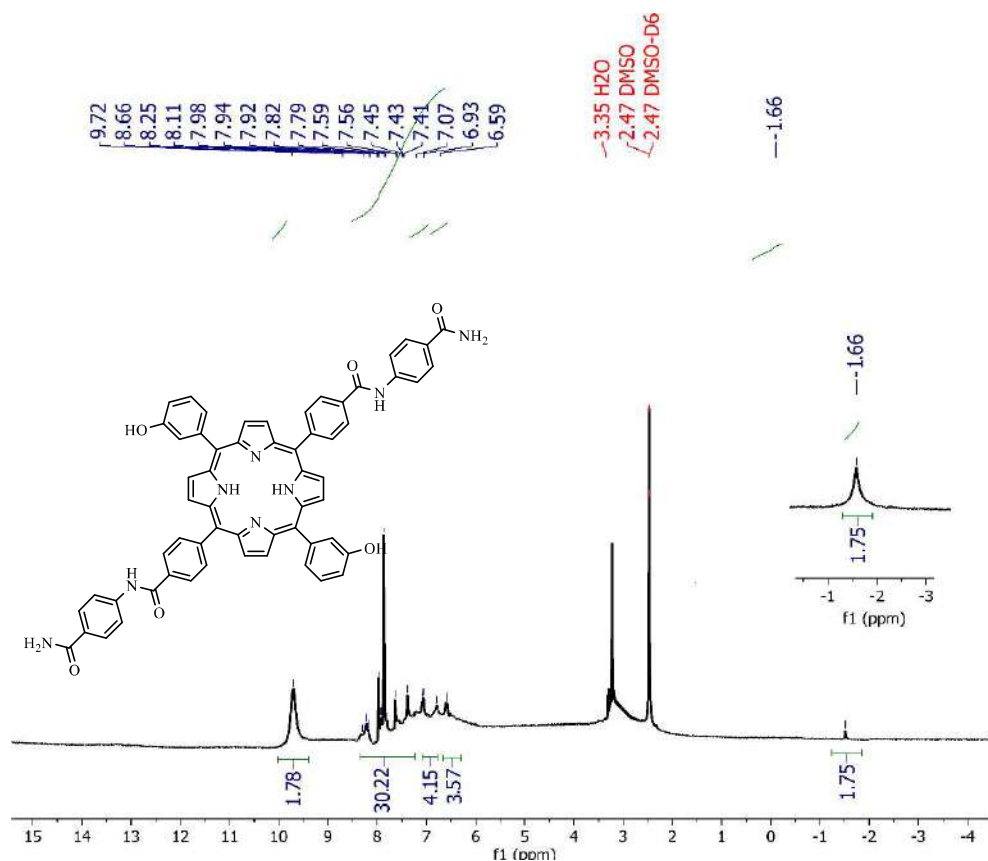

Figure 88: FT-IR spectrum of compound (13e)
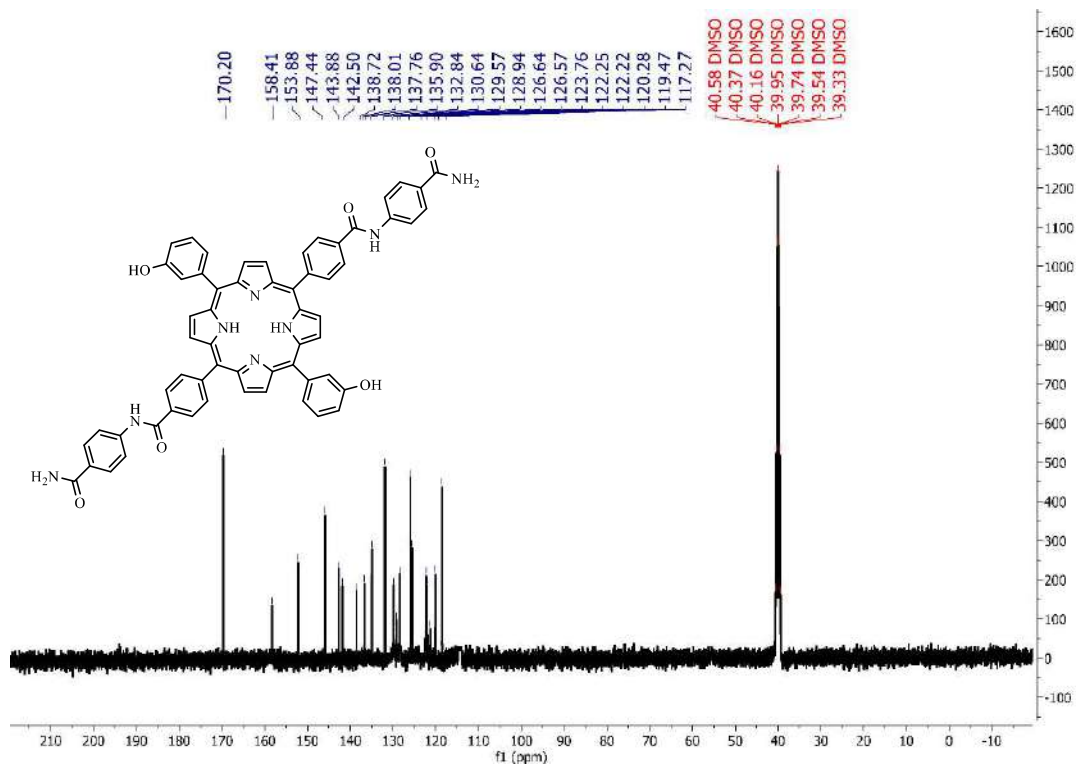
Figure 89: ^{1}HNMR spectrum of compound (13e)

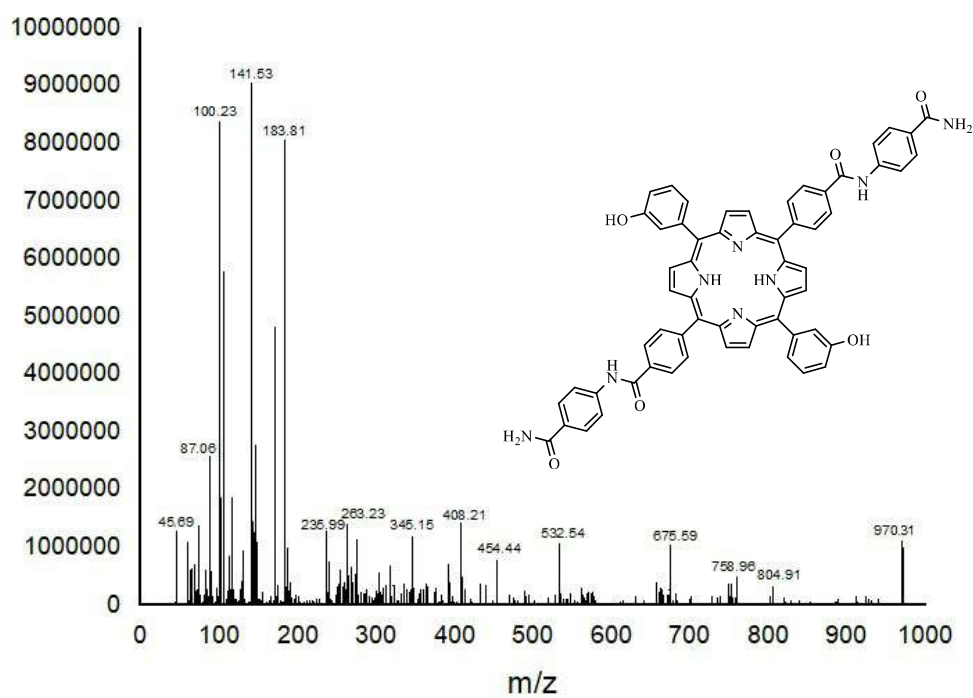**Figure 90:** ^{13}CNMR spectrum of compound (13e)

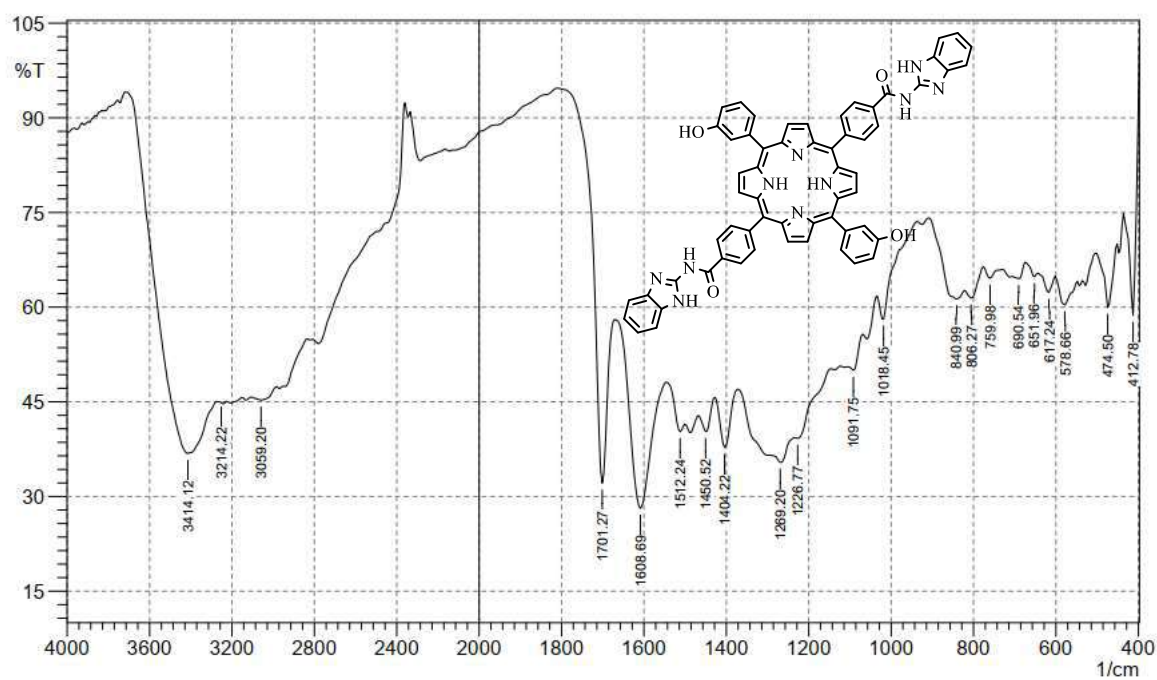**Figure 91:** Mass spectrum of compound (13e)

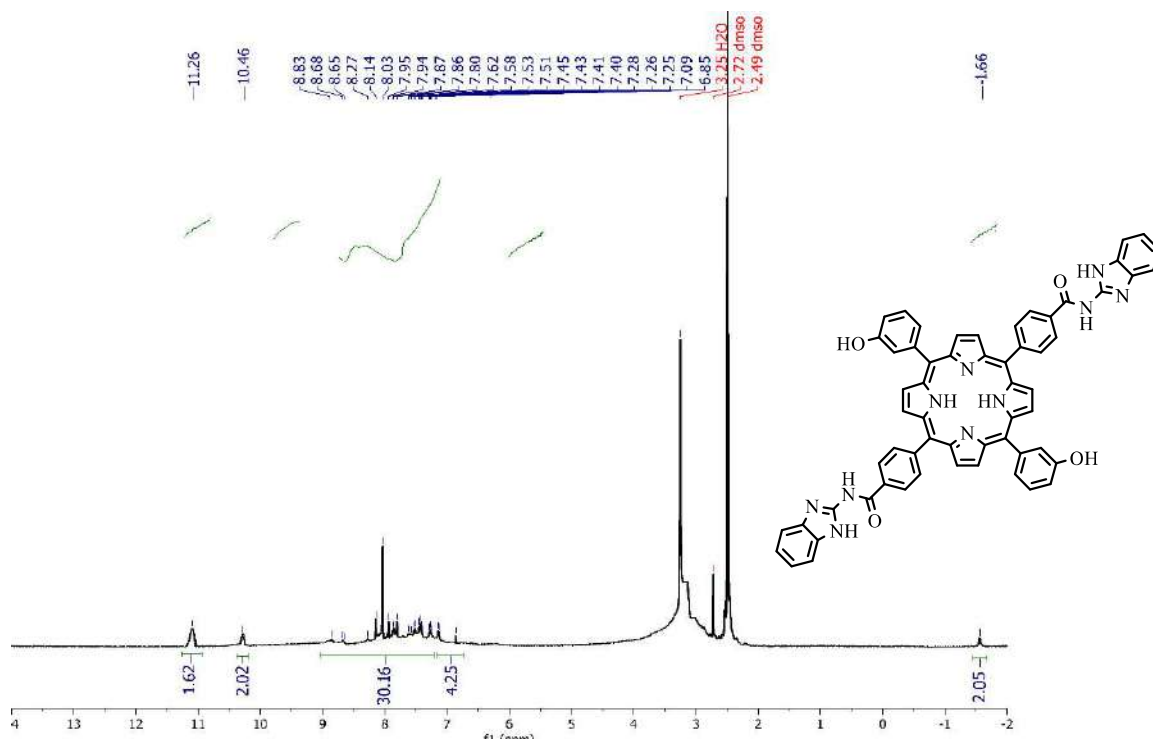**Figure 92:** FT-IR spectrum of compound (13f)

Figure 93: ^{1}HNMR spectrum of compound (13f)

الخلاصة

الخلاصة

تضمن هذا العمل تصنيع سلسلتين جديدتين من المشتقات الحلقية غير المتجانسة الجديدة من العديد من مشتقات البورفيرين (4,4',4",4"'-(البورفيرين-5، 10، 15، 20-تيترايل) حمض البنزويك) مركب (3)، (4-(10,15,20-تريس (3-هيدروكسي فينيل) بورفيرين-5-يل) حمض البنزويك) مركب (8)، و (4، '4-(10، 20-مكرر (3-هيدروكسي فينيل) بورفيرين-5، 15-دييل) حمض البنزويك) مركب (12) انجزت عملية تحضير هذه المركبات عن طريق تفاعل بيرول مع 4-فورميل حمض البنزويك في نسب المولية مختلفة. بعد ذلك، تم إنتاج الأميدات المكونة لمشتقات البورفيرين (5a-f) و(6a-f) عن طريق تفاعل المركب (3) مع أمينات مختلفة وبنسبة مولية مختلفة في وعاء واحد. حضر مشتق البورفيرين-مكون أميدات (9a-d) و(11a-e) عن طريق تفاعل المركب (8) مع أمينات مختلفة بنسبة مولية مختلفة في وعاء واحد. كما حضر مشتق البورفيرين-مكون أميدات (13a-f) عن طريق تفاعل المركب (12) مع أمينات مختلفة بنسبة مولية 1:2 في وعاء واحد.

وقد حضر كرفن كونتم دوت (GQD) من النشا كبادئ في وعاء واحد باستخدام العملية الحرارية المائية. كما تم تحضير المتراكب النانوي TiO$_2$/GQD باستخدام تقنية الموجات فوق الصوتية المتعمقة لاستخدامها كأنود في الخلية الشمسية. وجدن التحليلات ان GQD هو مادة نانوية وتمتلك معدل حجم بلوري ومعدل حجم جسيمات مساوي الى 9.25 نانومتر و11.05 نانومتر، وقد ازدادت القيم بعد تكوين المتراكب الى 34.39 نانو متر و79.47 نانومتر على التوالي.

حضر شبه الموصل الكادميوم فرايت (CdFe$_2$O$_4$) من نترات الحديديك (Fe(NO$_3$)$_3$.9H$_2$O)وكلوريد الكادميوم (CdCl$_2$.2H$_2$O)عن طريق طريقة الترسيب بوجود مغير شد سطحي موجب الشحنة (CTAB). كما حضر المتراكب TiO$_2$/CdFe$_2$O$_4$ باستخدام تقنية الموجات فوق الصوتية واستخدامها كأنود في الخلايا الشمسية ، لوحظ من خلال نتائج الXRD زيادة الحجم البلوري لـCdFe$_2$O$_4$ بعد تكوين متراكبه من 21.07 نانومتر الى 36.96 نانومتر

في هذا العمل، تم استخدام TiO$_2$ مع الأصباغ 3 و8 كأنودات لتحليل الخلايا الشمسية الحساسة للصبغة (DSSCs). وجد بان أفضل كفاءة التحويل الكهروضوئية (PEC%) مع TiO$_2$مع الصبغات 3 و8 والتي اعطت جهد لتحسين أداء الخلايا الشمسية. بالإضافة إلى ذلك، تم الانتفاع من المتراكب TiO$_2$/CdFe$_2$O$_4$ عند استخدامه كأنود في الخلية DSSCs وقد اعطت أعظم كفاءة مقارنة باستخدام المتراكب TiO$_2$/GQD كأنود.

وتم التحقيق في نشاط المواد المركبة كمثبط للتآكل باستخدام الكربون الصلب (CS) كنموذج للمواد المتآكلة. وأظهرت النتائج التي تم الحصول عليها أن مشتقات البورفيرينات المحضرة كانت مثبطات فعالة للتآكل

أ

الخلاصة

في محلول حمض الهيدروكلوريك (0.1M) للكربون الصلب. في حالة المشتق (5c)، تم تسجيل أقصى كفاءة تثبيط (%IE) وكانت حوالي 74٪.

جامعة كربلاء
كلية العلوم
قسم الكيمياء

توظيف مشتقات جديدة للبورفرين لبعض التطبيقات

أطروحة مقدمة الى كلية العلوم / جامعة كربلاء

وهي جزء من متطلبات نيل درجة الدكتوراة في علوم الكيمياء

من قبل

محمد ثامر جعفر

بكالوريوس علوم في الكيمياء (2007) جامعة المستنصرية
ماجستير علوم في الكيمياء العضوية (2013) جامعة القاهرة

إشراف

<table>
<tr><td>أ. د رحمن طعمة هيول</td><td>أ. د لمى مجيد احمد</td></tr>
<tr><td>أ. د لمى مجيد احمد</td><td></td></tr>
</table>

1445 هــ   **2023 م**